Elastodynamic Marchenko inverse scattering

A multiple-elimination strategy for imaging of elastodynamic seismic reflection data

Reinicke Urruticoechea, Christian

DOI
10.4233/uuid:2122e7cc-0f07-40af-88cd-b5b789974562

Publication date
2020

Document Version
Final published version

Citation (APA)
Reinicke Urruticoechea, C. (2020). *Elastodynamic Marchenko inverse scattering: A multiple-elimination strategy for imaging of elastodynamic seismic reflection data*. [Dissertation (TU Delft), Delft University of Technology]. https://doi.org/10.4233/uuid:2122e7cc-0f07-40af-88cd-b5b789974562

Elastodynamic Marchenko inverse scattering

A multiple-elimination strategy for imaging of elastodynamic seismic reflection data

Elastodynamic Marchenko inverse scattering

A multiple-elimination strategy for imaging of elastodynamic seismic reflection data

Dissertation

for the purpose of obtaining the degree of doctor
at Delft University of Technology,
by the authority of the Rector Magnificus, prof. dr. ir. T.H.J.J. van der Hagen,
chair of the Board for Doctorates,
to be defended publicly on
Friday, 13 March 2020 at 10:00 o'clock

by

Christian REINICKE URRUTICOECHEA

Master of Science in Applied Geophysics,
Delft University of Technology, Netherlands,
born in Munich, Germany.

This dissertation has been approved by the promotor:
Prof. dr. ir. C. P. A. Wapenaar

Composition of the doctoral committee:

Rector Magnificus	chairman
Prof. dr. ir. C. P. A. Wapenaar	Delft University of Technology, promotor

Independent members:

Prof. dr. A. Curtis	The University of Edinburgh, United Kingdom
Prof. dr. ir. E. C. Slob	Delft University of Technology
Prof. dr. W. A. Mulder	Delft University of Technology
Prof. dr. ir. D. J. Verschuur	Delft University of Technology
Prof. dr. ir. J. T. Fokkema	Delft University of Technology

Other members:

Dr. M. S. Dukalski	Aramco Overseas Company B.V.

Keywords: Marchenko, de-multiple, inverse scattering, elastodynamic waves

ISBN 978-94-6384-111-5

Typesetting system: LaTeX.
Printed in The Netherlands by Ipskamp printing, Amsterdam.

An electronic version of this dissertation is available at
`http://repository.tudelft.nl/`.

To my family.

Summary

The Marchenko method offers a new perspective on eliminating internal multiples. Instead of predicting internal multiples based on events, the Marchenko method formulates an inverse problem that is solved for an inverse transmission response. This approach is particularly advantageous when internal multiples generate complicated interference patterns, such that individual events cannot be identified.

Moreover, the retrieved inverse transmissions can be used for a wide range of applications. For instance, we present a numerical example of the single-sided homogeneous Green's function representation in elastic media. These applications require a generalization of the Marchenko method beyond the acoustic case. Formally these extensions are nearly straightforward, as can be seen in the chapter on plane-wave Marchenko redatuming in elastic media. Despite the formal ease of these generalizations, solving the aforementioned inverse problem becomes significantly more difficult in the elastodynamic case.

We analyze fundamental challenges of the elastodynamic Marchenko method. Elastic media support coupled wave-modes with different propagation velocities. These velocity differences lead to fundamental limitations, which are due to differences between the temporal ordering of reflection events and the ordering of reflectors in depth. Other multiple-elimination methods such as the inverse scattering series encounter similar limitations, due to violating a so-called monotonicity assumption. Nevertheless, we show that the Marchenko method imposes a slightly weaker form of the monotonicity assumption because it does not rely on event-based multiple prediction.

Another challenge arises from the initial estimate that is required by the Marchenko method. In the acoustic case, this initial estimate can be as simple as a direct transmission from the recording surface to the redatuming level. In the presence of several wave-modes, an acoustic direct transmission generalizes to a so-called forward-scattered transmission, which is not a single event but a wavefield with a finite temporal duration. Former formulations of the elastodynamic Marchenko method require this forward-scattered transmission as an initial estimate. However, in practice, this initial estimate is often unknown.

We present an alternative formulation of the elastodynamic Marchenko method that simplifies the initial estimate to a trivial one. This approach replaces the inverse transmission, which is often referred to as a focusing function, by a so-called backpropagated focusing function. This strategy allows us to remove internal multiples, however, unwanted forward-scattered waves persist in the data. This insight suggests that forward-scattered waves cannot be predicted by the Marchenko method: either they are provided as prior knowledge, or they remain unaddressed.

The remaining forward-scattered waves may be eliminated by exploiting minimum-phase behavior as additional constraint. This approach is inspired by recent developments of the acoustic Marchenko method that use a minimum-phase constraint to handle short-period multiples. Generalizing this strategy to the elastodynamic case is challenging because wavefields are no longer described by scalars but by matrices. Hence, we start by analyzing the meaning of minimum-phase in a multi-dimensional sense. This investigation illustrates that the aforementioned backpropagation turns the focusing function into a minimum-phase object. This insight suggests that, from a mathematical view point, the backpropagated focusing function can be seen as a more fundamental version of the focusing function. Moreover, we present attempts of using this property as additional constraint to remove unwanted forward-scattered waves.

Given the remaining theoretical challenges of the elastodynamic Marchenko method, we analyze the performance of an acoustic approximation. We evaluate the effect of applying the acoustic Marchenko method to elastodynamic reflection data. For this analysis, we look for geological settings where an acoustic approximation could be impactful. The Middle East is a promising candidate because, due to its nearly horizontally-layered geology, elastic scattering effects are weaker for short-offsets, which are the main contributors to structural images. Therefore, we construct a synthetic Middle East model based on regional well-log data as well as knowledge about the regional geology. In contrast to field data examples, the synthetic study allows us to include or exclude elastic effects. Hence, we can inspect the artifacts caused by an acoustic approximation. The results indicate that the acoustic Marchenko method can be sufficient for multiple-free structural imaging in geological settings akin to the Middle East.

Samenvatting

De Marchenko methode biedt een nieuw perspectief op het elimineren van interne meervoudige reflecties (zgn. multiples). In plaats van het voorspellen van interne meervoudige reflecties op basis van individuele reflectie aankomsten (zgn. events), formuleert de Marchenko methode een inversie probleem dat wordt opgelost voor een geïnverteerde transmissierespons. Deze benadering is buitengewoon geschikt wanneer interne meervoudige reflecties gecompliceerde interferentiepatronen genereren, zodat individuele aankomsten niet geïdentificeerd kunnen worden.

Daarnaast kunnen de verkregen geïnverteerde transmissies worden gebruikt voor een breed scala aan toepassingen. We presenteren bijvoorbeeld een numeriek voorbeeld van de enkelzijdige homogene Greense functie representatie in elastische media. Deze toepassingen vereisen een generalisatie van de Marchenko methode die verder gaat dan de akoestische situatie. Formeel zijn deze uitbreidingen bijna triviaal, zoals te zien is in het hoofdstuk over Marchenko redatumen met vlakke golven in elastische media. Ondanks het feit dat deze generalisaties formeel gemakkelijk zouden moeten zijn, wordt het oplossen van het bovengenoemde inversie probleem aanzienlijk moeilijker in het elastodynamische geval.

We analyseren fundamentele uitdagingen van de elastodynamische Marchenko methode. Elastische media ondersteunen gekoppelde golfmodi met verschillende voortplantingssnelheden. Deze snelheidsverschillen leiden tot fundamentele beperkingen, die het gevolg zijn van verschillen tussen de temporele volgorde van reflectie aankomsten en de volgorde van reflectoren in de diepte. Andere eliminatiemethoden voor meervoudige reflecties, zoals de inverse verstrooiïngsreeks (ook bekend als ISS), ondervinden vergelijkbare beperkingen vanwege het schenden van een zogenaamde monotoniciteitsveronderstelling. Desalniettemin laten we zien dat de Marchenko methode een iets zwakkere vorm van de monotoniciteitsveronderstelling oplegt, omdat deze niet afhankelijk is van een op aankomsten gebaseerde voorspelling van meervoudige reflecties.

Een andere uitdaging komt voort uit de initiële schatting die de Marchenko methode vereist. Deze initiële schatting kan in het akoestische geval erg simpel zijn.

Bijvoorbeeld, de directe transmissie van het opname-oppervlak naar het redatumen niveau kan hiervoor gebruikt worden. In de aanwezigheid van verschillende golfmodi, generaliseert een akoestische directe transmissie naar een zogenaamde voorwaarts verstrooide transmissie, dus niet een enkele aankomst maar een compleet golfveld met een eindige tijdsduur. Eerdere formuleringen van de elastodynamische Marchenko methode vereisen deze voorwaarts verstrooide transmissie als een initiële schatting. In de praktijk is deze initiële schatting vaak niet bekend.

We presenteren een alternatieve formulering van de elastodynamische Marchenko methode die de initiële schatting vereenvoudigt tot een triviale. Deze benadering vervangt de inverse transmissie, ook wel bekend als een focuseringsfunctie, door een zogenaamde teruggepropageerde focuseringsfunctie. Met deze strategie kunnen we interne meervoudige reflecties verwijderen, maar ongewenste voorwaarts verstrooide golven blijven in de data aanwezig. Dit inzicht suggereert dat voorwaarts verstrooide golven niet kunnen worden voorspeld met de Marchenko methode: ofwel ze worden verstrekt als voorkennis, of ze blijven achterwege.

De resterende voorwaarts verstrooide golven kunnen worden geëlimineerd door minimum-fase als extra voorwaarde op te leggen. Deze benadering is geïnspireerd op recente ontwikkelingen van de akoestische Marchenko methode die een minimumfasebeperking gebruiken om meervoudige reflecties met een klein onderling tijdverschil te verwerken. Het generaliseren van deze strategie naar het elastodynamische geval is een uitdaging omdat golfvelden niet langer worden beschreven door scalairen, maar door matrices. Daarom beginnen we met het analyseren van de betekenis van minimumfase in een multidimensionale betekenis. Dit onderzoek illustreert dat het bovengenoemde terugpropageren de focuseringsfunctie verandert in een object met minimale fase. Dit inzicht suggereert dat, vanuit een wiskundig oogpunt, de teruggepropageerde focuseringsfunctie kan worden gezien als een meer fundamentele versie van de focuseringsfunctie. Bovendien presenteren we pogingen om deze eigenschap te gebruiken als extra voorwaarde om ongewenste voorwaarts verstrooide golven te verwijderen.

Gezien de resterende theoretische uitdagingen van de elastodynamische Marchenko methode, analyseren we de mogelijkheden van een akoestische benadering. We evalueren het effect van het toepassen van de akoestische Marchenko methode op elastodynamische reflectie data. Voor deze analyse zoeken we naar geologische gebieden waar een akoestische benadering kan voldoen. Het Midden-Oosten is een veelbelovende kandidaat omdat, vanwege de bijna horizontaal gelaagde geologie, elastische verstrooiïngseffecten zwakker zijn voor data opgenomen door ontvangers dichtbij de bron, die de belangrijkste bijdrage leveren aan structurele afbeeldingen. Voor dit experiment construeren we een synthetisch Midden-Oosten model op basis van boorputdata in de regio en kennis van de regionale geologie. In tegenstelling tot studies met veld data, stelt de synthetische studie ons in staat om elastische effecten wel of niet mee te nemen. Daardoor kunnen we onbedoelde bijverschijnselen inspecteren die worden veroorzaakt door onverklaarbare aankomsten. De resultaten geven aan dat de akoestische Marchenko methode voldoende kan zijn voor structurele beeldvorming zonder verstoring door meervoudige reflecties in geologische omgevingen vergelijkbaar met het Midden-Oosten.

Contents

1

Introduction

Multiple reflections can be considered as perverse forms of primary energy.

Jakubowicz, 1998

Our society relies on a wide range of geotechnical operations. These activities include the exploration of natural resources such as hydrocarbon, water or heat reservoirs, the storage of nuclear waste and CO_2, subsurface monitoring, etc. Often images of the subsurface are used to identify suitable locations for the aforementioned applications. By developing more accurate imaging methods, we can contribute to localize target areas and to increase the safety and the efficiency of these operations.

Imaging workflows start with seismic experiments, which allow us to inspect the interior of the Earth. Often in those experiments, an active source emits a wavefield that interacts with the medium (i.e. Earth) via propagation and scattering. The history of this interaction is encrypted in the response of the medium. In practice, the response is not recorded on an enclosing boundary, such that extracting information from the recordings can become extremely challenging. In many cases, the recordings are limited to reflection data, i.e. sources and receivers are located at the surface of the Earth.

The term reflection data describes a wide range of acquisition designs. In the early days, only a single or very few measurements were recorded per seismic experiment. These recordings consist of individual channels, or time series, that represent a set of 1D responses of the 3D subsurface. As a result, the respective seismic processing tools usually rely on a 1D assumption, i.e. a horizontally-layered Earth model. Considering that scattering effects beyond 1D are challenging for these approaches, it is no surprise that scattering interactions between different elastic wave modes are even less well described.

Over the last decades, the quantity and the quality of reflection data have increased significantly. Since contemporary seismic surveys usually employ numerous sources and receivers, reflection data no longer represent just a single channel but a wavefield. Furthermore, modern acquisitions often record several components of the wavefield such as pressure and particle velocity. These multi-component recordings pave the way to also analyze elastic scattering effects. In parallel to the developments on the side of data acquisition, there has been a continuous development of new seismic processing techniques that aim to extract as much information as possible from the recorded data.

Modern seismic processing workflows can be divided into two major subprocesses. Firstly, large scale (spatial) variations of the medium are estimated. This process is often referred to as macro-velocity model building and relies on several tools such as tomography [*Sword*, 1944; *Dix*, 1955; *Billette and Lambaré*, 1998], normal-moveout analysis [*Levin*, 1971; *Doherty and Claerbout*, 1976; *Sattlegger*, 1978] and full waveform inversion [*Virieux and Operto*, 2009].

Secondly, smaller scale (spatial) variations of the medium are typically analyzed by migration-based techniques. These methods reconstruct the boundaries that delineate changes in the medium parameters, in such a way, that the resulting model is consistent with the reflection data, the macro-velocity model and the wave equation [*Schneider*, 1978; *Berkhout*, 1982; *Claerbout*, 1985]. A key assumption of traditional migration methods is a single-scattering approximation, i.e. it is assumed that recorded waves are only reflected once [with exceptions such as full-wavefield migration by *Davydenko and Verschuur*, 2017]. Hence, waves that are reflected multiple times (=multiples) are treated as if they were reflected a single time (=primaries), which leads to erroneous migration images.

Usually, there is a distinction between surface-related and internal multiples, both of which can generate imaging artifacts. These multiple-related artifacts are minor provided that: Either, the medium only scatters weakly, such that multiples are negligible. Or, seismic velocity variations are sufficiently strong, and preferably only increasing with depth. As a result, the normal-moveout of multiples is inconsistent with the macro-velocity model and only generates minor contributions to the migration result. However, there are many geological settings where multiples cannot be ignored and lead to severe migration artifacts. For example, in the Middle East internal multiples form a severe problem because the geology is characterized by sequential variations between high and low propagation velocities [*El-Emam et al.*, 2011]. Due to the importance of this issue, so-called multiple-elimination methods are needed and have developed into an entire research field within geophysics.

The handling of multiples in seismic reflection data is a longstanding problem [an overview is provided by *Verschuur*, 2013]. One of the first solution strategies has been predictive deconvolution. This method is based on a 1D assumption, which only in a few scenarios is reasonable, e.g. for the removal of multiples associated with vertical propagation inside a water layer. With the appearance of multi-dimensional acquisitions, wave-equation-based methods for multiple elimination came to light.

Firstly, there are methods for surface-related multiple removal. Early developments predict surface-related multiples via wavefield extrapolation, which subsequently are subtracted from the reflection data [*Berkhout and de Graaff*, 1982; *Wig-*

gins, 1988]. Later these model-driven approaches have been replaced by data-driven methods. The latter ones include not only multiple prediction and subtraction strategies [*Verschuur et al.*, 1992], but also methods that suppress surface-related multiples by sparse inversion [*Lin and Herrmann*, 2013]. All of these methods rely on an estimate of the reflection coefficient of the surface, which particularly in the marine case is often known.

Secondly, there are methods for the elimination of internal multiples. Typically these methods do not require any information about the reflection coefficients inside the medium, but they often assume that surface-related multiples have been removed. Methods such as the one by *Jakubowicz* [1998], or the inverse scattering series [ISS, *Weglein et al.*, 1997], predict internal multiples by combining triplets of primaries. Subsequently, the predicted multiples are adaptively subtracted. By applying this prediction-subtraction approach in a layer-stripping fashion, internal multiples are recursively removed. In case of sparsely-distributed (non-periodic) multiple generators, this strategy can perform well. However, as multiple generators become more numerous, challenges arise, e.g. when multiples coincide with primaries. In this scenario, primaries may be erroneously removed by the adaptive subtraction. Due to the layer-stripping approach, the removed primaries cannot be used to predict multiples, i.e. the prediction error accumulates. An alternative is provided by Marchenko-equation-based multiple-elimination methods, or briefly *the Marchenko method*, which completely abandon the concept of triplet- i.e. event-based multiple prediction.

The Marchenko method aims to remove internal multiples by retrieving an inverse transmission from the reflection response. The underlying multiple-elimination strategy is as follows [*Broggini and Snieder*, 2012; *Slob et al.*, 2014; *Wapenaar et al.*, 2014a]: First, the medium is partitioned in a shallower and a deeper part, which are often referred to as overburden and target, respectively. Secondly, up- and downgoing Green's functions associated with measurements at the surface and at the depth level, that separates the overburden from the target, are retrieved. Finally, all scattering interactions with the overburden including internal multiples can be removed via an Amundsen deconvolution of the retrieved Green's functions [*Wapenaar et al.*, 2000; *Amundsen*, 2001].

The Green's function retrieval represents the core of the Marchenko method. Starting with reciprocity theorems, one can derive two representation theorems that mutually relate the reflection response with the Green's functions and the so-called focusing functions. Since the Green's and focusing functions are decomposed in up- and downgoing components, they represent four one-way wavefields. Note that the downgoing focusing function is the aforementioned inverse transmission through the overburden. In practice, the two Green's as well as the two focusing functions are unknown. Hence, the two representation theorems form an underdetermined inverse problem with two equations and four unknowns. A simple temporal mute can be applied to the representation theorems that preserves the focusing functions but partially removes the Green's functions. In many cases, the remaining part of the Green's functions, i.e. the temporal overlap between Green's and focusing functions, is merely a direct wave through the overburden. This direct wave can often be estimated using a macro-velocity model, that can be obtained via the above-mentioned methods for large scale medium characterization. As a result, the two remaining unknowns, up- and downgoing focusing functions, can be retrieved from the (partially muted) representation theorems. These modified equations form a set of coupled Marchenko equations, which explains the name of this method. During recent years, many aspects of the Marchenko method have been investigated. In particular, there are already several field data examples [*Ravasi et al.*, 2016; *Staring et al.*, 2018]. Moreover, modified formulations have been developed to: alleviate the need for a macro-velocity model [*van der Neut and Wapenaar*, 2016], account for dissipation [*Slob*, 2016; *Cui et al.*, 2018], perform plane-wave imaging [*Meles et al.*, 2018], retrieve primary-only reflection data [*Zhang and Slob*, 2018], handle short-period multiples [*Dukalski et al.*, 2019; *Elison*, 2019], estimate the source wavelet [*Mildner et al.*, 2019a], monitor induced distributed double-couple sources [*Brackenhoff et al.*, 2019], etc.

The aforementioned developments of the Marchenko method only consider acoustic waves. Nevertheless, elastic media support compressional and shear waves, which are mutually coupled. Hence, for accurate multiple-elimination, elastic effects must be taken into account. This is particularly true when coupling between elastic modes is strong. Early attempts of elastic multiple-elimination are presented by *Ware and Aki* [1969]. However, their work is restricted to cases where the elastic modes are decoupled (they considered vertically propagating waves in horizontally-layered media).

This thesis focuses on the extension of the Marchenko method to elastodynamic waves. An early attempt of such an elastodynamic generalization has been made by *Da Costa Filho et al.* [2014]. However, these authors did not consider the fact that the elastodynamic Green's and focusing functions share a temporal overlap that is much more complicated than a direct wave. Since an estimate of this overlap is required by the above-described Marchenko method, further developments are necessary to make its elastodynamic extension an applicable multiple-elimination method. It has been shown (prior to this thesis) that the overlap between the elastodynamic Green's and focusing functions consists of a so-called forward-scattered transmission response [*Wapenaar*, 2014]. Although forward-scattered waves can also be generated by acoustic media, they can often be ignored for sufficiently-simple geometries. In contrast, coupled elastodynamic wave-modes can easily generate strong, and complicated, interference patterns of forward-scattered waves, that significantly affect the result of the Marchenko method [*Wapenaar and Slob*, 2015]. The objectives of this thesis are to further investigate and to overcome the challenges of extending the Marchenko method to elastic media. The thesis contains the following chapters:

- Chapter 2: *Elastodynamic single-sided homogeneous Green's function representation.*
  In this chapter, a single-sided representation of the homogeneous Green's function associated with sources and receivers inside an elastic medium is analyzed. The theory part of this chapter follows from the theory presented by *Wapenaar et al.* [2016a]. In contrast, the presented numerical examples of the single-sided elastodynamic homogeneous Green's function representation are

unprecedented.

- Chapter 3: *Elastodynamic Marchenko method using plane waves.*
  In this chapter, a Marchenko redatuming strategy using plane waves is derived. The presented work is an elastodynamic extension of the plane-wave Marchenko method by *Meles et al.* [2018]. This modification can be seen as a combination of imaging with areal sources [*Rietveld et al.*, 1992] and the Marchenko method.

- Chapter 4: *Comparison of monotonicity challenges encountered by the inverse scattering series and the Marchenko de-multiple method for elastic waves.*
  This chapter compares the conditions required by the elastodynamic inverse scattering series with those required by the elastodynamic Marchenko method. Further, a modified Marchenko method is proposed that simplifies the complicated initial estimate (the forward-scattered transmission) to a trivial one. Next, we indicate a strategy that may eliminate not only internal multiples but also unwanted forward-scattered waves. To proceed with the latter strategy a so-called normal product must be uniquely factorized with a minimum-phase condition, which is poorly understood beyond the scalar case.

- Chapter 5: *Towards normal product factorization with minimum-phase constraint.*
  This chapter aims to solve the aforementioned problem of factorizing a normal product. In general, this factorization problem is non-unique. To constrain this problem, the generalization of minimum-phase behavior from scalars to matrices is investigated. Furthermore, we present initial attempts of factorizing a normal product with a minimum-phase constraint.

- Chapter 6: *Impact of mode conversions on structural imaging with Marchenko de-multiple in geologies akin to the Middle East.*
  In this chapter, a synthetic case study is presented. For this analysis, synthetic data are desirable because elastic effects can be included or excluded. This study demonstrates that the acoustic Marchenko method can be sufficient to reliably handle internal multiples that are generated by an elastic medium. This work focuses on geological settings akin to the Middle East. The results show that the acoustic Marchenko method can already be used as a powerful multiple-elimination method for elastodynamic reflection data acquired in comparable geological settings.

- Appendices: *An acoustic imaging method for layered non-reciprocal media* and *Unified wave field retrieval and imaging method for inhomogeneous non-reciprocal media.*
  In the appendices, the Marchenko method is modified to be applied in non-reciprocal media. The author of this thesis developed software for wavefield modeling in non-reciprocal media and conducted the presented numerical experiments.

2

Elastodynamic single-sided homogeneous Green's function representation

Abstract The homogeneous Green's function is the difference between an impulse response and its time-reversal. According to existing representation theorems, the homogeneous Green's function associated with source-receiver pairs inside a medium can be computed from measurements at a boundary enclosing the medium. However, in many applications such as seismic imaging, time-lapse monitoring, medical imaging, non-destructive testing, etc., media are only accessible from one side. A recent development of wave theory has provided a representation of the homogeneous Green's function in an elastic medium in terms of wavefield recordings at a single (open) boundary. Despite its single-sidedness, the elastodynamic homogeneous Green's function representation accounts for all orders of scattering inside the medium. We present the theory of the elastodynamic single-sided homogeneous Green's function representation and illustrate it with numerical examples for 2D laterally-invariant media. For propagating waves, the resulting homogeneous Green's functions match the exact ones within numerical precision, demonstrating the accuracy of the theory. In addition, we analyse the accuracy of the single-sided representation of the homogeneous Green's function for evanescent wave tunnelling.

Published as: Reinicke, C., and Wapenaar, K. (2019), Elastodynamic single-sided homogeneous Green's function representation: Theory and numerical examples, *Wave Motion*, **89**, 245-264, https://doi.org/10.1016/j.wavemoti.2019.04.001.
Note that minor changes have been introduced to make the text consistent with the other chapters.

2.1 Introduction

The homogeneous Green's function is the difference between an impulse response and its time-reversal. In the absence of losses, the wave equation is symmetric in time. Therefore, an impulse response to a source and its time-reversal satisfy the same wave equation. By subtracting the wave equations for these two responses from each other, we obtain a wave equation with a source term equal to zero, and a solution: the homogeneous Green's function.

In optics, *Porter* [1970] used a closed-boundary representation of the homogeneous Green's function to retrieve the wavefield inside a medium. This representation has been the basis for inverse source problems [*Porter and Devaney*, 1982] as well as inverse-scattering methods [*Oristaglio*, 1989]. Unfortunately, in many practical situations, there is only single-sided access to the medium. When measurements are absent at a substantial part of the closed boundary, the retrieved homogeneous Green's function will suffer from significant artefacts. In particular in the presence of strong internal multiple scattering, these artefacts become more severe.

The closed-boundary representation can be modified to become an integral representation over the top and bottom boundaries of the medium if the medium has infinite horizontal extent [e.g. *Haines and de Hoop*, 1996; *Kennett et al.*, 1990]. Further, a recent progress of wave theory has demonstrated that, after appropriate modification of the homogeneous Green's function representation, the integral contribution from the bottom boundary vanishes [*Wapenaar et al.*, 2016a]. The result is a single-sided homogeneous Green's function representation. This representation correctly describes the wavefield inside the medium, including all orders of scattering, but excluding evanescent waves. The form of the single-sided representation is similar to the closed-boundary representation. However, the single-sided representation uses a so-called focusing function instead of the time-reversed Green's function [*Wapenaar et al.*, 2016a]. For acoustic waves, the focusing function can be retrieved from a single-sided reflection response and an estimate of the direct arrival, using the Marchenko method [e.g. *Broggini and Snieder*, 2012; *Wapenaar et al.*, 2014b; *Vasconcelos et al.*, 2015]. In the elastodynamic case, the approximate focusing function can be retrieved in a similar way [*Da Costa Filho et al.*, 2014; *Wapenaar*, 2014]. However, an exact retrieval of the elastodynamic focusing function requires additional information about the medium [*Wapenaar*, 2014]. In this paper, we assume that the elastodynamic focusing function is available (obtained either approximately by the Marchenko method or by direct modelling when the medium is known). The single-sided representation theorem provides the mathematical framework to place virtual sources and/or receivers inside the medium. Imaging techniques, e.g. for medical or geophysical applications with limited access to the medium, could benefit from this. Furthermore, virtual receivers inside a medium could be used for time-lapse monitoring purposes, i.e. to observe changes in a medium over time. Other potential applications could be forecasting the medium response to induced sources, or the localisation of passive sources inside a medium such as an earthquake [*Brackenhoff et al.*, 2019].

We outline the theory of the single-sided homogeneous Green's function representation for elastodynamic waves in lossless media. Further, we evaluate the accuracy of the elastodynamic single-sided homogeneous Green's function representation numerically for 2D layered media. For the evaluation we use a directly modelled homogeneous Green's function as a reference. Eventually, we present an example in which the wavefield has wavenumber-frequency components that are evanescent only inside a thin layer between the recording boundary and the target depth. We demonstrate that these evanescent wavenumber-frequency components of the elastodynamic homogeneous Green's function are accounted for by the single-sided representation, except for small numerical errors.

2.2 Theory

This section consists of three parts. In the first part we show the definition of the decomposed matrix-vector wave equation. In the second part we define the elastodynamic homogeneous Green's function, and in the third part, we introduce the elastodynamic single-sided homogeneous Green's function representation. A detailed derivation of this representation can be found in 2A.

■ 2.2.1 Matrix-vector wave equation for decomposed wavefields

We represent the elastodynamic wavefield using powerflux-normalised P- and S-wavefield potentials. Besides, we choose the depth direction x_3 as a preferential direction of propagation. For this reason, we decompose the wavefield in downward and upward propagating waves [*de Hoop and de Hoop*, 1994; *Frasier*, 1970; *Wapenaar*, 1996b], and we define a 6×1 wave vector $\mathbf{p}$ containing decomposed wavefields and a 6×1 source vector $\mathbf{s}$ containing sources for these decomposed wavefields,

$$\mathbf{p} = \begin{pmatrix} \mathbf{p}^+ \\ \mathbf{p}^- \end{pmatrix}, \quad \mathbf{p}^+ = \begin{pmatrix} \Phi^+ \\ \Psi^+ \\ \Upsilon^+ \end{pmatrix}, \quad \mathbf{p}^- = \begin{pmatrix} \Phi^- \\ \Psi^- \\ \Upsilon^- \end{pmatrix}, \quad \mathbf{s} = \begin{pmatrix} \mathbf{s}^+ \\ \mathbf{s}^- \end{pmatrix}. \tag{2.2.1}$$

The superscript + refers to downgoing waves, the superscript − to upgoing waves. The wavefield potentials $\Phi^\pm$, $\Psi^\pm$, $\Upsilon^\pm$ represent the P, S1 and S2 waves, respectively (in cylindrical coordinates in a laterally-invariant medium, S1 and S2 waves are SV and SH waves). The decomposed source terms $\mathbf{s}^\pm$ are defined analogous to the decomposed wavefields $\mathbf{p}^\pm$. After applying a forward Fourier transform from the space-time to the space-frequency domain,

$$\mathbf{p}(\mathbf{x}, \omega) = \int \mathbf{p}(\mathbf{x}, t) \mathrm{e}^{\mathrm{i}\omega t} \mathrm{d}t, \tag{2.2.2}$$

the matrix-vector wave equation for decomposed wavefields can be written as,

$$\partial_3 \mathbf{p}(\mathbf{x}, \omega) - \mathcal{B}\, \mathbf{p}(\mathbf{x}, \omega) = \mathbf{s}(\mathbf{x}, \omega). \tag{2.2.3}$$

Here, i is an imaginary unit ($\mathrm{i}^2 = -1$), ∂_3 denotes a spatial derivative in the x_3 direction and the operator $\mathcal{B} = \mathcal{B}(\mathbf{x}, \omega)$ accounts for the propagation and the mutual coupling of the decomposed fields [an expression of $\mathcal{B}$ can be found in *Wapenaar et al.*, 2016a]. The spatial coordinates are denoted by $\mathbf{x} = (x_1, x_2, x_3)^T$, the time is denoted by t and the frequency is denoted by ω. The superscript T denotes a transpose. Further details about decomposed wavefields in 3D inhomogeneous media can be found in [*Wapenaar and Berkhout*, 1989; *Kennett et al.*, 1990; *Fishman*, 1993; *de Hoop and de Hoop*, 1994; *Fishman et al.*, 2000; *Thomson*, 2015].

2.2.2 Homogeneous Green's function

Consider the decomposed matrix-vector wave equation with a delta source term, $\mathbf{s} = \mathbf{I}\delta(\mathbf{x} - \mathbf{x}_s)$, where $\mathbf{I}$ is an identity matrix of appropriate size. The solution of this equation,

$$\partial_3 \mathbf{\Gamma}(\mathbf{x}, \mathbf{x}_s, \omega) - \mathcal{B}\,\mathbf{\Gamma}(\mathbf{x}, \mathbf{x}_s, \omega) = \mathbf{I}\delta(\mathbf{x} - \mathbf{x}_s), \tag{2.2.4}$$

is the Green's matrix $\mathbf{\Gamma}(\mathbf{x}, \mathbf{x}_s, \omega)$ containing decomposed wavefields,

$$\mathbf{\Gamma}(\mathbf{x}, \mathbf{x}_s, \omega) = \begin{pmatrix} \mathbf{G}^{+,+} & \mathbf{G}^{+,-} \\ \mathbf{G}^{-,+} & \mathbf{G}^{-,-} \end{pmatrix} (\mathbf{x}, \mathbf{x}_s, \omega). \tag{2.2.5}$$

Here, the first superscript describes the direction of the decomposed wavefields at the receiver position $\mathbf{x}$, the second superscript describes the direction of the decomposed source fields at the source position $\mathbf{x}_s$. The 3×3 submatrices $\mathbf{G}^{\pm,\pm}$ are defined as,

$$\mathbf{G}^{\pm,\pm}(\mathbf{x}, \mathbf{x}_s, \omega) = \begin{pmatrix} G^{\pm,\pm}_{\Phi,\Phi} & G^{\pm,\pm}_{\Phi,\Psi} & G^{\pm,\pm}_{\Phi,\Upsilon} \\ G^{\pm,\pm}_{\Psi,\Phi} & G^{\pm,\pm}_{\Psi,\Psi} & G^{\pm,\pm}_{\Psi,\Upsilon} \\ G^{\pm,\pm}_{\Upsilon,\Phi} & G^{\pm,\pm}_{\Upsilon,\Psi} & G^{\pm,\pm}_{\Upsilon,\Upsilon} \end{pmatrix} (\mathbf{x}, \mathbf{x}_s, \omega), \tag{2.2.6}$$

where the first subscript describes the wavefield potential at the receiver position $\mathbf{x}$ and the second subscript describes the wavefield potential at the source position $\mathbf{x}_s$. In this paper, we use 6×6 matrices to describe complete decomposed elastodynamic wavefields (e.g. in Equation 2.2.5) and 3×3 matrices to describe their four decomposed parts (e.g. in Equation 2.2.6). Ignoring evanescent waves, the operator $\mathcal{B}$ and its complex-conjugate $\mathcal{B}^*$ are mutually related as follows [combining Equations 70 and 88 in *Wapenaar*, 1996a],

$$\mathcal{B} = \mathbf{K}\mathcal{B}^*\mathbf{K}. \tag{2.2.7}$$

The superscript $*$ denotes a complex-conjugate. The matrix $\mathbf{K}$ as well as matrices $\mathbf{J}$ and $\mathbf{N}$ which we will use later are defined as,

$$\mathbf{K} = \begin{pmatrix} \mathbf{O} & \mathbf{I} \\ \mathbf{I} & \mathbf{O} \end{pmatrix},\ \mathbf{J} = \begin{pmatrix} \mathbf{I} & \mathbf{O} \\ \mathbf{O} & -\mathbf{I} \end{pmatrix},\ \mathbf{N} = \begin{pmatrix} \mathbf{O} & \mathbf{I} \\ -\mathbf{I} & \mathbf{O} \end{pmatrix}, \tag{2.2.8}$$

where $\mathbf{O}$ is a null matrix of appropriate size. The matrices $\mathbf{K}$ and $\mathbf{J}$ can be thought of as a Pauli matrices, the matrix $\mathbf{N}$ is a symplectic matrix.

We complex-conjugate Equation 2.2.4 and substitute the operator $\mathcal{B}^*$ using Equation 2.2.7. By pre- and post-multiplying the result by the matrix $\mathbf{K}$, we obtain,

$$\partial_3 \left[\mathbf{K}\mathbf{\Gamma}^*(\mathbf{x}, \mathbf{x}_s, \omega)\mathbf{K}\right] - \mathcal{B}\ \left[\mathbf{K}\mathbf{\Gamma}^*(\mathbf{x}, \mathbf{x}_s, \omega)\mathbf{K}\right] = \mathbf{I}\delta(\mathbf{x} - \mathbf{x}_s). \tag{2.2.9}$$

Here, we used the identity $\mathbf{KK} = \mathbf{I}$. According to this equation, the quantity $\mathbf{K}\mathbf{\Gamma}^*(\mathbf{x}, \mathbf{x}_s, \omega)\mathbf{K}$ is another solution of the wave equation. It is the Fourier transform of a time-reversed Green's function, but the diagonal as well as the off-diagonal elements $\mathbf{G}^{\pm,\pm}$ are interchanged. By subtracting Equation 2.2.9 from Equation 2.2.4 we obtain the homogeneous wave equation, i.e. a wave equation with a source term equal to zero,

$$\partial_3 \mathbf{\Gamma}_h(\mathbf{x}, \mathbf{x}_s, \omega) - \mathcal{B}\,\mathbf{\Gamma}_h(\mathbf{x}, \mathbf{x}_s, \omega) = \mathbf{O}. \tag{2.2.10}$$

A solution of the homogeneous wave equation is the homogeneous Green's function,

$$\mathbf{\Gamma}_h(\mathbf{x}, \mathbf{x}_s, \omega) = \mathbf{\Gamma}(\mathbf{x}, \mathbf{x}_s, \omega) - \mathbf{K}\mathbf{\Gamma}^*(\mathbf{x}, \mathbf{x}_s, \omega)\mathbf{K}, \tag{2.2.11}$$

which contains block-matrices as follows,

$$\begin{aligned}\mathbf{\Gamma}_h(\mathbf{x}, \mathbf{x}_s, \omega) &= \begin{pmatrix} \mathbf{G}_h^{+,+} & \mathbf{G}_h^{+,-} \\ \mathbf{G}_h^{-,+} & \mathbf{G}_h^{-,-} \end{pmatrix}(\mathbf{x}, \mathbf{x}_s, \omega) \\ &= \begin{pmatrix} \mathbf{G}^{+,+} - (\mathbf{G}^{-,-})^* & \mathbf{G}^{+,-} - (\mathbf{G}^{-,+})^* \\ \mathbf{G}^{-,+} - (\mathbf{G}^{+,-})^* & \mathbf{G}^{-,-} - (\mathbf{G}^{+,+})^* \end{pmatrix}(\mathbf{x}, \mathbf{x}_s, \omega). \end{aligned} \tag{2.2.12}$$

Equation 2.2.11 states that, in the space-frequency domain, the homogeneous Green's function is the Green's function minus its complex-conjugate, pre- and post multiplied by matrix $\mathbf{K}$. From the source-receiver reciprocity relation of the decomposed Green's function [*Wapenaar et al.*, 2016a],

$$\mathbf{\Gamma}(\mathbf{x}, \mathbf{x}_s, \omega) = \mathbf{N}\mathbf{\Gamma}^T(\mathbf{x}_s, \mathbf{x}, \omega)\mathbf{N}, \tag{2.2.13}$$

and the identity $\mathbf{KN} = -\mathbf{NK}$, it follows that the homogenous Green's function obeys the source-receiver reciprocity relation,

$$\mathbf{\Gamma}_h(\mathbf{x}, \mathbf{x}_s, \omega) = \mathbf{N}\mathbf{\Gamma}_h^T(\mathbf{x}_s, \mathbf{x}, \omega)\mathbf{N}. \tag{2.2.14}$$

2.2.3 Elastodynamic single-sided homogeneous Green's function representation

Consider a medium which is bounded by a reflection-free boundary $\partial\mathbb{D}_0$ at the top ($x_3 = x_{3,0}$) as depicted in Figure 2.1a. Let $\mathbf{R}(\mathbf{x}, \mathbf{x}', \omega)$ be the reflection response associated with a source for downgoing waves located at $\mathbf{x}'$ just above $\partial\mathbb{D}_0$, and a receiver for upgoing waves located at $\mathbf{x}$ on $\partial\mathbb{D}_0$. We define the depth level of $\mathbf{x}'$ as $\partial\mathbb{D}_0'$. In the notation of decomposed wavefields, we can state that $\mathbf{R}(\mathbf{x}, \mathbf{x}', \omega) = \mathbf{G}^{-,+}(\mathbf{x}, \mathbf{x}', \omega)$. The direct (downgoing) wave from $\mathbf{x}'$ to $\mathbf{x}$ on $\partial\mathbb{D}_0$ is part of the decomposed Green's function $\mathbf{G}^{+,+}(\mathbf{x}, \mathbf{x}', \omega) = \mathbf{I}\delta(\mathbf{x}_H - \mathbf{x}_H')$. Here, the subscript H refers to the horizontal components, i.e. $\mathbf{x}_H = (x_1, x_2)^T$. Since the medium is reflection-free above $\partial\mathbb{D}_0$, the decomposed Green's functions associated with sources for upgoing waves at $\mathbf{x}'$ and receivers at $\mathbf{x}$ on $\partial\mathbb{D}_0$ are zero, $\mathbf{G}^{\pm,-}(\mathbf{x}, \mathbf{x}', \omega) = \mathbf{O}$. According to the matrix notation in Equation 2.2.12, we can write the homogeneous Green's matrix $\mathbf{\Gamma}_h(\mathbf{x},\mathbf{x}',\omega)$ for $\mathbf{x}$ at $\partial\mathbb{D}_0$ in terms of the reflection response $\mathbf{R}(\mathbf{x},\mathbf{x}',\omega)$ and an identity matrix $\mathbf{I}$ of appropriate size,

$$\mathbf{\Gamma}_h(\mathbf{x},\mathbf{x}',\omega) = \begin{pmatrix} \mathbf{I}\delta(\mathbf{x}_H - \mathbf{x}'_H) & -\mathbf{R}^*(\mathbf{x},\mathbf{x}',\omega) \\ \mathbf{R}(\mathbf{x},\mathbf{x}',\omega) & -\mathbf{I}\delta(\mathbf{x}_H - \mathbf{x}'_H) \end{pmatrix}. \tag{2.2.15}$$

Next, we introduce the focusing function $\mathbf{F}(\mathbf{x},\mathbf{x}_s,\omega)$. The focusing function is defined in a so-called truncated medium which is identical to the true medium for $x_{3,0} \leq x_3 < x_{3,s}$ and homogeneous for $x_3 \geq x_{3,s}$, where $x_{3,s}$ is the depth of the focal point at $\mathbf{x}_s$ (see Figure 2.1b). We assume that $\mathbf{x}_s$ is located below $\partial\mathbb{D}_0$. The decomposed focusing matrix consists of a down- and an upgoing part,

$$\mathbf{F}(\mathbf{x},\mathbf{x}_s,\omega) = \begin{pmatrix} \mathbf{F}^+ \\ \mathbf{F}^- \end{pmatrix} (\mathbf{x},\mathbf{x}_s,\omega), \tag{2.2.16}$$

with,

$$\mathbf{F}^{\pm}(\mathbf{x},\mathbf{x}_s,\omega) = \begin{pmatrix} F^{\pm}_{\Phi,\Phi} & F^{\pm}_{\Phi,\Psi} & F^{\pm}_{\Phi,\Upsilon} \\ F^{\pm}_{\Psi,\Phi} & F^{\pm}_{\Psi,\Psi} & F^{\pm}_{\Psi,\Upsilon} \\ F^{\pm}_{\Upsilon,\Phi} & F^{\pm}_{\Upsilon,\Psi} & F^{\pm}_{\Upsilon,\Upsilon} \end{pmatrix} (\mathbf{x},\mathbf{x}_s,\omega). \tag{2.2.17}$$

The superscripts ± and the first subscript describe the wavefield direction and the wavefield potential at the receiver location $\mathbf{x}$, respectively. The second subscript describes the wavefield potential at the focusing position $\mathbf{x}_s$. The downgoing focusing function $\mathbf{F}^+(\mathbf{x},\mathbf{x}_s,\omega)$ for $\mathbf{x}$ at $\partial\mathbb{D}_0$ is the inverse of a transmission response of the truncated medium between $\partial\mathbb{D}_0$ and the depth level $x_3 = x_{3,s}$ [*Wapenaar et al.*, 2016a],

$$\int_{\partial\mathbb{D}_0} \mathbf{T}^+(\mathbf{x},\mathbf{x}',\omega)\mathbf{F}^+(\mathbf{x}',\mathbf{x}_s,\omega)\mathrm{d}^2\mathbf{x}'_H \Big|_{x_3=x_{3,s}} = \mathbf{I}\,\delta(\mathbf{x}_H - \mathbf{x}_{H,s}), \tag{2.2.18}$$

and the complete focusing function $\mathbf{F}$ obeys the focusing condition,

$$\mathbf{F}(\mathbf{x},\mathbf{x}_s,\omega)|_{x_3=x_{3,s}} = \mathbf{I}_1\,\delta(\mathbf{x}_H - \mathbf{x}_{H,s}). \tag{2.2.19}$$

Here, we introduced the matrix $\mathbf{I}_1 = (\mathbf{I},\mathbf{O})^T$. The upgoing focusing function $\mathbf{F}^-(\mathbf{x},\mathbf{x}_s,\omega)$ is the reflection response of the downgoing focusing function in the truncated medium. In a physical interpretation, the focusing function is the Fourier transform of a wavefield injected at the surface $\partial\mathbb{D}_0$, which focuses at time zero at the position $\mathbf{x}_s$ (see Figure 2.1b). Note, that the first event of the focusing function is injected at negative times.

Consider the homogeneous Green's function $\mathbf{\Gamma}_h(\mathbf{x},\mathbf{x}_s,\omega)$ related to a source at $\mathbf{x}_s$ inside the medium and receivers on the surface $\partial\mathbb{D}_0$ as depicted in Figure 2.2a. According to Equations 2A.17 and 2A.18 in the Appendix, the homogeneous Green's function $\mathbf{\Gamma}_h(\mathbf{x},\mathbf{x}',\omega)$ recorded on the top boundary and the focusing function $\mathbf{F}(\mathbf{x},\mathbf{x}_s,\omega)$ can construct a wavefield $\mathbf{\Gamma}_1(\mathbf{x},\mathbf{x}_s,\omega)$,

$$\mathbf{\Gamma}_1(\mathbf{x},\mathbf{x}_s,\omega) = \int_{\partial\mathbb{D}'_0} \mathbf{\Gamma}_h(\mathbf{x},\mathbf{x}',\omega)\mathbf{F}(\mathbf{x}',\mathbf{x}_s,\omega)\mathbf{I}_1^T\mathrm{d}^2\mathbf{x}', \tag{2.2.20}$$

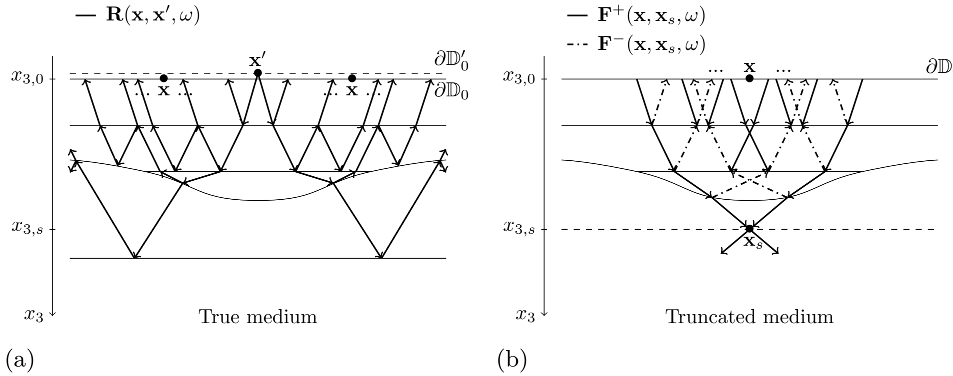

Figure 2.1: *Reflection response and focusing function. (a) $\mathbf{R}(\mathbf{x},\mathbf{x}',\omega)$ is the reflection response of a medium which is reflection-free above $\partial\mathbb{D}_0$. The source is located at $\mathbf{x}'$ on $\partial\mathbb{D}_0'$ (just above $\partial\mathbb{D}_0$), the receivers are located at $\mathbf{x}$ on $\partial\mathbb{D}_0$. (b) The decomposed focusing function $\mathbf{F}(\mathbf{x},\mathbf{x}_s,\omega)$ is defined in a truncated medium which is identical to the true medium for $x_3 < x_{3,s}$, and reflection-free for $x_3 \geq x_{3,s}$.*

from which the homogeneous Green's function $\mathbf{\Gamma}_h(\mathbf{x},\mathbf{x}_s,\omega)$ can be represented as,

$$\mathbf{\Gamma}_h(\mathbf{x},\mathbf{x}_s,\omega) = \mathbf{\Gamma}_1(\mathbf{x},\mathbf{x}_s,\omega) - \mathbf{K}\mathbf{\Gamma}_1^*(\mathbf{x},\mathbf{x}_s,\omega)\mathbf{K}. \tag{2.2.21}$$

Evaluating the matrix products in Equations 2.2.20-2.2.21 reveals that the forward-in-time propagating part of the homogeneous Green's function $\mathbf{\Gamma}_h(\mathbf{x},\mathbf{x}_s,\omega)$ is a superposition of the non-zero sub-matrices of $\mathbf{\Gamma}_1(\mathbf{x},\mathbf{x}_s,\omega)$, i.e. $\mathbf{G}^{-,+}(\mathbf{x},\mathbf{x}_s,\omega)$ and $\mathbf{G}^{-,-}(\mathbf{x},\mathbf{x}_s,\omega)$. Hence, Figure 2.2a also illustrates the wavefield $\mathbf{\Gamma}_1(\mathbf{x},\mathbf{x}_s,\omega)$.

The homogeneous Green's function $\mathbf{\Gamma}_h(\mathbf{x},\mathbf{x}',\omega)$ corresponds to sources and receivers at the surface ($\partial\mathbb{D}_0 \cup \partial\mathbb{D}_0'$). A physical interpretation of Equation 2.2.20 is that the focusing function focuses, or inverse-propagates, the sources of $\mathbf{\Gamma}_h(\mathbf{x},\mathbf{x}',\omega)$ from $\mathbf{x}'$ to $\mathbf{x}_s$.

In analogy, according to Equations 2A.12 and 2A.13 in the Appendix, the receivers of the homogeneous Green's function $\mathbf{\Gamma}_h(\mathbf{x},\mathbf{x}_s,\omega)$ are focused on, or inverse-propagated to, a virtual receiver location $\mathbf{x}_r$ inside the medium, according to,

$$\mathbf{\Gamma}_2(\mathbf{x}_r,\mathbf{x}_s,\omega) = \int_{\partial\mathbb{D}_0} \mathbf{I}_2\mathbf{F}^T(\mathbf{x},\mathbf{x}_r,\omega)\mathbf{N}\mathbf{\Gamma}_h(\mathbf{x},\mathbf{x}_s,\omega)\mathrm{d}^2\mathbf{x}, \tag{2.2.22}$$

from which the homogeneous Green's function $\mathbf{\Gamma}_h(\mathbf{x}_r,\mathbf{x}_s,\omega)$ can be constructed,

$$\mathbf{\Gamma}_h(\mathbf{x}_r,\mathbf{x}_s,\omega) = \mathbf{\Gamma}_2(\mathbf{x}_r,\mathbf{x}_s,\omega) - \mathbf{K}\mathbf{\Gamma}_2^*(\mathbf{x}_r,\mathbf{x}_s,\omega)\mathbf{K}. \tag{2.2.23}$$

The quantity $\mathbf{F}(\mathbf{x},\mathbf{x}_r,\omega)$ is the focusing function related to a focal point at $\mathbf{x}_r$. Further, we introduced the matrix $\mathbf{I}_2 = (\mathbf{O},\mathbf{I})^T$. Equations 2.2.20-2.2.23 together form an elastodynamic single-sided homogeneous Green's function representation: It expresses the homogeneous Green's function between $\mathbf{x}_s$ and $\mathbf{x}_r$ inside the medium

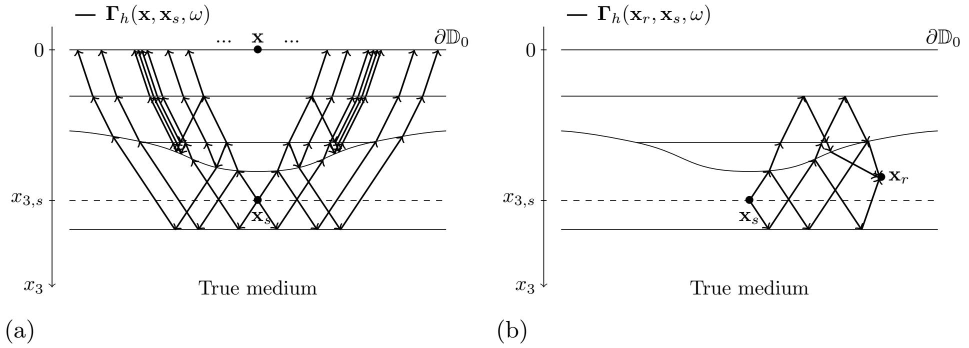

(a) (b)

Figure 2.2: *Homogeneous Green's functions. (a)* $\mathbf{\Gamma}_h(\mathbf{x}, \mathbf{x}_s, \omega)$ *is the homogeneous Green's function related to a source located inside the medium at* $\mathbf{x}_s$ *and receivers located on the surface* $\partial\mathbb{D}_0$ *at* $\mathbf{x}$. *(b)* $\mathbf{\Gamma}_h(\mathbf{x}_r, \mathbf{x}_s, \omega)$ *is the homogeneous Green's function related to a source located inside the medium at* $\mathbf{x}_s$ *and a receiver located inside the medium at* $\mathbf{x}_r$. *Both subfigures show the forward-in-time propagating part of the respective homogeneous Green's function.*

in terms of the single-sided data $\mathbf{\Gamma}_h(\mathbf{x}, \mathbf{x}', \omega)$ at the upper boundary $\partial\mathbb{D}_0 \cup \partial\mathbb{D}_0'$. An illustration of the homogeneous Green's function $\mathbf{\Gamma}_h(\mathbf{x}_r, \mathbf{x}_s, \omega)$ is displayed in Figure 2.2b. By evaluating the matrix products in Equations 2.2.22-2.2.23 it can be seen that the forward-in-time propagating part of the wavefield $\mathbf{\Gamma}_2(\mathbf{x}_r, \mathbf{x}_s, \omega)$ is represented by all paths in Figure 2.2b that are associated with upward propagating waves at $\mathbf{x}_r$. The representation formed by Equations 2.2.20-2.2.23 involves integrations along an open boundary of the medium, and therefore, only requires single-sided access to the medium.

2.3 Numerical example

In this section, we show a numerical example of the elastodynamic single-sided homogeneous Green's function representation for a 2D laterally-invariant medium. Further, we investigate the accuracy of the single-sided representation for wavenumber-frequency components of the elastodynamic homogeneous Green's function that are evanescent only inside a thin layer between the recording boundary and the virtual receiver depth. From here on, we consider a 2D medium, i.e. in all expressions of Section 2.2 the spatial coordinate $\mathbf{x}$ simplifies to $\mathbf{x} = (x_1, x_3)^T$ and the horizontal coordinate $\mathbf{x}_H$ simplifies to x_1. Besides, we only consider P and SV waves, indicated by the subscripts Φ and Ψ, respectively. In the provided numerical examples, we use modelled focusing functions. This allows us to analyse the properties of the single-sided representation, independent of approximations of the focusing function retrieval via the Marchenko method.

2.3.1 Wavenumber-frequency domain expressions

Since we consider a laterally-invariant model the required data can be modelled efficiently by wavefield extrapolation in the wavenumber-frequency domain [*Kennett and Kerry*, 1979; *Hubral et al.*, 1980]. However, in the theory section the single-sided homogeneous Green's function representation is formulated in the space-frequency domain. To transform the expressions to the wavenumber-frequency domain, we use the fact that all the presented expressions have a similar form, namely a product of two space-dependent functions $\mathbf{g}(x_1, x_3, x_1'', x_3'')$ and $\mathbf{f}(x_1'', x_3'', x_1', x_3')$, integrated across a horizontal surface $\partial\mathbb{D}''$,

$$\int_{\partial\mathbb{D}''} \mathbf{g}(x_1, x_3, x_1'', x_3'')\mathbf{f}(x_1'', x_3'', x_1', x_3')\mathrm{d}x_1''. \tag{2.3.1}$$

In laterally-invariant media, integrals of the above form can be rewritten as a spatial convolution,

$$\int_{\partial\mathbb{D}''} \mathbf{g}(x_1 - x_1'', x_3, 0, x_3'')\mathbf{f}(x_1'', x_3'', x_1', x_3')\mathrm{d}x_1'', \tag{2.3.2}$$

which corresponds to a multiplication in the wavenumber domain [*Arfken*, 1985],

$$\tilde{\mathbf{g}}(k_1, x_3, 0, x_3'')\tilde{\mathbf{f}}(k_1, x_3'', x_1', x_3'). \tag{2.3.3}$$

Here, we introduced the horizontal wavenumber k_1. Note, when we say wavenumber domain, we refer to the horizontal-wavenumber domain (k_1, x_3) on the receiver side (first coordinate). Wavefields in the wavenumber domain are written with a tilde on top. Expressions in the space and wavenumber domain are mutually related via the Fourier transform,

$$\tilde{\mathbf{g}}(k_1, x_3, x_1'', x_3'') = \int \mathbf{g}(x_1, x_3, x_1'', x_3'')\mathrm{e}^{-\mathrm{i}k_1 x_1}\mathrm{d}x_1. \tag{2.3.4}$$

We model the required input data, the reflection response $\tilde{\mathbf{R}}(k_1, x_{3,0}, 0, x_{3,0}', \omega)$ and the focusing functions $\tilde{\mathbf{F}}(k_1, x_{3,0}, 0, x_{3,s/r}, \omega)$, in the wavenumber-frequency domain by wavefield extrapolation. Since we model all fields for a source with a horizontal space coordinate $x_1 = 0$, we omit this coordinate in the following expressions. Next, we transform Equations 2.2.20-2.2.23 to the wavenumber domain according to Equations 2.3.2-2.3.4. After evaluating Equations 2.2.20-2.2.23 in the wavenumber-frequency domain, we transform the final result $\tilde{\mathbf{\Gamma}}_h(k_1, x_{3,r}, x_{3,s}, \omega)$ to the space-time domain via an inverse Fourier transform,

$$\mathbf{\Gamma}_h(\mathbf{x}_r, \mathbf{x}_s, t) = \frac{1}{(2\pi)^2} \iint \tilde{\mathbf{\Gamma}}_h(k_1, x_{3,r}, x_{3,s}, \omega)\, \mathrm{e}^{-\mathrm{i}[\omega t - k_1(x_{1,r} - x_{1,s})]}\, \mathrm{d}k_1 \mathrm{d}\omega. \tag{2.3.5}$$

Here, we replaced the horizontal receiver coordinate $x_{1,r}$ in the exponent by the horizontal offset between the receiver and the source, $x_{1,r} - x_{1,s}$, to account for the actual horizontal position of the source $x_{1,s}$.

2.3.2 Results

We present a numerical example of the elastodynamic single-sided homogeneous Green's function representation. The result is compared to the exact homogeneous Green's function, which is computed by wavefield extrapolation. For a clear illustration, we choose a simple model as depicted in Figure 2.3. Results for a more complex model can be found in 2B. Note that we use superscripts (i) to refer to the i^{th} layer of the medium.

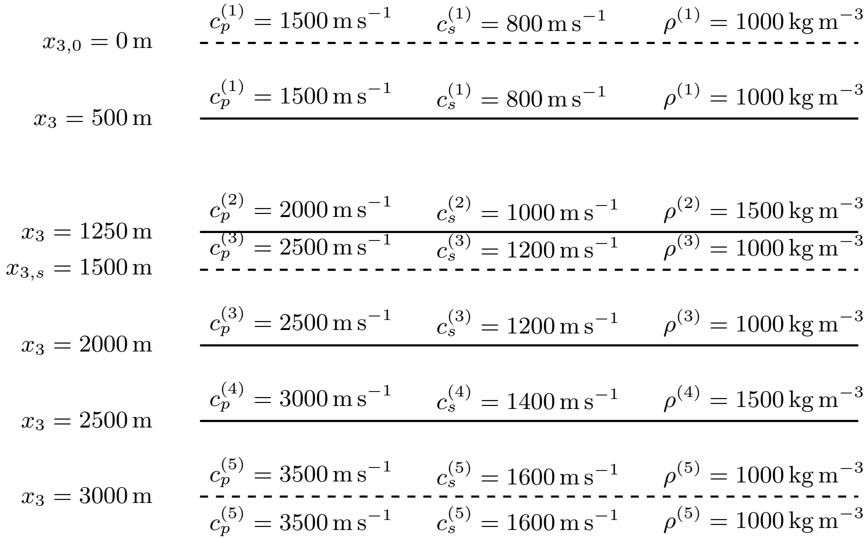

Figure 2.3: *Layered model. The model depth ranges from* $0\,\mathrm{m}$ *to* $3000\,\mathrm{m}$*, the lateral distance ranges from* $-12\,812.5\,\mathrm{m}$ *to* $12\,800\,\mathrm{m}$*. The P-wave velocity, S-wave velocity and density are denoted by* $c_p^{(i)}$*,* $c_s^{(i)}$ *and* $\rho^{(i)}$ *respectively. The superscripts* (i) *refer to the* i^{th} *layer of the medium. The top boundary and the virtual source depth are denoted by* $x_{3,0}$ *and* $x_{3,s}$*, respectively. Solid lines represent medium interfaces and dashed lines represent (scattering-free) depth levels.*

According to 2A, the single-sided homogeneous Green's function representation ignores evanescent waves, which are associated with imaginary-valued vertical-wavenumbers $k_3(c_{p/s}, k_1, \omega) = \mathrm{i}\sqrt{k_1^2 - \frac{\omega^2}{c_{p/s}^2}}$. Thus, all wavenumber-frequency components that satisfy the relation,

$$|k_1| > \frac{\omega}{c_{max}}, \tag{2.3.6}$$

should be excluded from the analysis. Here, c_{max} is the maximum propagation velocity of the truncated medium.

In the following, before displaying a wavefield in the space-time domain, we mute evanescent waves according to Equation 2.3.6 using the maximum P-wave velocity of the truncated medium c_{max}, apply an inverse Fourier transform according to Equation 2.3.5 and convolve the resulting wavefield with a 30 Hz Ricker wavelet [defined by Eq. 7 in *Wang*, 2015]. Note that, we create a virtual source as well as a virtual receiver, meaning that there are two truncated media, bounded at the bottom by $x_{3,s}$ and $x_{3,r}$, respectively. The above mentioned maximum P-wave velocity c_{max} is the overall maximum P-wave velocity of both truncated media.

The reflection response $\tilde{\mathbf{R}}$ and the focusing functions $\tilde{\mathbf{F}}^{\pm}$ are modelled by wavefield extrapolation using the modelling parameters shown in Table 2.1.

Number of frequency samples	1025
Frequency sample interval	$0.511\,\mathrm{s}^{-1}$
Number of wavenumber samples	2048
Wavenumber sample interval	$0.245 \times 10^{-3}\,\mathrm{m}^{-1}$

Table 2.1: *Modelling parameters.*

The modelled reflection response $\tilde{\mathbf{R}}(k_1, x_{3,0}, x'_{3,0}, \omega)$ contains P-wave and S-wave recordings. The components associated with a P-wave source are superimposed and shown in the space-time domain in Figure 2.4a. For clearer illustration, we only show source-receiver offsets between $-2000\,\mathrm{m}$ and $+2000\,\mathrm{m}$ and times between 0 s and 4 s. The reflection response contains primary reflections, converted reflections and internal multiples. Mode conversions between P- and S-waves do not occur at zero-incidence. Therefore, events with a gap at $x_1 = 0\,\mathrm{m}$ are easily identified as converted waves.

Next, we define a virtual source inside the medium at $\mathbf{x}_s = (0\,\mathrm{m}, 1500\,\mathrm{m})^T$. Thus, we model a focusing function $\tilde{\mathbf{F}}(k_1, x_{3,0}, x_{3,s}, \omega)$ with focusing depth equal to 1500 m. The up- and downgoing P- and S-wave components of the focusing function, that are associated with a P-wave focus, are superimposed and displayed in the space-time domain in Figure 2.4b. Since the focusing function contains both causal and acausal events it is displayed for times between -2 s and $+2$ s.

The reflection response and focusing function of Figure 2.4a and 2.4b are used to compute a homogeneous Green's function $\tilde{\mathbf{\Gamma}}_h(k_1, x_{3,0}, x_{3,s}, \omega)$ related to the virtual source at $\mathbf{x}_s$ and receivers at the surface. The computation is performed as stated in Equations 2.2.20-2.2.21. Figure 2.4c shows a superposition of the up- and downgoing P- and S-wave components of the resulting homogeneous Green's function in the space-time domain. Only responses to a virtual P-wave source are displayed. Figure 2.4c illustrates that the acausal part of the homogeneous Green's function is a time-reversed and polarity-flipped version of the causal part.

Subsequently, we compute the single-sided representation of the homogeneous Green's function $\tilde{\mathbf{\Gamma}}_h(k_1, x_{3,r}, x_{3,s}, \omega)$ associated with virtual receivers at $x_{3,r} = 1700\,\mathrm{m}$ according to Equations 2.2.22-2.2.23. We superpose the downgoing components of the homogeneous Green's function, $\tilde{\mathbf{G}}_h^{+,+}(k_1, x_{3,r}, x_{3,s}, \omega) + \tilde{\mathbf{G}}_h^{+,-}(k_1, x_{3,r}, x_{3,s}, \omega)$, and display the absolute value of the result in Figure 2.5. Here, we display

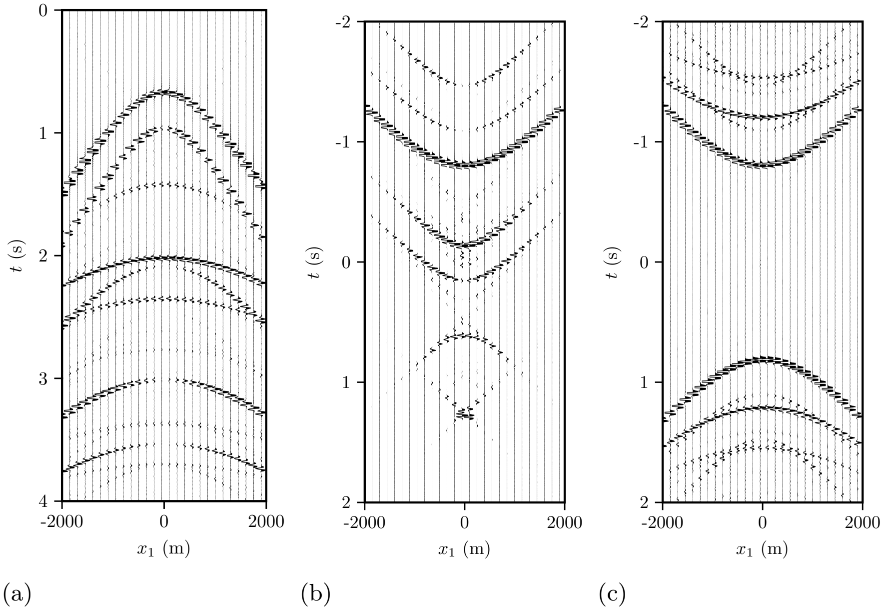

Figure 2.4: *Virtual source retrieval. (a) Reflection response* $\mathbf{R}(x_1, x_{3,0}, x'_{3,0}, t)$*. (b) focusing function* $\mathbf{F}(x_1, x_{3,0}, x_{3,s}, t)$ *for a focal point at* $\mathbf{x}_s = (0\,\mathrm{m}, 1500\,\mathrm{m})^T$*. (c) Homogeneous Green's function* $\mathbf{\Gamma}_h(x_1, x_{3,0}, x_{3,s}, t)$*, obtained from the single-sided representation, for a virtual source at* $\mathbf{x}_s = (0\,\mathrm{m}, 1500\,\mathrm{m})^T$ *and receivers at the surface. Fields in (a) and (c) are associated with a P-wave source, and the field in (b) is associated with a P-wave focus. A* k_1*-*ω *filter was applied to all displayed fields before transformation to the space-time domain. The traces in Figures (a) and (c) were multiplied with a gain function (*$\times\ \mathrm{e}^{0.5|t|}$*) to emphasise the late arrivals. Note that the plots have different clipping.*

the four elastic components separately. Due to the symmetry of the homogeneous Green's function $\tilde{\mathbf{\Gamma}}_h(k_1, x_{3,r}, x_{3,s}, \omega)$ (see Equation 2.2.12), the sum of its upgoing components, $\tilde{\mathbf{G}}_h^{-,+}(k_1, x_{3,r}, x_{3,s}, \omega) + \tilde{\mathbf{G}}_h^{-,-}(k_1, x_{3,r}, x_{3,s}, \omega)$, produces an identical result. Further, since the medium is horizontally-layered we only show positive wavenumbers k_1. In Figure 2.5, the amplitude of the $\Phi\Phi$, $\Phi\Psi$ and $\Psi\Phi$ components of the quantity, $\tilde{\mathbf{G}}_h^{+,+}(k_1, x_{3,r}, x_{3,s}, \omega) + \tilde{\mathbf{G}}_h^{+,-}(k_1, x_{3,r}, x_{3,s}, \omega)$, decreases rapidly for $|k_1| > \frac{\omega}{c_p^{(3)}}$, i.e. beyond the dashed red line. The velocity $c_p^{(3)}$ is the maximum propagation velocity in the truncated medium, and therefore, the line $|k_1| = \frac{\omega}{c_p^{(3)}}$ separates propagating from evanescent waves. As shown in 2A, the elastodynamic single-sided homogeneous Green's function representation does not take into account wavenumber-frequency components that are evanescent on the boundaries of the domain (here $x_3 = x_{3,0}$ and $x_3 = x_{3,r}$). Thus, for wavenumbers $|k_1| > \frac{\omega}{c_p^{(3)}}$ the retrieved quantity, $\tilde{\mathbf{G}}_h^{+,+}(k_1, x_{3,r}, x_{3,s}, \omega) + \tilde{\mathbf{G}}_h^{+,-}(k_1, x_{3,r}, x_{3,s}, \omega)$, is not representing the analytic elastodynamic homogeneous Green's function. Further, in the wavenumber

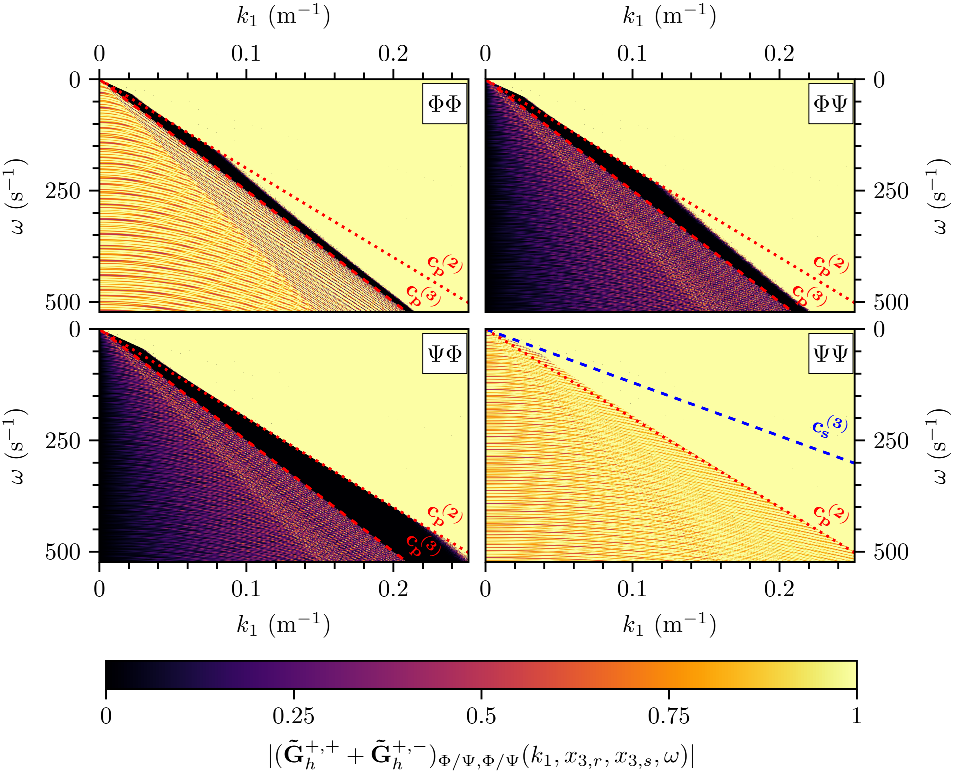

Figure 2.5: *Analysis of the retrieved elastodynmaic homogeneous Green's function. The four figures show the single-sided representation of the elastodynamic homogeneous Green's function after summing its receiver-side downgoing components and taking the absolute value of the result* $|\tilde{\mathbf{G}}_h^{+,+}(k_1, x_{3,r}, x_{3,s}, \omega) + \tilde{\mathbf{G}}_h^{+,-}(k_1, x_{3,r}, x_{3,s}, \omega)|$. *The elastodynamic homogeneous Green's function is associated with a virtual source at* $\mathbf{x}_s = (0\,\mathrm{m}, 1500\,\mathrm{m})^T$ *and virtual receivers at* $x_{3,r} = 1700\,\mathrm{m}$. *We only show positive wavenumbers* k_1. *In addition, we draw lines,* $k_1 = \frac{\omega}{c_{p/s}^{(i)}}$, *defined by the P-/S-wave velocity* $c_{p/s}^{(i)}$ *in the* i^{th} *layer of the model. The amplitudes in the plain yellow areas increase rapidly and were clipped for values greater than one.*

regime $|k_1| >> \frac{\omega}{c_p^{(3)}}$, the quantity, $\tilde{\mathbf{G}}_h^{+,+}(k_1, x_{3,r}, x_{3,s}, \omega) + \tilde{\mathbf{G}}_h^{+,-}(k_1, x_{3,r}, x_{3,s}, \omega)$, becomes unstable. This instability could be due to either the behaviour of the elastodynamic single-sided homogeneous Green's function representation for evanescent wavenumber-frequency components, or numerical instabilities, or both. Nevertheless, the analytic elastodynamic homogeneous Green's function is characterised by an exponential amplitude decay for evanescent wavenumber-frequency components. The amplitude of the ΨΨ component of the quantity, $\tilde{\mathbf{G}}_h^{+,+}(k_1, x_{3,r}, x_{3,s}, \omega) + \tilde{\mathbf{G}}_h^{+,-}(k_1, x_{3,r}, x_{3,s}, \omega)$, is in the order of one for $|k_1| < \frac{\omega}{c_p^{(2)}}$ and increases rapidly for

$|k_1| > \frac{\omega}{c_p^{(2)}}$, beyond the indicated dotted red line. Hence, for the $\Psi\Psi$ component of the quantity, $\tilde{\mathbf{G}}_h^{+,+}(k_1, x_{3,r}, x_{3,s}, \omega) + \tilde{\mathbf{G}}_h^{+,-}(k_1, x_{3,r}, x_{3,s}, \omega)$, the transition from propagating to evanescent waves is defined by the P-wave velocity of the second layer $c_p^{(2)}$, instead of the P-wave velocity of the third layer $c_p^{(3)}$. This is expected because its $\Psi\Psi$ component only requires an S-wave focus in the third layer of the medium. Creating an S-wave focus in the third layer only allows for P-wave conversions above layer (3). As such, the highest P-wave velocity associated with an S-wave focus in layer (3) is $c_p^{(2)}$. In other words, the unstable behaviour of the $\Psi\Psi$ component for $|k_1| > \frac{\omega}{c_p^{(2)}}$ (to the right of the dotted red line) is caused by waves that are S-waves at the source, convert to P-waves in the second layer and convert back to S-waves before reaching the receivers. For unconverted S-waves the highest propagation velocity is $c_s^{(3)}$, i.e. those waves are propagating for $|k_1| < \frac{\omega}{c_s^{(3)}}$ (to the left of the dashed blue line). However, these propagating S-waves are obscured by the unstable behaviour of the parts of the $\Psi\Psi$ component that convert to P-waves in the second layer.

We evaluate the accuracy of the elastodynamic single-sided homogeneous Green's function representation by comparing it to the exact elastodynamic homogeneous Green's function. To that end, we model the elastodynamic homogeneous Green's function $\tilde{\mathbf{\Gamma}}_{h,mod}(k_1, x_{3,r}, x_{3,s}, \omega)$ for an actual source at $\mathbf{x}_s = (0\,\mathrm{m}, 1500\,\mathrm{m})^T$. Next, we compute the relative error of the single-sided representation of the elastodynamic homogeneous Green's function according to,

$$\tilde{\mathbf{E}}(k_1, x_{3,r}, x_{3,s}, \omega) = \frac{|(\tilde{\mathbf{G}}_h^{+,+} + \tilde{\mathbf{G}}_h^{+,-} - \tilde{\mathbf{G}}_{h,mod}^{+,+} - \tilde{\mathbf{G}}_{h,mod}^{+,-})(k_1, x_{3,r}, x_{3,s}, \omega)|}{|(\tilde{\mathbf{G}}_{h,mod}^{+,+} + \tilde{\mathbf{G}}_{h,mod}^{+,-})(k_1, x_{3,r}, x_{3,s}, \omega)|}, \tag{2.3.7}$$

where the absolute value is evaluated element-wise. The resulting relative error $\tilde{\mathbf{E}}(k_1, x_{3,r}, x_{3,s}, \omega)$ is shown in Figure 2.6. For $|k_1| < \frac{\omega}{c_p^{(3)}}$, the single-sided representation of the quantity, $\tilde{\mathbf{G}}_h^{+,+}(k_1, x_{3,r}, x_{3,s}, \omega) + \tilde{\mathbf{G}}_h^{+,-}(k_1, x_{3,r}, x_{3,s}, \omega)$, is accurate within a relative error $\tilde{\mathbf{E}}(k_1, x_{3,r}, x_{3,s}, \omega)$ of about 10^{-15}, i.e. within numerical precision. For $|k_1| > \frac{\omega}{c_p^{(3)}}$, the relative error $\tilde{\mathbf{E}}(k_1, x_{3,r}, x_{3,s}, \omega)$ increases drastically, except for the $\Psi\Psi$ component $\tilde{E}_{\Psi\Psi}(k_1, x_{3,r}, x_{3,s}, \omega)$. As explained above, the single-sided representation of the $\Psi\Psi$ component of the homogeneous Green's function $\tilde{\Gamma}_{h,\Psi\Psi}(k_1, x_{3,r}, x_{3,s}, \omega)$ only requires an S-wave focus in the third layer of the medium, such that the $\Psi\Psi$ component of the quantity, $\tilde{\mathbf{G}}_h^{+,+}(k_1, x_{3,r}, x_{3,s}, \omega) + \tilde{\mathbf{G}}_h^{+,-}(k_1, x_{3,r}, x_{3,s}, \omega)$, is accurate within numerical precision up to wavenumbers defined by the P-wave velocity of the second layer of the medium, $|k_1| < \frac{\omega}{c_p^{(2)}}$.

The resulting elastodynamic homogeneous Green's function $\tilde{\mathbf{\Gamma}}_h(k_1, x_{3,r}, x_{3,s}, \omega)$ is a decomposed wavefield, described by up- and downgoing P- and S-waves. To obtain the full homogeneous Green's function $\tilde{\mathbf{G}}_h(k_1, x_{3,r}, x_{3,s}, \omega)$, that is associated with measurable wavefield quantities, we apply wavefield composition,

$$\tilde{\mathbf{G}}_h(k_1, x_{3,r}, x_{3,s}, \omega) = \tilde{\mathcal{L}}(k_1, x_{3,r}, \omega)\tilde{\mathbf{\Gamma}}_h(k_1, x_{3,r}, x_{3,s}, \omega)\tilde{\mathcal{L}}^{-1}(k_1, x_{3,s}, \omega), \tag{2.3.8}$$

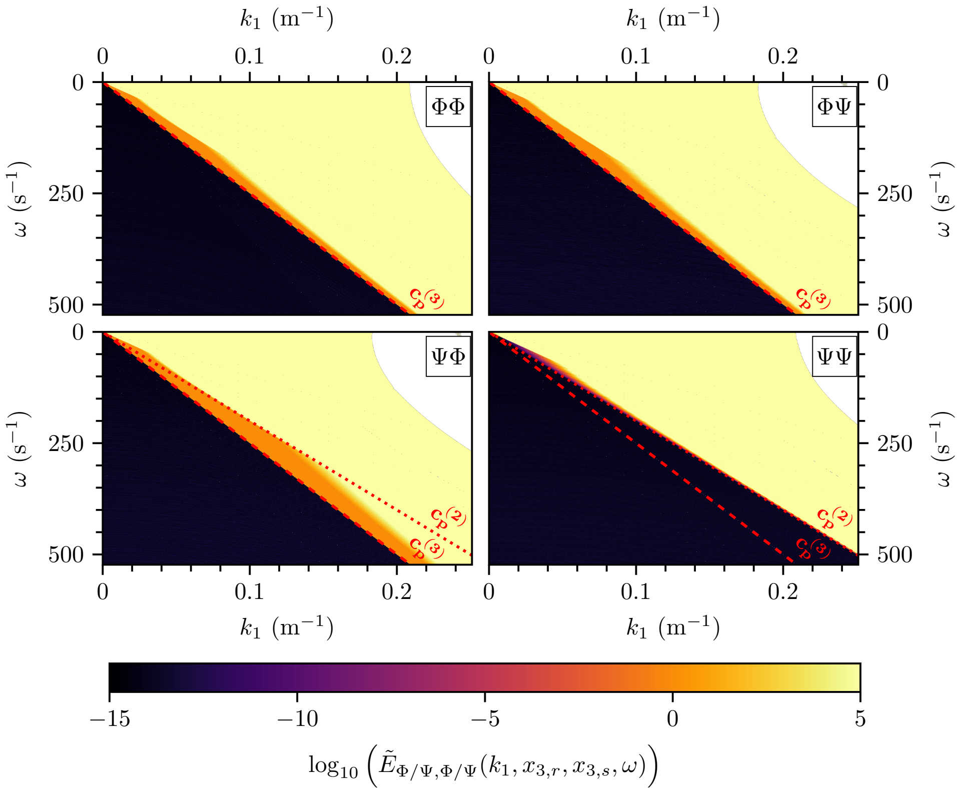

Figure 2.6: *Relative error of the retrieved elastodynamic homogeneous Green's function. The four figures show the relative error defined by Equation 2.3.7. The red lines are* $k_1 = \frac{\omega}{c^{(i)}_{p/s}}$ *defined by the P-wave velocity* $c_p^{(i)}$ *in the* i^{th} *layer of the model. The amplitudes in the plain yellow area increase rapidly and were clipped for values greater than five. Inside the white area the relative error could not be represented as a number due to limited numerical precision (double-precision). Of course, these values are still defined but their representation requires a higher numerical precision.*

where $\tilde{\mathcal{L}}(k_1, x_{3,r/s}, \omega)$ is the composition operator. Further details about wavefield composition can be found in *Wapenaar et al.* [2016a]. The full homogeneous Green's function $\tilde{\mathbf{G}}_h(k_1, x_{3,r}, x_{3,s}, \omega)$ relates force sources $\mathbf{f}$ and deformation sources $\mathbf{h}$ to traction recordings $\boldsymbol{\tau}$ and particle velocity recordings $\mathbf{v}$,

$$\tilde{\mathbf{G}}_h(k_1, x_{3,r}, x_{3,s}, \omega) = \begin{pmatrix} \tilde{\mathbf{G}}^{\boldsymbol{\tau},\mathbf{f}} - (\tilde{\mathbf{G}}^{\boldsymbol{\tau},\mathbf{f}})^* & \tilde{\mathbf{G}}^{\boldsymbol{\tau},\mathbf{h}} + (\tilde{\mathbf{G}}^{\boldsymbol{\tau},\mathbf{h}})^* \\ \tilde{\mathbf{G}}^{\mathbf{v},\mathbf{f}} + (\tilde{\mathbf{G}}^{\mathbf{v},\mathbf{f}})^* & \tilde{\mathbf{G}}^{\mathbf{v},\mathbf{h}} - (\tilde{\mathbf{G}}^{\mathbf{v},\mathbf{h}})^* \end{pmatrix} (k_1, x_{3,r}, x_{3,s}, \omega). \tag{2.3.9}$$

From Equation 2.3.9 follows that, in the space-time domain, the $(\boldsymbol{\tau}, \mathbf{f})$ and $(\mathbf{v}, \mathbf{h})$ components of the full homogenous Green's function are anti-symmetric in time, and hence, vanish at time zero. This is undesirable for imaging applications because imaging uses the wavefield at time zero for $\mathbf{x}_r = \mathbf{x}_s$. However, in the space-time domain the $(\boldsymbol{\tau}, \mathbf{h})$ and $(\mathbf{v}, \mathbf{f})$ components are non-zero at time zero for $\mathbf{x}_r = \mathbf{x}_s$, and can be used for imaging.

After transforming the elastodynamic homogenous Green's function to the space-time domain $\mathbf{G}_h(\mathbf{x}_r, \mathbf{x}_s, t)$, we display its (v_3, f_3) component, $G^{v_3,f_3}(\mathbf{x}_r, \mathbf{x}_s, t) + G^{v_3,f_3}(\mathbf{x}_r, \mathbf{x}_s, -t)$, in Figure 2.7. The time slices illustrate the symmetry of the homogeneous Green's function $\mathbf{G}_h^{\mathbf{v},\mathbf{f}}$ in time. At time zero the wavefield focuses. The focus is distorted by linear artefacts. The artefacts occur because the homogeneous Green's function was filtered by a k_1-ω mask that is determined by the maximum propagation velocity at a given virtual receiver depth $x_{3,r}$. The k_1-ω mask mutes the part of the propagating S-wavefield that overlaps with the evanescent P-wavefield, causing linear artefacts in the space-time domain. According to Snell's law, the inclination angle α of these linear artefacts is determined by,

$$\frac{1}{c_p} = \frac{\sin(\alpha)}{c_s}. \tag{2.3.10}$$

Using $c_p^{(3)} = 2500\,\mathrm{m\,s^{-1}}$ and $c_s^{(3)} = 1200\,\mathrm{m\,s^{-1}}$, we find that the linear artefact at the focusing position at time zero has an inclination angle $\alpha = 28.7°$ (see Figure 2.7). An inspection of the time slices, e.g. for $t = 0.15\,\mathrm{s}$ and $t = 0.45\,\mathrm{s}$, demonstrates that the single-sided representation of the elastodynamic homogeneous Green's function contains primary waves, converted waves, and multiply scattered waves.

We evaluate the accuracy of the elastodynamic single-sided homogeneous Green's function representation by comparing it to the exact elastodynamic homogeneous Green's function. To that end, we modelled the elastodynamic homogeneous Green's function for an actual source at $\mathbf{x}_s = (0\,\mathrm{m}, 1500\,\mathrm{m})^T$. The modelled elastodynamic homogeneous Green's function is subtracted from the elastodynamic homogeneous Green's function obtained from the single-sided representation. To exclude evanescent waves, the result $\Delta\tilde{\mathbf{\Gamma}}_h(k_1, x_{3,r}, x_{3,s}, \omega)$ is element-wise multiplied by a k_1-ω filter $\tilde{\mathbf{M}}$ determined by the maximum propagation velocity of the medium. Next, we compute the normalised Frobenius norm $N_F = \frac{1}{\sqrt{4nt4nr}} \|\tilde{\mathbf{M}} \circ \Delta\tilde{\mathbf{\Gamma}}_h(k_1, x_{3,r}, x_{3,s}, \omega)\|_2$ at each virtual receiver depth level $x_{3,r}$, where the symbol $\circ$ denotes a Hadamard product. The normalisation factor is a function of the number of time samples nt and the number of space samples nr. We choose the normalisation factor $\sqrt{4nt4nr}$ because $\Delta\tilde{\mathbf{\Gamma}}_h(k_1, x_{3,r}, x_{3,s}, \omega)$ consists of four $nt \times nr$ block-matrices. In Figure 2.8, we show the resulting residual norm as a function of virtual receiver depth $x_{3,r}$. The difference plot demonstrates that, for all modelled wavenumber-frequency components of the propagating wavefield, the elastodynamic single-sided homogeneous Green's function representation is accurate within numerical precision. For the evaluation, we used the residual of the elastodynamic decomposed homogeneous Green's function $\Delta\tilde{\mathbf{\Gamma}}_h(k_1, x_{3,r}, x_{3,s}, \omega)$ instead of its composed equivalent to exclude effects of the wavefield composition (see Equation 2.3.8) from the analysis. In this case, however, the wavefield composition also performs within numerical precision.

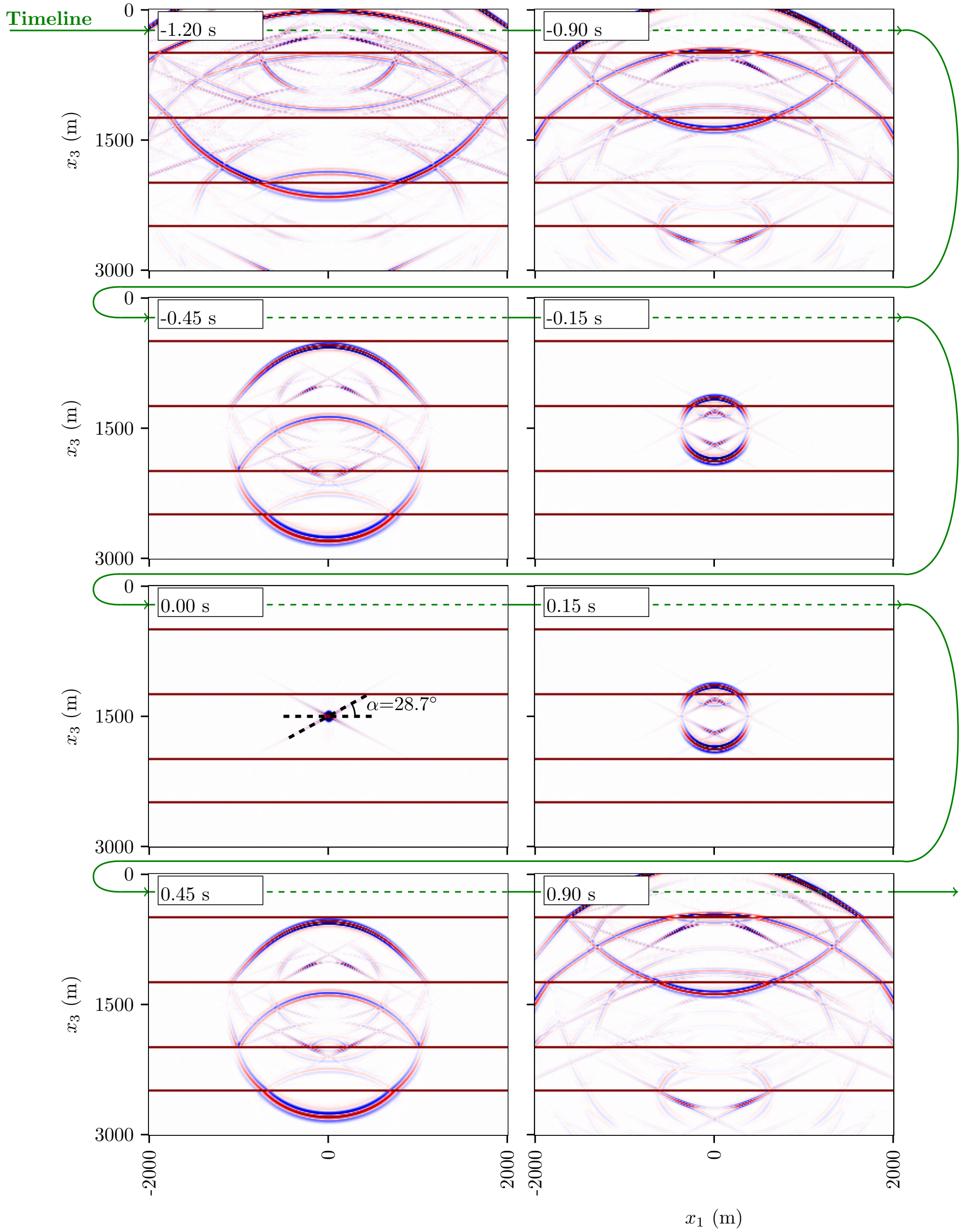

Figure 2.7: *Single-sided representation of the elastodynamic homogeneous Green's function. The time slices show the single-sided representation of the elastodynamic homogeneous Green's function* $\mathbf{G}_h^{v_3,f_3}(\mathbf{x}_r, \mathbf{x}_s, t)$ *related to a virtual source* (f_3) *at* $\mathbf{x}_s = (0\,\mathrm{m}, 1500\,\mathrm{m})^T$ *and virtual receivers* (v_3) *placed on a grid with a depth range from* $0\,\mathrm{m}$ *to* $3000\,\mathrm{m}$ *and a lateral distance range from* $-2000\,\mathrm{m}$ *to* $2000\,\mathrm{m}$*. The spatial sampling interval is* $12.5\,\mathrm{m}$ *in both horizontal and vertical directions. The time slices were multiplied by a gain function* $(\times \mathrm{e}^{1.5|t|})$ *to emphasise the late arrivals. At time zero, we indicate the slope angle* α *of a linear artefact caused by applying a* k_1*-*ω *mask.*

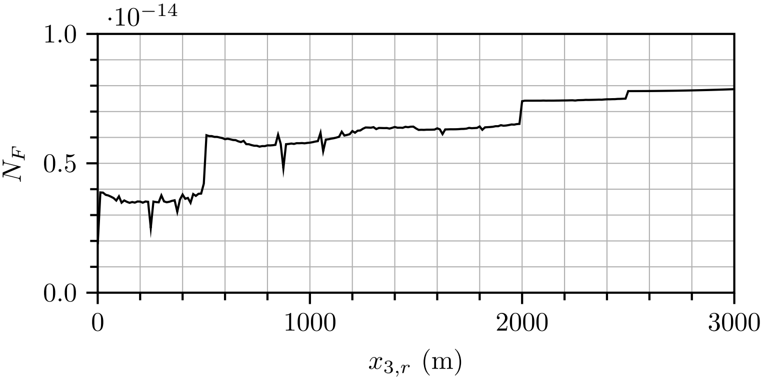

Figure 2.8: *Error analysis. Normalised Frobenius norm N_F of the difference $\Delta\tilde{\mathbf{\Gamma}}_h(k_1, x_{3,r}, x_{3,s}, \omega)$ between the elastodynamic single-sided homogeneous Green's function representation (see Figure 2.7) and its modelled equivalent as a function of virtual receiver depth $x_{3,r}$.*

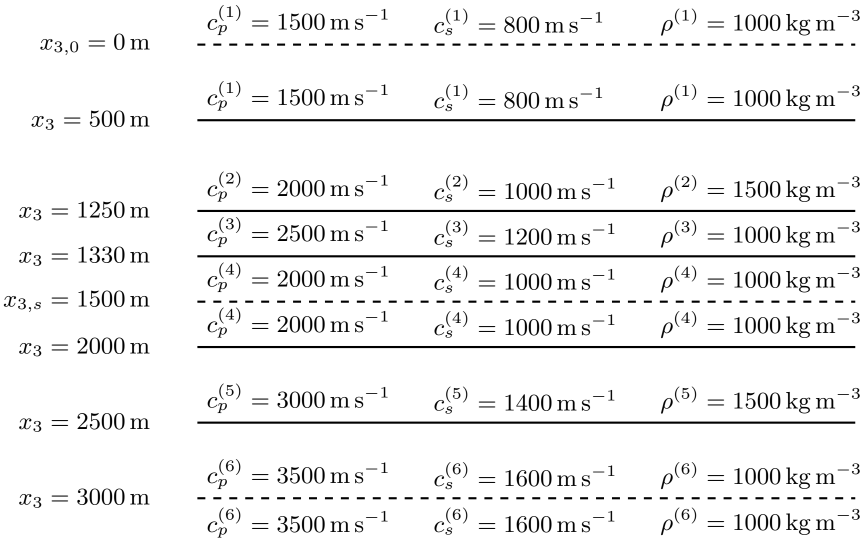

Figure 2.9: *Layered model. As Figure 2.3 but with an additional thin layer between $x_3 = 1250\,\mathrm{m}$ and $x_3 = 1300\,\mathrm{m}$. For the sake of readability, the distances between the interfaces are not proportional because the third layer is only $80\,\mathrm{m}$ thick.*

2.3.3 Evanescent wave tunnelling

In this section, we investigate tunnelling of evanescent waves using a new model (see Figure 2.9). The new model is nearly identical to the model in Figure 2.3. However, the layer between $x_3 = 1250\,\mathrm{m}$ and $x_3 = 2000\,\mathrm{m}$ is replaced by a thin layer ranging from $x_3 = 1250\,\mathrm{m}$ to $x_3 = 1330\,\mathrm{m}$ and a thicker layer ranging from $x_3 = 1330\,\mathrm{m}$ to $x_3 = 2000\,\mathrm{m}$. For the thin layer, the P- and S-wave velocities are $2500\,\mathrm{m\,s^{-1}}$ and $1200\,\mathrm{m\,s^{-1}}$, respectively. For the layer below, the propagation velocities are smaller, $c_p^{(4)} = 2000\,\mathrm{m\,s^{-1}}$ and $c_s^{(4)} = 1000\,\mathrm{m\,s^{-1}}$.

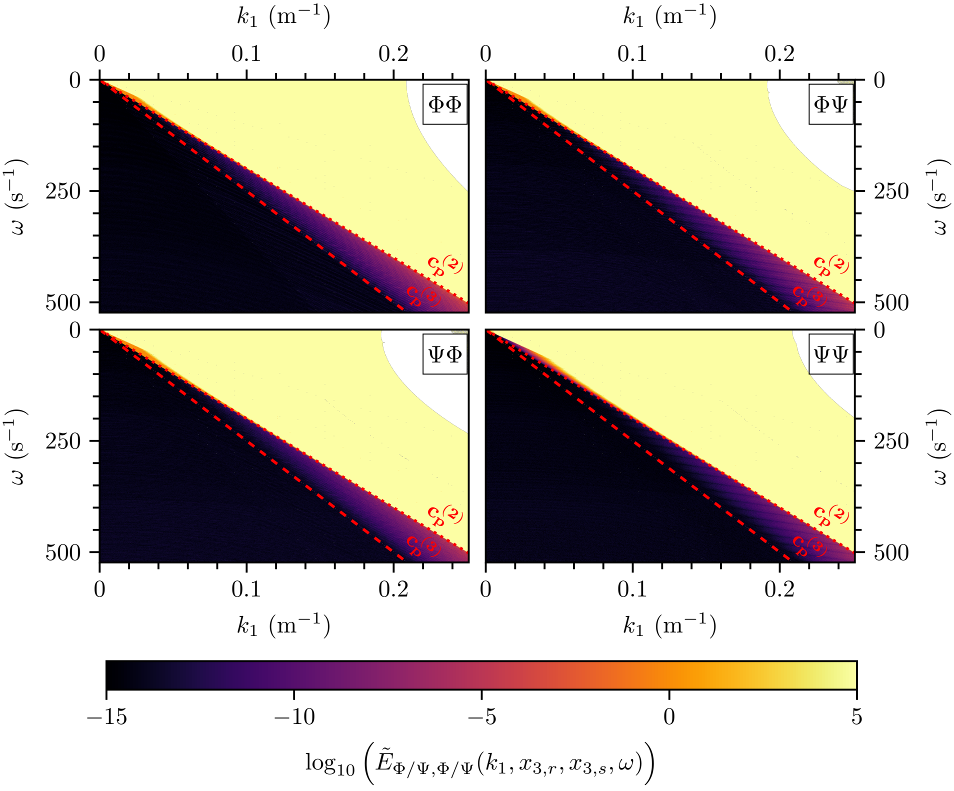

Figure 2.10: *Relative error of the retrieved elastodynamic homogeneous Green's function. As Figure 2.6, but this time for the model in Figure 2.9 with the thin high-velocity layer. Note that also for tunnelled waves (the region between the dashed and dotted red lines) the relative errors are very small.*

Next, we evaluate the single-sided representation of the elastodynamic homogeneous Green's function $\tilde{\mathbf{\Gamma}}_h(k_1, x_{3,r}, x_{3,s}, \omega)$ according to Equations 2.2.20-2.2.23, for a virtual source at $x_{3,s} = 1500\,\mathrm{m}$ and a virtual receiver at $x_{3,r} = 1700\,\mathrm{m}$.

To analyse the result, we model the elastodynamic homogeneous Green's function $\tilde{\mathbf{\Gamma}}_{h,mod}(k_1, x_{3,r}, x_{3,s}, \omega)$ as a reference and compute the relative error $\tilde{\mathbf{E}}(k_1, x_{3,r}, x_{3,s}, \omega)$ according to Equation 2.3.7. Figure 2.10 shows the resulting relative error. For wavenumber-frequency components that are only propagating in the truncated medium, i.e. $|k_1| < \frac{\omega}{c_p^{(3)}}$, the relative error $\tilde{\mathbf{E}}(k_1, x_{3,r}, x_{3,s}, \omega)$ is in the order of 10^{-15}, as expected. For larger wavenumbers, $|k_1| > \frac{\omega}{c_p^{(3)}}$, we would expect a rapid increase of the relative error $\tilde{\mathbf{E}}(k_1, x_{3,r}, x_{3,s}, \omega)$ due to instabilities, similar to Figure 2.6. However, Figure 2.10 shows that for wavenumbers, $\frac{\omega}{c_p^{(3)}} < |k_1| < \frac{\omega}{c_p^{(2)}}$, the relative error $\tilde{\mathbf{E}}(k_1, x_{3,r}, x_{3,s}, \omega)$ ranges from about 10^{-15} to about 10^{-6}. The relative error is not within numerical precision but still very small. We interpret this effect as evanescent wave tunnelling. In the theory section, we excluded evanescent waves. However, this restriction is only required on the boundaries on which the reciprocity theorem of the correlation-type is evaluated (see 2A). Therefore, the theory does not exclude evanescent wave tunnelling. Besides, the theory does not make any assumption about the thickness of the tunnelled layer. In the presented numerical example, we observed that the relative error of the tunnelling experiment depends on the thickness Δx_3 of the tunnelled layer. This observation is expected because the amplitude of the tunnelled evanescent waves is reduced by the factor,

$$\exp\left(-\sqrt{k_1^2 - \frac{\omega^2}{c^2}}\Delta x_3\right). \tag{2.3.11}$$

The single-sided representation compensates for this amplitude decay. For increasing thickness of the tunnelled layer, i.e. stronger amplitude decay, the amplitude ratio of tunnelled and propagating waves becomes smaller, and the numerical errors become larger. To estimate the maximum amplitude decay in the presented example, we maximise $\sqrt{k_1^2 - \frac{\omega^2}{c^2}}$ (see Equation 2.3.11) inside the wavenumber regime, $\frac{\omega}{c_p^{(3)}} < |k_1| < \frac{\omega}{c_p^{(2)}}$. Thus, we choose $c = c_p^{(3)}$, maximise the frequency $\omega = 1025 \times 0.511\,\mathrm{s}^{-1}$ (see Table 2.1) and maximise the horizontal wavenumber $k_1 = \frac{\omega}{c_p^{(2)}}$. The resulting amplitude decay factor,

$$\begin{aligned}
&\exp\left(-\sqrt{k_1^2 - \frac{\omega^2}{c^2}}\Delta x_3\right) \\
&\quad = \exp\left(-\sqrt{\left(\frac{1025 \times 0.511\,\mathrm{s}^{-1}}{2000\,\mathrm{m\,s}^{-1}}\right)^2 - \left(\frac{1025 \times 0.511\,\mathrm{s}^{-1}}{2500\,\mathrm{m\,s}^{-1}}\right)^2} \times 80.0\,\mathrm{m}\right) \\
&\quad = \exp\left(-0.157\,\mathrm{m}^{-1} \times 80.0\,\mathrm{m}\right) \\
&\quad = 3.51 \times 10^{-6},
\end{aligned} \tag{2.3.12}$$

shows that, for tunnelling through the high-velocity layer of 80.0 m thickness, the smallest amplitude ratio of tunnelled and propagating waves is already in the order of 10^{-6}.

2.4 Discussion and conclusion

2.4.1 Discussion

We presented numerical examples of the single-sided homogeneous Green's function representation in elastic laterally-invariant media. Such 1D models are relatively simple, but they allow us to model the required fields with very high numerical accuracy via wavefield extrapolation. Nonetheless, the theory is valid for laterally varying media, and has already been tested numerically for acoustic waves [*Wapenaar et al.*, 2016b]. In the future, we will extend the here presented numerical example to elastic laterally varying media.

Here, we modelled the focusing functions. In practise, for the acoustic situation the focusing functions can be retrieved from the reflection response combined with a smooth velocity model via the Marchenko method, which is described by *Broggini et al.* [2012a], *van der Neut et al.* [2015] and others. For example, *Wapenaar et al.* [2016b] presented an acoustic single-sided homogeneous Green's function representation that uses focusing functions retrieved via the Marchenko method. *Da Costa Filho et al.* [2014] and *Wapenaar* [2014] extended the Marchenko method to elastodynamic waves, however, it still requires more prior knowledge of the medium than in the acoustic case. In the here presented numerical example, we used numerically modelled elastodynamic focusing functions to analyse the properties of the elastodynamic single-sided homogeneous Green's function representation, independent of approximations of the focusing functions. Currently, we are developing the (elastodynamic) Marchenko method further to minimise the required amount of prior knowledge of the medium.

According to the theory, the single-sided representation of the elastodynamic homogeneous Green's function is accurate for waves that are non-evanescent at the virtual source and receiver depth levels. In our first numerical experiment, we only consider propagating waves and confirm the theory within numerical precision. In our second experiment, we investigate wavefield components that are evanescent inside a thin layer, but propagating at the virtual source and receiver depth levels. In this case, the numerical result for the elastodynamic homogeneous Green's function using the single-sided representation performs well also for evanescent waves, except for a small relative error. The latter experiment is a tunnelling experiment, which performs better if the tunnelled layer is thin with respect to the inverse of the absolute vertical wavenumber. Although evanescent wave tunnelling appears to be possible in theory, in practice it will suffer from noise and it will not be possible to retrieve the evanescent components of the focusing function via the Marchenko method.

2.4.2 Conclusion

We presented a numerical example demonstrating that single-sided access to a medium suffices to correctly retrieve the non-evanescent components of an elastodynamic homogeneous Green's function with virtual sources and virtual receivers inside the medium. Despite the single-sided access to the medium, all events of the homogeneous Green's function including primaries, internal multiples and converted waves are represented correctly. Waves that are evanescent, either on the recording boundary, or at the virtual source/receiver depth level, are neglected by the single-sided representation of the elastodynamic homogeneous Green's function, and hence, can lead to artefacts. Nevertheless, the evanescent components can be filtered to suppress these artefacts. The remaining, i.e. propagating, components can be used e.g. for imaging.

In addition, we observed in a numerical experiment that the elastodynamic single-sided homogeneous Green's function representation can tunnel evanescent components through a thin layer. In theory, this tunnelling of evanescent waves is independent of the thickness of the tunnelled layer. In practise, the single-sided representation of tunnelled waves has limited numerical accuracy because it has to compensate for the exponential amplitude decay of evanescent waves, which is stronger for thicker layers. Hence, the tunnelled layer has to be sufficiently thin with respect to the inverse of the absolute vertical wavenumber of the evanescent wave. Note that we refer to tunnelling because the single-sided representation requires that at the virtual source and receiver depth levels the elastodynamic homogeneous Green's function is propagating.

To conclude, we provided a mathematical framework to create virtual wavefield measurements inside a medium that is only accessible from a single side. We foresee potential applications in the fields of imaging, time-lapse monitoring, forecasting of the medium response as well as localisation of passive sources.

Acknowledgements

We thank Carlos Alberto da Costa Filho and one anonymous reviewer for their constructive comments that helped us to improve the paper. Further, we would like to acknowledge the Waves project for offering such a great research network. Last but not least, we are grateful to our co-workers for all the inspiring discussions. This work was supported by the European Union's Horizon 2020 research and innovation programme: Marie Skłodowska-Curie [grant number 641943] and European Research Council [grant number 742703].

2A Elastodynamic single-sided homogenous Green's function representation

In the following, we summarise the derivation of the elastodynamic single-sided homogeneous Green's function representation [*Wapenaar et al.*, 2016a]. First, we show the decomposed reciprocity theorems and introduce the two states that are used in the derivation. Second, we explain the properties of the focusing function. Third, we derive the elastodynamic single-sided homogeneous Green's function representation by inserting the focusing function and the Green's function in the decomposed reciprocity theorems.

■ 2A.1 Reciprocity theorems and the two states

We define a domain $\mathbb{D}$ with infinite horizontal extent. The x_3 axis is defined along the depth direction as downward pointing. The domain is enclosed by $\partial\mathbb{D}_0$ ($x_3 = x_{3,0}$) at the top, $\partial\mathbb{D}_r$ ($x_3 = x_{3,r}$) at the bottom and a cylindrical boundary $\partial\mathbb{D}_{cyl}$ with infinite radius at the side. Besides, we introduce two wavefield states A and B with independent decomposed wavefield vectors $\mathbf{p}_{A,B}$ as well as independent decomposed source vectors $\mathbf{s}_{A,B}$, both in the space-frequency domain. We assume the medium in which these wavefields and sources exist is lossless, and that the medium parameters of the states A and B are identical inside the domain $\mathbb{D}$. Now we can formulate the reciprocity theorems of the convolution- and correlation-type,

$$\int_{\partial\mathbb{D}} \mathbf{p}_A^T \mathbf{N} \mathbf{p}_B n_3 \mathrm{d}^2\mathbf{x} = \int_{\mathbb{D}} \left(\mathbf{s}_A^T \mathbf{N} \mathbf{p}_B + \mathbf{p}_A^T \mathbf{N} \mathbf{s}_B\right) \mathrm{d}^3\mathbf{x}, \tag{2A.1}$$

$$\int_{\partial\mathbb{D}} \mathbf{p}_A^\dagger \mathbf{J} \mathbf{p}_B n_3 \mathrm{d}^2\mathbf{x} = \int_{\mathbb{D}} \left(\mathbf{s}_A^\dagger \mathbf{J} \mathbf{p}_B + \mathbf{p}_A^\dagger \mathbf{J} \mathbf{s}_B\right) \mathrm{d}^3\mathbf{x}. \tag{2A.2}$$

Here, the dagger symbol † denotes transposition and complex-conjugation. On the boundary $\partial\mathbb{D}$, the derivation of the reciprocity theorem of the correlation-type (Equation 2A.2) uses the symmetry relation $\mathcal{L}^\dagger \mathbf{K} = \mathbf{J}\mathcal{L}^{-1}$, which only holds for propagating waves [*Wapenaar*, 1996c]. Note that $\mathcal{L} = \mathcal{L}(\mathbf{x}, \omega)$ is the operator matrix that composes wavefields. Consequently, we neglect evanescent waves on the boundary $\partial\mathbb{D}$. The boundary $\partial\mathbb{D}$ consists of the top and bottom boundaries of the domain, $\partial\mathbb{D}_0 \cup \partial\mathbb{D}_r$. Integral contributions over the cylindrical boundary $\partial\mathbb{D}_{cyl}$ vanish (if the medium has infinite horizontal extent) because the integrand is proportional to one divided by the radius squared ($\propto \frac{1}{R^2}$) whereas the cylindrical surface is proportional to the radius ($\propto R$). In the boundary integrals, n_3 is the x_3 component of the outward-pointing normal vector on the boundary $\partial\mathbb{D}$ ($n_3 = -1$ on $\partial\mathbb{D}_0$, $n_3 = +1$ on $\partial\mathbb{D}_r$).

The single-sided homogeneous Green's function representation is derived by evaluating the two reciprocity theorems using a specific definition of states A and B. First, we define state B in the actual medium. Let the upper boundary $\partial\mathbb{D}_0$ be at $x_3 = x_{3,0}$. Above $\partial\mathbb{D}_0$, i.e. $x_3 \leq x_{3,0}$, the state B medium is reflection-free. Below $\partial\mathbb{D}_0$, i.e. $x_3 > x_{3,0}$, the actual medium is inhomogeneous and elastic. We define the state B wavefield to be the medium's Green's function $\mathbf{\Gamma}(\mathbf{x}, \mathbf{x}_s, \omega)$ related to a source at $\mathbf{x}_s$ with $x_{3,s} > x_{3,0}$, and a receiver at $\mathbf{x}$,

$$\mathbf{p}_B = \mathbf{\Gamma}(\mathbf{x}, \mathbf{x}_s, \omega), \quad \mathbf{s}_B = \mathbf{I}\delta(\mathbf{x} - \mathbf{x}_s). \tag{2A.3}$$

Second, we define state A. We choose a point $\mathbf{x}_r$ below $\partial\mathbb{D}_0$. The state A medium is defined equal to the state B medium for $x_{3,0} \leq x_3 \leq x_{3,r}$, and for $x_3 \geq x_{3,r}$ the state A medium is reflection-free. Often, the state A medium is referred to as the so-called truncated medium. The state A wavefield is defined as the focusing function $\mathbf{F}(\mathbf{x}, \mathbf{x}_r, \omega)$. By definition the source term of the focusing function is zero,

$$\mathbf{p}_A = \mathbf{F}(\mathbf{x}, \mathbf{x}_r, \omega), \quad \mathbf{s}_A = \mathbf{0}. \tag{2A.4}$$

2A.2 Focusing function

The downgoing part of the focusing function $\mathbf{F}^+(\mathbf{x}, \mathbf{x}_r, \omega)$ is the inverse of a transmission response related to sources at the boundary $\partial\mathbb{D}_0$ and a receiver at $\mathbf{x}_r$,

$$\int_{\partial\mathbb{D}_0} \mathbf{T}^+(\mathbf{x}, \mathbf{x}', \omega)\mathbf{F}^+(\mathbf{x}', \mathbf{x}_r, \omega)\mathrm{d}^2\mathbf{x}'_H \Big|_{x_3=x_{3,r}} = \mathbf{I}\ \delta(\mathbf{x}_H - \mathbf{x}_{H,r}), \tag{2A.5}$$

and it obeys the focusing condition,

$$\mathbf{F}(\mathbf{x}, \mathbf{x}_r, \omega)|_{x_3=x_{3,r}} = \mathbf{I}_1\ \delta(\mathbf{x}_H - \mathbf{x}_{H,r}), \tag{2A.6}$$

with $\mathbf{F}$ containing $\mathbf{F}^+$ and $\mathbf{F}^-$, see Equation 2.2.16. The upgoing focusing function $\mathbf{F}^-(\mathbf{x}, \mathbf{x}_r, \omega)$ is the reflection response of the downgoing focusing function in the truncated medium.

In a physical interpretation the focusing function, when transformed to the time domain, is a wavefield injected at $\partial\mathbb{D}_0$, which focuses at time zero at the location $\mathbf{x}_r$. Figure 2.1b depicts the focusing function in a cartoon. The solid arrows represent the downgoing focusing function $\mathbf{F}^+$. When the downgoing focusing function is sent into the truncated medium it is partially reflected, leading to the upgoing focusing function, indicated by dashed arrows in Figure 2.1b. In the absence of a coda, the upgoing focusing function would be reflected downward again. Consequently, the focusing function would not focus at $\mathbf{x}_r$. This scenario is prevented by sending a coda of the downgoing focusing function into the medium to cancel the downward reflections of the upgoing focusing function. The coda is also shown in Figure 2.1b.

For a 3D acoustic medium, the focusing function can be retrieved from the reflection response of the medium combined with a smooth velocity model via the Marchenko method [e.g. *Broggini and Snieder*, 2012; *Wapenaar et al.*, 2014b; *Vasconcelos et al.*, 2015]. For an elastic medium, the focusing function retrieval still requires additional information about the medium [*Wapenaar*, 2014].

2A.3 Derivation

We insert states A and state B (Equations 2A.3, 2A.4) in the reciprocity theorems of the convolution- and the correlation-type (Equations 2A.1, 2A.2) and evaluate them in the domain $\mathbb{D}_r$ bounded by $\partial\mathbb{D}_0$ at the top and by $\partial\mathbb{D}_r$ at the bottom. Note that the state A and state B media are identical in the domain $\mathbb{D}_r$, which is a necessary condition for Equations 2A.1-2A.2. Using the focusing condition of Equation 2A.6, we find,

$$\begin{aligned}\mathbf{I}_1^T\mathbf{N}\boldsymbol{\Gamma}(\mathbf{x}_r, \mathbf{x}_s, \omega) - H(x_{3,r} - x_{3,s})\mathbf{F}^T(\mathbf{x}_s, \mathbf{x}_r, \omega)\mathbf{N} = \\ \int_{\partial\mathbb{D}_0} \mathbf{F}^T(\mathbf{x}, \mathbf{x}_r, \omega)\mathbf{N}\boldsymbol{\Gamma}(\mathbf{x}, \mathbf{x}_s, \omega)\ \mathrm{d}^2\mathbf{x}_H,\end{aligned} \tag{2A.7}$$

and,

$$\begin{aligned}\mathbf{I}_1^T\mathbf{J}\boldsymbol{\Gamma}^*(\mathbf{x}_r, \mathbf{x}_s, \omega) - H(x_{3,r} - x_{3,s})\mathbf{F}^T(\mathbf{x}_s, \mathbf{x}_r, \omega)\mathbf{J} = \\ \int_{\partial\mathbb{D}_0} \mathbf{F}^T(\mathbf{x}, \mathbf{x}_r, \omega)\mathbf{J}\boldsymbol{\Gamma}^*(\mathbf{x}, \mathbf{x}_s, \omega)\ \mathrm{d}^2\mathbf{x}_H.\end{aligned} \tag{2A.8}$$

$H(x_3)$ is the Heaviside function. We multiply Equation 2A.8 by $\mathbf{K}$ from the right and substitute the identities $\mathbf{J} = \mathbf{NK}$ as well as $\mathbf{JK} = \mathbf{N}$,

$$\mathbf{I}_1^T\mathbf{NK}\mathbf{\Gamma}^*(\mathbf{x}_r, \mathbf{x}_s, \omega)\mathbf{K} - H(x_{3,r} - x_{3,s})\mathbf{F}^T(\mathbf{x}_s, \mathbf{x}_r, \omega)\mathbf{N} = \int_{\partial\mathbb{D}_0} \mathbf{F}^T(\mathbf{x}, \mathbf{x}_r, \omega)\mathbf{NK}\mathbf{\Gamma}^*(\mathbf{x}, \mathbf{x}_s, \omega)\mathbf{K}\ \mathrm{d}^2\mathbf{x}_H. \tag{2A.9}$$

We eliminate the term with the Heaviside function by subtracting Equation 2A.9 from Equation 2A.7. The resulting expression can be written in terms of the homogeneous Green's function (using Equation 2.2.11),

$$\mathbf{I}_1^T\mathbf{N}\mathbf{\Gamma}_h(\mathbf{x}_r, \mathbf{x}_s, \omega) = \int_{\partial\mathbb{D}_0} \mathbf{F}^T(\mathbf{x}, \mathbf{x}_r, \omega)\mathbf{N}\mathbf{\Gamma}_h(\mathbf{x}, \mathbf{x}_s, \omega)\ \mathrm{d}^2\mathbf{x}_H. \tag{2A.10}$$

The multiplication by $\mathbf{I}_1^T\mathbf{N}$ from the left in Equation 2A.10 deletes the upper submatrices of the homogeneous Green's function $\mathbf{\Gamma}_h(\mathbf{x}_r, \mathbf{x}_s, \omega)$. We retrieve the complete matrix $\mathbf{\Gamma}_h(\mathbf{x}_r, \mathbf{x}_s, \omega)$ by multiplying Equation 2A.10 by $\mathbf{I}_2$ from the left,

$$\mathbf{\Gamma}_2(\mathbf{x}_r, \mathbf{x}_s, \omega) = \mathbf{I}_2\mathbf{I}_1^T\mathbf{N}\mathbf{\Gamma}_h(\mathbf{x}_r, \mathbf{x}_s, \omega) = \begin{pmatrix} \mathbf{O} & \mathbf{O} \\ \mathbf{G}^{-,+} - (\mathbf{G}^{+,-})^* & \mathbf{G}^{-,-} - (\mathbf{G}^{+,+})^* \end{pmatrix}, \tag{2A.11}$$

and by using Equations 2.2.11 and 2.2.12,

$$\mathbf{\Gamma}_h(\mathbf{x}_r, \mathbf{x}_s, \omega) = \mathbf{\Gamma}_2(\mathbf{x}_r, \mathbf{x}_s, \omega) - \mathbf{K}\mathbf{\Gamma}_2^*(\mathbf{x}_r, \mathbf{x}_s, \omega)\mathbf{K}. \tag{2A.12}$$

From Equations 2A.10 and 2A.11 it follows that the Green's function $\mathbf{\Gamma}_2(\mathbf{x}_r, \mathbf{x}_s, \omega)$ is defined as,

$$\mathbf{\Gamma}_2(\mathbf{x}_r, \mathbf{x}_s, \omega) = \int_{\partial\mathbb{D}_0} \mathbf{I}_2\mathbf{F}^T(\mathbf{x}, \mathbf{x}_r, \omega)\mathbf{N}\mathbf{\Gamma}_h(\mathbf{x}, \mathbf{x}_s, \omega)\mathrm{d}^2\mathbf{x}. \tag{2A.13}$$

Equations 2A.12-2A.13 together form the single-sided homogeneous Green's function representation for $\mathbf{\Gamma}_h(\mathbf{x}_r, \mathbf{x}_s, \omega)$. The right-hand side of Equation 2A.13 contains the homogeneous Green's function $\mathbf{\Gamma}_h(\mathbf{x}, \mathbf{x}_s, \omega)$, for which we can obtain a single-sided representation in a similar way. First, in Equation 2A.10, we substitute $\mathbf{x}$ by $\mathbf{x}'$ on $\partial\mathbb{D}_0'$ (just above $\partial\mathbb{D}_0$), $\mathbf{x}_s$ by $\mathbf{x}$ (on $\partial\mathbb{D}_0$) and $\mathbf{x}_r$ by $\mathbf{x}_s$,

$$\mathbf{I}_1^T\mathbf{N}\mathbf{\Gamma}_h(\mathbf{x}_s, \mathbf{x}, \omega) = \int_{\partial\mathbb{D}_0'} \mathbf{F}^T(\mathbf{x}', \mathbf{x}_s, \omega)\mathbf{N}\mathbf{\Gamma}_h(\mathbf{x}', \mathbf{x}, \omega)\ \mathrm{d}^2\mathbf{x}_H'. \tag{2A.14}$$

Second, we multiply Equation 2A.14 by $\mathbf{N}$ from the right, transpose the result and apply source-receiver reciprocity $(\mathbf{N}\mathbf{\Gamma}_h^T(\mathbf{x}_s, \mathbf{x}, \omega)\mathbf{N} = \mathbf{\Gamma}_h(\mathbf{x}, \mathbf{x}_s, \omega))$,

$$\mathbf{\Gamma}_h(\mathbf{x}, \mathbf{x}_s, \omega)\mathbf{I}_1 = \int_{\partial\mathbb{D}_0'} \mathbf{\Gamma}_h(\mathbf{x}, \mathbf{x}', \omega)\mathbf{F}(\mathbf{x}', \mathbf{x}_s, \omega)\ \mathrm{d}^2\mathbf{x}_H'. \tag{2A.15}$$

Multiplication by matrix $\mathbf{I}_1$ deletes part of the homogeneous Green's function $\mathbf{\Gamma}_h(\mathbf{x}, \mathbf{x}_s, \omega)$. The full matrix $\mathbf{\Gamma}_h(\mathbf{x}, \mathbf{x}_s, \omega)$ is constructed by multiplying by $\mathbf{I}_1^T$ from the right,

$$\mathbf{\Gamma}_1(\mathbf{x}, \mathbf{x}_s, \omega) = \mathbf{\Gamma}_h(\mathbf{x}, \mathbf{x}_s, \omega)\mathbf{I}_1\mathbf{I}_1^T = \begin{pmatrix} \mathbf{G}^{+,+} - (\mathbf{G}^{-,-})^* & \mathbf{O} \\ \mathbf{G}^{-,+} - (\mathbf{G}^{+,-})^* & \mathbf{O} \end{pmatrix}, \tag{2A.16}$$

and by using the definition of the homogeneous Green's function (Equations 2.2.11, 2.2.12),

$$\mathbf{\Gamma}_h(\mathbf{x}, \mathbf{x}_s, \omega) = \mathbf{\Gamma}_1(\mathbf{x}, \mathbf{x}_s, \omega) - \mathbf{K}\mathbf{\Gamma}_1^*(\mathbf{x}, \mathbf{x}_s, \omega)\mathbf{K}, \tag{2A.17}$$

where $\mathbf{\Gamma}_1(\mathbf{x}, \mathbf{x}_s, \omega)$ is defined as,

$$\mathbf{\Gamma}_1(\mathbf{x}, \mathbf{x}_s, \omega) = \int_{\partial\mathbb{D}_0'} \mathbf{\Gamma}_h(\mathbf{x}, \mathbf{x}', \omega)\mathbf{F}(\mathbf{x}', \mathbf{x}_s, \omega)\mathbf{I}_1^T \mathrm{d}^2\mathbf{x}'. \tag{2A.18}$$

Equations 2A.17-2A.18 together form the single-sided homogeneous Green's function representation for $\mathbf{\Gamma}_h(\mathbf{x}, \mathbf{x}_s, \omega)$.

In summary, we derived a single-sided representation of the homogeneous Green's function $\mathbf{\Gamma}_h(\mathbf{x}_r, \mathbf{x}_s, \omega)$ consisting of two steps. In the first step (Equations 2A.17-2A.18) a virtual source is created inside the medium. In the second step (Equations 2A.12-2A.13) a virtual receiver is created inside the medium.

2B 20-layer model

The numerical experiment of the Section 2.3.2 is repeated for the 20 layer model shown in Figure 2.11.

We model the reflection response and the required focusing functions to create a virtual source at $\mathbf{x}_s = (0\,\mathrm{m}, 1500\,\mathrm{m})^T$ and virtual receivers on a grid with a depth range from 0 m to 3000 m and a lateral distance range from −2000 m to 2000 m. The spatial sampling interval is 12.5 m in both the vertical and horizontal direction.

From the reflection response and the focusing function we compute the single-sided representation of the elastodynamic homogeneous Green's function $\tilde{\mathbf{\Gamma}}_h(k_1, x_{3,r}, x_{3,s}, \omega)$ and apply a k_1-ω filter (determined by the P-wave velocity as a function of the virtual receiver depth $x_{3,r}$). We compose the result according to Equation 2.3.8 and obtain the full elastodynamic homogeneous Green's function $\tilde{\mathbf{G}}_h(k_1, x_{3,r}, x_{3,s}, \omega)$. Next, we apply a transformation to the space-time domain and a convolution with a 30 Hz Ricker wavelet. Figure 2.12 displays the (v_3, f_3) component of the resulting elastodynamic homogeneous Green's function $\mathbf{G}_h^{v,f}(\mathbf{x}_r, \mathbf{x}_s, t)$.

To analyse the accuracy of the single-sided representation, we model the elastodynamic homogeneous Green's function for an actual source at $\mathbf{x}_s = (0\,\mathrm{m}, 1500\,\mathrm{m})^T$. We compute the difference between the modelled and the single-sided representation of the elastodynamic homogeneous Green's function. To exclude the evanescent wavefield, we element-wise multiply the residual $\Delta\tilde{\mathbf{\Gamma}}_h(k_1, x_{3,r}, x_{3,s}, \omega)$ by a k_1-ω filter $\tilde{\mathbf{M}}$, which is determined by the maximum propagation velocity of the medium. Subsequently, we evaluate the normalised Frobenius norm $N_F = \frac{1}{\sqrt{4nt4nr}}\|\tilde{\mathbf{M}} \circ \Delta\tilde{\mathbf{\Gamma}}_h(k_1, x_{3,r}, x_{3,s}, \omega)\|_2$ and show the result as a function of virtual receiver depth $x_{3,r}$ in Figure 2.13. The error plot demonstrates that, also in case of the 20 layer

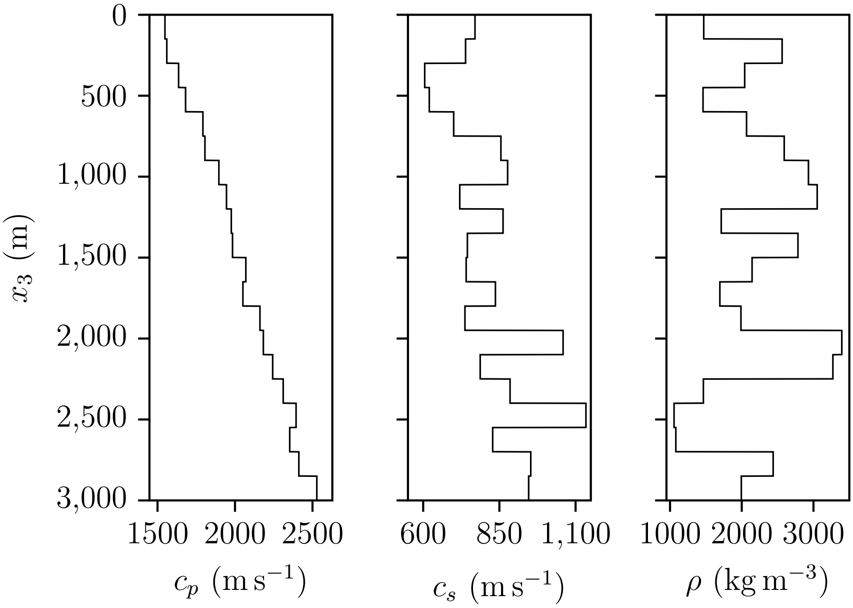

Figure 2.11: *Layered model. The model depth ranges from* $0\,\mathrm{m}$ *to* $3000\,\mathrm{m}$*, the lateral distance ranges from* $-12\,812.5\,\mathrm{m}$ *to* $12\,800\,\mathrm{m}$*. The P-wave velocity, S-wave velocity and density are denoted by* c_p*,* c_s *and* ρ*, respectively.*

model, the single-sided homogeneous Green's function representation is accurate for propagating waves within numerical precision.

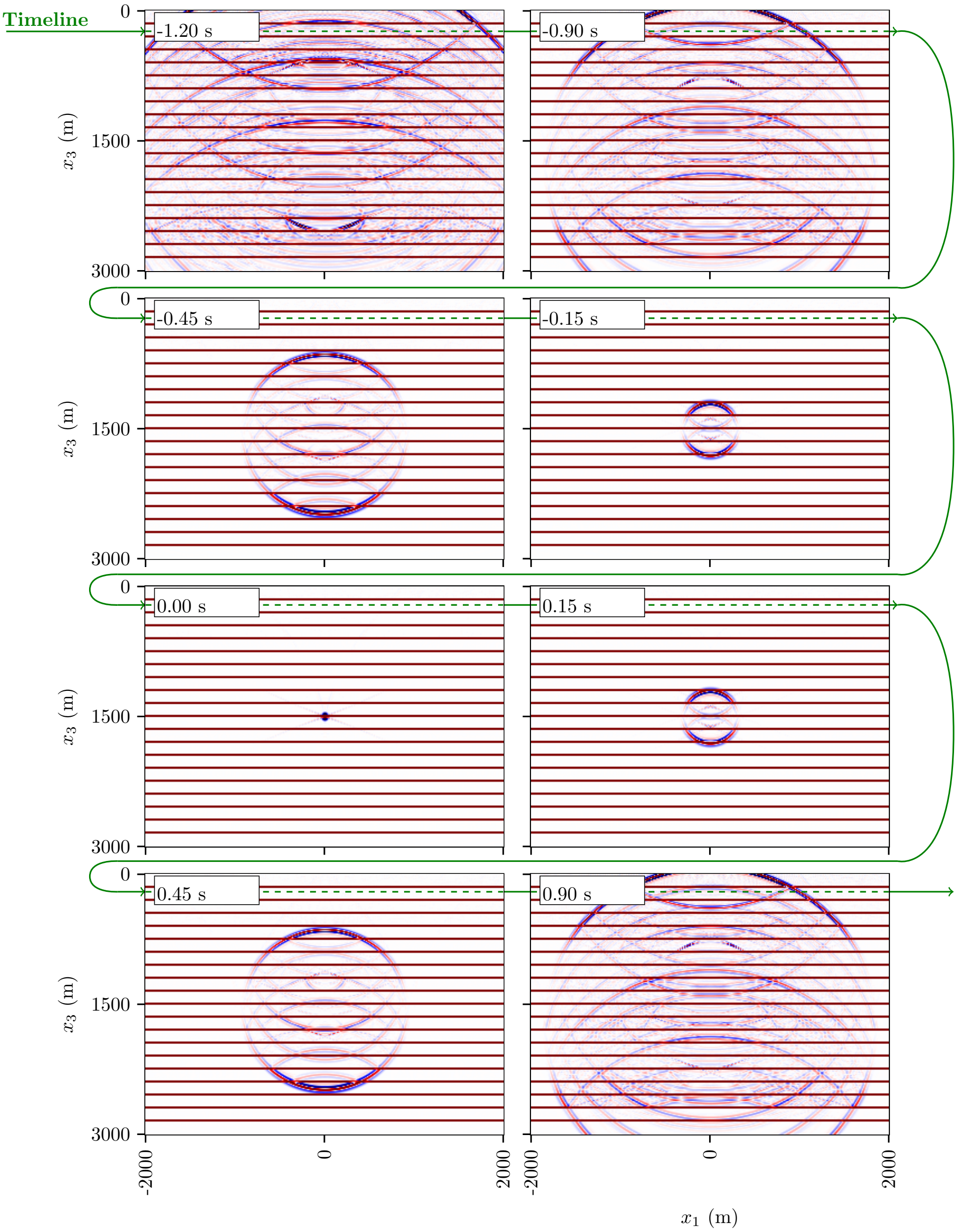

Figure 2.12: *Single-sided representation of the elastodynamic homogeneous Green's function. The time slices show the result of the elastodynamic single-sided homogeneous Green's function representation* $\mathbf{G}_h^{v,f}(\mathbf{x}_r, \mathbf{x}_s, t)$ *related to virtual source* (f_3) *at* $\mathbf{x}_s = (0\,\mathrm{m}, 1500\,\mathrm{m})^T$ *and virtual receivers* (v_3) *placed on a grid with a depth range from* $0\,\mathrm{m}$ *to* $3000\,\mathrm{m}$ *and a lateral distance range from* $-2000\,\mathrm{m}$ *to* $2000\,\mathrm{m}$*. The spatial sampling interval is* $12.5\,\mathrm{m}$ *in both horizontal and vertical direction. The time slices were multiplied by a gain function* ($\times \mathrm{e}^{1.5|t|}$) *to emphasise the late arrivals.*

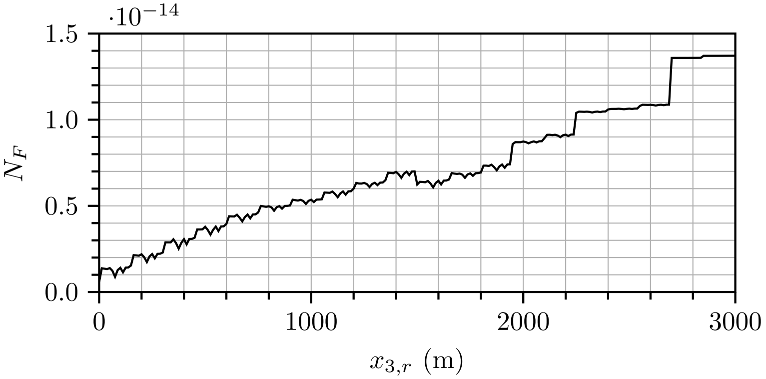

Figure 2.13: *Error analysis. Normalised Frobenius norm N_F of the difference $\Delta\tilde{\mathbf{\Gamma}}_h(k_1, x_{3,r}, x_{3,s}, \omega)$ between the elastodynamic single-sided homogeneous Green's function representation (see Figure 2.12) and its modelled equivalent as a function of virtual receiver depth $x_{3,r}$.*

3

Elastodynamic Marchenko method using plane waves

Abstract The Marchenko method is capable to create virtual sources inside a medium that is only accessible from an open-boundary. The resulting virtual data can be used to retrieve images free of artefacts caused by internal multiples. Conventionally, the Marchenko method retrieves a so-called focusing wavefield that focuses the data from the recording surface to a point inside the medium. Recently, it was suggested to modify the focusing condition such that the new focusing wavefield creates a virtual plane wave source inside the medium, instead of a virtual point source. The virtual plane wave data can be used to image an entire surface inside the medium in a single step rather than imaging individual points on the surface. Consequently, the imaging process is accelerated significantly. We provide an extension of plane wave Marchenko redatuming for elastodynamic waves and demonstrate its performance numerically.

Published as: Reinicke, C., Meles, G. A., and Wapenaar, K. (2018), Elastodynamic Plane Wave Marchenko Redatuming: Theory and Examples, *80th EAGE Conference and Exhibition 2018*. Note that minor changes have been introduced to make the text consistent with the other chapters.

3.1 Introduction

In many imaging applications the medium of interest is observed using reflection measurements acquired on an open-boundary. Recently, a novel imaging technique, the Marchenko method, has been developed with the aim to retrieve images free of artefacts caused by internal multiples. The conventional Marchenko method creates a virtual point source inside the medium, accounting for primary as well as multiply scattered waves [*Broggini et al.*, 2012b; *van der Neut et al.*, 2015]. From the virtual response an image at the virtual source location is computed [*Behura et al.*, 2014]. Hence, the imaging process is performed point-wise. *Meles et al.* [2018] combine the areal-source methods for primaries by *Rietveld et al.* [1992] with the spatially-extended virtual source Marchenko method presented by *Broggini et al.* [2012b] to create a virtual plane wave source at an arbitrary surface inside the medium. Using the virtual plane wave response the entire surface can be imaged in one step rather than imaging each point on the surface individually. We extend plane wave Marchenko redatuming for elastodynamic waves, analogous to the elastodynamic extension of conventional Marchenko redatuming by *Wapenaar* [2014].

3.2 Elastodynamic plane wave Marchenko redatuming: Theory

First, we will introduce the conventional elastodynamic single-sided Green's function representations that allow to create virtual point sources inside a medium. For a detailed derivation we refer to *Wapenaar* [2014]. Second, we will modify these equations such that they create virtual plane wave sources instead of virtual point sources. Consider an elastic medium without losses. Suppose the medium has infinite lateral extent and is bounded by a reflection-free surface $\partial\mathbb{D}_0$ at the top. Moreover, we consider elastodynamic power-flux normalised wavefield potentials. The single-sided Green's function representations can be written as,

$$\mathbf{G}^{-,+}(\mathbf{x}',\mathbf{x}_f,\omega) = \int_{\partial\mathbb{D}_0} \mathbf{R}(\mathbf{x}',\mathbf{x},\omega)\mathbf{F}^{+}(\mathbf{x},\mathbf{x}_f,\omega)\mathrm{d}^2\mathbf{x} - \mathbf{F}^{-}(\mathbf{x}',\mathbf{x}_f,\omega), \tag{3.2.1}$$

$$\{\mathbf{G}^{-,-}(\mathbf{x}',\mathbf{x}_f,\omega)\}^* = \int_{\partial\mathbb{D}_0} \mathbf{R}^*(\mathbf{x}',\mathbf{x},\omega)\mathbf{F}^{-}(\mathbf{x},\mathbf{x}_f,\omega)\mathrm{d}^2\mathbf{x} - \mathbf{F}^{+}(\mathbf{x}',\mathbf{x}_f,\omega). \tag{3.2.2}$$

Here, the one-way Green's functions $\mathbf{G}^{-,\pm}(\mathbf{x}',\mathbf{x}_f,\omega)$ are 3×3 matrices,

$$\mathbf{G}^{-,\pm}(\mathbf{x}',\mathbf{x}_f,\omega) = \begin{pmatrix} G^{-,\pm}_{\Phi,\Phi} & G^{-,\pm}_{\Phi,\Psi} & G^{-,\pm}_{\Phi,\Upsilon} \\ G^{-,\pm}_{\Psi,\Phi} & G^{-,\pm}_{\Psi,\Psi} & G^{-,\pm}_{\Psi,\Upsilon} \\ G^{-,\pm}_{\Upsilon,\Phi} & G^{-,\pm}_{\Upsilon,\Psi} & G^{-,\pm}_{\Upsilon,\Upsilon} \end{pmatrix}(\mathbf{x}',\mathbf{x}_f,\omega), \tag{3.2.3}$$

where the superscript "$+$" describes downgoing waves, the superscript "$-$" describes upgoing waves. The subscripts Φ, Ψ and Υ represent P-, S1- and S2-wavefield potentials, respectively. The first super- and subscripts refer to the wavefield at the receiver position $\mathbf{x}'$ on $\partial\mathbb{D}_0$, the second super- and subscripts refer to the wavefield at the source position $\mathbf{x}_f$ inside the medium. The spatial coordinates and the frequency are denoted as $\mathbf{x} = (x_1, x_2, x_3)^T$ and ω, respectively. The superscript "T" denotes a transpose and the superscript "$*$" denotes a complex-conjugate. The quantity $\mathbf{R}(\mathbf{x}', \mathbf{x}, \omega)$ is the reflection response of the medium recorded on $\partial\mathbb{D}_0$. The focusing function $\mathbf{F}^{\pm}(\mathbf{x}, \mathbf{x}_f, \omega)$ is defined in a truncated medium which is identical to the physical medium between $\partial\mathbb{D}_0$ and $\partial\mathbb{D}_f$ ($x_3 = x_{3,f}$) but reflection-free above $\partial\mathbb{D}_0$ and below $\partial\mathbb{D}_f$. We formulate the focusing functions in the space-time domain to emphasise its spatial and temporal behaviour. The downgoing part of the focusing function $\mathbf{F}^{+}(\mathbf{x}', \mathbf{x}_f, t)$ is the inverse of the transmission response $\mathbf{T}^{+}(\mathbf{x}, \mathbf{x}', t)$ of the truncated medium [*Wapenaar et al.*, 2016a],

$$\int_{-\infty}^{t} \int_{\partial\mathbb{D}_0} \mathbf{T}^{+}(\mathbf{x}, \mathbf{x}', t - t')\mathbf{F}^{+}(\mathbf{x}', \mathbf{x}_f, t')\, \mathrm{d}^2\mathbf{x}'_H \mathrm{d}t' \bigg|_{x_3 = x_{3,f}} = \delta(t)\, \delta(\mathbf{x}_H - \mathbf{x}_{H,f})\, \mathbf{I}. \tag{3.2.4}$$

The subscript "H" refers to the horizontal coordinates $\mathbf{x}_H = (x_1, x_2)^T$ and $\mathbf{I}$ is an identity matrix of appropriate size. From Eq. 3.2.4 follows that the downgoing focusing function satisfies the focusing condition,

$$\mathbf{F}^{+}(\mathbf{x}, \mathbf{x}_f, t)\big|_{x_3 = x_{3,f}} = \delta(t)\, \delta(\mathbf{x}_H - \mathbf{x}_{H,f})\, \mathbf{I}. \tag{3.2.5}$$

Thus, the focusing function $\mathbf{F}(\mathbf{x}, \mathbf{x}_f, t)$ focuses in time and in space. The upgoing part of the focusing function $\mathbf{F}^{-}(\mathbf{x}, \mathbf{x}_f, t)$ is the reflection response of the downgoing focusing function in the truncated medium. In physical interpretation the single-sided Green's function representations (Eqs. 3.2.1 and 3.2.2) can be understood as follows. The focusing function focuses, or inverse propagates, the source-side of the reflection response $\mathbf{R}(\mathbf{x}', \mathbf{x}, \omega)$ from the recording surface $\partial\mathbb{D}_0$ to the focusing point $\mathbf{x}_f$ inside the medium. Hence, a virtual source is created inside the medium at $\mathbf{x}_f$. Following the acoustic plane wave Marchenko redatuming by *Meles et al.* [2018], we suggest to define a modified focusing function $\bar{\mathbf{F}}^{\pm}(\mathbf{x}, \mathbf{p}_H, x_{3.f}, t)$ that focuses as a plane wave in time but not in space. Therefore, the modified downgoing focusing function obeys the modified focusing condition,

$$\bar{\mathbf{F}}^{+}(\mathbf{x}, \mathbf{p}_H, x_{3,f}, t)\big|_{x_3 = x_{3,f}} = \delta(t - \mathbf{p}_H \cdot \mathbf{x}_H)\, \mathbf{I}, \tag{3.2.6}$$

where $\mathbf{p}_H = (p_1, p_2)^T$ denotes the horizontal ray-parameter. The conventional and the modified focusing conditions in Eqs. 3.2.5 and 3.2.6 are very similar but the temporal focus $\delta(t)$ is replaced by an offset-dependent focus in time $\delta(t - \mathbf{p}_H \cdot \mathbf{x}_H)$ and the spatial focus $\delta(\mathbf{x}_H - \mathbf{x}_{H,f})$ is removed. In the space-frequency domain, we obtain the modified focusing function $\bar{\mathbf{F}}^{\pm}(\mathbf{x}, \mathbf{p}_H, x_{3.f}, t)$ by multiplying the focusing function $\mathbf{F}^{\pm}(\mathbf{x}, \mathbf{x}_f, \omega)$ by the plane wave $\mathrm{e}^{\mathrm{j}\omega\mathbf{p}_H \cdot \mathbf{x}_{H,f}}$ and by integrating the result over the focusing surface $\partial\mathbb{D}_f$,

$$\bar{\mathbf{F}}^{\pm}(\mathbf{x}, \mathbf{p}_H, x_{3,f}, \omega) = \int_{\partial\mathbb{D}_f} \mathbf{F}^{\pm}(\mathbf{x}, \mathbf{x}_{H,f}, x_{3,f}, \omega)\, \mathrm{e}^{\mathrm{j}\omega\mathbf{p}_H \cdot \mathbf{x}_{H,f}} \mathrm{d}^2\mathbf{x}_{H,f}. \tag{3.2.7}$$

Further, we define the plane wave responses $\bar{\mathbf{G}}^{-,\pm}(\mathbf{x}, \mathbf{p}_H, x_{3,f}, \omega)$ that are associated to a plane wave source $\delta(t - \mathbf{p}_H \cdot \mathbf{x}_{H,f})$ at $\partial\mathbb{D}_f$ and recorded at $\mathbf{x}$ on $\partial\mathbb{D}_0$,

$$\bar{\mathbf{G}}^{-,\pm}(\mathbf{x}, \mathbf{p}_H, x_{3,f}, \omega) = \int_{\partial\mathbb{D}_f} \mathbf{G}^{-,\pm}(\mathbf{x}, \mathbf{x}_{H,f}, x_{3,f}, \omega)\, \mathrm{e}^{\mathrm{j}\omega\mathbf{p}_H \cdot \mathbf{x}_{H,f}} \mathrm{d}^2\mathbf{x}_{H,f}. \tag{3.2.8}$$

Next, we multiply Eqs. 3.2.1 and 3.2.2 by $\mathrm{e}^{\mathrm{j}\omega\mathbf{p}_H\cdot\mathbf{x}_{H,f}}$, integrate the result over the focusing surface $\partial\mathbb{D}_f$, use Eqs. 3.2.7 and 3.2.8 and find the modified single-sided Green's function representations,

$$\begin{aligned}\bar{\mathbf{G}}^{-,+}(\mathbf{x}',\mathbf{p}_H,x_{3,f},\omega) &= \int_{\partial\mathbb{D}_0}\mathbf{R}(\mathbf{x}',\mathbf{x},\omega)\;\bar{\mathbf{F}}^{+}(\mathbf{x},\mathbf{p}_H,x_{3,f},\omega)\mathrm{d}^2\mathbf{x}\\ &\qquad - \bar{\mathbf{F}}^{-}(\mathbf{x}',\mathbf{p}_H,x_{3,f},\omega), \qquad (3.2.9)\\ \{\bar{\mathbf{G}}^{-,-}(\mathbf{x}',-\mathbf{p}_H,x_{3,f},\omega)\}^* &= \int_{\partial\mathbb{D}_0}\mathbf{R}^*(\mathbf{x}',\mathbf{x},\omega)\bar{\mathbf{F}}^{-}(\mathbf{x},\mathbf{p}_H,x_{3,f},\omega)\mathrm{d}^2\mathbf{x}\\ &\qquad - \bar{\mathbf{F}}^{+}(\mathbf{x}',\mathbf{p}_H,x_{3,f},\omega). \qquad (3.2.10)\end{aligned}$$

Eqs. 3.2.9 and 3.2.10 are nearly equivalent to the conventional single-sided Green's function representations [*Wapenaar*, 2014]. However, the focusing function $\mathbf{F}$ is replaced by a modified version $\bar{\mathbf{F}}$ that focuses in time but not in space. Besides, the Green's functions $\mathbf{G}^{-,\pm}$ are replaced by the virtual plane wave responses $\bar{\mathbf{G}}^{-,\pm}$ which are associated to a virtual plane wave source $\delta(t-\mathbf{p}_H\cdot\mathbf{x}_H)$ at $x_{3,f}$ instead of a virtual point source at $\mathbf{x}_f$.

The modified single-sided Green's function representations (Eqs. 3.2.9 and 3.2.10) are an underdetermined system that can only be solved if a separation operator exists. For the acoustic case, *Meles et al.* [2018] postulate that such an operator exists, and demonstrate its performance numerically. The (acoustic) separation operator is based on the kinematics of a direct transmission associated to plane wave source at the focusing depth and recorded at the surface $\partial\mathbb{D}_0$. Correspondingly, we hypothesise that in the elastodynamic case a separation operator $\bar{\mathbf{W}}$ exists. The separation operator $\bar{\mathbf{W}}$ is based on the kinematics of a forward-scattered transmission $\bar{\mathbf{T}}^{-}_{fs}(\mathbf{x}',\mathbf{p}_H,x_{3,f},\omega)$ associated to a plane wave source defined by the horizontal ray-parameter $\mathbf{p}_H$ at $\partial\mathbb{D}_f$ and recorded at $\partial\mathbb{D}_0$. Now we define the modified operator $\bar{\mathbf{W}}$,

$$\bar{W}_{\Phi,\Phi}(\mathbf{x}',\mathbf{p}_H,x_{3,f},t) = H(t^d_{\Phi,\Phi}-\epsilon-t+\mathbf{p}_H\cdot\mathbf{x}'_H)-H(-t^d_{\Phi,\Phi}+\epsilon-t+\mathbf{p}_H\cdot\mathbf{x}'_H). \quad (3.2.11)$$

For better readability we only defined one component of the modified operator $\bar{\mathbf{W}}$. The remaining elements are defined analogously. The function $H()$ is the Heaviside function. The variable $t^d_{\Phi,\Phi}$ is the travel time of the first event of the plane wave response $\bar{G}^{-,-}_{\Phi,\Phi}(\mathbf{x}',\mathbf{p}_H=\mathbf{0},x_{3,f},t)$. In addition, we introduced a small positive constant ϵ to account for the finite width of the wavelet. Note that the modified operator $\bar{\mathbf{W}}$ is applied to the modified single-sided Green's function representations in form of a Hadamard product.

Under the assumption that the operator $\bar{\mathbf{W}}(\mathbf{x}',\mathbf{p}_H,x_{3,f},t)$ exists the modified single-sided Green's function representations can be solved analogous to the conventional Marchenko scheme [*Wapenaar*, 2014] by replacing $\mathbf{G}^{-,\pm}(\mathbf{x}',\mathbf{x}_f,\omega)$ by $\bar{\mathbf{G}}^{-,\pm}(\mathbf{x}',\mathbf{p}_H,x_{3,f},\omega)$, $\mathbf{F}(\mathbf{x}',\mathbf{x}_f,\omega)$ by $\bar{\mathbf{F}}(\mathbf{x}',\mathbf{p}_H,x_{3,f},\omega)$, and $\mathbf{W}(\mathbf{x}',\mathbf{x}_f,t)$ by $\bar{\mathbf{W}}(\mathbf{x}',\mathbf{p}_H,x_{3,f},t)$.

3.3 Elastodynamic plane wave Marchenko redatuming: Numerical example

We evaluate the performance of the presented plane wave Marchenko redatuming for an elastic 1.5D model shown in Fig. 3.1a, where we use the coordinates $\mathbf{x} = (x_1, x_3)^T$. We model reflection data $\mathbf{R}(\mathbf{x}', \mathbf{x}, t)$ for a point source (see Fig. 3.1b). We choose a focusing depth $x_{3,f} = 1200\,\mathrm{m}$. For better visualisation, in all figures we only show wavefields related to a P-wave source and a P-wave focus. The initial downgoing focusing function $\bar{\mathbf{F}}_0^+$ (see Fig. 3.2a) is computed by inverting the forward-scattered transmission response $\bar{\mathbf{T}}_{fs}^-(\mathbf{x}', p_1, x_{3,f}, t)$ related to an incident plane wave defined by the horizontal ray-parameter $p_1 = 5 \times 10^{-5}\,\mathrm{s\,m^{-1}}$. When we inject the initial downgoing focusing function $\bar{\mathbf{F}}_0^+$ on the surface $\partial\mathbb{D}_0$ in the truncated medium and record it on $\partial\mathbb{D}_f$ we observe a plane wave $\delta(t - p_1 x_1)$ plus a coda (see Fig. 3.2b), i.e. the initial downgoing focusing function does not focus in time on $\partial\mathbb{D}_f$. Next, we evaluate five iterations of the modified Marchenko series and use the resulting downgoing focusing function $\bar{\mathbf{F}}^+$ (see Fig. 3.2c) to repeat the experiment. Now we observe a temporal focus $\delta(t - p_1 x_1)$ on $\partial\mathbb{D}_f$ without a coda (see Fig. 3.2d), indicating that we retrieved the correct downgoing focusing function. We evaluate Eqs. 3.2.9 and 3.2.10 using the retrieved modified focusing functions to obtain the virtual plane wave responses $\bar{\mathbf{G}}^{-,\pm}(\mathbf{x}', p_1, x_{3,f}, t)$. Fig. 3.2e shows a superposition of $\bar{\mathbf{G}}^{-,+}(\mathbf{x}', p_1, x_{3,f}, t)$ and $\bar{\mathbf{G}}^{-,-}(\mathbf{x}', p_1, x_{3,f}, t)$. The retrieved virtual plane wave responses include primary, multiply-scattered as well as converted waves. To illustrate that the choice of the ray-parameter p_1 is arbitrary we repeat the above experiments using a different ray-parameter $p_1 = 0\,\mathrm{s\,m^{-1}}$ (see

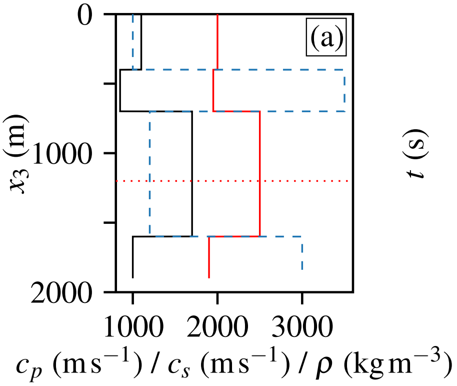

Figure 3.1: *(a) Layered model (1.5D) with a lateral distance range from* $-12\,812.5\,\mathrm{m}$ *to* $12\,800\,\mathrm{m}$*. The model parameters are P-wave velocity* c_p *(red solid line), S-wave velocity* c_s *(black solid line) and density* ρ *(blue dashed line). The red dashed line indicates the focusing depth* $x_{3,f} = 1200\,\mathrm{m}$*. (b) Reflection response* $\mathbf{R}(\mathbf{x}', \mathbf{x}, t)$*. To visualise the late arrivals we applied a temporal gain* $\mathrm{e}^{0.5t}$*.*

Figs. 3.2f-j). In this case we observe less events because at zero-incidence there are no conversions between P- and S-waves.

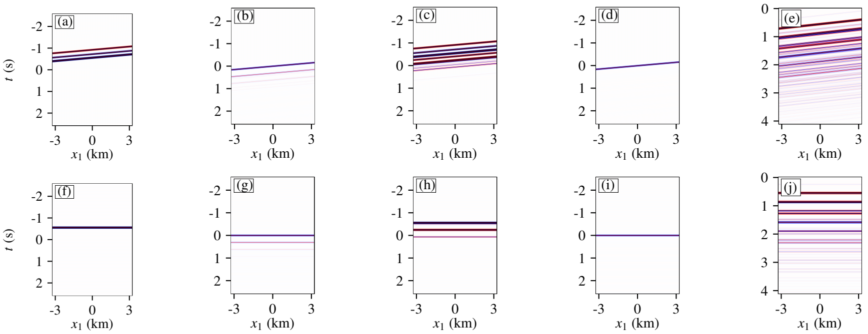

Figure 3.2: *Initial modified focusing function* $\bar{\mathbf{F}}_0^+(\mathbf{x}, p_1, x_{3,f}, t)$ *for a ray-parameter* $p_1 = 5 \times 10^{-5}\,\mathrm{s\,m^{-1}}$ *at the surfaces (a)* $\partial\mathbb{D}_0$ *and (b)* $\partial\mathbb{D}_f$*. Modified focusing function* $\bar{\mathbf{F}}^+(\mathbf{x}, p_1, x_{3,f}, t)$ *at the surfaces (c)* $\partial\mathbb{D}_0$ *and (d)* $\partial\mathbb{D}_f$*. (e) Superposition of the up- and downgoing virtual plane wave responses* $\bar{\mathbf{G}}^{-,\pm}(\mathbf{x}', p_1, x_{3,f}, t)$*. (f-j) Repetition of (a-e) for a different ray-parameter* $p_1 = 0\,\mathrm{s\,m^{-1}}$*.*

3.4 Conclusions

We extended the modified Marchenko redatuming by *Meles et al.* [2018] for elastodynamic waves. By modifying the focusing condition we obtained modified single-sided Green's function representations that allowed to create virtual plane wave sources (and receivers) inside the medium, only using the medium's reflection response recorded at an open-boundary and the forward-scattered transmission response between the recording and the focusing surfaces. The virtual plane wave responses are retrieved for single ray-parameters, i.e. they might be used for AVA inversion. Further, the virtual plane wave responses can be used to image the focusing surface $\partial\mathbb{D}_f$ in a single step. By imaging an entire surface, instead of a single point, the imaging process is accelerated significantly.

Acknowledgements

We would like to thank Jan Thorbecke, Evert Slob, Lele Zhang, Joeri Brackenhoff, Myrna Staring and Joost van der Neut for their collaboration and insightful discussions. We are also grateful to the European Unions Horizon 2020 research and innovation programme for funding this project (Marie Skłodowska-Curie grant agreement No 641943 and European Research Council grant agreement No 742703).

4

Comparison of monotonicity challenges encountered by the inverse scattering series and the Marchenko de-multiple method for elastic waves

Für alles Schöne,
Muss man zahlen.

Rammstein, 2019.

Abstract The single-sided reflection response of strongly scattering media often contains complicated interferences between primaries and (internal) multiples, which can lead to imaging artefacts unless handled correctly. Internal multiples can be predicted, e.g. by the Jakubowicz method or by the inverse scattering series (ISS), as long as monotonicity, i.e. "correct" temporal event ordering, is obeyed. Alternatively, the (conventional) Marchenko method removes all overburden-related wavefield interactions by formulating an inverse problem that can be solved if Green's and so-called focusing functions are separable in the time domain, except for an overlap that must be predicted. For acoustic waves, the assumptions of the aforementioned methods are often satisfied within the recording regimes used for seismic imaging. Elastic media, however, support wave propagation via coupled modes that travel with distinct velocities. Compared to the acoustic case, not only does the multiple issue become significantly more severe, but also violation of monotonicity becomes much more likely. By quantifying the assumptions of the ISS and the conventional

---

This chapter is currently under review for publication in Geophysics (submitted on 13 October 2019).

Marchenko method, unexpected similarities as well as differences between the two methods come to light. Our analysis demonstrates that the conventional Marchenko method relies on a weaker form of monotonicity. However, this advantage must be compensated by providing more prior information, which in the elastic case is an outstanding challenge. Rewriting, or re-mixing, the conventional Marchenko scheme removes the need for prior information but leads to a stricter monotonicity condition, which is now almost as strict as for the ISS. Finally, we present two strategies how the re-mixed Marchenko solutions can be used for imperfect, but achievable, de-multiple purposes.

4.1 Introduction

Structural images are often derived from a single-sided reflection response. However, traditional imaging methods assume single-scattering reflections (primaries only), such that other events, in particular multiples, create artefacts, which can be significant when the imaging target is buried under a strongly scattering overburden. In elastic media, this problem is worse: each interface couples compressional (P) and shear (S) waves, increasing the number of (unwanted) events drastically. Additionally, due to different propagation speeds of elastic modes, the (converted) primaries associated with an individual reflector arrive at different times, distributing information about this reflector in time. Hence, imaging artefacts can arise not only from (converted) multiples but also from converted primaries, i.e. forward-scattered waves. Reflection data driven methods are not (yet) capable of predicting forward-scattering but they are theorized to be able to handle (converted) multiples.

Wave-equation-based de-multiple methods, such as *Jakubowicz* [1998], or the inverse scattering series [ISS, *Weglein et al.*, 1997], predict and subtract internal multiples under two assumptions,

[1] that the temporal ordering of primaries corresponds to the reflector ordering in depth, and

[2] that internal multiples are recorded after their generating primaries (= primaries associated with the internal multiple generators).

These requirements, known as *monotonicity*, are satisfied for acoustic waves, except for special cases shown by *Nita and Weglein* [2009]. In elastic media, however, violation of monotonicity becomes much easier because of mode conversions. Regardless of monotonicity, both the ISS and the Jakubowicz method are applied in a layer-stripping fashion, which can be expensive and susceptible to error accumulation. To our knowledge, there has been no proposal to track, or quantify, the accumulated error.

A Marchenko-equation-based alternative for acoustic waves allows to remove all internal multiples associated with an entire group of layers, without adaptive subtraction [e.g. *Broggini et al.*, 2012a; *Wapenaar et al.*, 2013; *Slob et al.*, 2014]. This method formulates an inverse problem with two equations (derived from reciprocity theorems) and four unknowns: up- and downgoing Green's functions as well as so-called up- and downgoing focusing functions. The Green's and focusing functions can be separated in the time domain, except for an unavoidable overlap ($\boldsymbol{\chi}_+$). Given this overlap, two unknowns can be eliminated by muting. Subsequently, two coupled Marchenko equations are obtained and solved for the focusing functions, which once found yield the Green's functions. Upon multi-dimensional deconvolution of the retrieved Green's functions, overburden-related scattering interactions, including internal multiples, can be removed. We refer to this approach as the *conventional Marchenko method.*

The elastodynamic extension of the Marchenko method bears several challenges. Firstly, speed differences between modes can lead to a second overlap ($\boldsymbol{\chi}_-$), which so far cannot be predicted without knowing the medium and only vanishes conditionally. Secondly, the previously-mentioned unavoidable overlap ($\boldsymbol{\chi}_{+}$) between Green's and focusing functions is no longer easily predictable without significantly more prior information, or additional constraints. Similar restrictions were encountered by prior work on inverse scattering of coupled modes. Nevertheless, these cases ignored the overlaps, either by assuming sufficiently small velocity differences between modes [*Zakharov and Shabat*, 1973; *Bava and Ghione*, 1984], or by excluding coupling [*Ware and Aki*, 1969].

To overcome the challenge related to the overlap $\boldsymbol{\chi}_{+}$, we derive a *re-mixed*, as opposed to the above-mentioned *conventional*, Marchenko method: the Green's and focusing functions are transformed such that the unavoidable, highly complex, overlap ($\boldsymbol{\chi}_{+}$) re-mixes into a trivial one. This strategy can be seen as a combination and generalization of the Marchenko schemes by *van der Neut and Wapenaar* [2016] and *Dukalski et al.* [2019].

The ISS as well as the conventional and re-mixed Marchenko methods tackle the same de-multiple problem but appear to rely on different requirements. So far, the requirements of the aforementioned methods are only formulated verbally, which makes a direct comparison of the de-multiple methods difficult. Therefore, we quantify these assumptions in a form of medium-, angle of incidence and redatuming depth dependent *separability conditions*. This analysis demonstrates that the monotonicity assumptions of the ISS are very similar to, but stricter than, the separability condition of the conventional Marchenko method. After re-mixing, the Marchenko method can be applied without prior medium information (no need for the overlap $\boldsymbol{\chi}_{+}$). Although, compared to the conventional Marchenko scheme, the separability condition becomes stricter, it still remains slightly more relaxed than the monotonicity assumption [1] of the ISS. This advantage of the (re-mixed) Marchenko method comes from handling the overburden as one complex multiple generator, rather than a stack of independent multiple generators.

Finally, we demonstrate how the solutions of the re-mixed Marchenko method can be used to remove internal multiples, except for internal multiples that predate their generating primaries. In contrast to the ISS, which encounters the same limitation, see assumption [2], the re-mixed Marchenko method tracks the error caused by the remaining internal multiples. This tracked error is expected to persist in field data studies [e.g. *Ravasi et al.*, 2016; *Staring et al.*, 2018] but could be eliminated by transforming the re-mixed solutions back to the conventional ones, using energy conservation and the minimum-phase property of the focusing function, similar to *Dukalski et al.* [2019]. The latter strategy relies on the reconstruction of a minimum-phase matrix from its normal product, which is subject to ongoing research and will be published elsewhere.

This paper is structured as follows: first, we briefly outline the conventional Marchenko scheme, quantify its assumptions as a separability condition and interpret the required initial estimate. Second, we derive the re-mixed Marchenko scheme, which leads to a stricter separability condition. Third, we quantify monotonicity conditions of the ISS, which we compare to the requirements of the aforementioned (re-mixed) Marchenko method. Finally, we illustrate our findings with numerical examples. In this analysis, we assume surface-related multiples are removed during preprocessing, and thus, use the terms multiples and internal multiples as synonyms. Although we consider the simplest yet non-trivial case, horizontally-layered elastic media, our analysis is already highly relevant for the Middle East [e.g. see *El-Emam et al.*, 2001], and extends qualitatively to more general cases.

■ Notation

We consider 2D lossless horizontally-layered elastic media in x-z coordinates. According to Snell's law horizontal-slownesses s_x (= horizontal ray-parameter) are conserved,

$$s_x = \frac{\sin\big(\alpha_{p/s}(z)\big)}{c_{p/s}(z)} = \text{constant}, \tag{4.1.1}$$

where the subscripts refer to P- and S-waves. Further, $\alpha_{p/s}$ and $c_{p/s}$ are the propagation angle with respect to the vertical axis (z) and the propagation velocity, respectively. A representation in the horizontal-slowness intercept-time (s_x, τ) domain allows to separate 2D wavefields $U(x, z, t)$ into a set of decoupled 1D wavefields,

$$U(s_x, z, \tau) = \int_{-\infty}^{\infty} U(x, z, \tau + s_x x)\mathrm{d}x. \tag{4.1.2}$$

In this paper, we use the terms time and intercept-time interchangeably, and insist on time-domain expressions because we will discuss temporal separations between wavefields further onwards.

We restrict our analysis to propagating waves, i.e. $|s_x| \leq \frac{1}{c_p}$ (assuming $c_p > c_s$), and neglect measurement-induced limitations, such as a finite bandwidth, because here we wish to focus on a fundamentally physical (not measurement-borne) limitation. Further, we work with power-flux normalized P- and S- one-way wavefields [*Frasier*, 1970; *Ursin*, 1983], organized in 2 × 2 matrices per discrete horizontal-slowness and time,

$$\mathbf{U}(s_x, z, \tau) = \begin{pmatrix} U_{pp} & U_{ps} \\ U_{sp} & U_{ss} \end{pmatrix} (s_x, z, \tau). \tag{4.1.3}$$

The elements of the arbitrary wavefield $\mathbf{U}(s_x, z, \tau)$ are associated with source- (second subscript) and receiver-side (first subscript) wavefield potentials (P and S).

Finally, we introduce a detail-hiding notation that omits coordinates and implies temporal convolutions when two matrices $\mathbf{U}_1$ and $\mathbf{U}_2$ are multiplied, for example $\mathbf{U}_1\mathbf{U}_2$ stands for,

$$\int_{-\infty}^{\infty} \mathbf{U}_1(s_x, z, \tau - \tau')\mathbf{U}_2(s_x, z, \tau')\mathrm{d}\tau'. \tag{4.1.4}$$

4.2 Marchenko Green's function retrieval

Suppose all the multiples due to the overburden above the redatuming depth z_i shall be removed. For this purpose, we might use the Green's functions, $\mathbf{G}^{-,+}(s_x, z_0, z_i, \tau)$

and
$\mathbf{G}^{-,-}(-s_x, z_0, z_i, \tau)$, associated with down- "+" and upward "−" radiating sources (second superscript) at the redatuming depth z_i, respectively, and recordings of upgoing waves "−" (first superscript) at the acquisition level z_0 (see Fig. 4.1). From these Green's functions, a redatumed reflection response $\mathbf{R}_{rd}(s_x, z_i, \tau)$, free of overburden-related scattering, can be obtained via an *Amundsen* [2001] deconvolution,

$$\mathbf{G}^{-,+} = -\boldsymbol{\sigma}_z \mathbf{G}^{-,-} \mathbf{R}_{rd}^{\mathrm{T}} \boldsymbol{\sigma}_z. \tag{4.2.1}$$

Here, we exploit wavefield symmetries in horizontally-layered media via a transpose in P-S space (superscript "T") and via the Pauli matrix $\boldsymbol{\sigma}_z$, which is multiplied by a temporal, $\tau = 0$, delta spike (for consistent detail-hiding notation). These symmetries allow us to proceed with the retrieved Green's functions $\mathbf{G}^{-,\pm}$, although they are associated with horizontal-slownesses s_x of opposite sign (a derivation can be found in Appendix A). The challenge is to retrieve these Green's functions from a reflection response $\mathbf{R}(s_x, z_0, \tau)$ recorded at a scattering-free surface z_0 at the top, which can be accomplished by a Marchenko method.

First, we highlight the underlying assumptions and the prior information required by the conventional Marchenko method. Second, we provide a physical interpretation of the prior information, and third, we propose an alternative Marchenko formulation, which trades prior information for stricter assumptions. It will be shown that, both the conventional Marchenko method as well as its alternative formulation rely on separability conditions, which we express quantitatively. In the next section, this quantification will allow us to compare the requirements of the Marchenko method to those of the ISS.

■ 4.2.1 Quantitative separability condition

We briefly outline the elastodynamic Marchenko method, derived by one of the authors [*Wapenaar*, 2014], and quantify the assumptions as a separability condition.

Instead of predicting multiples by combining all possible triplets of primaries associated with the overburden [*Coates and Weglein*, 1996], the Marchenko method solves an inverse problem formed by two equations, the convolution- and correlation-type representation theorems,

$$\mathbf{G}^{-,+} \qquad + \mathbf{F}_1^- = \mathbf{R}\mathbf{F}_1^+, \tag{4.2.2}$$

$$\left(\mathbf{G}^{-,-}\right)^* + \mathbf{F}_1^+ = \mathbf{R}^\dagger \mathbf{F}_1^-, \tag{4.2.3}$$

with four unknowns: the Green's functions $\mathbf{G}^{-,\pm}$ and the focusing functions $\mathbf{F}_1^\pm(s_x, z_0, z_i, \tau)$. The latter ones are defined in a truncated medium that is identical to the overburden, but scattering-free above z_0 and below z_i. The superscripts denote a time-reversal ($*$) and a time-reversal combined with a transpose in P-S space ($\dagger$). Further, an illustration of Eqs. 4.2.2-4.2.3 can be found in Fig. 4.1 for an acoustic medium and in Figs. 4.2a and 4.3a for an elastic medium.

In an attempt to constrain Eqs. 4.2.2-4.2.3, two temporal projectors, $\mathbf{P}^\pm$, are applied as a Hadamard matrix product in P-S space (details about the projectors

Illustration of the representation theorems ($c_s = 0$)

(a) Convolution-type (see Eqs. 6 and 8)

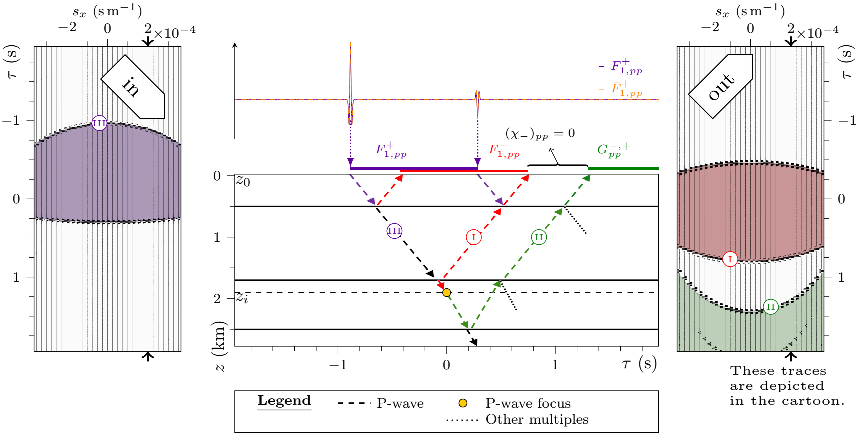

(b) Correlation-type (see Eqs. 7 and 9)

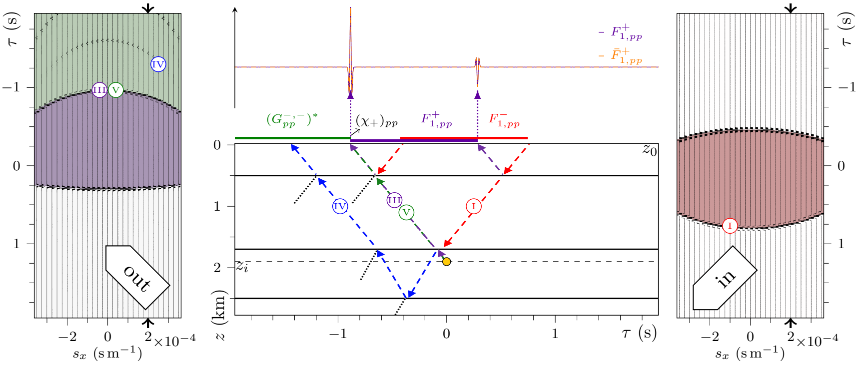

Figure 4.1: *Illustration of the (a) convolution- and (b) correlation-type representation theorems. This figure depicts an acoustic experiment to help the interpretation of the elastic experiments shown in Figs. 4.2 and 4.3. The representation theorems describe a scattering experiment: special fields (the focusing functions* $\mathbf{F}^{\pm}_1$*) are injected into a medium (see arrows saying "in"), the arrow diagram in the centre depicts the scattering paths for a single horizontal-slowness* s_x *(marked with black arrows in* s_x*-*τ *gathers) and another special field scatters back to the recording surface* z_0 *(see arrows saying "out"). Note that, all wavefields are consistently color-coded in Figs. 4.1-4.3. The scattering of* $\mathbf{F}^+_1$ *(violet in panel a) and* $\mathbf{F}^-_1$ *(red in panel b) by a (a) time-forwarding and (b) time-reversing medium results in superpositions of focusing and Green's functions,* $\mathbf{F}^-_1 + \mathbf{G}^{-,+}$ *and* $\mathbf{F}^+_1 + (\mathbf{G}^{-,-})^*$*, respectively. The top trace shows true (violet) and retrieved (orange) focusing functions* $F^+_{1,pp}$ *and* $\bar{F}^+_{1,pp}$*, respectively. The last event of* $\mathbf{F}^-_1$ *(event I) and the first event of* $\mathbf{G}^{-,+}$ *(event II) are represented by red and green paths, respectively (also see* s_x*-*τ *gathers). Similarly, the first event of* $\mathbf{F}^+_1$ *(event III) and the last event of* $(\mathbf{G}^{-,-})^*$ *(event V) are highlighted by violet and green travel paths, respectively. The fastest multiple of* $(\mathbf{G}^{-,-})^*$ *(event IV) propagates along the blue path. At the recording surface* z_0*, the overlap between focusing and Green's functions only contains a direct wave (events III and V). The overlap(s) between focusing and Green's functions appear to have a trivial* s_x*-dependency (illustrated by the* s_x*-*τ *gathers), however, this will change in the elastic case (see Fig. 4.2). For illustration purposes, all responses are convolved with a* 30 Hz *Ricker wavelet. Medium parameters can be found in appendix C.*

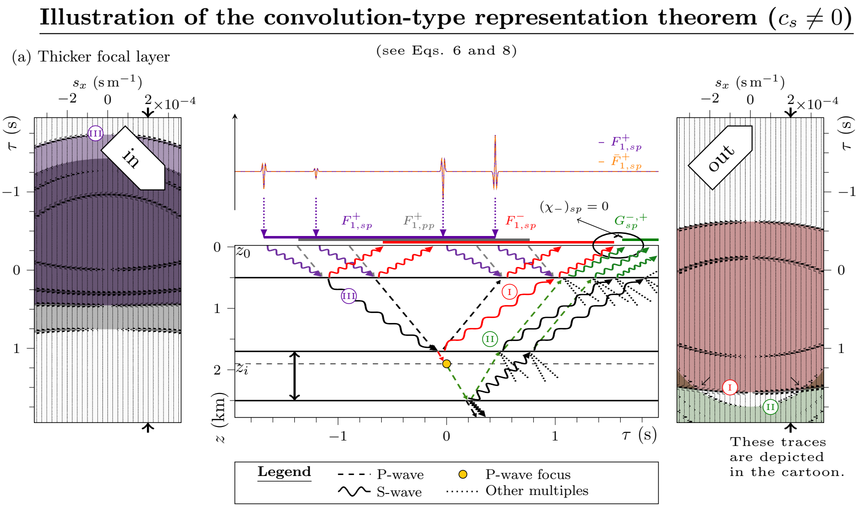

(a) Thicker focal layer

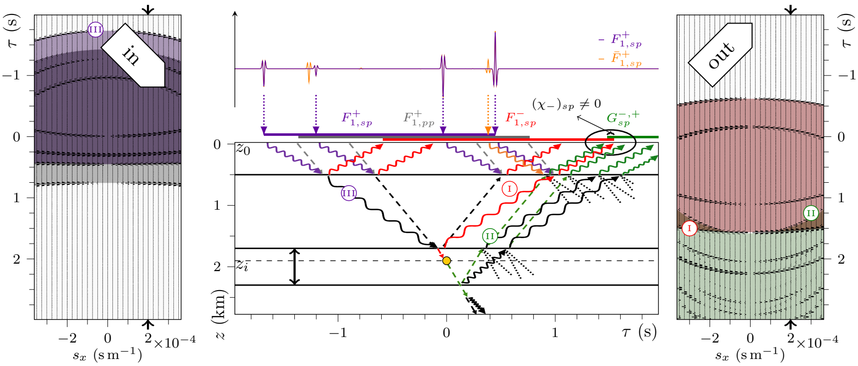

(b) Thinner focal layer

Figure 4.2: *(a) Idem as Fig. 4.1a for the same medium supporting elastic wave propagation (arbitrarily chosen sp component shown). Compared to the acoustic experiment shown in Fig. 4.1a, the number of scattering paths increased drastically because at each interface the injected wavefield is reflected and transmitted as P- and S-waves. Moreover, creation of a P-wave focus requires injection of P- (grey color for $F^+_{1,pp}$) and S-waves (violet color for $F^+_{1,sp}$). Due to the mode coupling, the $\mathbf{F}^-_1/\mathbf{G}^{-,+}$ separability is only violated for sufficiently large horizontal-slownesses, $|s_x| > 2.54 \times 10^{-4}\,\mathrm{s\,m^{-1}}$ (indicated by black arrows inside the top-right s_x-τ gather). For smaller horizontal-slownesses, the separability conditions (see Eqs. 4.2.7 and 4.2.8) are satisfied and the Marchenko method retrieves the correct focusing function (see top trace). (b) Idem as panel (a), except that the thickness of the focusing layer is reduced such that the first event of $G^{-,+}_{sp}$ (event II) predates the last event of $F^-_{1,sp}$ (event I), leading to a temporal overlap (see black ellipse in the cartoon and and red-green area overlap in s_x-τ gathers). If we erroneously assume zero overlap $\boldsymbol{\chi}_- = \mathbf{O}$, the Marchenko method forces the overlapping part of the Green's function to become part of the upgoing focusing function $\bar{\mathbf{F}}^-_1$. As a result, the retrieved downgoing focusing function $\bar{\mathbf{F}}^+_1$ contains an artefact (see orange arrow) that cancels a multiple generated by event II. The other artefacts of the retrieved focusing function $\bar{\mathbf{F}}^+_1$ (e.g. around $\tau = -1.25\,\mathrm{s}$) are caused by similar mechanisms but are not immediately easy to interpret here.*

can be found in Appendix B). In other publications, the projectors are also referred to as window functions, both terms describe exactly the same thing. Without loss of generality, the projectors preserve the focusing functions but mute the Green's functions, except for the temporal overlaps, $\mathbf{P}^{-}\left[\mathbf{G}^{-,+}\right]=\boldsymbol{\chi}_{-}$ and $\mathbf{P}^{+}\left[(\mathbf{G}^{-,-})^{*}\right]=\boldsymbol{\chi}_{+}$, such that Eqs. 4.2.2-4.2.3 simplify to,

$$\boldsymbol{\chi}_{-}+\mathbf{F}_{1}^{-}=\mathbf{P}^{-}\left[\mathbf{R}\mathbf{F}_{1}^{+}\right], \tag{4.2.4}$$

$$\boldsymbol{\chi}_{+}+\mathbf{F}_{1}^{+}=\mathbf{P}^{+}\left[\mathbf{R}^{\dagger}\mathbf{F}_{1}^{-}\right]. \tag{4.2.5}$$

Note that, keeping the overlap $\boldsymbol{\chi}_{-}$ explicit will lead to key insights of this paper. The solution strategy hopes that the overlaps $\boldsymbol{\chi}_{\pm}$ can be estimated, such that the inverse problem resembles a set of coupled Marchenko equations that can be solved recursively,

$$\mathbf{F}_{1}^{+}=\sum_{k=0}^{\infty}\boldsymbol{\Xi}_{k}, \text{ with, } \boldsymbol{\Xi}_{k}=\mathbf{P}^{+}\left[\mathbf{R}^{\dagger}\mathbf{P}^{-}\left[\mathbf{R}\boldsymbol{\Xi}_{k-1}\right]\right], \tag{4.2.6}$$

using $\boldsymbol{\Xi}_{0}=-\boldsymbol{\chi}_{+}-\mathbf{P}^{+}\left[\mathbf{R}^{\dagger}\boldsymbol{\chi}_{-}\right]$ as initial estimate, and assuming convergence of the series [which only has been shown for the acoustic case, *Dukalski and de Vos*, 2017]. From the retrieved solution $\mathbf{F}_{1}^{+}$, the remaining unknowns can be constructed.

Estimating the overlaps remains very challenging. In order to proceed, the Marchenko method firstly assumes $\boldsymbol{\chi}_{-}$ is a null matrix $\mathbf{O}$, and secondly, requires $\boldsymbol{\chi}_{+}$ as prior information (a physical interpretation of $\boldsymbol{\chi}_{+}$ follows in the next subsection).

The assumption, $\boldsymbol{\chi}_{-}=\mathbf{O}$, demands that the focusing function $\mathbf{F}_{1}^{-}$ and the Green's function $\mathbf{G}^{-,+}$ remain separable in the time domain (see $\mathbf{F}_{1}^{-}/\mathbf{G}^{-,+}$ separability in Figs. 4.1a and 4.2a). Although true for 1.5D acoustic media, this assumption can be violated in 1.5D elastic media (see Fig. 4.2b), and only holds under the *separability condition*,

$$\sum_{k=1}^{i-1}\Delta z^{(k)}\left(s_{z,s}^{(k)}-s_{z,p}^{(k)}\right)<2\,\Delta z^{(i)}s_{z,p}^{(i)}, \tag{4.2.7}$$

which is derived in Appendix B. Variables $\Delta z^{(k)}$ and $s_{z,p/s}^{(k)}$ denote the thickness and the vertical-slownesses of P- and S-waves in the k^{th} layer, respectively (the layer labelling is depicted in Fig. 4.5a). The right-hand side of Eq. 4.2.7 describes the two-way travel time of a P-wave through the i^{th} layer (embedding the redatuming level), and the left-hand side is the one-way travel time difference between a P- and an S-wave propagating from the shallowest to the deepest interface of the overburden.

Note that, the Marchenko separability condition becomes more restrictive if identical projectors, $\mathbf{P}^{+}$ and $\mathbf{P}^{-}$, are used, and is domain-dependent [analogous to *Sun and Innanen*, 2019]: the s_x-τ domain is favorable, particularly in 1.5D media, because horizontal-slownesses can be treated separately, reducing the risk of a non-zero overlap $\boldsymbol{\chi}_{-}$. For example, in the space-time domain a non-zero overlap $\boldsymbol{\chi}_{-}$ becomes much more likely e.g. due to events of the Green's function $\mathbf{G}^{-,+}$ associated with small angle of incidence predating events of the focusing function $\mathbf{F}_{1}^{-}$ associated with large angles of incidence. If measurements of several horizontal-slownesses are available, a transformation to the hyperbolic Radon domain may slightly relax the presented separability condition.

4.2.2 Physical interpretation of the overlap $\boldsymbol{\chi}_+$

In 1.5D acoustic media, the overlap $\boldsymbol{\chi}_+$ is a direct wave propagating from the redatuming level z_i to the acquisition surface z_0.

Wapenaar and Slob [2015] demonstrate that, in elastic media, the unavoidable overlap, $\boldsymbol{\chi}_+$, does not simply consist of direct P- and S-waves, but of all waves that forward-scatter from the redatuming level z_i to the acquisition surface z_0 (such as events III and V in Figs. 4.1b and 4.3a). This physical interpretation of $\boldsymbol{\chi}_+$ describes a special case and can become less intuitive in a general case: multiples that propagate mainly as P-waves (such as event IV) may outpace forward-scattered waves that propagate mainly as S-waves (such as event III), and thereby become part of the overlap $\boldsymbol{\chi}_+$, as depicted in Fig. 4.3b. We refer to these events as *fast multiples*, and their occurrence is prevented if the separability condition,

$$\sum_{k=1}^{i-1} \Delta z^{(k)} \left(s_{z,s}^{(k)} - s_{z,p}^{(k)} \right) < 2 \min \left\{ \Delta z^{(k)} s_{z,p}^{(k)} \middle| \, k \in [1,i] \right\}, \tag{4.2.8}$$

holds (derived in Appendix B). The minimum function, $\min\{\cdot\}$, selects the smallest element of the given set, which in this case is the delay between the fastest multiple and the fastest primary propagating from z_i to z_0.

If the separability condition in Eq. 4.2.8 is violated, the conventional Marchenko method requires the fast multiples as prior information. Even in the special case where Eq. 4.2.8 holds such that the overlap $\boldsymbol{\chi}_+$ simplifies to only forward-scattered waves, it still consists of 2^{n-1} events per elastic component, where n is the number of reflectors inside the overburden. Thus, finding the initial estimate $\boldsymbol{\chi}_+$ without further constraints becomes very unrealistic for an unknown model.

4.2.3 Marchenko with trivial initial estimate

In this section, we modify the conventional Marchenko scheme to remove the need for prior information contained by $\boldsymbol{\chi}_+$, in exchange for a stricter separability condition.

We exploit the freedom to convolve the representation theorems in Eqs. 4.2.2-4.2.3 with an arbitrary time-dependent matrix $\mathbf{B}(s_x, z_i, z_0, \tau)$ from the right,

$$\mathbf{U}^{-,+} \qquad + \mathbf{V}_1^- = \mathbf{R}\mathbf{V}_1^+, \tag{4.2.9}$$

$$\left(\mathbf{U}^{-,-}\right)^* + \mathbf{V}_1^+ = \mathbf{R}^\dagger \mathbf{V}_1^-, \tag{4.2.10}$$

where we introduced $\mathbf{V}_1^\pm = \mathbf{F}_1^\pm \mathbf{B}$, $\mathbf{U}^{-,+} = \mathbf{G}^{-,+}\mathbf{B}$ and $\mathbf{U}^{-,-} = \mathbf{G}^{-,-}\mathbf{B}^*$. This approach allows us to arrive at a different set of equations and can be interpreted as a form of preconditioning [*Dukalski and de Vos*, 2017]. Alike *Dukalski et al.* [2019], *Elison et al.* [2019] and *Mildner et al.* [2019b], we assume an unknown, though later recoverable, $\mathbf{B}$, contrary to other authors who use a known $\mathbf{B}$ [*van der Neut and*

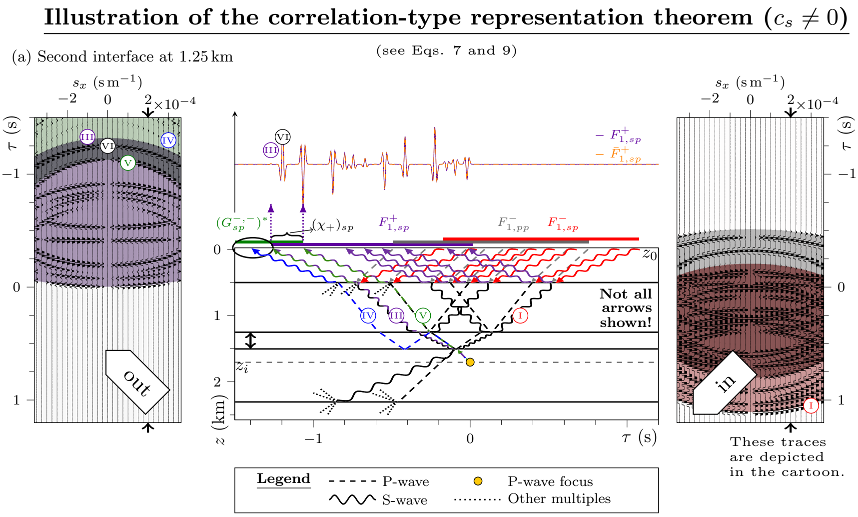
(a) Second interface at 1.25 km

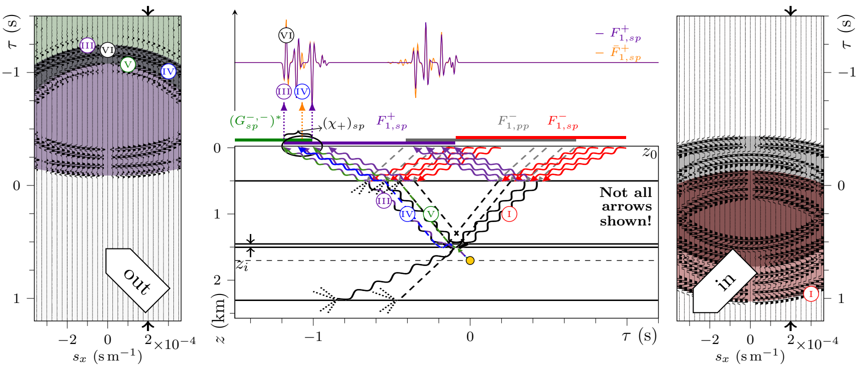
(b) Second interface moved downwards to 1.45 km

Figure 4.3: *(a) Idem as Fig. 4.1b but now the medium is elastic and contains an additional interface (arbitrarily chosen sp component shown). Since the additional layer generates so many extra events we do not draw all paths in the cartoon. In contrast to the acoustic case in Fig. 4.1b, creation of a P-wave focus requires injection of P- (grey color for $F^-_{1,pp}$) and S-waves (red color for $F^-_{1,sp}$). Due to P-S coupling at each interface, the overlap $\boldsymbol{\chi}_+$, which is bounded by the first event of $\mathbf{F}^+_1$ (event III) and the last event of $(\mathbf{G}^{-,-})^*$ (event V), contains not only of a direct wave, but all forward-scattered waves. The s_x-τ gather shows that the temporal separation between forward-scattered waves (e.g. events III, V and VI) and multiples (e.g. event IV) decreases with increasing horizontal-slowness. (b) Idem as panel Fig. 4.3a, except that the second interface from above has been moved downwards creating a thinner layer (layer thickness reduced from 250 m to 50 m). As a result, the overlap $\boldsymbol{\chi}_+$ contains not only the forward-scattered waves but also fast multiples (see event IV in ellipse). Approximating the overlap $\boldsymbol{\chi}_+$ only by forward-scattered waves, i.e. ignoring fast multiples such as event IV, leads to an erroneous focusing function $\bar{\mathbf{F}}^+_1$ (see orange and violet traces for comparison). Errors occur not only within the temporal extent of the overlap $\boldsymbol{\chi}_+$ but also at other times.*

Wapenaar, 2016; *Singh et al.*, 2017; *Ravasi*, 2017; *Meles et al.*, 2018; *Reinicke et al.*, 2018; *Wapenaar and van IJsseldijk*, 2019].

Next, we define the unknown $\mathbf{B}$ such that the overlap $\boldsymbol{\chi}_{+}$ unfolds onto an identity. This strategy can be seen as applying an unknown transformation (convolution with $\mathbf{B}$) that maps the typically unknown initial guess $\boldsymbol{\chi}_{+}$ onto a trivial one. As a result, the solutions are also transformed from $\mathbf{F}_1^{\pm}$ to $\mathbf{V}_1^{\pm} = \mathbf{F}_1^{\pm}\mathbf{B}$. We emphasise that the operator $\mathbf{B}$ is not a mere time-shift as in the acoustic scheme by *van der Neut and Wapenaar* [2016], or a form of a wavelet as in the scheme by *Dukalski et al.* [2019] and *Elison* [2019], but a much more general matrix filter. Now Eq. 4.2.10 can be easily separated,

$$\mathbf{P}_B^{+}\left[\left(\mathbf{U}^{-,-}\right)^{*}\right] = \boldsymbol{\chi}_{+}^{B} = \mathbf{I}, \tag{4.2.11}$$

$$\mathbf{P}_B^{+}\left[\mathbf{V}_1^{+}\right] \qquad = \mathbf{V}_1^{+}, \tag{4.2.12}$$

where $\mathbf{I}$ is an identity matrix multiplied by a temporal delta function. Note that the projector $\mathbf{P}_B^{+}$ can be very different from the projector $\mathbf{P}^{+}$ in Eq. 4.2.5 (details about the projectors can be found in Appendix B). After applying a projector to Eq. 4.2.9,

$$\mathbf{P}_B^{-}\left[\mathbf{U}^{-,+}\right] = \boldsymbol{\chi}_{-}^{B}, \tag{4.2.13}$$

$$\mathbf{P}_B^{-}\left[\mathbf{V}_1^{-}\right] \quad = \mathbf{V}_1^{-}, \tag{4.2.14}$$

we can simplify Eqs. 4.2.9 and 4.2.10 to,

$$\boldsymbol{\chi}_{-}^{B} + \mathbf{V}_1^{-} = \mathbf{P}_B^{-}\left[\mathbf{R}\mathbf{V}_1^{+}\right], \tag{4.2.15}$$

$$\mathbf{I} \quad + \mathbf{V}_1^{+} = \mathbf{P}_B^{+}\left[\mathbf{R}^{\dagger}\mathbf{V}_1^{-}\right]. \tag{4.2.16}$$

Compared to Eqs. 4.2.4-4.2.5, the overlaps $\boldsymbol{\chi}_{\pm}$ are *re-mixed* into $\boldsymbol{\chi}_{-}^{B}$ and $\boldsymbol{\chi}_{+}^{B} = \mathbf{I}$, and thus, we refer to $\mathbf{B}$ as the *re-mixing operator.* For the special case that the re-mixed overlap $\boldsymbol{\chi}_{-}^{B}$ remains zero we can retrieve re-mixed solutions,

$$\mathbf{V}_1^{+} = \sum_{k=0}^{\infty} \boldsymbol{\Xi}_k, \text{ with, } \boldsymbol{\Xi}_k = \mathbf{P}_B^{+}\left[\mathbf{R}^{\dagger}\mathbf{P}_B^{-}\left[\mathbf{R}\boldsymbol{\Xi}_{k-1}\right]\right], \tag{4.2.17}$$

using a trivial initial estimate $\boldsymbol{\Xi}_0 = -\boldsymbol{\chi}_{+}^{B}$. Further onwards, we will introduce a de-multiple strategy that only requires the resulting re-mixed Green's functions $\mathbf{U}^{-,\pm}$ as input.

The advantage of a trivial initial estimate, $\boldsymbol{\chi}_{+}^{B} = \mathbf{I}$, comes at a cost: although unknown, the re-mixing operator is associated with a source at the surface at z_0 and a receiver at the redatuming depth z_i. Thus, $\mathbf{B}$ moves the focal point to the acquisition surface. This process reduces the temporal separation between the focusing function $\mathbf{F}_1^{-}$ and the Green's function $\mathbf{G}^{-,+}$ by the temporal extent of the re-mixing operator (see Fig. 4.4). As a result, an originally zero overlap, $\boldsymbol{\chi}_{-} = \mathbf{O}$, can become non-zero, $\boldsymbol{\chi}_{-}^{B} \neq \mathbf{O}$. This is because the re-mixed Marchenko method

	Separability condition	**Satisfied**	**Violated**
Conventional	Eq. 4.2.7	$\chi_- = \mathbf{O}$	$\chi_- \neq \mathbf{O}$ with finite duration
	Eq. 4.2.8	χ_+ *only* contains forward-scattered waves	χ_+ contains forward-scattered waves *and* fast multiples
Re-mixed	Eq. 4.2.18	$\chi_-^B = \mathbf{O}$	$\chi_-^B \neq \mathbf{O}$ with finite duration
	Unconditionally	$\chi_+^B = \mathbf{I}$	not applicable

Table 4.1: *This table summarizes the effect of satisfying, and violating, the separability conditions of the conventional and the re-mixed Marchenko method.*

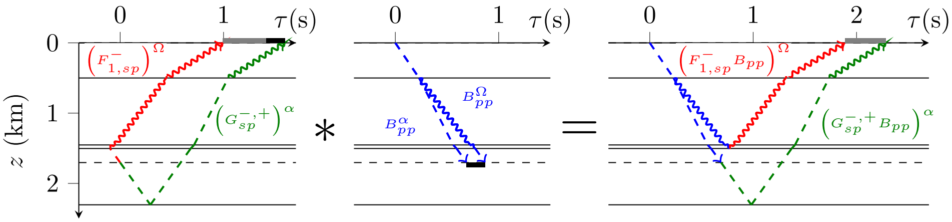

Figure 4.4: *Effect of re-mixing on temporal separation, illustrated analogously to Figs. 4.2-4.3. Re-mixing reduces temporal distance between* $\mathbf{F}_1^-$ *and* $\mathbf{G}^{-,+}$ *(see grey and black bar) by the duration of the re-mixing operator (see black bar). We depict the first (superscript* α*) and last (superscript* Ω*) events of* $\mathbf{F}_1^-$ *(red),* $\mathbf{G}^{-,+}$ *(green) and* $\mathbf{B}$ *(blue). The travel times of the first and the last event of* $\mathbf{B}$ *are derived in Appendix B.*

relies on a stricter separability condition than the conventional Marchenko method (see Eq. 4.2.7), and it holds if (a derivation can be found in Appendix B),

$$\sum_{k=1}^{i-1} \Delta z^{(k)} \left(s_{z,s}^{(k)} - s_{z,p}^{(k)} \right) < \Delta z^{(i)} s_{z,p}^{(i)}. \tag{4.2.18}$$

The effect of satisfying, or violating, the aforementioned separability conditions is summarized in Tab. 4.1.

4.3 Inverse scattering series

The ISS relies on monotonicity assumptions [1] and [2] (see *Introduction*), which have always been formulated verbally. We quantify these assumptions in a form of two inequalities. Subsequently, we compare them against the conventional and re-mixed Marchenko methods.

■ 4.3.1 Quantifying monotonicity in terms of separability conditions

Consistent with the previous section, we aim to remove multiples related to the overburden above z_i. Monotonicity assumption [1] in the introduction requires that the P-wave travel time through each layer inside the overburden is sufficiently long to separate the (converted) primaries of adjacent reflectors in time (compare Figs. 4.5a and b), and has to hold for each elastic component. This requirement can be formulated as a separability condition (derived in Appendix B),

$$\sum_{k=1}^{j-1} \Delta z^{(k)} \left(s_{z,s}^{(k)} - s_{z,p}^{(k)} \right) < \Delta z^{(j)} s_{z,p}^{(j)}, \ \forall\, j \in [2, i]. \tag{4.3.1}$$

Monotonicity assumption [2] states that multiples are recorded after their generating primaries and can be formulated as (derived in Appendix B),

$$\sum_{k=1}^{i-1} \Delta z^{(k)} \left(s_{z,s}^{(k)} - s_{z,p}^{(k)} \right) < \min \left\{ \Delta z^{(k)} s_{z,p}^{(k)} \middle| \, k \in [1, i] \right\}. \tag{4.3.2}$$

Violating monotonicity causes erroneous multiple predictions at the arrival times of primaries [e.g. see Fig. 16 in *Sun and Innanen*, 2019]. Match-subtracting the mis-predicted multiples will remove the respective primaries, and consequently, multiples generated by those primaries cannot be predicted.

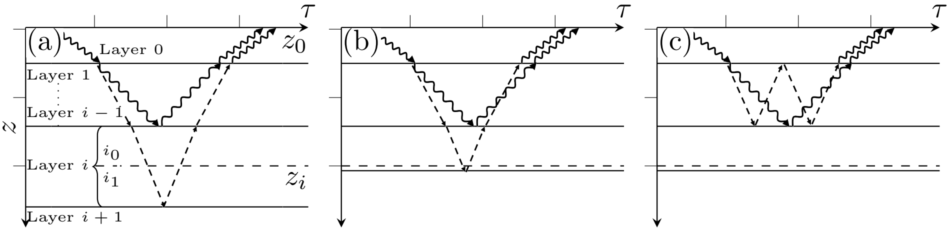

Figure 4.5: *Two primary reflections (arbitrarily chosen ss component) that, (a) obey and (b) violate monotonicity assumption [1]. (c) A multiple that predates a primary of one of its generators, violating monotonicity assumption [2]. Dashed and sinusoidal lines represent P- and S-waves, respectively. Layers are labelled with respect to the redatuming depth z_i.*

■ 4.3.2 Analysis of Marchenko and ISS separability conditions

Now we compare the assumptions of the conventional and re-mixed Marchenko methods (see Eqs. 4.2.7, 4.2.8 and 4.2.18) with the monotonicity assumptions of the ISS (see Eqs. 4.3.1 and 4.3.2).

All of the aforementioned methods rely on separability conditions that have the same term on the left-hand side. This term describes the travel time difference between P- and S-waves propagating from the shallowest to the deepest reflector of the overburden. Hence, the likelihood of violating these separability conditions increases with depth and vertical-slowness differences between P- and S-waves ($s_{z,s} - s_{z,p}$).

The re-mixed Marchenko scheme and the ISS can both be evaluated without prior medium information, which makes for a fair comparison: the separability condition of the re-mixed Marchenko scheme is nearly identical to the monotonicity assumption [1] of the ISS (compare Eqs. 4.2.18 and 4.3.1). However, the condition for the re-mixed Marchenko scheme (see Eq. 4.2.18) only needs to be obeyed by the redatuming layer i, rather than by each layer inside the overburden (see Eq. 4.3.1). For example, a sufficiently slim layer inside the overburden can be prohibitive for the ISS while the re-mixed Marchenko method can handle it, as long as the redatuming layer i provides sufficient temporal support, $\Delta z^{(i)} s_{s,p}^{(i)}$. Hence, the requirement of the re-mixed Marchenko scheme, i.e. the separability of $\mathbf{V}_1^-$ from $\mathbf{U}^{-,+}$, can be seen as a relaxed version of monotonicity condition [1].

In contrast, the separability condition of the conventional Marchenko method is more relaxed due to the additional factor of two (compare Eqs. 4.2.7, 4.2.18 and 4.3.1). This relaxation emerges because the conventional Marchenko scheme demands temporal separability in terms of one- instead of two-way travel time ($\mathbf{F}_1^- \leftrightarrow \mathbf{V}_1^-$ and $\mathbf{G}^{-,+} \leftrightarrow \mathbf{U}^{-,+}$). However, the more relaxed separability condition must be compensated by estimating the remaining overlap $\boldsymbol{\chi}_+$, i.e. by providing prior information. Hence, the re-mixed Marchenko method trades prior information for a stricter assumption. This trade-off was not observed by *van der Neut and Wapenaar* [2016] because they did not consider forward-scattered waves.

Further, elastic overburden removal via the ISS entails a high risk of violating the monotonicity assumption [2], which is quantified by Eq. 4.3.2: with increasing depth the right-hand side of the condition decreases or remains constant, while the left-hand side increases. In other words, increasing depth leads to a higher probability of fast multiples occurring, i.e. multiples outpacing their generating primaries. Fast multiples can also be encountered by the conventional Marchenko method, which requires them to be included in the initial estimate. The occurrence of fast multiples in the conventional Marchenko method and the ISS differs by a factor of two (compare Eqs. 4.2.8 and 4.3.2), which is again a matter of one- and two-way travel times. The re-mixed Marchenko scheme cannot predict fast multiples either, but stores them in the re-mixing operator $\mathbf{B}$.

Note that, the discussed separability conditions only consider the temporal event ordering, but neglect the amplitudes of the events. Errors due to violating the separability conditions may be negligible close to zero-incidence where mode conversions are weak, but become increasingly significant with increasing angle of incidence.

4.4 De-multiple strategies for re-mixed Marchenko scheme

Now we propose two de-multiple strategies derived from the re-mixed Marchenko solutions. The first one only requires the re-mixed solutions but does not remove all overburden interactions, and hence, further improvements are desirable. The second one aims to remove all overburden interactions by exploiting energy conservation and the minimum-phase property of the focusing function. The latter approach is discussed conceptually and further details will be presented in the future.

■ 4.4.1 Re-mixed Marchenko de-multiple method

The two Green's functions $\mathbf{G}^{-,\pm}$ are related by the redatumed reflection response $\mathbf{R}_{rd}$ (see Eq. 4.2.1), that is free of overburden interactions, and thus, is a form of overburden-borne multiple and forward-scattering elimination. In contrast, the re-mixed Green's functions $\mathbf{U}^{-,\pm}$ are mutually related by a different, multiple-free, reflection response. This relation can be seen by inserting an identity, $\mathbf{B}^{*}\left(\mathbf{B}^{*}\right)^{-1}$, in Eq. 4.2.1, multiplying the result by $\mathbf{B}$ from the right, and substituting the Green's functions by their re-mixed versions,

$$\mathbf{U}^{-,+} = -\boldsymbol{\sigma}_z \mathbf{U}^{-,-}\left(\mathbf{B}^{*}\right)^{-1}\mathbf{R}_{rd}^{\mathrm{T}}\boldsymbol{\sigma}_z\mathbf{B}. \tag{4.4.1}$$

Here, we introduced a convolutional and matricial inverse of $\mathbf{B}$, where the superscript "-1" denotes a Moore-Penrose pseudo-inverse. Unlike the Green's function $\mathbf{G}^{-,\pm}$, the re-mixed ones are easily calculable provided that the separability condition Eq. 4.2.18 holds. Upon deconvolution of Eq. 4.4.1, we obtain,

$$\left(\mathbf{B}^{*}\right)^{-1}\mathbf{R}_{rd}^{\mathrm{T}}\boldsymbol{\sigma}_z\mathbf{B}. \tag{4.4.2}$$

This quantity is the desired redatumed reflection response, dressed with all overburden interactions described by $\mathbf{B}$ on the source- and receiver-sides. In a 1.5D acoustic case, $\mathbf{B}$ simplifies to a time-shift defined by the overburden and a global transmission-amplitude correction. In the elastic case, in the absence of fast multiples (see Eq. 4.2.8) $\mathbf{B}$ is an inverse forward-scattered transmission through the overburden. This insight ties back to the statement in the introduction that forward-scattering cannot be predicted by existing methods. If Eq. 4.2.8 is violated $\mathbf{B}$ also carries the imprint of fast multiples (e.g. see Fig. 4.6). In particular media, forward-scattered waves and fast multiples can by chance destructively interfere, bringing $\mathbf{B}$ close to the inverse of a time-reversed direct transmission.

Moreover, the re-mixed Marchenko scheme allows to understand and track the impact of forward-scattering and fast multiples via the re-mixing operator (see Eq. 4.4.2). In contrast, layer-stripping approaches suffer from erroneous primary predictions due fast multiples. These in turn may generate further mis-predictions, accumulating an untraceable error.

■ 4.4.2 Alternative de-multiple strategy

We conjecture it could be possible to remove all overburden interactions, including forward-scattering and (fast) multiples, by exploiting further physical constraints:

energy conservation and the minimum-phase property of the focusing function. In the following, we make the first steps in this direction.

The up- and downgoing focusing functions conserve energy,

$$\left(\mathbf{F}_1^+\right)^\dagger \mathbf{F}_1^+ - \left(\mathbf{F}_1^-\right)^\dagger \mathbf{F}_1^- = \mathbf{I}, \tag{4.4.3}$$

i.e. the net energy injected at z_0 equals the transmitted energy at z_i - a delta source at time zero. Firstly, by evaluating energy conservation of the re-mixed focusing function, $\mathbf{V}_1^\pm = \mathbf{F}_1^\pm \mathbf{B}$, and using Eq. 4.4.3, we obtain the normal product of the re-mixing operator,

$$\left(\mathbf{F}_1^+\mathbf{B}\right)^\dagger \mathbf{F}_1^+\mathbf{B} - \left(\mathbf{F}_1^-\mathbf{B}\right)^\dagger \mathbf{F}_1^-\mathbf{B} = \mathbf{B}^\dagger\mathbf{B}. \tag{4.4.4}$$

Secondly, we find a convolutional and matricial Moore-Penrose pseudo-inverse of $\mathbf{B}^\dagger\mathbf{B}$, and convolve the result by the re-mixed focusing function $\mathbf{V}_1^+$ from the left and right,

$$\mathbf{F}_1^+\mathbf{B}\left(\mathbf{B}^\dagger\mathbf{B}\right)^{-1}\left(\mathbf{F}_1^+\mathbf{B}\right)^\dagger = \mathbf{F}_1^+\left(\mathbf{F}_1^+\right)^\dagger. \tag{4.4.5}$$

The result is the normal product of the desired focusing function $\mathbf{F}_1^+$ and can be seen as a generalized power spectrum. Note that, Eqs. 4.4.3-4.4.5 also hold for band-limited wavefields. If the focusing function $\mathbf{F}_1^+$ can be retrieved from its normal product $\mathbf{F}_1^+\left(\mathbf{F}_1^+\right)^\dagger$, the desired Green's functions and hence the redatumed reflection response $\mathbf{R}_{rd}$, free of all overburden interactions, can be obtained (from Eq. 4.2.1).

The focusing function $\mathbf{F}_1^+$ is an inverse transmission response,

$$\mathbf{T}^+\mathbf{F}_1^+ = \mathbf{I}, \tag{4.4.6}$$

where $\mathbf{T}^+$ is the transmission response of the truncated medium. In 1D acoustics, this relation implies that the focusing function is a minimum-phase scalar function, except for a linear phase-shift, and hence, possesses a unique amplitude-phase relationship via the Kolmogorov relation [*Claerbout*, 1985]. This property allows *Dukalski et al.* [2019] and *Elison* [2019] to factorize the (scalar) normal product $\mathbf{F}_1^+\left(\mathbf{F}_1^+\right)^\dagger$, and thereby, predict short-period multiples that are generated in a horizontally-layered acoustic overburden. In our case, the focusing function as a matrix is still an inverse transmission, and therefore, remains a minimum-phase object in a matrix sense. *Tunnicliffe-Wilson* [1972] proposes a method that factorizes the normal products of a sub-class of minimum-phase matrices. The generalization of this method is subject of ongoing research and will be published in the future.

4.5 Numerical examples

For horizontally-layered media, all required wavefields can be modelled efficiently by wavefield extrapolation without band-limitation [*Kennett and Kerry*, 1979; *Hubral et al.*, 1980]. Further, we choose the P- and S-wave velocities as well as the horizontal-slownesses such that all events are on-sample. This allows us to better inspect the separability conditions of the conventional and re-mixed Marchenko

methods because
measurement-induced limitations are absent.

First, we consider the experiment in Fig. 4.2a that satisfies the separability condition of the conventional Marchenko method stated by Eq. 4.2.7. Using the correct initial estimate $\boldsymbol{\chi}_+$, which is obtained by applying the projector $\mathbf{P}^+$ to a modelled Green's function (i.e. the medium is known a-priori), the elastodynamic Marchenko method finds the correct focusing function (see trace in Fig. 4.2a). However, when repeating this experiment for the model in Fig. 4.2b, which violates the separability condition in Eq. 4.2.7, the projector $\mathbf{P}^-$ erroneously preserves the first event of $\mathbf{G}^{-,+}$ (event II). Assuming, $\boldsymbol{\chi}_- = \mathbf{O}$, forces this event to become part of the focusing function $\bar{\mathbf{F}}_1^-$ (the bar distinguishes retrieved from true solutions). To cancel multiples caused by this event, the retrieved $\bar{\mathbf{F}}_1^+$ contains an artefact (see orange arrow in Fig. 4.2b). Via the same mechanism, further artefacts are introduced.

Second, for the experiment shown in Fig. 4.3a, which still satisfies the separability condition in Eq. 4.2.7 as well as the condition in Eq. 4.2.8, the Marchenko series (see Eq. 4.2.6) finds the correct solution (see trace in Fig. 4.3a), using the forward-scattered part of the Green's function $(\mathbf{G}^{-,-})^*$ as initial estimate. By downward-shifting the second interface, as depicted in Fig. 4.3b, Eq. 4.2.8 is violated and the overlap $\boldsymbol{\chi}_+$ is populated with fast multiples. If the initial estimate ignores these fast multiples, the Marchenko series does not converge to the true solution. For example, event IV, which is a (fast) multiple belonging to the Green's function, is now (erroneously) part of the focusing function (indicated by the orange-dotted line in Fig. 4.3b). To compensate for these errors the Marchenko series introduces further artefacts (particularly see errors after $t = -0.6\,\mathrm{s}$ in Fig. 4.3b).

Third, we repeat the previous experiment with the re-mixed Marchenko scheme, which simplifies the highly sophisticated initial estimate $\boldsymbol{\chi}_+$ to a trivial one $\boldsymbol{\chi}_+^B = \mathbf{I}$. We use the re-mixed solutions to remove multiples according Eq. 4.4.2. Since there is only one reflector below the redatuming level one would hope to eliminate all scattering effects except for a single primary (event A in Fig. 4.6). Indeed, a significant amount of overburden interactions has been removed, revealing the primary A, which was masked by a strong multiple (see traces and cartoon in Fig. 4.6). Nevertheless, the redatumed response still contains forward-scattered waves (e.g. events B and D) as well as fast multiples (e.g. event C). These remaining scattering effects are caused by re-mixing. The corresponding operator is angle-dependent because it is implicitly defined by the overlap $\boldsymbol{\chi}_+$ (see s_x-τ gathers in Fig. 4.3). Following the alternative de-multiple strategy, that aims to remove all overburden interactions, we can already recover the normal product of the desired focusing function $\mathbf{F}_1^+$ near-to-perfectly (no figure), with a relative error below 1 ppm (for the model in Figs. 4.3b and 4.6). Experiments on retrieving the focusing function from its normal product are beyond the scope of this paper.

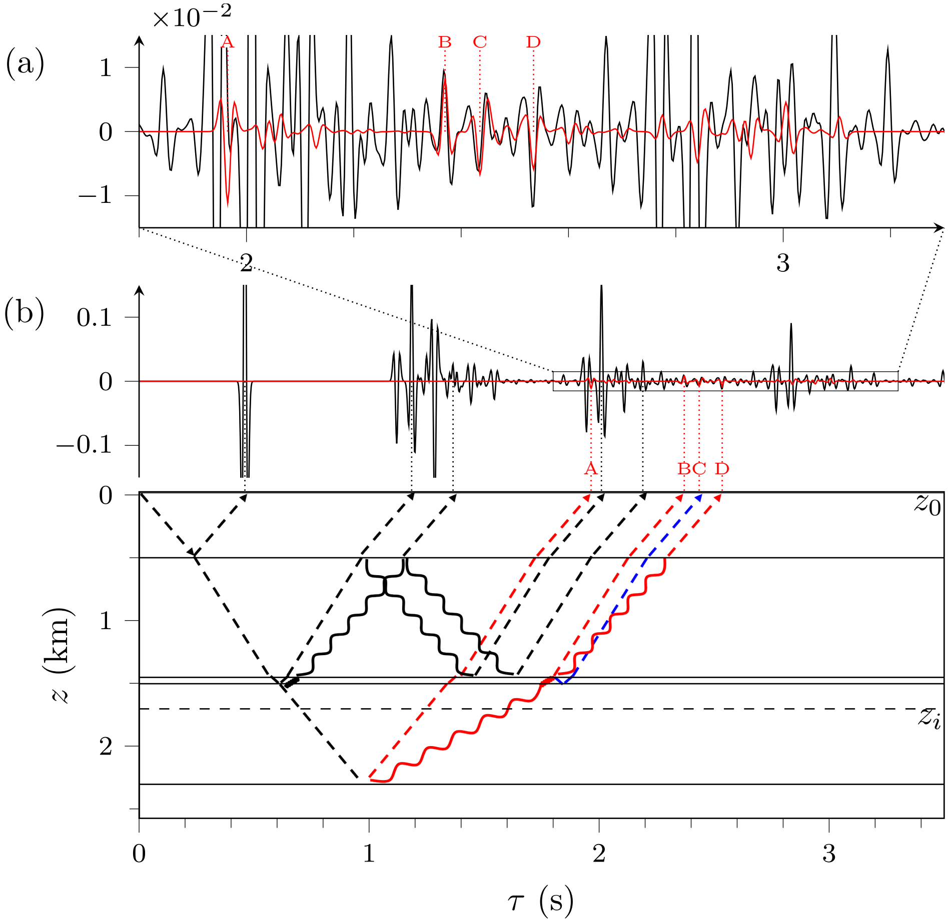

Figure 4.6: *Reflection response (black traces) and de-multiple result (red traces) according to Eq. 4.4.2 (arbitrarily chosen pp component, $s_x = 2 \times 10^{-4}\,\mathrm{s\,m^{-1}}$). Panel (a) shows a close-up of the box in panel (b). Again, dashed and sinusoidal lines represent P- and S-waves, respectively. The cartoon highlights (1) some of the overburden interactions removed by the de-multiple scheme (black lines), and (2) the four strongest events remaining in the redatumed result (red and blue lines): event A is the desired target-related primary reflection, events B and D are forward-scattered waves, and event C (highlighted in blue) is a fast multiple. Dotted lines point to the arrivals associated with the cartoon arrows. For illustration purposes, all responses are convolved with a 30 Hz Ricker wavelet and a global scaling factor is used to adjust the de-multiple result to the reflection response.*

4.6 Conclusion

Monotonicity, i.e. "correct" temporal ordering of events, is crucial for all of the discussed de-multiple methods. Due to conversions between modes with different propagation speeds, elastic media generate more reflection events than equivalent acoustic media, which can be seen as temporal stretching of information. This temporal stretching leads to a higher risk of undesired temporal event ordering and becomes more severe with increasing speed differences between modes and increasing redatuming depth. Through the analysis of these elastic effects similarities and differences between the ISS and the Marchenko method came to light.

First, we quantified the separability condition of the conventional Marchenko method and the monotonicity assumptions of the ISS. The resulting conditions revealed that both the conventional Marchenko method and the ISS rely on a form of monotonicity, but in terms of one- and two-way travel times, respectively. Hence, the conditions for the conventional Marchenko method are more relaxed. However, this advantage must be compensated by providing an initial estimate, i.e. prior information, which becomes challenging in practice.

Second, we re-mixed the Marchenko scheme to remove the need for prior information, which allows for a fair comparison against the ISS. By re-mixing, the Marchenko separability condition becomes stricter, but remains slightly more relaxed than the monotonicity condition of the ISS because the re-mixed Marchenko scheme only requires the redatuming layer, instead of each layer in the overburden, to be sufficiently thick (in terms of P-wave travel time).

Third, we presented two strategies how the re-mixed Marchenko equations can be used for multiple elimination. The first one can be easily implemented and removes all multiples that arrive after their generating primaries. Similar to the ISS, multiples that predate their generating primaries as well as forward-scattered waves cannot (yet) be predicted, however, the re-mixed Marchenko scheme stores the respective error in the re-mixing operator. The second strategy aims to remove all overburden-related effects, including forward-scattering and (fast) multiples, by removing the re-mixing operator form the Marchenko solutions. For this purpose, additional physical constraints are taken into account, namely energy conservation and the minimum-phase property of the focusing function. The latter approach suggests that the prediction of forward-scattered waves and fast multiples requires minimum-phase matrix factorization, which is subject to ongoing research.

This analysis sheds light on fundamental challenges of the elastic de-multiple problem but further developments are needed.

Acknowledgements

This work was supported by the European Union's Horizon 2020 research and innovation programme: Marie Sklodowska-Curie [grant number 641943] and European Research Council [grant number 742703]. Further, we would like to thank our coworkers for inspiring discussions.

4A Derivation of the redatuming relation

In this appendix, we derive the expression in Eq. 4.2.1 that relates the redatumed reflection response $\mathbf{R}_{rd}(s_x, z_i, \tau)$ to the retrieved Green's functions $\mathbf{G}^{-,\pm}(\pm s_x, z_0, z_i, \tau)$. For this derivation, we write all coordinates explicitly, but matrix products still imply temporal convolutions according to Eq. 4.1.4.

The starting point is the more familiar redatuming relation,

$$\mathbf{G}^{-,+}(s_x, z_i, z_0, \tau) = \mathbf{R}_{rd}(s_x, z_i, \tau)\mathbf{G}^{+,+}(s_x, z_i, z_0, \tau). \tag{4A.1}$$

Next, we use source-receiver reciprocity [e.g. see *Wapenaar*, 2014],

$$\mathbf{G}^{\mp,+}(s_x, z_i, z_0, \tau) = \pm \left[\mathbf{G}^{-,\pm}(-s_x, z_0, z_i, \tau)\right]^{\mathrm{T}}, \tag{4A.2}$$

and to interchange source and receiver in Eq. 4A.1,

$$\begin{aligned}\mathbf{G}^{-,+}(s_x, z_0, z_i, \tau) &= \left[\mathbf{G}^{-,+}(-s_x, z_i, z_0, \tau)\right]^{\mathrm{T}} \\ &= \left[\mathbf{G}^{+,+}(-s_x, z_i, z_0, \tau)\right]^{\mathrm{T}} \left[\mathbf{R}_{rd}(-s_x, z_i, \tau)\right]^{\mathrm{T}} \\ &= -\mathbf{G}^{-,-}(s_x, z_0, z_i, \tau) \left[\mathbf{R}_{rd}(-s_x, z_i, \tau)\right]^{\mathrm{T}}.\end{aligned} \tag{4A.3}$$

In horizontally-layered media, wavefields associated with positive and negative horizontal-slownesses s_x are mutually related via multiplication by a Pauli matrix $\boldsymbol{\sigma}_z$ (multiplied by a temporal delta spike) from the left and right, which yields,

$$\begin{aligned}&\mathbf{G}^{-,+}(s_x, z_0, z_i, \tau) = \\ &\qquad = -\boldsymbol{\sigma}_z \mathbf{G}^{-,-}(-s_x, z_0, z_i, \tau)\boldsymbol{\sigma}_z\boldsymbol{\sigma}_z \left[\mathbf{R}_{rd}(s_x, z_i, \tau)\right]^{\mathrm{T}} \boldsymbol{\sigma}_z \\ &\qquad = -\boldsymbol{\sigma}_z \mathbf{G}^{-,-}(-s_x, z_0, z_i, \tau) \left[\mathbf{R}_{rd}(s_x, z_i, \tau)\right]^{\mathrm{T}} \boldsymbol{\sigma}_z.\end{aligned} \tag{4A.4}$$

4B Derivation of separability conditions

In this appendix, we formulate the separability conditions of the ISS, and of the original as well as the re-mixed representation theorems. Furthermore, we derive explicit expression of the projectors $\mathbf{P}^{\pm}$ and $\mathbf{P}^{\pm}_{B}$.

Consider a homogeneous layer (labelled by k) of thickness $\Delta z^{(k)}$ as well as P- and S-wave velocities $c_p^{(k)}$ and $c_s^{(k)}$. For a plane wave with horizontal slowness s_x, P- and S-waves propagate with the vertical slowness,

$$s_{z,p/s}^{(k)} = \sqrt{\left(c_{p/s}^{(k)}\right)^{-2} - s_x^2}. \tag{4B.1}$$

The resulting one-way travel time of such plane waves through layer k is,

$$\tau_{p/s}^{(k)} = \Delta z^{(k)} s_{z,p/s}^{(k)}. \tag{4B.2}$$

In the following, we assume that the P-wave velocity,

$$c_p = \sqrt{\frac{\lambda + 2\mu}{\rho}}, \tag{4B.3}$$

is greater than the S-wave velocity,

$$c_s = \sqrt{\frac{\mu}{\rho}}, \tag{4B.4}$$

[*de Hoop*, 1995], which is the case for most materials: The shear modulus μ and the density ρ are always positive. The first Lamé parameter λ can be negative but for all natural materials known to the authors the relation $\lambda > -\mu$ holds.

■ 4B.1 Separability of conventional representation theorems

In the following, we derive the separability conditions implied by the conventional Marchenko scheme.

First, we analyze the separability of the focusing function $\mathbf{F}_1^-$ from the Green's function $\mathbf{G}^{-,+}$ on the left-hand side of Eq. 4.2.2. To guarantee separability, the last and first events of the focusing and Green's functions must satisfy the condition,

$$\tau_\Omega(F_{1,ab}^-) < \tau_\alpha(G_{ab}^{-,+}), \tag{4B.5}$$

for each elastic component combination ab. Here, the functions τ_α and τ_Ω denote the first and last arrival times at the recording level z_0, respectively. We sum the one-way travel times along the travel path of the last event of $F_{1,ab}^-$ (e.g. for $F_{1,sp}^-$ see event I in Fig. 4.2a, see Fig. 4.5 for layer labelling $i_{0/1}$),

$$\tau_\Omega(F_{1,ab}^-) = \tau_a^{(0)} + \sum_{k=1}^{i-1} \tau_s^{(k)} - \tau_b^{(i_0)}, \tag{4B.6}$$

and along the travel path of the first event of $G_{ab}^{-,+}$ (e.g. for $G_{sp}^{-,+}$ see event II in Fig. 4.2a),

$$\tau_\alpha(G_{ab}^{-,+}) = \tau_a^{(0)} + \sum_{k=1}^{i} \tau_p^{(k)} + \tau_b^{(i_1)}. \tag{4B.7}$$

We substitute Eqs. 4B.6 and 4B.7 in Eq. 4B.5, replace the one-way travel times by Eq. 4B.2 and obtain the separability condition of Eq. 4.2.7,

$$\sum_{k=1}^{i-1} \Delta z^{(k)} \left(s_{z,s}^{(k)} - s_{z,p}^{(k)} \right) < 2\, \Delta z^{(i)} s_{z,p}^{(i)}. \tag{4B.8}$$

Second, we derive a condition under which the overlap $\boldsymbol{\chi}_+$ simplifies to the forward-scattered part of the Green's function $(\mathbf{G}^{-,-})^*$. This scenario requires that the fastest multiple of the (time-reversed) Green's function $\left(\mathbf{G}^{-,-}\right)^*$ reaches the recording level before the first event of the focusing function $\mathbf{F}_1^+$ (which defines the first event of the overlap $\boldsymbol{\chi}_+$),

$$\tau_\Omega\left((G^{-,-}_{m,ab})^*\right) < \tau_\alpha(F^+_{1,ab}). \tag{4B.9}$$

Here, we use the subscript m to refer to the multiples of a wavefield. We sum the one-way travel times along the path of the fastest multiple of the Green's function $\left(G^{-,-}_{m,ab}\right)^*$ (e.g. for $(G^{-,-}_{m,sp})^*$ see event IV in Fig. 4.3a),

$$\tau_\Omega((G^{-,-}_{m,ab})^*) = -\tau_a^{(0)} - \sum_{k=1}^{i-1}\tau_p^{(k)} - 2\,\min\left\{\tau_p^{(k)}\middle|\, k\in[1,i]\right\} - \tau_b^{(i_0)}, \tag{4B.10}$$

and along the travel path of the first event of the focusing function $F^+_{1,ab}$ (e.g. for $F^+_{1,sp}$ see event III in Fig. 4.3a),

$$\tau_\alpha(F^+_{1,ab}) = -\tau_a^{(0)} - \sum_{k=1}^{i-1}\tau_s^{(k)} - \tau_b^{(i_0)}. \tag{4B.11}$$

We substitute Eqs. 4B.10 and 4B.11 in Eq. 4B.9, express the one-way travel times according to Eq. 4B.2 and arrive at the condition,

$$\sum_{k=1}^{i-1}\Delta z^{(k)}\left(s^{(k)}_{z,s} - s^{(k)}_{z,p}\right) < 2\,\min\left\{\Delta z^{(k)}s^{(k)}_{z,p}\middle|\, k\in[1,i]\right\}. \tag{4B.12}$$

This condition can only be satisfied if the separability condition in Eq. 4B.8 holds.

If the separability condition in Eq. 4B.8 holds the projector $\mathbf{P}^-$, acting as a Hadamard matrix product in P-S space, separates the convolution-type representation theorem in Eq. 4.2.2 according to,

$$\mathbf{P}^-\left[\mathbf{G}^{-,+}\right] = \boldsymbol{\chi}_- = \mathbf{O}, \tag{4B.13}$$

$$\mathbf{P}^-\left[\mathbf{F}_1^-\right] = \mathbf{F}_1^-. \tag{4B.14}$$

We define the projector $\mathbf{P}^-$ such that all events after the last arrival of the focusing function $\mathbf{F}_1^-$ are muted,

$$P^-_{ab} = \mathrm{H}\left(-\tau + \tau_\Omega(F^-_{1,ab})\right) = \mathrm{H}\left(-\tau + \tau_a^{(0)} + \sum_{k=1}^{i-1}\tau_s^{(k)} - \tau_b^{(i_0)}\right), \tag{4B.15}$$

where we use Eq. 4B.6. The function $\mathrm{H}(\tau)$ denotes the Heaviside function, $\mathrm{H}(\tau < 0) = 0$ and $\mathrm{H}(\tau \geq 0) = 1$. In analogy, the correlation-type representation theorem in Eq. 4.2.3 can be separated with a projector $\mathbf{P}^+$,

$$\mathbf{P}^+\left[(\mathbf{G}^{-,-})^*\right] = \boldsymbol{\chi}_+, \tag{4B.16}$$

$$\mathbf{P}^+\left[\mathbf{F}_1^+\right] = \mathbf{F}_1^+, \tag{4B.17}$$

that mutes all events before the first arrival of the focusing function $\mathbf{F}_1^+$,

$$P_{ab}^+ = \mathrm{H}\left(\tau - \tau_\alpha(F_{1,ab}^+)\right) = \mathrm{H}\left(\tau + \tau_a^{(0)} + \sum_{k=1}^{i-1}\tau_s^{(k)} + \tau_b^{(i_0)}\right). \tag{4B.18}$$

In the latter expression we use Eq. 4B.11.

■ 4B.2 Separability of re-mixed representation theorems

In the Sec. 4.2.3*Marchenko with trivial initial estimate*, we introduced an unknown operator $\mathbf{B}$ to transform the overlap $\boldsymbol{\chi}_+$ between the focusing function $\mathbf{F}_1^+$ and the Green's function $(\mathbf{G}^{-,-})^*$ to a trivial one. Thus, the re-mixed correlation-type representation theorem in Eq. 4.2.10 is separable by definition, except for an identity matrix. However, the separability of the re-mixed convolution-type representation theorem in Eq. 4.2.9 is not guaranteed and is assessed below.

The re-mixed representation theorem in Eq. 4.2.9 is separable if the last event of the re-mixed focusing function $\mathbf{V}_1^-$ arrives at the recording surface before the first event of the re-mixed Green's function $\mathbf{U}^{-,+}$,

$$\tau_\Omega(V_{1,ab}^-) < \tau_\alpha(U_{ab}^{-,+}), \tag{4B.19}$$

which can be re-written as,

$$\tau_\Omega(F_{1,as}^-) + \tau_\Omega(B_{sb}) < \tau_\alpha(G_{ap}^{-,+}) + \tau_\alpha(B_{pb}). \tag{4B.20}$$

Now, we define the first and last arrival times of the re-mixing operator $\mathbf{B}$. The re-mixing operator projects the Green's function $(\mathbf{G}^{-,-})^*$ onto an identity matrix plus an acausal coda. Hence, the first event of the re-mixing operator coincides with the first event of the inverse $((\mathbf{G}^{-,-})^*)^{-1}$. For example, the first, but time-reversed, event of B_{ps} is depicted by path V in Fig. 4.3b. We sum the one-way travel times along this path for an arbitrary component ab,

$$\tau_\alpha(B_{ab}) = \tau_a^{(i)} + \sum_{k=1}^{i-1}\tau_p^{(k)} + \tau_b^{(0)}. \tag{4B.21}$$

Further, we heuristically assume that the re-mixing operator has the same temporal extent as the overlap $\boldsymbol{\chi}_+$ between the focusing function $\mathbf{F}_1^+$ and the Green's function $(\mathbf{G}^{-,-})^*$, which is $\sum_{k=1}^{i-1}\left(\tau_s^{(k)} - \tau_p^{(k)}\right)$. As a result, the one-way travel time of the last event of the re-mixing operator is,

$$\tau_\Omega(B_{ab}) = \tau_a^{(i)} + \sum_{k=1}^{i-1}\tau_s^{(k)} + \tau_b^{(0)}. \tag{4B.22}$$

Thorough empirical investigations confirm this result. Upon substituting Eqs. 4B.6-4B.7 and Eqs. 4B.21-4B.22 in Eq. 4B.20 and using Eq. 4B.2, we find the separability condition for the re-mixed Marchenko scheme,

$$\sum_{k=1}^{i-1} \Delta z^{(k)} \left(s_{z,s}^{(k)} - s_{z,p}^{(k)} \right) < \Delta z^{(i)} s_{z,p}^{(i)}. \tag{4B.23}$$

Now we derive expressions for the re-mixed projectors $\mathbf{P}_B^{\pm}$. Analogous to the derivation of the separability conditions, we use arrival times of first and last events of specific wavefields to find the re-mixed projectors. From Eqs. 4.2.11-4.2.12 follows that the re-mixing operator $\mathbf{B}$ unfolds the overlap $\boldsymbol{\chi}_+$ between the focusing function $\mathbf{F}_1^+$ and the Green's function $\left(\mathbf{G}^{-,-}\right)^*$, except for an identity matrix. In consequence, the diagonal elements of the projector $\mathbf{P}_B^+$ should only preserve positive times, including time zero to account for Eq. 4.2.11,

$$P_{B,pp}^+ = P_{B,ss}^+ = \mathrm{H}\left(\tau\right). \tag{4B.24}$$

The first arrival times of the individual matrix elements, $V_{ab}^+ = F_{1,ac}^+ B_{cb}$, only differ by an a-wave propagation of $F_{1,ac}^+$ and a b-wave propagation of B_{cb}, both through the top layer. Hence, the diagonal elements of the projector $\mathbf{P}_B^+$ in Eq. 4B.24 can be generalized to an arbitrary projector element,

$$P_{B,ab}^+ = \mathrm{H}\left(\tau + (1-\delta_{ab})\Delta z^{(0)} \left(s_{z,a}^{(0)} - s_{z,b}^{(0)} \right)\right), \tag{4B.25}$$

where δ_{ab} denotes the Kronecker delta.

Next, we derive an expression for the projector $\mathbf{P}_B^-$. The re-mixing operator is not designed to modify the focusing function $\mathbf{F}_1^-$ or the Green's function $\mathbf{G}^{-,+}$ in a special way. Therefore, in a general case the arrival time of the last event of the re-mixed focusing function $V_{ab}^- = F_{1,ac}^- B_{cb}$ is obtained by adding the last arrival times of the focusing function $F_{1,as}^-$ and the re-mixing operator B_{sb},

$$\begin{aligned} P_{B,ab}^- &= \mathrm{H}\left(\tau - \left[\tau_\Omega\left(F_{1,as}^-\right) + \tau_\Omega\left(B_{sy}\right)\right]\right) \\ &= \mathrm{H}\left(\tau - \Delta z^{(0)}\left(s_{z,a}^{(0)} + s_{z,b}^{(0)} \right) - 2\sum_{k=1}^{i-1} \Delta z^{(k)} s_{z,s}^{(k)}\right), \end{aligned} \tag{4B.26}$$

where we used Eqs. 4B.2, 4B.6 and 4B.22.

Although the expressions for the re-mixed projectors might appear complicated, they can be constructed easily from: (1) a smooth P- and S-wave velocity model combined with (2) an estimate of the position of the shallowest reflector and (3) an estimate of the position of the reflector above the redatuming depth. The latter estimate could be obtained e.g. by selecting a redatuming depth below a strong reflector that can be easily localized. Compared to the conventional elastodynamic Marchenko method the required a-priori knowledge is significantly reduced.

■ 4B.3 From monotonicity to separability conditions

In this appendix, we quantify the monotonicity assumptions of the ISS as separability conditions.

The monotonicity assumption [1] requires temporal ordering of primaries according to the reflector ordering in depth. Hence, for an arbitrary elastic component of the reflection response, R_{ab}, the slowest primary associated with an interface $j-1$ (at the bottom of layer $j-1$) must reach the recording surface before the fastest primary associated with the next, deeper, interface j (see Fig. 4.5),

$$\tau_\Omega(R_{ab}^{(j-1)}) < \tau_\alpha(R_{ab}^{(j)}). \tag{4B.27}$$

The superscripts refer to (converted) primary reflections associated with the interfaces $j-1$ and j. Now, we sum the travel times along the travel path of these two primaries, leading to,

$$\tau_\Omega(R_{ab}^{(j-1)}) = \tau_a^{(0)} + 2\sum_{k=1}^{j-1} \tau_s^{(k)} + \tau_b^{(0)}, \tag{4B.28}$$

and,

$$\tau_\alpha(R_{ab}^{(j)}) = \tau_a^{(0)} + 2\sum_{k=1}^{j} \tau_p^{(k)} + \tau_b^{(0)}. \tag{4B.29}$$

Next, we substitute Eqs. 4B.28 and 4B.29 in Eq. 4B.27, replace the travel times by Eq. 4B.2, and obtain a separability condition,

$$\sum_{k=1}^{j-1} \Delta z^{(k)} \left(s_{z,s}^{(k)} - s_{z,p}^{(k)}\right) < \Delta z^{(j)} s_{z,p}^{(j)}. \tag{4B.30}$$

Redatuming from the recording level z_0 to z_i requires that all interfaces between these two depth levels satisfy monotonicity, i.e. Eq. 4B.30 becomes the separability condition in Eq. 4.3.1.

The monotonicity assumption [2] requires that multiples are recorded after their generating primaries. Hence, for redatuming to the depth level z_i the slowest primary reflection associated with the interface $i-1$ must predate the fastest multiple generated by the same interface,

$$\tau_\Omega\left(R_{ab}^{(i-1)}\right) < \tau_\alpha\left(R_{m,ab}^{(i-1)}\right), \tag{4B.31}$$

where $R_{m,ab}^{(i-1)}$ represents the multiples generated by the interface $i-1$. Again, we sum the travel times along the paths of these two events,

$$\tau_\Omega\left(R_{ab}^{(i-1)}\right) = \tau_a^{(0)} + 2\sum_{k=1}^{i-1} \tau_s^{(k)} + \tau_b^{(0)}, \tag{4B.32}$$

and,

$$\tau_\alpha\left(R_{m,ab}^{(i-1)}\right) = \tau_a^{(0)} + 2\sum_{k=1}^{i-1} \tau_p^{(k)} + 2\min\left\{\tau_p^{(k)} \middle| k \in [1,i]\right\} + \tau_b^{(0)}. \tag{4B.33}$$

Upon substituting Eqs. 4B.32 and 4B.33 in Eq. 4B.31 and replacing the travel times by Eq. 4B.2, the monotonicity assumption [2] can be written as,

$$\sum_{k=1}^{i-1} \Delta z^{(k)} \left(s_{z,s}^{(k)} - s_{z,p}^{(k)} \right) < \min \left\{ \Delta z^{(k)} s_{z,p}^{(k)} \middle| \, k \in [1, i] \right\}, \tag{4B.34}$$

which is the separability condition in Eq. 4.3.2. Note that, for multiple generators above the interface $i-1$, the condition in Eq. 4B.34 is relaxed because the left-hand side will remain constant or decrease, while the right-hand side will remain constant or increase.

4C Medium parameters

This appendix contains the medium parameters used for the experiments shown in Figs. 4.1-4.3 (see Tab. 4C.1 and 4C.2). Note that, the values of the medium parameters are adjusted to ensure all events associated with the horizontal-slowness, $s_x = 2 \times 10^{-4}$ m, are recorded on-sample. The values are within a reasonable range but are not associated with any specific material. We used exaggerated density contrasts to generate strong, well-visible, events. In realistic media the contrasts may be weaker but much more numerous. Hence, there will be many weak, as opposed to a few strong, converted waves. The Marchenko method and the separability conditions are independent of the number and strength of these events, and thus, our analysis can be generalized for more realistic media.

z(m)	c_p(m s^{-1})	c_s(m s^{-1})	ρ(kg m^{-3})
-∞ - 500	1993.63	898.38	4200
500 - 1700	1897.78	1099.20	1100
1700 - 2501.07	2500.00	1386.75	6000
2501.07 - ∞	2695.26	1611.32	3500

Table 4C.1: *This table contains the medium parameters used for the experiment shown in Figs. 4.1 and 4.2a (for the acoustic experiment the shear wave velocity is set to zero). The focusing depth is at* $z_f = 1902.07\,\mathrm{m}$. *The experiment shown in Fig. 4.2b uses the same medium parameters, except that the bottom interface is moved from* $z = 2501.07\,\mathrm{m}$ *to* $z = 2299.00\,\mathrm{m}$.

z(m)	$c_p(\mathrm{m\,s^{-1}})$	$c_s(\mathrm{m\,s^{-1}})$	$\rho(\mathrm{kg\,m^{-3}})$
$-\infty$ - 500	1993.63	898.38	1100
500 - 1250.56	2500	1796.05	4200
1250.56 - 1503.15	1505.43	1050.85	1700
1503.15 - 2304.24	1900.00	1006.04	6000
2304.24 - ∞	2695.26	1396.65	3500

Table 4C.2: *This table contains the medium parameters used for the experiment shown in Fig. 4.3a. The focusing depth is at* $z_f = 1703.42\,\mathrm{m}$. *The experiment shown in Fig. 4.3b uses the same medium parameters, except that the second interface from above is moved from* $z = 1250.56\,\mathrm{m}$ *to* $z = 1452.63\,\mathrm{m}$.

5

Towards normal product factorization with minimum-phase constraint

Abstract The Marchenko redatuming strategy presented in chapter 4 of this thesis retrieves the so-called normal product of the desired solution. Reconstructing the desired solution from its normal product forms a new problem that is addressed in this chapter. In the scalar case, normal products simplify to autocorrelations. The factorization of an autocorrelation is not unique, but can be constrained with a minimum-phase condition. Firstly, we study a generalized concept of minimum-phase for matrices. Secondly, we discuss the so-called Wilson algorithm that in several, non-trivial, cases perfectly retrieves the desired minimum-phase matrix from its normal product. Further, we discuss limitations of the Wilson algorithm.

This chapter is a documentation that will soon be turned into a publication.

5.1 Introduction

In chapter 4 of this thesis, we propose a redatuming strategy that recovers a so-called normal product of the desired solution. To proceed with this method, the desired solution must be retrieved from its normal product. However, the factorization of normal products is not unique, i.e. additional constraints are required. We demonstrate that the desired solution possesses a minimum-phase property, which we aim to use as a constraint for the factorization. This strategy is an extension of the scalar case presented by *Wapenaar et al.* [2003] and *Dukalski et al.* [2018], where normal products simplify to autocorrelations that can already be factorized with a minimum-phase constraint [e.g. *Skingle et al.*, 1977].

The concept of minimum-phase is not new to the geophysics community. Often minimum-phase behavior is thought of as a property of a seismic wavelet [e.g. *Yilmaz*, 2001]. However, minimum-phase behavior is a much more general mathematical property. For example, scattering matrices such as reflections and transmissions can also be classified as (non-)minimum-phase functions. *Claerbout* [1968] demonstrates that 1D acoustic transmission responses are minimum-phase functions when measured from the onset of signal. This example highlights that minimum-phase can be a property of an entire wavefield, as opposed to "just" a wavelet.

For our purposes, a generalization of minimum-phase behavior beyond the scalar case is needed. It appears that this topic is hardly discussed within the geophysics community. However, there is a significant amount of research on minimum-phase matrices within control-theory. In this field, minimum-phase functions, which can be matrices, are designed to dynamically control and stabilize systems [e.g. *Bode*, 1940; *Rosenbrock*, 1969; *Shaked and Soroka*, 1986; *Johansson*, 1997]. By building on their findings, we discuss minimum-phase behavior as a constraint for the factorization of the aforementioned normal product.

This chapter is structured as follows. Firstly, we demonstrate the relevance and the challenge of factorizing a normal product with a minimum-phase constraint. Secondly, we review the mathematical definition of minimum-phase. Thirdly, we summarize the factorization of minimum-phase scalar functions. Finally, we document our gained knowledge about matricial minimum-phase behavior, and discuss initial attempts of matricial normal product factorization. Despite our advances, the latter problem is not fully solved and further research is needed.

5.2 Motivation and problem statement

We are interested in retrieving a transmission response using a minimum-phase constraint. A necessary condition for minimum-phase behavior is the existence of an inverse. Using a unified wavefield representation, we demonstrate that the invertibility of transmission responses holds for all wave types in up to 3D space, provided that wavefield decomposition exists. Subsequently, we explain why the minimum-phase property can be extremely relevant not only as a constraint for Marchenko redatuming, but as a universal tool for signal processing in general.

Note that, we use a detail-hiding notation that omits all coordinates. Moreover, all quantities are frequency-dependent, unless stated differently.

5.2.1 Invertibility of transmission responses

In a unified representation, the wave equation can be formulated in the space, $\mathbf{x} = (x, y, z)$, frequency, ω, domain as,

$$\partial_z \mathbf{q} - \boldsymbol{\mathcal{A}} \mathbf{q} = \mathbf{d}. \tag{5.2.1}$$

Here, we use the notation of *Wapenaar et al.* [2016a], where the vectors, $\mathbf{q}$ and $\mathbf{d}$, contain the wavefield and source components, respectively. The definition of the operator, $\boldsymbol{\mathcal{A}}$, is not needed for the following derivation [details can be found in *Wapenaar et al.*, 2016a]. Further, we arbitrarily choose the z-axis as preferential direction of propagation.

A crucial assumption is that the operator, $\boldsymbol{\mathcal{A}}$, is diagonalizable,

$$\boldsymbol{\mathcal{A}} = \boldsymbol{\mathcal{L}} \boldsymbol{\mathcal{H}} \boldsymbol{\mathcal{L}}^{-1}, \tag{5.2.2}$$

which implies that the inverse operator, $\boldsymbol{\mathcal{L}}^{-1}$, exists everywhere in the medium. The operator, $\boldsymbol{\mathcal{L}}$, is often interpreted as composition operator that constructs the wave vector, $\mathbf{q}$, from a so-called one-way wavefield, $\mathbf{p}$ [*de Hoop and de Hoop*, 1994; *Frasier*, 1970; *Wapenaar*, 1996b],

$$\mathbf{q} = \boldsymbol{\mathcal{L}} \mathbf{p} = \boldsymbol{\mathcal{L}} \begin{pmatrix} \mathbf{p}^+ \\ \mathbf{p}^- \end{pmatrix}. \tag{5.2.3}$$

The one-way wavefield contains components propagating along a preferential direction (here the z-axis). For consistency with other chapters of this thesis, we define a downward-pointing z-axis such that the one-way wavefield components are down- (superscript $+$) and upgoing (superscript $-$).

Now we derive expressions for scattering operators to prove the invertibility of transmission responses. This derivation assumes discontinuously changing medium parameters, such that propagation and scattering effects are decoupled. Firstly, consider a horizontal interface that partitions the medium into an upper (superscript i) and a lower part (superscript $i+1$). Using continuity of the wavefield $\mathbf{q}$ along the z-direction, combined with Eq. 5.2.3, the fields just above the interface, $\mathbf{p}_i^{\pm}$, are related with the fields just below the interface, $\mathbf{p}_{i+1}^{\pm}$,

$$\begin{pmatrix} \mathbf{p}_{i+1}^+ \\ \mathbf{p}_{i+1}^- \end{pmatrix} = \boldsymbol{\mathcal{L}}_{i+1}^{-1} \boldsymbol{\mathcal{L}}_i \begin{pmatrix} \mathbf{p}_i^+ \\ \mathbf{p}_i^- \end{pmatrix}. \tag{5.2.4}$$

Secondly, we extend this expression for a package of N interfaces. For this purpose, we define the operator, $\boldsymbol{\mathcal{W}}_i = \exp\left[\boldsymbol{\mathcal{H}}_i (z_{i+1} - z_i)\right]$, that accounts for the one-way wavefield propagation between two interfaces, i and $i+1$, which are located at z_i and z_{i+1}, respectively. Assuming that the top interface (subscript $i = 0$) is transparent, the wavefield at the top interface is mutually related with the field just below the N^{th} interface according to,

$$\begin{pmatrix} \mathbf{p}_N^+ \\ \mathbf{p}_N^- \end{pmatrix} = \prod_{i=0}^{N-1} \left(\boldsymbol{\mathcal{L}}_{i+1}^{-1} \boldsymbol{\mathcal{L}}_i \boldsymbol{\mathcal{W}}_i \right) \begin{pmatrix} \mathbf{p}_0^+ \\ \mathbf{p}_0^- \end{pmatrix}. \tag{5.2.5}$$

The operator in the above equation can be represented as a 2×2 block matrix,

$$\prod_{i=0}^{N-1} \left(\boldsymbol{\mathcal{L}}_{i+1}^{-1} \boldsymbol{\mathcal{L}}_i \boldsymbol{\mathcal{W}}_i \right) = \begin{pmatrix} \mathbf{A} & \mathbf{B} \\ \mathbf{C} & \mathbf{D} \end{pmatrix}. \tag{5.2.6}$$

The diagonalization in Eq. 5.2.2 assumes that the operators, $\boldsymbol{\mathcal{L}}_i$, are invertible. Moreover, we exclude evanescent waves such that a band-limited inverse of the diagonal propagation operators, $\boldsymbol{\mathcal{W}}_i$, exists. Under this assumption, the inverse operator exists,

$$\left[\prod_{i=0}^{N-1} \left(\boldsymbol{\mathcal{L}}_{i+1}^{-1} \boldsymbol{\mathcal{L}}_i \boldsymbol{\mathcal{W}}_i \right) \right]^{-1} = \begin{pmatrix} \mathbf{X}^{-1} & -\mathbf{Y} \\ -\mathbf{D}^{-1}\mathbf{C}\mathbf{X}^{-1} & \mathbf{D}^{-1} + \mathbf{D}^{-1}\mathbf{C}\mathbf{Y} \end{pmatrix}, \tag{5.2.7}$$

where we made the substitutions, $\mathbf{X} = \left(\mathbf{A} - \mathbf{B}\mathbf{D}^{-1}\mathbf{C}\right)$ and $\mathbf{Y} = \mathbf{X}^{-1}\mathbf{B}\mathbf{D}^{-1}$ [*Bernstein*, 2005]. Finally, we rearrange Eq. 5.2.5 to define a scattering matrix,

$$\begin{pmatrix} \mathbf{p}_N^+ \\ \mathbf{p}_0^- \end{pmatrix} = \begin{pmatrix} \mathbf{T}^+ & \mathbf{R}^\cap \\ \mathbf{R}^\cup & \mathbf{T}^- \end{pmatrix} \begin{pmatrix} \mathbf{p}_0^+ \\ \mathbf{p}_N^- \end{pmatrix}, \tag{5.2.8}$$

which relates in- and outgoing fields via transmission operators from above ($\mathbf{T}^+$) and below ($\mathbf{T}^-$) as well as reflection operators from above ($\mathbf{R}^\cup$) and below ($\mathbf{R}^\cap$). The resulting expression,

$$\begin{pmatrix} \mathbf{T}^+ & \mathbf{R}^\cap \\ \mathbf{R}^\cup & \mathbf{T}^- \end{pmatrix} = \begin{pmatrix} \mathbf{A} - \mathbf{B}\mathbf{D}^{-1}\mathbf{C} & \mathbf{B}\mathbf{D}^{-1} \\ -\mathbf{D}^{-1}\mathbf{C} & \mathbf{D}^{-1} \end{pmatrix}, \tag{5.2.9}$$

together with the existence of the inverses, $\mathbf{D}^{-1}$ and $\mathbf{X}^{-1}$, in Eq. 5.2.7, demonstrates that the transmission responses, $\mathbf{T}^\pm$, are invertible. In contrast, the invertibility of the reflection responses is not guaranteed.

Note that, the above derivation only relies on the diagonalization of the operator $\boldsymbol{\mathcal{A}}$. The result is independent of the wave type, the normalization of $\boldsymbol{\mathcal{L}}$ and the spatial dimensionality. Hence, invertibility is a fundamental property of transmissions.

■ 5.2.2 Retrieval of inverse transmissions

The Marchenko method aims to remove overburden-related scattering effects by retrieving the inverse of the overburden transmission $\mathbf{T}^+$. This inverse is often referred to as focusing function $\mathbf{F}_1^+$ [e.g. *Wapenaar*, 2014],

$$\mathbf{T}^+\mathbf{F}_1^+ = \mathbf{I}, \tag{5.2.10}$$

where **I** is a band-limited identity operator. In this notation, matrix products include a spatial integration over the acquisition surface, however, this detail is of minor importance in this chapter. From here onwards, we consider flux-normalized wavefields [*Frasier*, 1970; *Ursin*, 1983], which simplifies our analysis because the resulting one-way propagators preserve the reciprocity properties of the Green's function [*Wapenaar*, 1998].

In sufficiently simple cases, e.g. layered acoustic media and full bandwidth recordings, the Marchenko method does not require additional constraints . However, in presence of band-limitation, short-period multiples can arise, that are not handled correctly [*Dukalski et al.*, 2019; *Elison et al.*, 2020]. Moreover, in the elastodynamic situation, errors occur because forward-scattered waves cannot be predicted by the conventional Marchenko method [*Reinicke*, 2020, chapter 4 of this thesis].

The aforementioned authors propose to overcome these limitations by using additional constraints. They show that the errors due to short-period multiples and forward-scattering are stored in the form of a convolutional operator that blurs the true (desired) solutions, $\mathbf{F}_1^+$. In other words, the retrieved solution is a convolutional product of the desired ones with an unknown operator. By evaluating the correlation-type reciprocity theorem with both states equal to the true focusing functions, one obtains a relation that can be seen as a generalized energy conservation [*Dukalski et al.*, 2018]. Using this relation, one can recover the normal product, $\mathbf{F}_1^+ \left(\mathbf{F}_1^+\right)^\dagger$ [Eqs. 27-29 in chapter 4 of this thesis show this derivation in the horizontal-slowness intercept-time domain, *Reinicke*, 2020]. Here, the superscript † denotes a complex-conjugate transpose. Recovering the true focusing function, $\mathbf{F}_1^+$, from its normal product, $\mathbf{F}_1^+ \left(\mathbf{F}_1^+\right)^\dagger$, forms a new problem.

In the elastodynamic case, the focusing function is a matrix, for which the normal product factorization remains unsolved. Even in simple case of layered elastic media, where each horizontal-slowness (s_x) can be handled independently, the focusing function is a 2 × 2 matrix in P-S space,

$$\mathbf{F}_1^+ = \begin{pmatrix} F_{1,pp}^+ & F_{1,ps}^+ \\ F_{1,sp}^+ & F_{1,ss}^+ \end{pmatrix}. \tag{5.2.11}$$

Here, P- and S-wave receivers and sources are denoted by the first and second subscripts, respectively [for details see chapter 4 of this thesis *Reinicke*, 2020].

The factorization problem simplifies in the special case of acoustic waves. In absence of shear wave components, the focusing function reduces to a scalar, F_1^+. In consequence, the normal product simplifies an autocorrelation, i.e. an amplitude (or power) spectrum,

$$\mathbf{F}_1^+ \left(\mathbf{F}_1^+\right)^\dagger \to F_1^+ \left(F_1^+\right)^* = |F_1^+|^2. \tag{5.2.12}$$

Without additional constraints, the factorization of the autocorrelation is still non-unique. *Dukalski et al.* [2019] and *Elison et al.* [2020] overcome this challenge by exploiting the minimum-phase property of the *back-propagated* focusing function. Details about the back-propagation and its significance will be explained further onwards.

We aim to extend this strategy from scalars to matrices. The above-mentioned method has been developed only for cases where also the eigenvalues of the focusing function possess a minimum-phase property. This is advantageous because in this case the normal product, $\mathbf{F}_1^+ \left(\mathbf{F}_1^+\right)^\dagger$, reduces to a set of independent autocorrelations, $|F_1^+|^2$, that can be factorized individually using existing 1D methods. In order to generalize this strategy, we consider the minimum-phase property in a multi-dimensional operator sense and present ideas how to exploit this property as a constraint for normal product factorization.

Although this work is motivated by our research on the Marchenko method, we emphasize that a generalization of minimum-phase factorization can be valuable to a much wider range of signal processing techniques. An outstanding example is the retrieval of a transmission response from reflection data [*Wapenaar et al.*, 2003], which could be extended beyond layered acoustic media.

5.3 Concept of minimum phase

Control theory and signal processing refer to the response of a linear time-invariant (LTI) system as a transfer function. For example, in seismics, the Earth is an LTI system because it is time-invariant on the time scale of the measurement. Each frequency component, ω, of a transfer function, h, can be described independently. Hence, transfer functions are preferably used in the frequency domain, which is mutually related to the time (t) domain by the Fourier transform,

$$h(\omega) = \int_{-\infty}^{\infty} h(t)\mathrm{e}^{\mathrm{i}\omega t}\mathrm{d}t,\ \mathrm{i}^2 = -1. \tag{5.3.1}$$

In general, transfer functions can be associated with single- or multi-input variables and with single- or multi-output variables. Hence, the literature [e.g. *Johansson*, 1997] often refers to transfer functions as single-input single-output (SISO), multi-input multi-output (MIMO), etc. (SIMO and MISO).

A special "family" of transfer functions is formed by minimum-phase operators. By definition a minimum-phase operator is stable, causal and invertible with a stable and causal inverse [*Bode*, 1945; *Sherwood and Trorey*, 1965; *Skingle et al.*, 1977]. The simplest example is formed by scalar transfer functions (SISO). In this case, the properties of a minimum-phase transfer function, h, can be defined explicitly:

[1] $\int |h(\omega)|\mathrm{d}\omega < \infty$ (stability),

[2] $h(t < 0) = 0$ (causality),

[3] $h^{-1}(\omega)$ exists and satisfies [1] and [2].

The inverse, h^{-1}, is defined in the frequency domain and becomes a convolutional inverse in the time domain. The properties [1]-[3] of a scalar minimum-phase function, h, impose a unique phase-amplitude relation [*Smith*, 2007]. In consequence, the autocorrelation, hh^*, can be factorized uniquely. Recently, this factorization has been extended to account for band-limitation [*Dukalski et al.*, 2018]. Nevertheless, we restrict our analysis to the simpler case of full bandwidth signals, without excluding that band-limitation can be taken into account.

A typical example of a physical, delayed, minimum-phase function is the transmission response [*Claerbout*, 1968]. Naturally, transmission responses are causal and stable. Moreover, we demonstrated that inverse transmissions, i.e. focusing functions F_1^+, exist. Except for a linear phase-shift, focusing functions are causal. Further, since focusing functions have a finite duration [e.g. see Eq. 3 in *Slob et al.*, 2014], they are also stable. Hence, from the onset of signal onwards, i.e. after correction for a linear phase-shift, scalar transmission responses satisfy all criteria of a minimum-phase function.

Extending the concept of minimum-phase to matrices, i.e. beyond SISO systems, is a wide-ranging challenge [e.g. see *Johansson*, 1997]. The first difficulty arises from generalizing the definition of minimum-phase, particularly stability and causality, to matrices. The second, significantly more challenging, problem is the reconstruction of a minimum-phase matrix from its normal product. Before discussing these matrix generalizations, we revisit the scalar case to better illustrate the problem.

5.4 Minimum-phase factorization for scalars

Firstly, we discuss the degrees of freedom associated with the factorization of an autocorrelation (=1D normal product). Secondly, we outline two methods that uniquely factorize the autocorrelation of a minimum-phase function.

■ 5.4.1 Degrees of freedom

Without further constraints, the factorization of the autocorrelation, i.e. the amplitude spectrum, is not unique,

$$\left(F_1^+ \mathrm{U}(1)\right)^* F_1^+ \mathrm{U}(1) = F_1^+ \left(F_1^+\right)^* . \tag{5.4.1}$$

This expression illustrates that there is a freedom of multiplying the solution by a U(1) element [*Cornwell*, 1997],

$$\mathrm{U}(1) = \mathrm{e}^{\mathrm{i}\phi(\omega)}, \tag{5.4.2}$$

and a freedom of complex conjugation, that cancel out in the autocorrelation. These degrees of freedom allow for an arbitrary phase spectrum. However, the minimum-phase property of delayed focusing functions, $\mathbf{F}_1^+$, constrains those freedoms.

For example, consider the transfer functions,

$$g = 1 + \alpha \mathrm{e}^{\mathrm{i}\omega t_1}, \tag{5.4.3}$$

$$h = \alpha + \mathrm{e}^{\mathrm{i}\omega t_1}, \tag{5.4.4}$$

which respectively contain two spikes, one at time zero and another one at time, t_1. Alternatively, these transfer functions can be written as discrete-time vectors,

$$g = (1, 0, ..., 0\,, \alpha, 0, ...), \tag{5.4.5}$$

$$h = (\alpha, 0, ..., 0, 1, 0, ...). \tag{5.4.6}$$

						α	0	...	0	1	0	...	$h * h_c^{-1}$
...	0	$-\frac{1}{\alpha^2}$	0	...	0	$\frac{1}{\alpha}$							1
	...	0	$-\frac{1}{\alpha^2}$	0	...	0	$\frac{1}{\alpha}$						0
				⋮									⋮
				...	0	$-\frac{1}{\alpha^2}$	0	...	0	$\frac{1}{\alpha}$			0

Table 4C.1: *Convolution (denoted by "$*$") between the functions h and h_c^{-1}. The top row represents the function h (see Eq. 5.4.6) in a discrete-time domain. The lower rows represent the time-reversed inverse filter, h_c^{-1}, for several temporal shifts with respect to the function h. The convolution result shown in the right column is a temporal unit delta function (except for errors that will remain at the boundary).*

For both functions, one of the two spikes is scaled by a real number, $\alpha \in \mathbb{R}$. Although both functions yield identical power spectra (i.e. autocorrelations in the time domain),

$$|g|^2 = |h|^2, \tag{5.4.7}$$

their phase spectra differ by the U(1) freedom, $\mathrm{e}^{\mathrm{i}\phi}$, with,

$$\phi = -\mathrm{i}\,\ln\left(\frac{\alpha + \mathrm{e}^{\mathrm{i}\omega t_1}}{1 + \alpha \mathrm{e}^{\mathrm{i}\omega t_1}}\right) \pmod{2\pi}. \tag{5.4.8}$$

Assuming that $|\alpha| < 1$ and $t > 0$, the transfer function g as well as its inverse,

$$g^{-1} = 1 + \sum_{k=1}^{\infty} \left[(-\alpha)^k \mathrm{e}^{\mathrm{i}k\omega t_1}\right] = 1 - \alpha \mathrm{e}^{\mathrm{i}\omega t_1} + \alpha^2 \mathrm{e}^{2\mathrm{i}\omega t_1} - \ldots\,, \tag{5.4.9}$$

are stable and causal. Hence, the function g possesses a minimum-phase behavior and can be reconstructed from the power spectrum in Eq. 5.4.7 (details on the reconstruction will follow later). Although the function h is stable and causal, its inverse is acausal,

$$h^{-1} = \mathrm{e}^{-\mathrm{i}\omega t_1} + \sum_{k=1}^{\infty} \left[(-\alpha)^k \mathrm{e}^{-\mathrm{i}(k+1)\omega t_1}\right] = \mathrm{e}^{-\mathrm{i}\omega t} - \alpha \mathrm{e}^{-2\mathrm{i}\omega t_1} + \alpha^2 \mathrm{e}^{-3\mathrm{i}\omega t_1} - \ldots\,. \tag{5.4.10}$$

One could still design a causal inverse filter, h_c^{-1}, however this filter is unstable,

$$h_c^{-1} = \frac{1}{\alpha} + \sum_{k=1}^{\infty} \left[\frac{(-1)^k}{\alpha^{k+1}} \mathrm{e}^{\mathrm{i}k\omega t_1}\right] = \frac{1}{\alpha} - \frac{1}{\alpha^2}\mathrm{e}^{\mathrm{i}\omega t_1} + \frac{1}{\alpha^3}\mathrm{e}^{2\mathrm{i}\omega t_1} - \ldots\,. \tag{5.4.11}$$

The discrete-time convolutional model in Tab. 4C.1 illustrates that the filter, h_c^{-1}, acts as an inverse on the function h. Neither the inverse h^{-1}, nor the inverse

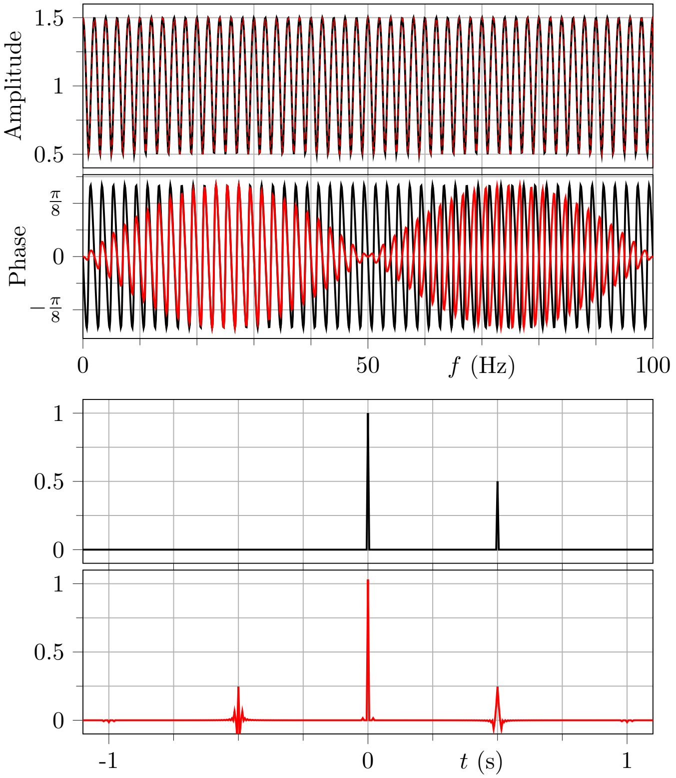

Figure 5.1: *Transfer functions, g (black) and h' (red), shown in Eqs. 5.4.12 and 5.4.13. These transfer functions are identical except for a scaling by a* $\mathrm{U}(1)$ *freedom, which affects the phase spectrum as well as the time-domain shape of the functions.*

filter h_c^{-1} is simultaneously causal and stable. Hence, the function, h, is not a minimum-phase function. For each amplitude spectrum, there are countless other phase spectra, but only one is a minimum-phase function.

To highlight the frequency dependence of the $\mathrm{U}(1)$ element, we consider a numerical example,

$$g(\omega) = 1 + \frac{1}{2}\mathrm{e}^{\mathrm{i}\omega 0.5\,\mathrm{s}}, \tag{5.4.12}$$

$$h'(\omega) = g\,\mathrm{e}^{\mathrm{i}\,\sin\left(\frac{\omega}{100\,\mathrm{Hz}}\right)}, \tag{5.4.13}$$

where we use the scaled angular frequency $f_0 = \frac{\omega_0}{2\pi} = 100\,\mathrm{Hz}$. Fig. 5.1 illustrates that the functions, g and h', posses identical amplitude spectra, but different phase spectra. In this example, the $\mathrm{U}(1)$ freedom, applied in Eq. 5.4.13, changes the time-domain shape of the minimum-phase function, g, significantly. The result, h', is not only acausal, i.e. obviously a non-minimum-phase function, but also contains several additional events.

We remark that the minimum-phase transfer function g of the previous examples (see Eqs. 5.4.3 and 5.4.12) is closely related to a focusing function F_1^+: in a layered acoustic medium with two interfaces, the focusing function F_1^+ has the same mathematical form as the function g, except for a linear phase-shift and a global scaling factor [e.g. see Eq. 3 in *Slob et al.*, 2014]. The linear phase-shift and the global scaling factor can be removed from the focusing function by *back-propagation* with a direct transmission T_d^+ [*van der Neut and Wapenaar*, 2016],

$$V^+ = F_1^+ T_d^+. \tag{5.4.14}$$

The back-propagated focusing function, V^+, is a minimum-phase object, whereas the focusing function, F_1^+, only possesses a minimum-phase behavior from the onset of the signal onwards [*Claerbout*, 1968; *Ware and Aki*, 1969]. In the scalar case, the effect of back-propagation may appear trivial. However, as we will see later, back-propagation can become significantly more sophisticated and powerful beyond the scalar situation discussed by *Elison et al.* [2020].

5.4.2 Phase-amplitude relation

In the scalar case, the minimum-phase properties defined by (i)-(iii) impose a unique phase-amplitude relation.

A well known phase reconstruction method is the Kolmogorov [e.g. *Skingle et al.*, 1977],

$$\mathrm{Arg}\left[g\right] = -\mathscr{H}\left[\log\left(|g|\right)\right], \tag{5.4.15}$$

that reconstructs the phase, $\mathrm{Arg}\left[\cdot\right]$, of a minimum-phase function, g. Since the natural logarithm, $\log\left(\cdot\right)$, is only defined for arguments greater than zero, it implies invertibility of g. Further, the Hilbert transform, $\mathscr{H}\left[\cdot\right]$, retrieves a phase spectrum such that the function, g, and its inverse are causal. Often, there is an incorrect belief that the first event of a minimum-phase function is always the strongest one. Although this is often the case, it does not follow from minimum-phase properties.

The focusing function, F_1^+, is an inverse transmission response. Hence, it satisfies the Kolmogorov relation up to a linear phase-shift,

$$\mathrm{Arg}\left[F_1^+\right] = -\mathscr{H}\left[\log\left(|F_1^+|\right)\right] + \omega t_d, \tag{5.4.16}$$

which is defined by the onset time t_d of the focusing function. back-propagation shifts the onset of signal to time zero such that the back-propagated focusing function, V^+, satisfies Eq. 5.4.15 without linear phase-shift correction.

For example, consider the back-propagated focusing function, V^+, associated with a layered acoustic medium defined by P-wave velocity, c_p, and density, ρ (see Tab. 4C.2). In layered media, wavefields decouple per horizontal-slowness, s_x, and we arbitrarily consider, $s_x = 2 \times 10^{-4}\,\mathrm{s\,m^{-1}}$, to model the back-propagated focusing function, V^+, shown in Fig. 5.2. Subsequently, we reconstruct the phase $\mathrm{Arg}\left[V^+\right]$ from the amplitude spectrum $|V^+|$ using Eq. 5.4.15. The relative error between the

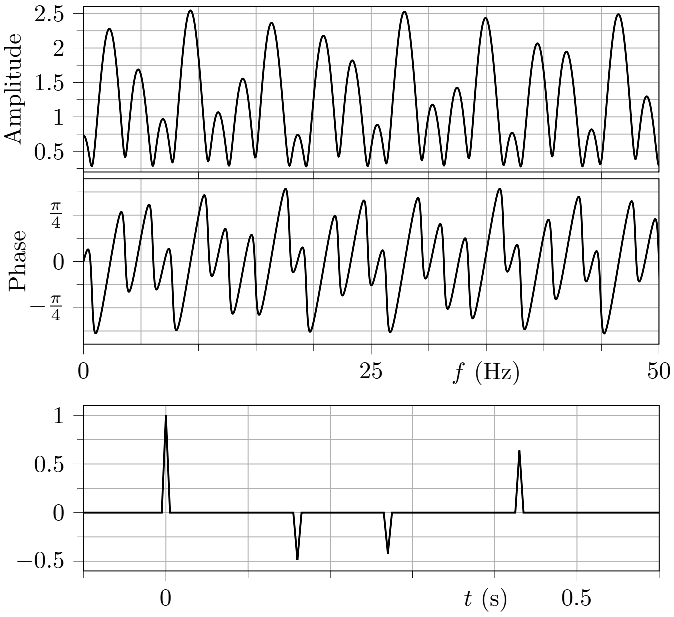

Figure 5.2: *back-propagated focusing function, V^+, associated with the layered acoustic model shown in Tab. 4C.2 and the horizontal-slowness, $s_x = 2 \times 10^{-4}\,\mathrm{s\,m^{-1}}$.*

z (km)	c_p ($\mathrm{m\,s^{-1}}$)	ρ ($\mathrm{kg\,m^{-3}}$)
$-\infty$ - 207.88	1700	1100
207.88 - 507.88	3000	7050
507.88 - 918.81	2600	2400
918.81 - ∞	3700	9000

Table 4C.2: *Layered acoustic model that is used to generate the back-propagated focusing function, V^+, shown in Fig. 5.2. The depth positions of the interfaces are adjusted for perfect sampling of wavefields associated with the horizontal-slowness, $s_x = 2 \times 10^{-4}\,\mathrm{s\,m^{-1}}$.*

reconstructed and modeled functions, $\bar{V}^+$ and V^+, is within machine precision,

$$\frac{\|\bar{V}^+ - V^+\|_2}{\|V^+\|_2} = 6.1 \times 10^{-15}, \qquad (5.4.17)$$

where the symbol $\|\cdot\|_2$ represents the $\mathcal{L}_2$-norm. Further, we denote reconstructed fields with a bar on top to distinguish them from modeled ones.

The Kolmogorov relation in Eqs. 5.4.15 and 5.4.16 is very well suited for scalar functions. However, to the author's knowledge there is no generalization of the

Kolmogorov relation to all matrices. One reason why such a matrix extension is difficult, is because the derivation of the Kolmogorov relation rewrites the logarithm of a product as a sum of logarithms,

$$\log\left(F_1^+\right) = \log\left(|F_1^+|\mathrm{e}^{\mathrm{i}\mathrm{Arg}\left[F_1^+\right]}\right) = \log\left(|F_1^+|\right) + \mathrm{i}\mathrm{Arg}\left[F_1^+\right]. \tag{5.4.18}$$

However, this step does not always hold for matrices because matrix multiplications are non-commutative. Alternative methods that can be generalized to matrices are provided by *Wilson* [1969] and *Janashia et al.* [2013].

We are particularly interested in the method by *Wilson* [1969]. This method recursively reconstructs a minimum-phase function, g, from its power spectrum (autocorrelation in the time-domain). *Wilson* [1969] uses the Newton-Raphson method to derive a relation between the power spectrum, an estimate, g_n, and its update, g_{n+1},

$$g_n g_{n+1}^* + g_{n+1} g_n^* = g_n g_n^* + g g^*. \tag{5.4.19}$$

Multiplication by $(g_n)^{-1}$ and $(g_n^*)^{-1}$,

$$g_{n+1}^* \left(g_n^*\right)^{-1} + \left(g_n\right)^{-1} g_{n+1} = 1 + \left(g_n\right)^{-1} g g^* \left(g_n^*\right)^{-1}, \tag{5.4.20}$$

leads to a superposition of a strictly causal term, $(g_n)^{-1} g_{n+1}$, with its time-reverse, where causality follows from the minimum-phase property of the function g. The acausal term can be removed by applying a mute, $\Theta\left[\cdot\right]$, that represents multiplication by the Heaviside function, $\mathrm{H}(t)$, in the time domain,

$$\mathrm{H}(t) = \begin{cases} 1, & t > 0, \\ \frac{1}{2}, & t = 0, \\ 0, & t < 0. \end{cases} \tag{5.4.21}$$

By rearranging the result a recursive algorithm is obtained,

$$g_{n+1} = g_n \Theta\left[1 + \left(g_n\right)^{-1} |g|^2 \left(g_n^*\right)^{-1}\right]. \tag{5.4.22}$$

The aforementioned author shows that a trivial initial estimate, $g_0 = 1$, is sufficient to arrive at the desired solution g.

Now we use the recursive algorithm given by Eq. 5.4.22 to reconstruct the back-propagated focusing function, V^+ (see Fig. 5.2), from its autocorrelation (see Fig. 5.3). The algorithm converges to machine precision within only seven iterations (see bottom panel in Fig. 5.3). We do not show the retrieved solution because it is undistinguishable from the modeled one in Fig. 5.2.

We illustrate the convergence of Eq. 5.4.22 via a simple example. Suppose the minimum-phase function g, defined by Eq. 5.4.3, is reconstructed from its power spectrum,

$$|g(\omega)|^2 = 1 + \alpha\mathrm{e}^{\mathrm{i}\omega t_1} + \alpha\mathrm{e}^{-\mathrm{i}\omega t_1} + \alpha^2. \tag{5.4.23}$$

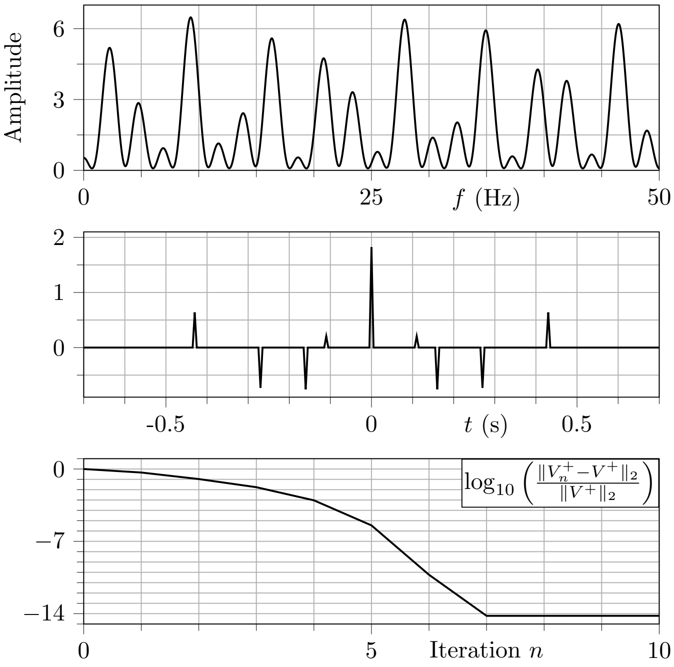

Figure 5.3: *autocorrelation of the back-propagated focusing function $|V^+|^2$ (top two panels) and convergence of the Wilson reconstruction of V^+ (bottom panel). The autocorrelation is associated with the back-propagated focusing function depicted in Fig. 5.2. Since the phase spectrum of the autocorrelation is zero, it is not shown. Using the Wilson algorithm (see Eq. 5.4.22), the back-propagated focusing function is reconstructed within machine precision as indicated by the convergence plot.*

The first iteration of Eq. 5.4.22 yields,

$$g_1(\omega) = 1 + \alpha \mathrm{e}^{\mathrm{i}\omega t_1} + \frac{1}{2}\alpha^2, \tag{5.4.24}$$

which contains a quadratic error term, $\frac{1}{2}\alpha^2$, that decreases further with higher iterations.

5.5 Minimum-phase factorization for matrices

Autocorrelations form a special case of normal products. Unfortunately, the factorization of autocorrelations involves assumptions that do no generalize to normal products. As a result, several "new" challenges must be overcome to factorize normal products. Firstly, we discuss the concept of minimum-phase for matrices. Secondly, we provide a physical interpretation of a general normal product. Thirdly, we analyze the additional degrees of freedom, associated with normal product factorization, that only exist in the multi-dimensional situation. Finally, we present a slightly modified version of the minimum-phase matrix factorization method by *Tunnicliffe-Wilson* [1972][1].

In this analysis, we consider the simplest, non-trivial, matrix case, which is formed by frequency-dependent 2 × 2 matrices,

$$\mathbf{M} = \begin{pmatrix} a & b \\ c & d \end{pmatrix} . \tag{5.5.1}$$

Nevertheless, our analysis extends to arbitrary full-rank square-matrices. We do not exclude that our analysis can be generalized to non-square matrices.

5.5.1 Matricial minimum-phase property

Diagonal matrices are a natural extension from scalars to matrices. An example of a scalar (i.e. SISO) minimum-phase function is given by g defined in Eq. 5.4.3. By arranging several minimum-phase functions alike g on the diagonal of a matrix, we obtain a trivial example of a matricial (i.e. MIMO) minimum-phase object with decoupled channels,

$$\mathbf{\Lambda} = \begin{pmatrix} 1-\alpha \mathrm{e}^{\mathrm{i}\omega t_1} & 0 \\ 0 & 1+\alpha \mathrm{e}^{\mathrm{i}\omega t_1} \end{pmatrix} , \text{ and } |\alpha| < 1. \tag{5.5.2}$$

It may appear intuitive that the above matrix has a minimum-phase property. However, as we will show further onwards, there are less obvious cases of minimum-phase matrices.

We start by discussing the meaning of stability, causality and invertibility in a matrix sense. The matrix generalization of invertibility is straightforward and simply requires a non-zero determinant,

$$\det(\mathbf{M}) = ad - bc \neq 0, \tag{5.5.3}$$

such that the matrix inverse exists,

$$\mathbf{M}^{-1} = \frac{1}{\det(\mathbf{M})} \begin{pmatrix} d & -b \\ -c & a \end{pmatrix} . \tag{5.5.4}$$

In contrast, the meaning of stability and causality in a matrix sense is not immediately clear. Existing literature defines the minimum-phase property of a matrix via its determinant: A minimum-phase matrix possesses a (scalar) minimum-phase determinant [*Wiener*, 1955; *Rosenbrock*, 1969; *Horowitz et al.*, 1986]. On the one hand, this definition is desirable because it keeps the minimum-phase property basis-invariant,

$$\det(\mathbf{M}) = \det\left(\mathbf{Q}\mathbf{M}\mathbf{Q}^{-1}\right) , \tag{5.5.5}$$

---

[1] The references *Wilson* [1969] and *Tunnicliffe-Wilson* [1972] are authored by the same person.

where $\mathbf{Q}$ is an arbitrary invertible matrix of the same size as $\mathbf{M}$. On the other hand, this generalization does not restrict the phase behavior of individual matrix elements. For example, suppose the matrix,

$$\mathbf{Q} = \begin{pmatrix} 1 - 2\alpha \mathrm{e}^{\mathrm{i}\omega t_1} & 1 \\ 1 + \alpha \mathrm{e}^{-\mathrm{i}\omega t_1} & 1 + \alpha \mathrm{e}^{-\mathrm{i}\omega t_1} \end{pmatrix}, \tag{5.5.6}$$

is used to apply a frequency-dependent basis transformation to the minimum-phase matrix, $\mathbf{\Lambda}$, in Eq. 5.5.2. The resulting matrix,

$$\mathbf{Q}\mathbf{\Lambda}\mathbf{Q}^{-1} = \begin{pmatrix} 2 - \alpha \mathrm{e}^{\mathrm{i}\omega t_1} & -\frac{1-2\alpha \mathrm{e}^{\mathrm{i}\omega t_1}}{1+\alpha \mathrm{e}^{-\mathrm{i}\omega t_1}} \\ 1 + \alpha \mathrm{e}^{-\mathrm{i}\omega t_1} & \alpha \mathrm{e}^{\mathrm{i}\omega t_1} \end{pmatrix}, \tag{5.5.7}$$

is still a minimum-phase matrix but it contains non-minimum-phase matrix-elements (e.g. see acausal element $1 + \alpha \mathrm{e}^{-\mathrm{i}\omega t_1}$).

Moreover, defining minimum-phase matrices via their determinant has several consequences. First of all, it follows that the determinant of a minimum-phase matrix, $\mathbf{M}$, satisfies the Kolmogorov relation (analogously to Eq. 5.4.15),

$$\mathrm{Arg}\left[\det\left(\mathbf{M}\right)\right] = -\mathscr{H}\left[\log\left(\left|\det\left(\mathbf{M}\right)\right|\right)\right]. \tag{5.5.8}$$

This highlights that scalars form a special case, in which the determinant simplifies to $\mathbf{M}$. Second, the determinant is equal to the product of the eigenvalues, λ_i, of a matrix,

$$\det\left(\mathbf{M}\right) = \prod_i \lambda_i. \tag{5.5.9}$$

Hence, in a general 2×2 case, the two eigenvalues have an arbitrary frequency-dependent phase-freedom Φ,

$$\mathrm{Arg}\left[\lambda_1\right] = -\mathscr{H}\left[\log\left(\left|\lambda_1\right|\right)\right] + \Phi, \tag{5.5.10}$$

$$\mathrm{Arg}\left[\lambda_2\right] = -\mathscr{H}\left[\log\left(\left|\lambda_2\right|\right)\right] - \Phi. \tag{5.5.11}$$

In special cases where all eigenvalues observe a minimum-phase property, the absolute eigenvalues, $|\lambda_i|$, of a matrix, $\mathbf{M}$, can be derived from the normal product, $\mathbf{M}\mathbf{M}^{\dagger}$. *Wapenaar et al.* [2003] and *Elison et al.* [2020] investigate such a special situation by restricting their analysis to (inverse) transmission responses of layered acoustic media, where also the phase freedom vanishes, $\Phi = 0$.

Here, we consider a more general case, which is formed by *elastic* layered media. Alike layered acoustic media, wavefields still decouple per horizontal-slowness, and without loss of generality, we restrict our analysis to a single horizontal-slowness, $s_x = 2 \times 10^{-4}\,\mathrm{s\,m}^{-1}$. In contrast to layered acoustic media, wavefields are now represented by 2×2 matrices in P-S space as shown in Eq. 5.2.11. For the following numerical examples, we use the layered medium defined in Tab. 4C.3, where c_s denotes the S-wave velocity.

z (km)	c_p ($\mathrm{m\,s^{-1}}$)	c_s ($\mathrm{m\,s^{-1}}$)	ρ ($\mathrm{kg\,m^{-3}}$)
$-\infty$ - 201.29	1718.42	900	1100
201.29 - 516.50	2978.57	1200	7050
516.50 - 925.33	2662.07	1500	2400
925.33 - ∞	3676.02	1700	9000

Table 4C.3: *Layered elastic model. The depth positions of the interfaces and the P-wave velocities are adjusted for perfect sampling of wavefields associated with the horizontal-slowness,* $s_x = 2 \times 10^{-4}\,\mathrm{s\,m^{-1}}$.

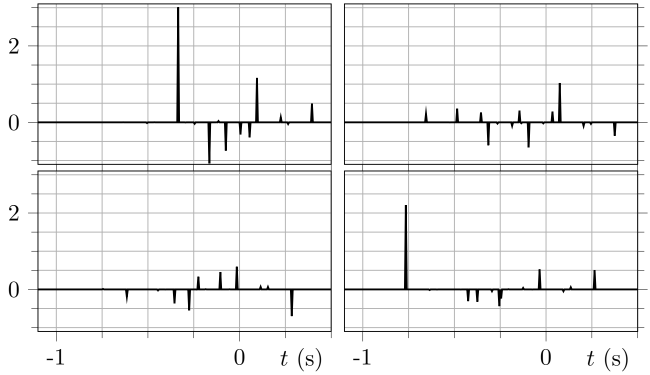

Figure 5.4: *Focusing function* $\mathbf{F}_1^+$ *associated with the medium in Tab. 4C.3. Each panel shows one elastic component in the time domain. The panels are arranged analogously to the P-S matrix elements in Eq. 5.2.11.*

Next, we model the focusing function, $\mathbf{F}_1^+$ (see Fig. 5.4). This response is the inverse of a transmission response to a source at $z = 0\,\mathrm{m}$ recorded at $z = 979.56\,\mathrm{m}$. In Fig. 5.5, we depict the eigenvalues, $\lambda_{1/2}$, as well as the determinant of the focusing function, $\det\left(\mathbf{F}_1^+\right)$. The eigenvalues do clearly not satisfy minimum-phase properties, and the phase freedom Φ (see Eqs. 5.5.10 and 5.5.11) is significantly more complicated than a linear phase-shift. Nevertheless, using the Kolmogorov relation (see Eq. 5.5.8), it can be shown that the determinant is a minimum-phase function from the onset of the signal at the time t_0 (within machine precision),

$$\frac{\|\mathrm{Arg}\left[\det\left(\mathbf{F}_1^+\right)\right] + \mathscr{H}\left[\log\left(|\det\left(\mathbf{F}_1^+\right)|\right)\right] - \omega t_0\|_2}{\|\mathrm{Arg}\left[\det\left(\mathbf{F}_1^+\right)\right]\|_2} = 5.6 \times 10^{-14}. \tag{5.5.12}$$

The minimum-phase property of the determinant, after applying a linear phase-shift correction, can be visualized in an Argand diagram (see Fig. 5.6). As expected for a minimum-phase function, there is no intersection with the negative real axis.

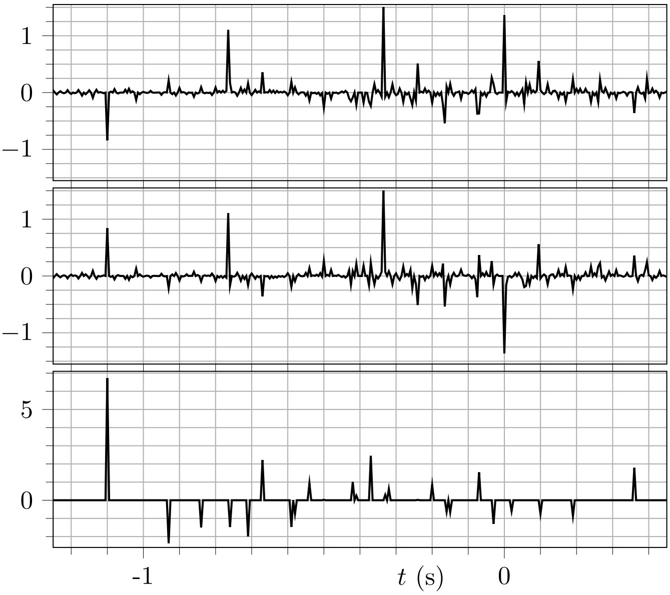

Figure 5.5: *Eigenvalues (top two panels) and determinant (bottom panel) of the focusing function,* $\mathbf{F}_1^+$*, shown in Fig. 5.4. All quantities are shown in time domain.*

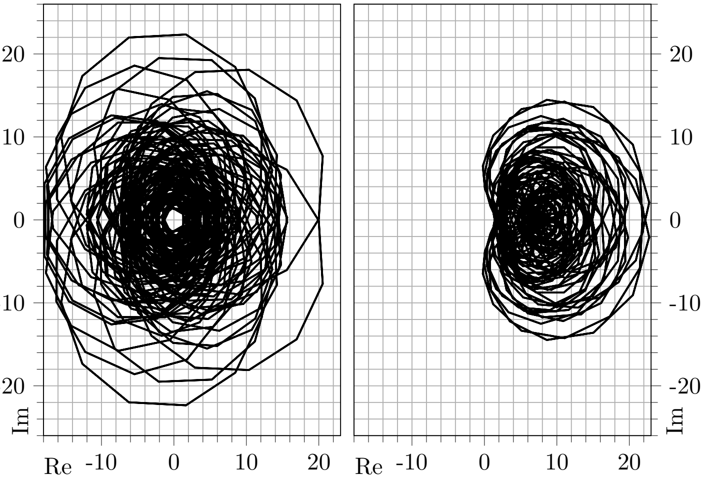

Figure 5.6: *Argand diagram of the determinant,* $\det(\mathbf{F}_1^+)$*, without (left) and with (right) linear phase-shift correction,* $+\omega t_0$*. The real (Re) and imaginary (Im) parts of the (frequency-domain) function are represented on the horizontal and vertical axes, respectively. A time-domain illustration of the determinant,* $\det(\mathbf{F}_1^+)$*, is shown in Fig. 5.5.*

Analogous to the acoustic case, the linear phase-shift correction of the determinant, $\det(\mathbf{F}_1^+)$, can be compensated by back-propagation. However, there are several possibilities to extend back-propagation to the elastic case. In the following, we present the two elastic back-propagation schemes that we find to be most insightful.

A simple extension is obtained by generalizing the direct transmission from an acoustic, T_d^+ (see Eq. 5.4.14), to an elastic one,

$$\mathbf{T}_d^+ = \begin{pmatrix} \tau_{pp} \mathrm{e}^{\mathrm{i}\omega t_p^{(d)}} & 0 \\ 0 & \tau_{ss} \mathrm{e}^{\mathrm{i}\omega t_s^{(d)}} \end{pmatrix}. \tag{5.5.13}$$

Here, $t_p^{(d)}$ and $t_s^{(d)}$ denote the travel time of a directly transmitted P- and S- wave, respectively. Moreover, the real-valued scalars, τ_{pp} and τ_{ss}, are defined by the transmission coefficients. The resulting field,

$$\mathbf{V}_d^+ = \mathbf{F}_1^+ \mathbf{T}_d^+, \tag{5.5.14}$$

is shown in Fig. 5.7: Only its *ss* component (bottom-left matrix element) is a scalar minimum-phase function (see red line in *ss* panel). The *pp* component is close to a minimum-phase function. However, its phase spectrum contains minor deviations from a minimum-phase phase spectrum (see red line in *pp* panel). This deviation is caused by weak acausal events, which are highlighted by a black circle. Further, the *ps* and *sp* components are clearly not minimum-phase functions, e.g. their amplitude spectra contain zero elements, which cannot be inverted. Although (some of) the individual matrix elements do not possess a minimum-phase property, the determinant does (see Fig. 5.8). In contrast to the determinant of the focusing function, $\det(\mathbf{F}_1^+)$, there is no need for a linear phase-shift correction because it is already applied via the direct transmission,

$$\begin{aligned} \mathrm{Arg}\left[\det\left(\mathbf{V}_d^+\right)\right] &= \mathrm{Arg}\left[\det\left(\mathbf{F}_1^+\right)\det\left(\mathbf{T}_d^+\right)\right] \\ &= \mathrm{Arg}\left[\det\left(\mathbf{F}_1^+\right)\right] + \mathrm{Arg}\left[\det\left(\mathbf{T}_d^+\right)\right] \\ &= \mathrm{Arg}\left[\det\left(\mathbf{F}_1^+\right)\right] + \omega(t_p^{(d)} + t_s^{(d)}) \\ &= \mathrm{Arg}\left[\det\left(\mathbf{F}_1^+\right)\right] + \omega t_0. \end{aligned} \tag{5.5.15}$$

Note that, the travel times of the direct P- and S-waves add to the onset time of the determinant $\det(\mathbf{F}_1^+)$, $t_0 = t_p^{(d)} + t_s^{(d)}$. The multiplication by the direct transmission, $\mathbf{T}_d^+$, does also affect the eigenvalues. However, the eigenvalues of the field $\mathbf{V}_d^+$ (see Fig. 5.8), alike the eigenvalues of $\mathbf{F}_1^+$, deviate from a minimum-phase function by non-linear phase shifts, $\pm\Phi$.

In chapter 4 of this thesis, we introduce a more general back-propagated focusing function,

$$\mathbf{V}^+ = \mathbf{F}_1^+ \mathbf{B}. \tag{5.5.16}$$

The diagonal elements of this quantity are equal to a unit delta function (in time) plus a strictly causal coda. In special cases, the operator, $\mathbf{B}$, reduces to a forward-scattered transmission response $\mathbf{T}_{fs}^+$, i.e. a transmission response that includes mode

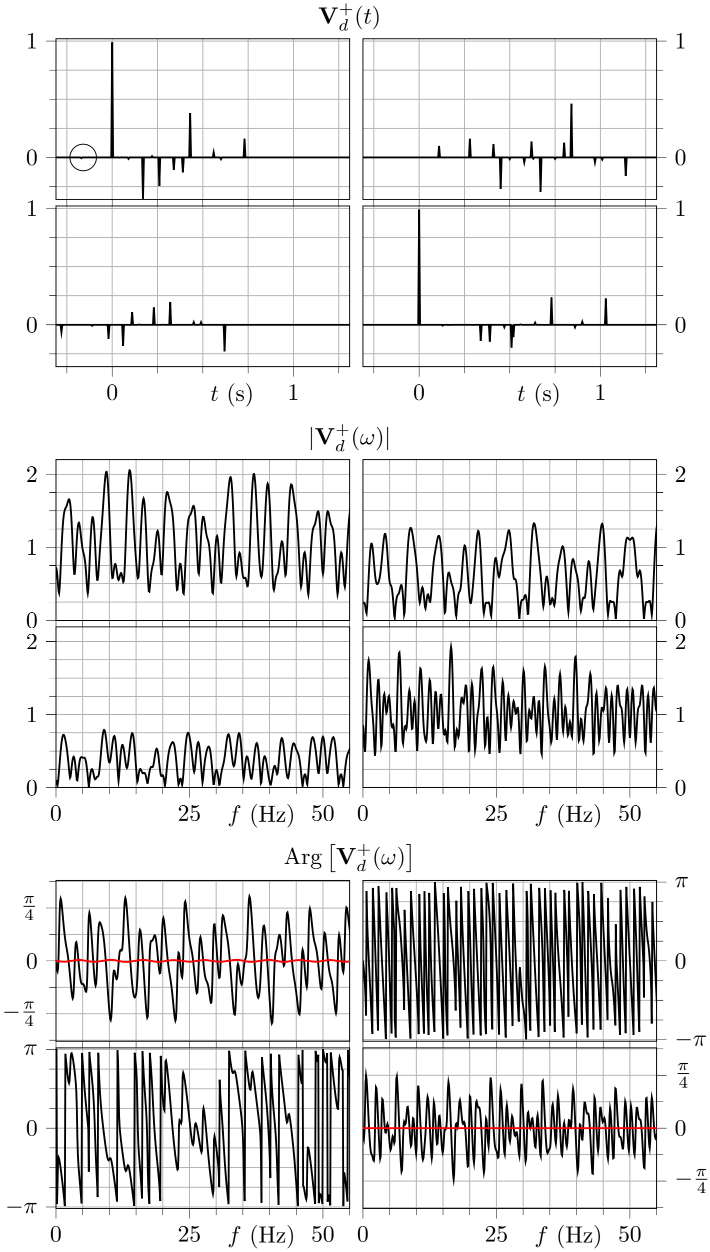

Figure 5.7: *Wavefield $\mathbf{V}_d^+$ associated with the medium in Tab. 4C.3. The three vertical blocks show the time-domain traces, the amplitude spectrum and the phase spectrum of the field. Each block contains four panels that are associated with the four elastic components and are arranged analogously to the P-S matrix elements in Eq. 5.2.11. The red lines depict the deviation of the phase spectra from their respective minimum-phase spectra (only shown for the diagonal elements pp and ss).*

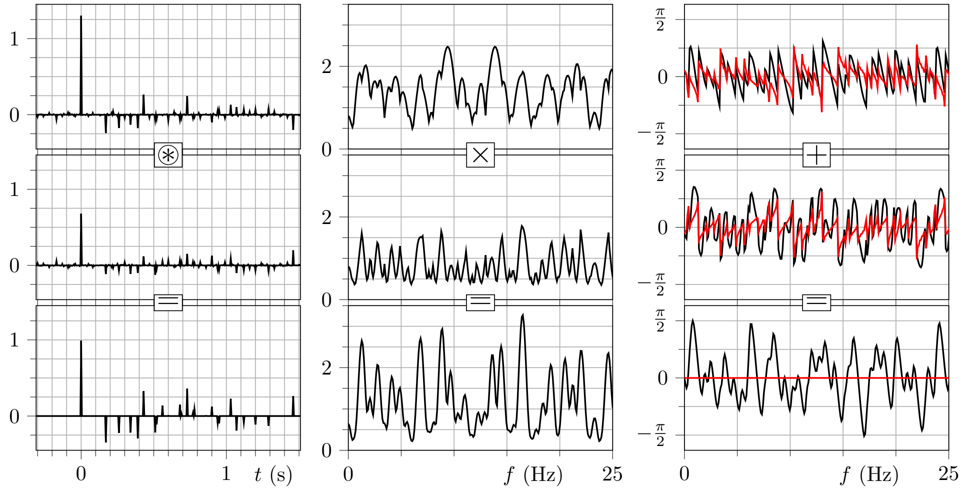

Figure 5.8: *Eigenvalues (rows one and two) and determinant (row three) of the wavefield, $\mathbf{V}_d^+$, shown in Fig. 5.7. From left to right, the columns show the time-domain traces, the amplitude spectra and the phase spectra. The red lines depict the deviation of the phase spectra from their respective minimum-phase spectra. The operators indicate the mutual link between the panels per column. The symbol $\circledast$ denotes temporal convolution.*

conversions but excludes internal multiples. An example of a back-propagated focusing function, $\mathbf{V}^+$, is depicted in Fig. 5.9, where $\mathbf{B} = \mathbf{T}_{fs}^+$. In contrast to the response $\mathbf{V}_d^+$ in Fig. 5.7, not only the element V_{ss}^+, but both diagonal elements are minimum-phase functions (see comparison to minimum-phase phase spectra indicated by red lines). We emphasize that the minimum-phase behavior of the diagonals is merely an observation, but perhaps this is a characteristic of an arbitrary back-propagated focusing function, $\mathbf{V}^+$. The individual off-diagonals remain non-minimum-phase functions (see zeros in amplitude spectra and acausal events in V_{sp}^+). The eigenvalues and the determinant of the back-propagated focusing function $\mathbf{V}^+$ are nearly identical to those of the field $\mathbf{V}_d^+$ (compare Figs. 5.8 and 5.10).

■ 5.5.2 Properties of normal products

Now we discuss the properties of normal products, which can be seen as generalized autocorrelations.

In the matrix case, there are two normal products, which are generally not equal,

$$\mathbf{M}\mathbf{M}^\dagger \neq \mathbf{M}^\dagger\mathbf{M}. \tag{5.5.17}$$

Hence, if both normal products are known, there are more equations to constrain the reconstruction of the matrix, $\mathbf{M}$. However, in case of the previously-mentioned Marchenko method, only one normal product, $\mathbf{F}_1^+\left(\mathbf{F}_1^+\right)^\dagger$, is retrieved. Therefore, we restrict our analysis to the normal product, $\mathbf{M}\mathbf{M}^\dagger$.

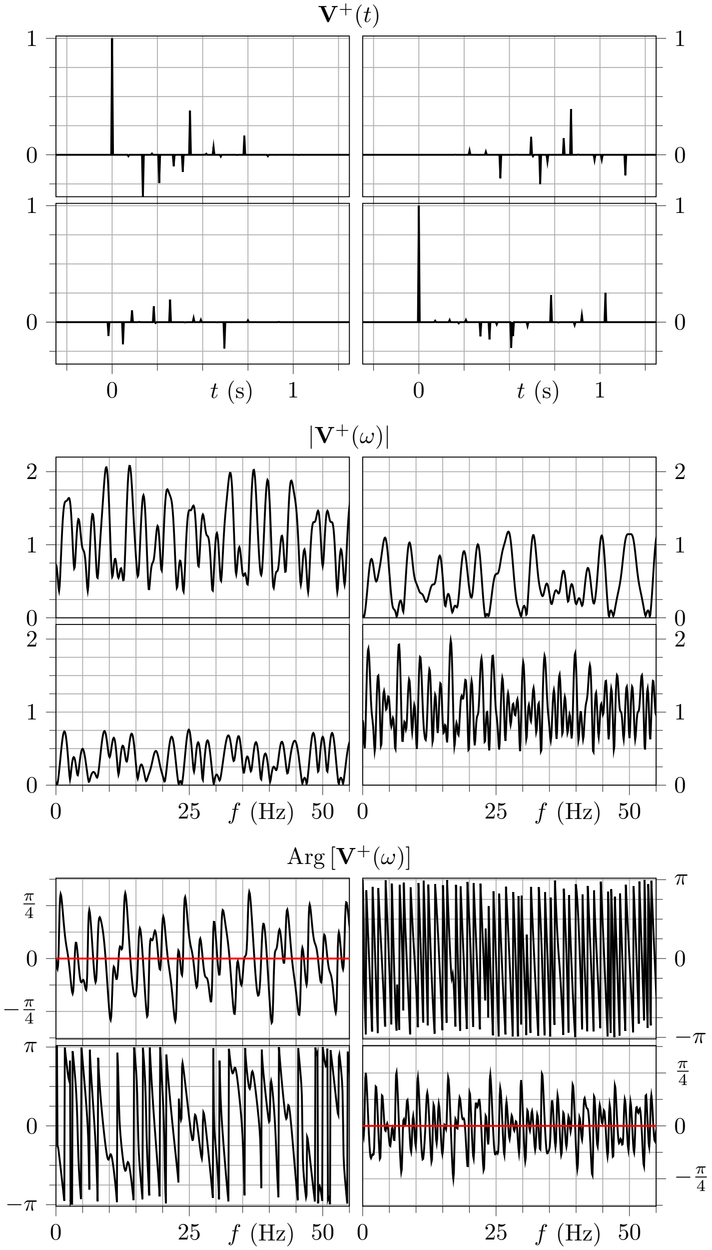

Figure 5.9: *Idem as Fig. 5.7 but for* $\mathbf{V}^+$.

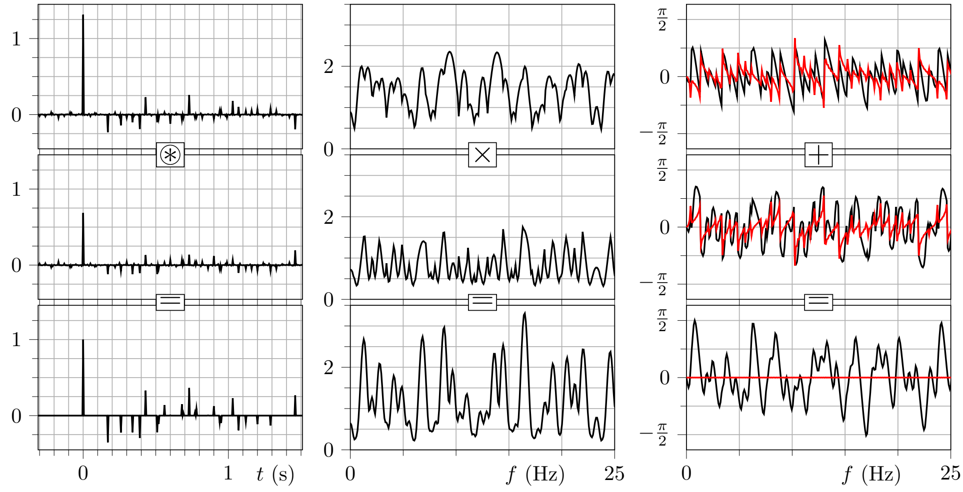

Figure 5.10: *Idem as Fig. 5.8 but for* $\mathbf{V}^+$.

The matrix, $\mathbf{M}$, and its normal product, $\mathbf{M}\mathbf{M}^\dagger$, are closely related via their singular values. To demonstrate this insight, we write matrix $\mathbf{M}$ in terms of its singular-value decomposition [*Stewart*, 1993],

$$\mathbf{M} = \boldsymbol{\Upsilon}\boldsymbol{\Sigma}\boldsymbol{\Gamma}^\dagger, \tag{5.5.18}$$

where the matrices, $\boldsymbol{\Upsilon}$ and $\boldsymbol{\Gamma}$, are unitary, and the diagonal matrix, $\boldsymbol{\Sigma}$, contains the singular values, $\sigma_i > 0$. Now the normal product can be written as,

$$\mathbf{M}\mathbf{M}^\dagger = \boldsymbol{\Upsilon}\ \mathrm{diag}\left(\sigma_1^2, \sigma_2^2\right)\ \boldsymbol{\Upsilon}^\dagger, \tag{5.5.19}$$

which gives it the notion of a matrix-generalized power spectrum of matrix $\mathbf{M}$. Hence, the factorization of the normal product, $\mathbf{M}\mathbf{M}^\dagger$, can be seen as a phase retrieval of the matrix $\mathbf{M}$. Moreover, the singular values as well as the determinant,

$$|\det\left(\mathbf{M}\mathbf{M}^\dagger\right)|^2 = |\sigma_1\sigma_2|^2, \tag{5.5.20}$$

are basis-invariant, which demonstrates that the power spectrum of a matrix is independent of the basis representation.

Next, we provide a numerical example of a normal product. Consider the matrix,

$$\mathbf{M} = \begin{pmatrix} 1 + 0.5\mathrm{e}^{\mathrm{i}\omega t_1} & \mathrm{e}^{\mathrm{i}2\omega t_1} \\ -\mathrm{e}^{-\mathrm{i}2\omega t_1} & 1 + 0.4\mathrm{e}^{\mathrm{i}4\omega t_1} \end{pmatrix}, \tag{5.5.21}$$

with $t_1 = 0.05\,\mathrm{s}$, which is depicted in the time domain in Fig. 5.11. The normal

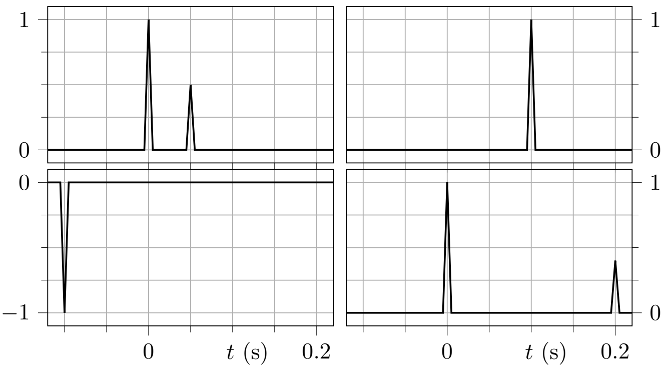

Figure 5.11: *Matrix* $\mathbf{M}$ *defined by Eq. 5.5.21. Each panel shows one element of the matrix* $\mathbf{M}$ *in the time domain. The panels are arranged analogously to the matrix elements in Eq. 5.5.1.*

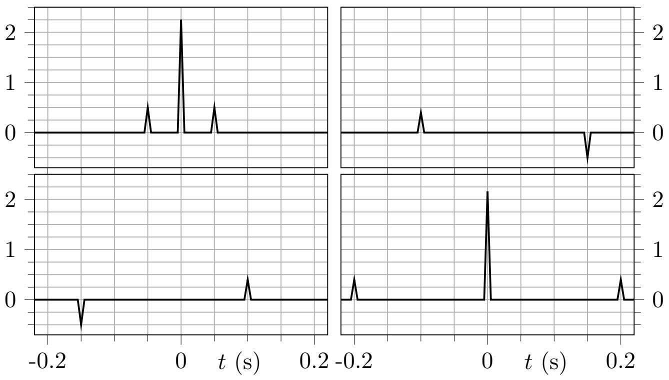

Figure 5.12: *Idem as Fig. 5.11 but for the normal product,* $\mathbf{M}\mathbf{M}^\dagger$*, defined by Eq. 5.5.22.*

product of $\mathbf{M}$ is given by,

$$\mathbf{M}\mathbf{M}^\dagger = \begin{pmatrix} 2.25+\cos(\omega t_1) & x \\ x^* & 2.16+0.8\cos(4\omega t_1) \end{pmatrix}, \tag{5.5.22}$$

with $x = 0.4\mathrm{e}^{-\mathrm{i}2\omega t_1} + 0.5\mathrm{e}^{\mathrm{i}3\omega t_1}$, and is shown in the time domain in Fig. 5.12. Note that, the diagonals of the normal product, $\mathbf{M}\mathbf{M}^\dagger$, are phase-less. In contrast, the off-diagonals of $\mathbf{M}\mathbf{M}^\dagger$ have non-zero phase spectra (see definition of x) and are mutually related via complex conjugation in the frequency domain, i.e. by a time-reversal. Moreover, Fig. 5.13 shows the singular values of the normal product, which are defined in Eq. 5.5.19.

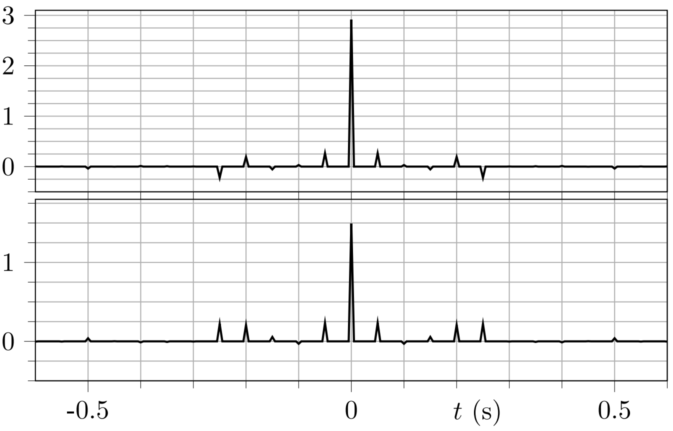

Figure 5.13: *Singular values, σ_1^2 (top panel) and σ_2^2 (bottom panel) in the time domain. The singular values are associated with the normal product, $\mathbf{MM}^\dagger$, as defined by Eq. 5.5.22.*

■ 5.5.3 Degrees of freedom

Compared to the scalar case, the factorization of normal products has additional degrees of freedom. Upon multiplication by an arbitrary unitary 2 × 2 matrix, i.e. by a U(2) element, the normal product of the matrix, $\mathbf{M}$, is preserved,

$$\mathbf{M}\mathrm{U}(2)\left(\mathbf{M}\mathrm{U}(2)\right)^\dagger = \mathbf{MM}^\dagger. \tag{5.5.23}$$

Subsequently, we discuss the U(2) element, which describes the group of 2 × 2 unitary matrices. By definition the complex-conjugate transpose of a unitary matrix is equal to its inverse,

$$\mathrm{U}(2)\left[\mathrm{U}(2)\right]^\dagger = \mathbf{I}. \tag{5.5.24}$$

An arbitrary U(2) element can be represented as a product of an SU(2) element with a U(1) element [*Cornwell*, 1997],

$$\begin{aligned}&\mathrm{U}(2) = \mathrm{SU}(2)\mathrm{U}(1) = \\ &\begin{pmatrix} \mathrm{e}^{-\mathrm{i}\frac{\gamma+\alpha}{2}}\cos\left(\frac{\beta}{2}\right) & -\mathrm{e}^{\mathrm{i}\frac{\gamma-\alpha}{2}}\sin\left(\frac{\beta}{2}\right) \\ \mathrm{e}^{-\mathrm{i}\frac{\gamma-\alpha}{2}}\sin\left(\frac{\beta}{2}\right) & \mathrm{e}^{\mathrm{i}\frac{\gamma+\alpha}{2}}\cos\left(\frac{\beta}{2}\right) \end{pmatrix}\mathrm{e}^{\mathrm{i}\phi}.\end{aligned} \tag{5.5.25}$$

The SU(2) element is a special U(2) element with a determinant equal to one. In the above expression, the SU(2) element is parameterized with the Euler angles α, β and γ [*Hamada*, 2015], and can be generated from exponentials, $\mathrm{SU}(2) = \mathrm{e}^{-\frac{\mathrm{i}}{2}\boldsymbol{\sigma}_z\alpha}\mathrm{e}^{-\frac{\mathrm{i}}{2}\boldsymbol{\sigma}_y\beta}\mathrm{e}^{-\frac{\mathrm{i}}{2}\boldsymbol{\sigma}_z\gamma}$, where $\boldsymbol{\sigma}_{y/z}$ are Pauli matrices,

$$\boldsymbol{\sigma}_y = \begin{pmatrix} 0 & -\mathrm{i} \\ \mathrm{i} & 0 \end{pmatrix}, \boldsymbol{\sigma}_z = \begin{pmatrix} 1 & 0 \\ 0 & -1 \end{pmatrix}. \tag{5.5.26}$$

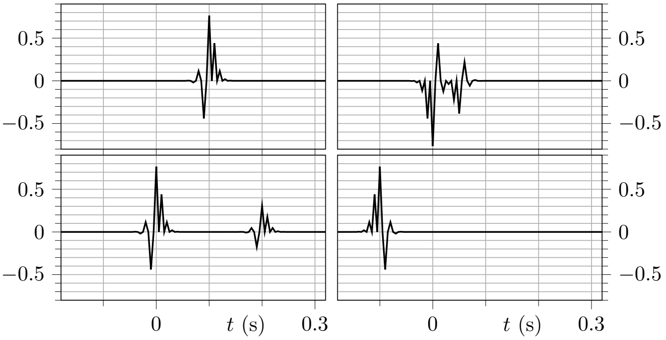

Figure 5.14: *Idem as Fig. 5.11 but for the matrix* $\mathbf{M}\mathrm{SU}(2)$ *defined by Eqs. 5.5.21 and 5.5.27.*

Using this parameterization, the SU(2) element can be interpreted as a series of rotations around the z-, y- and again z-axis by $\frac{\gamma}{2}$, $\frac{\beta}{2}$ and $\frac{\alpha}{2}$, respectively. Compared to the scalar case (factorization of autocorrelations), the SU(2) introduces three additional degrees of freedom.

We present a numerical example to illustrate the power of the degrees of freedom. To this end, we multiply the matrix, $\mathbf{M}$ (see Eq. 5.5.21 and Fig. 5.11), by the following SU(2) element (i.e. $\phi = 0$),

$$\begin{aligned}\mathrm{SU}(2) &= \mathrm{e}^{\frac{\mathrm{i}}{2}\boldsymbol{\sigma}_z \sin\left(\frac{\omega}{100\,\mathrm{Hz}}\right)} \mathrm{e}^{-\frac{\mathrm{i}}{2}\boldsymbol{\sigma}_y \pi} \mathrm{e}^{-\frac{\mathrm{i}}{2}\boldsymbol{\sigma}_z \sin\left(\frac{\omega}{100\,\mathrm{Hz}}\right)} \\ &= \begin{pmatrix} 0 & -\mathrm{e}^{\mathrm{i}\sin\left(\frac{\omega}{100\,\mathrm{Hz}}\right)} \\ \mathrm{e}^{-\mathrm{i}\sin\left(\frac{\omega}{100\,\mathrm{Hz}}\right)} & 0 \end{pmatrix}. \end{aligned} \tag{5.5.27}$$

Although this SU(2) element appears rather "simple", it drastically changes the time-domain shape of the matrix $\mathbf{M}$ (compare Figs. 5.11 and 5.14). In contrast, the normal product (see Fig. 5.12) and the determinant remain unchanged, which we could confirm within machine precision. The challenge of normal product factorization is to find the desired matrix, $\mathbf{M}$, instead of a rotated version, $\mathbf{M}\mathrm{SU}(2)\mathrm{U}(1)$.

The above example may appear contradictory to the scalar example in Eq. 5.4.13. In this scalar example, the minimum-phase property of the function, g, was destroyed by multiplication with the U(1) element, $\mathrm{e}^{\mathrm{i}\sin\left(\frac{\omega}{100\,\mathrm{Hz}}\right)}$, which resembles the SU(2) element in Eq. 5.5.27. However, there is a key difference between the two examples: The determinant of the SU(2) element is one, i.e. the SU(2) element possesses a minimum-phase property. In contrast, the determinant of the U(1) element is an acausal function, $\det\left(\mathrm{e}^{\mathrm{i}\sin\left(\frac{\omega}{100\,\mathrm{Hz}}\right)}\right) = \mathrm{e}^{\mathrm{i}\sin\left(\frac{\omega}{100\,\mathrm{Hz}}\right)}$, i.e. non-minimum-phase.

The factorization of autocorrelations has a freedom of complex conjugation, which does not generalize to normal products. This freedom is unique to the scalar case because scalar multiplications are commutative. On the one hand, the *individual* off-diagonal elements of the normal product are not necessarily symmetric in time, which can be seen in Eq. 5.5.22 and in Fig. 5.12. Thus, the matrices, $\mathbf{M}$ and

$\mathbf{M}^*$, generate different normal products, $\mathbf{M}\mathbf{M}^\dagger$ and $\left(\mathbf{M}\mathbf{M}^\dagger\right)^*$, respectively. On the other hand, one may expect a freedom of applying a complex-conjugate transpose. Nevertheless, the matrices, $\mathbf{M}$ and $\mathbf{M}^\dagger$, also lead to different normal products, $\mathbf{M}\mathbf{M}^\dagger$ and $\mathbf{M}^\dagger\mathbf{M}$, respectively (see Eq. 5.5.17).

■ 5.5.4 Minimum-phase matrix factorization

In this section, we discuss the factorization of a normal product, $\mathbf{M}\mathbf{M}^\dagger$, with a minimum-phase constraint. First, we will attempt to constrain the above-discussed degrees of freedom. Second, we will analyze a factorization method by *Tunnicliffe-Wilson* [1972].

Constrain degrees of freedom

Initially, we aimed to constrain the degrees of freedom that are associated with normal product factorization (see Eq. 5.5.25). This strategy starts with the eigenvalue decomposition of the normal product,

$$\mathbf{M}\mathbf{M}^\dagger = \mathbf{Q}\boldsymbol{\Lambda}\mathbf{Q}^\dagger. \tag{5.5.28}$$

By taking the principle square-root of the eigenvalues, we find a factorization solution,

$$\tilde{\mathbf{M}} = \mathbf{Q}\boldsymbol{\Lambda}^{\frac{1}{2}}\mathbf{Q}^\dagger. \tag{5.5.29}$$

However, the solution, $\tilde{\mathbf{M}}$, is not necessarily the desired one, and it does not necessarily possess a minimum-phase property. To map the solution, $\tilde{\mathbf{M}}$, onto the desired one, $\mathbf{M}$, the degrees of freedom, SU(2) and U(1), must be retrieved (see Eq. 5.5.25),

$$\mathbf{M} = \tilde{\mathbf{M}}\mathrm{SU}(2)\mathrm{U}(1) = \tilde{\mathbf{M}}\mathrm{SU}(2)\mathrm{e}^{\mathrm{i}\phi}. \tag{5.5.30}$$

We proceed by assuming that the desired solution, $\mathbf{M}$, possesses a minimum-phase property. For this purpose, we evaluate the determinant of Eq. 5.5.30,

$$\det(\mathbf{M}) = \det(\tilde{\mathbf{M}})\mathrm{e}^{2\mathrm{i}\phi}. \tag{5.5.31}$$

Next, we evaluate the phase spectrum of the above equation. The phase of the determinant, $\det(\mathbf{M})$, can be determined via the Kolmogorov relation (see Eq. 5.5.8),

$$\mathrm{Arg}\left[\det(\mathbf{M})\right] = -\mathscr{H}\left[\log\left(|\det(\mathbf{M})|\right)\right]. \tag{5.5.32}$$

The phase of the right-hand side of Eq. 5.5.31 can be written as,

$$\mathrm{Arg}\left[\det(\tilde{\mathbf{M}})\mathrm{e}^{2\mathrm{i}\phi}\right] = \mathrm{Arg}\left[\det(\tilde{\mathbf{M}})\right] + 2\phi. \tag{5.5.33}$$

By equating Eqs. 5.5.32 and 5.5.33, and by using the identity,

$$|\det(\mathbf{M})| = |\det(\mathbf{M}\mathbf{M}^\dagger)|^{\frac{1}{2}}, \tag{5.5.34}$$

we obtain,

$$\phi = -\frac{1}{2}\left(\mathscr{H}\left[\log\left(|\det(\mathbf{M}\mathbf{M}^{\dagger})|^{\frac{1}{2}}\right)\right] + \operatorname{Arg}\left[\det(\tilde{\mathbf{M}})\right]\right). \tag{5.5.35}$$

Unfortunately, the above strategy is insufficient to fully constrain the normal product factorization. The minimum-phase constraint of the determinant provides only one equation, namely the Kolmogorov relation. Hence, this constraint does not allow to further reduce the degrees of freedom, and three free parameters contained by the SU(2) element remain unknown. Due to this limitation, we seek for an alternative method, which is discussed in the following.

Wilson factorization

As mentioned in the scalar section, the Wilson factorization method (see Eq. 5.4.22) can be generalized to matrices. The generalized Wilson algorithm can be written as,

$$\mathbf{M}_{n+1} = \mathbf{M}_n \mathbf{\Theta}\left[\mathbf{I} + (\mathbf{M}_n)^{-1}\mathbf{M}\mathbf{M}^{\dagger}\left(\mathbf{M}_n^{\dagger}\right)^{-1}\right], \tag{5.5.36}$$

with $\mathbf{M}_0 = \mathbf{I}$ [details can be found in *Tunnicliffe-Wilson*, 1972]. Here, the function, $\mathbf{\Theta}$, element-wise mutes acausal events and scales the time-zero components of the diagonal elements by $\frac{1}{2}$. This scaling can be seen as a termination condition that ensures that the recursion converges, i.e. for, $\mathbf{M}_n = \mathbf{M}$, the solution is not updated,

$$\begin{aligned}\mathbf{M}_{n+1} &= \mathbf{M}_n \mathbf{\Theta}\left[\mathbf{I} + (\mathbf{M}_n)^{-1}\mathbf{M}\mathbf{M}^{\dagger}\left(\mathbf{M}_n^{\dagger}\right)^{-1}\right] \\ &= \mathbf{M}_n \mathbf{\Theta}\left[2\mathbf{I}\right] = \mathbf{M}_n.\end{aligned} \tag{5.5.37}$$

We wish to use the Wilson algorithm for the retrieval the back-propagated focusing functions, $\mathbf{V}_d^+$ and $\mathbf{V}^+$, from their respective normal products. In particular, we are interested in retrieving the function, $\mathbf{V}_d^+$, because it is equal to the focusing function, $\mathbf{F}_1^+$, up to a direct transmission (see Eq. 5.5.14). Hence, retrieving the field, $\mathbf{V}_d^+$, would allow us to proceed with the Marchenko redatuming strategy presented in chapter 4 of this thesis (assuming that the direct transmission can be estimated). For our purposes, the retrieval of the field, $\mathbf{V}^+$, is less interesting because it can already be obtained by the Marchenko method [see *Reinicke*, 2020, chapter 4 of this thesis]. Interestingly, the Wilson algorithm appears to perfectly reconstruct the field, $\mathbf{V}^+$, whereas the reconstruction of the field $\mathbf{V}_d^+$ remains imperfect. Thus, we firstly analyze the Wilson algorithm for the field $\mathbf{V}^+$, and secondly show our best result of reconstructing the field $\mathbf{V}_d^+$.

We consider the back-propagated focusing function $\mathbf{V}^+$ (see Fig. 5.9) and its normal product $\mathbf{V}^+\left(\mathbf{V}^+\right)^{\dagger}$ (see Fig. 5.15). To use the Wilson algorithm (see Eq. 5.5.36), an explicit definition of the mute, $\mathbf{\Theta}$, is required. The diagonal elements of the mute, $\mathbf{\Theta}$, can be easily defined by the Heaviside function (see Eq. 5.4.21),

$$\Theta_{pp}(t) = \Theta_{ss}(t) = \mathrm{H}(t), \tag{5.5.38}$$

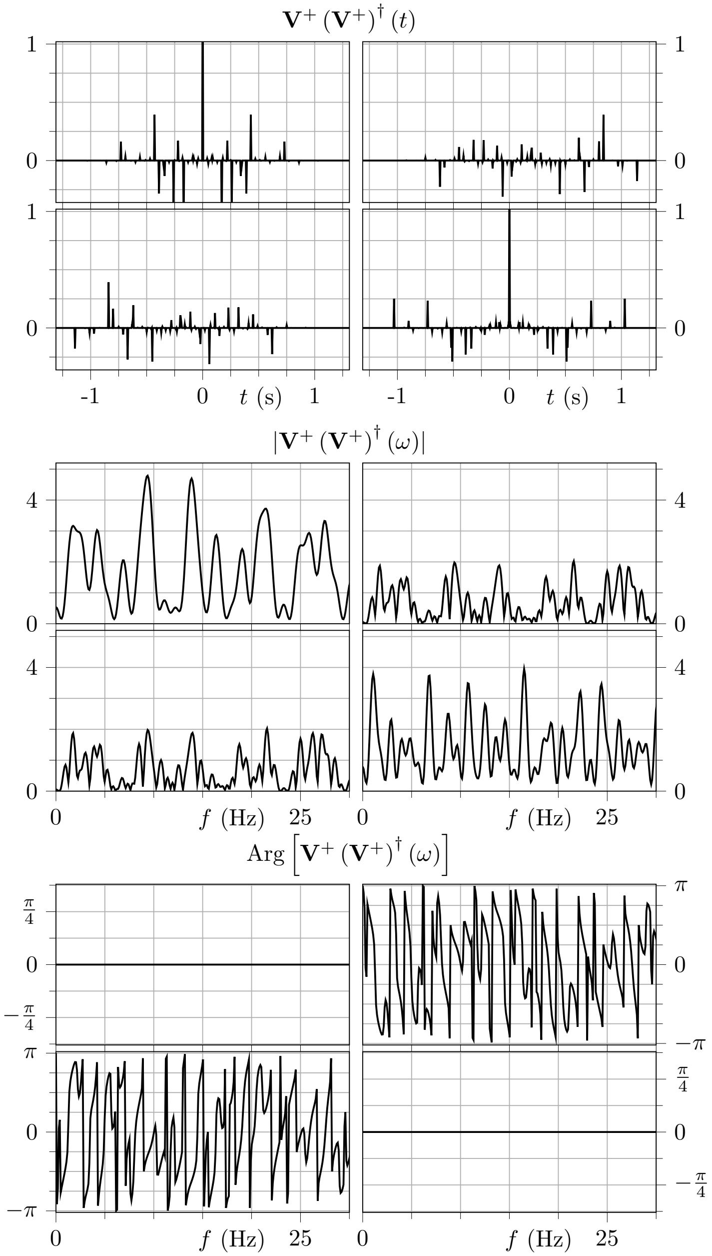

__Figure 5.15:__ Normal product, $\mathbf{V}^+ \left(\mathbf{V}^+\right)^\dagger$, of the back-propagated focusing function shown in Fig. 5.9. The panels are arranged analogously to Fig. 5.9.

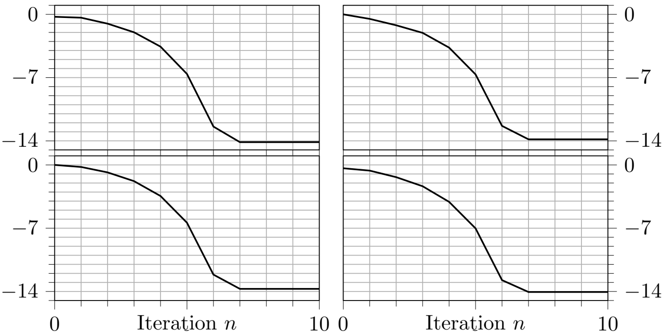

Figure 5.16: *Relative error of the retrieved field* $\mathbf{V}_n^+$ *as a function of the iteration number n. Each panel is associated with an elastic component xy and shows the relative error,* $\log_{10}\left(\frac{\|V^+_{xy,n}-V^+_{xy}\|_2}{\|V^+_{xy}\|_2}\right)$.

because the diagonal elements of the back-propagated focusing function are strictly causal. Moreover, the Heaviside function accounts for the scaling of the diagonal time-zero components by $\frac{1}{2}$, which is the aforementioned termination condition. For the off-diagonal elements, we define the mute such that events prior to the first arrival are muted,

$$\Theta_{ps}(t) = \begin{cases} 1, & t \geq t_{ps}, \\ 0, & t < t_{ps}, \end{cases} \tag{5.5.39}$$

and,

$$\Theta_{sp}(t) = \begin{cases} 1, & t \geq t_{sp}, \\ 0, & t < t_{sp}. \end{cases} \tag{5.5.40}$$

Note that the off-diagonals of the mute do no contain the scaling factor, $\frac{1}{2}$, because the aforementioned termination condition only affects the diagonals. The times, t_{ps} and t_{sp}, denote the travel times associated with the first event of the fields, V_{ps}^+ and V_{sp}^+, respectively [more details on the onset times t_{ps} and t_{sp} can be found in chapter 4 of this thesis, *Reinicke*, 2020]. Using the mute $\mathbf{\Theta}$, we retrieve the back-propagated focusing function according to Eq. 5.5.36. The convergence diagram (see Fig. 5.16) demonstrates that, after only seven iterations, the Wilson-factorization retrieves the correct solution, $\mathbf{V}^+$, within machine precision (for an illustration of $\mathbf{V}^+$ we refer to Fig. 5.9 which shows its modeled version).

Next, we attempt to factorize the normal product, $\mathbf{V}_d^+ \left(\mathbf{V}_d^+\right)^\dagger$. As shown in Fig. 5.7, the element $V_{d,pp}^+$ contains acausal events (see black circle), which leads to a new problem. One approach could be to define the *pp* component of the mute $\mathbf{\Theta}$ such that some acausal events are preserved, while its time-zero component still applies the scaling factor $\frac{1}{2}$ as a termination condition,

$$\Theta_{pp}(t) = \begin{cases} 1, & t \geq t_{pp} \text{ and } t \neq 0, \\ \frac{1}{2}, & t = 0, \\ 0, & t < t_{pp}. \end{cases} \tag{5.5.41}$$

Here, t_{pp} refers to the arrival time of the first event in $V^+_{d,pp}$ (see circle in Fig. 5.7). Unfortunately, with this mute the recursive evaluation of Eq. 5.5.36 diverges (no figure shown).

Hence, we modify our strategy. By applying another linear phase-shift, we obtain a field, $\tilde{\mathbf{V}}^+_d$, with strictly causal diagonal elements,

$$\tilde{\mathbf{V}}^+_d = \mathbf{V}^+_d \begin{pmatrix} \mathrm{e}^{-\mathrm{i}\omega t_{pp}} & 0 \\ 0 & 1 \end{pmatrix}. \tag{5.5.42}$$

Note that, this linear phase-shift cancels in the normal product,

$$\tilde{\mathbf{V}}^+_d \left(\tilde{\mathbf{V}}^+_d\right)^\dagger = \mathbf{V}^+_d \left(\mathbf{V}^+_d\right)^\dagger, \tag{5.5.43}$$

and could be easily included in the definition of the field $\mathbf{V}^+_d$ in Eq. 5.5.14. Subsequently, the mute $\boldsymbol{\Theta}$ can be defined analogously to Eqs. 5.5.38-5.5.40, where the times, t_{ps} and t_{sp}, are now defined by the first event of $\tilde{V}^+_{d,ps}$ and $\tilde{V}^+_{d,sp}$, respectively. A comparison between the retrieved result $\tilde{\mathbf{V}}^+_d$ and the desired solution $\mathbf{V}^+_d$ is shown in Fig. 5.17. According to Eq. 5.5.42, one would expect to observe a linear phase-shift between the fields $\tilde{\mathbf{V}}^+_d$ and $\mathbf{V}^+_d$. Although the Wilson algorithm does not reconstruct this phase-shift, the retrieved solution, $\tilde{\mathbf{V}}^+_d$, is nearly identical to the desired one, $\mathbf{V}^+_d$. The strongest artifacts are due to early events that are erroneously suppressed by the mute $\boldsymbol{\Theta}$ (see grey areas in Fig. 5.17).

Finally, we inspect the error of the above experiment. The relative error between the retrieved and desired fields is dominated by small artifacts (see Fig. 5.18). Nevertheless, the determinant is reconstructed accurately (see Fig. 5.18). Even if we simplified the off-diagonal mutes to,

$$\Theta_{ps}(t) = \Theta_{sp}(t) = \begin{cases} 1, & t \geq 0, \\ 0, & t < 0, \end{cases} \tag{5.5.44}$$

the correct determinant is retrieved (not shown). Hence, in both cases, the retrieved solutions, $\tilde{\mathbf{V}}^+_{d,1}$ (first experiment) and $\tilde{\mathbf{V}}^+_{d,2}$ (second experiment), can be mapped onto the desired one, $\mathbf{V}^+_d$, by multiplication with a residual SU(2) element. We determine these SU(2) elements by deconvolution,

$$\tilde{\mathbf{S}}_1 = \left(\tilde{\mathbf{V}}^+_{d,1}\right)^{-1} \mathbf{V}^+_d, \tag{5.5.45}$$

$$\tilde{\mathbf{S}}_2 = \left(\tilde{\mathbf{V}}^+_{d,2}\right)^{-1} \mathbf{V}^+_d. \tag{5.5.46}$$

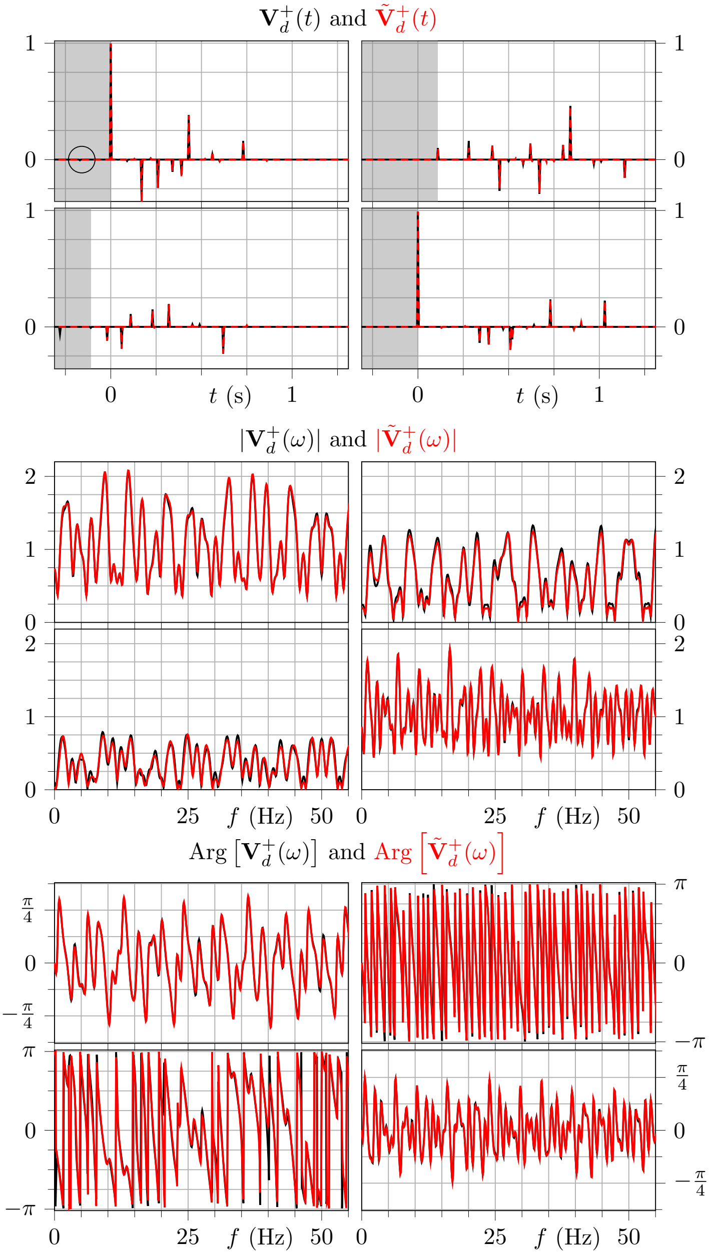

Figure 5.17: *Modeled back-propagated focusing function* $\mathbf{V}_d^+$ *(black) and retrieved field* $\tilde{\mathbf{V}}_d^+$ *(red). The panels are arranged analogously to Fig. 5.9. In the time-domain panels, grey areas indicate times that are muted during the retrieval of the field* $\tilde{\mathbf{V}}_d^+$*.*

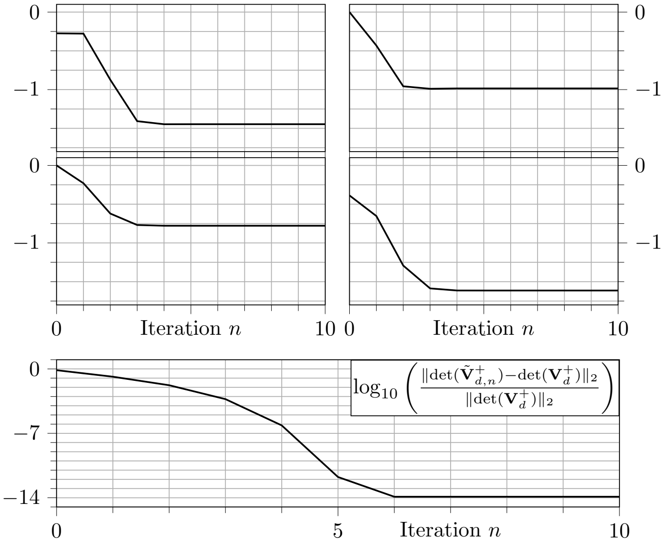

Figure 5.18: *Top two rows: Idem as Fig. 5.16 but for the relative error of the retrieved field* $\tilde{\mathbf{V}}^{+}_{d,n}$ *in comparison to the desired solution* $\mathbf{V}^{+}_{d}$. *Bottom row: Relative error of the determinant,* $\det(\tilde{\mathbf{V}}^{+}_{d,n})$, *in comparison to the desired one,* $\det(\mathbf{V}^{+}_{d})$.

Fig. 5.19 shows that the residual SU(2) elements, $\tilde{\mathbf{S}}_1$ and $\tilde{\mathbf{S}}_2$, are close to an identity matrix. For the first experiment, the deviation of the residual SU(2) element from an identity is smaller than for the second experiment. This observation suggests that the more specific mute in the first experiment helped to better constrain the solution.

5.6 Discussion, conclusions and outlook

We discussed minimum-phase behavior. This property imposes several constraints that could be used e.g. in a range of inverse problems such as the retrieval of a focusing function. Hence, we set out to review this property for scalars and started to explore the multi-dimensional situation. For this purpose, we reviewed developments from other research fields, in particular from control-theory, and tried to adopt them for geophysics.

We demonstrated that minimum-phase behavior is not limited to scalar functions but can be generalized to matrices. To this end, we analyzed various properties such as the matrix elements, singular values, eigenvalues and determinants. In special cases, the minimum-phase property of a matrix is reflected by its individual eigenvalues [e.g. for transmissions of layered acoustic media, as in *Wapenaar et al.*, 2003; *Elison et al.*, 2020]. However, in general, only the determinant of a matrix is characteristic for its minimum-phase behavior. On the one hand, this result

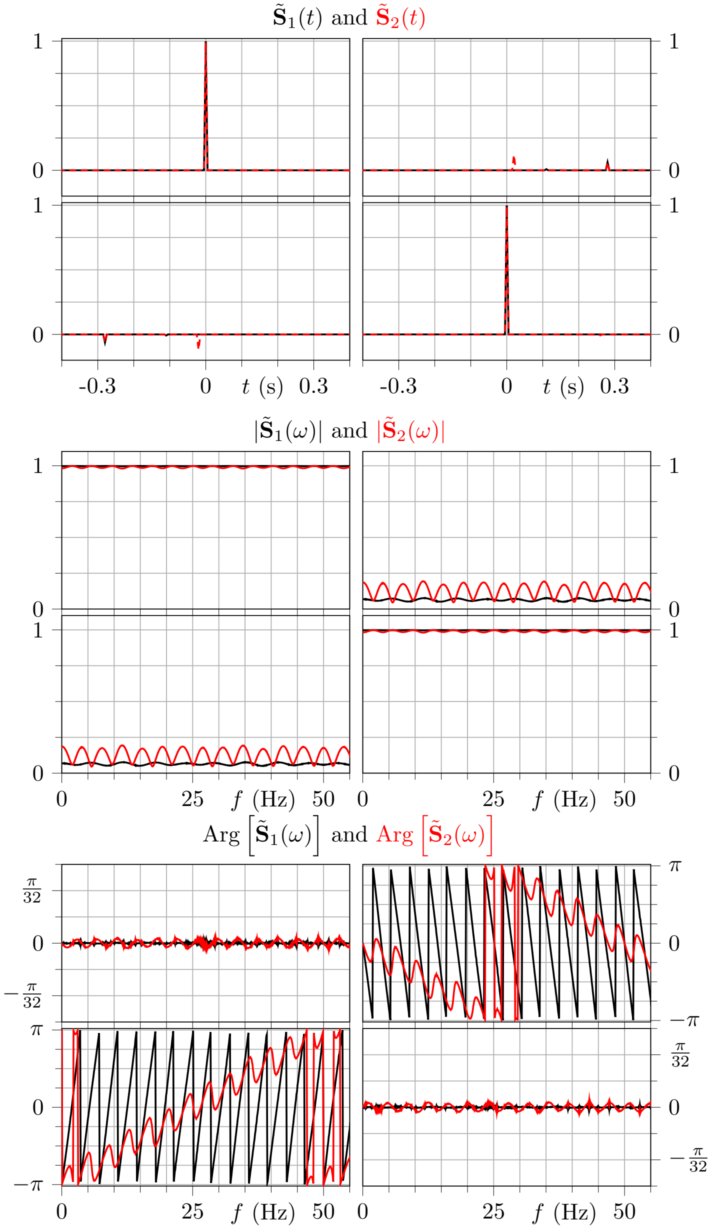

Figure 5.19: *Residual* $\mathrm{SU}(2)$ *elements of the retrieved fields* $\mathbf{V}^{+}_{d,1}$ *(black) and* $\mathbf{V}^{+}_{d,2}$ *(red). The panels are arranged as in Fig. 5.17, which shows the field* $\mathbf{V}^{+}_{d,1}$.

is desirable because it makes the minimum-phase property basis-invariant. On the other hand, a minimum-phase determinant can be associated with countless different matrices. Hence, a minimum-phase determinant describes a "group" of minimum-phase matrices, rather than a single matrix.

This chapter is motivated by the retrieval of a focusing function, $\mathbf{F}_1^+$. In particular, we are interested in exploiting properties of the focusing function as additional constraint to proceed with the Marchenko redatuming strategy presented in chapter 4 of this thesis. Hence, it has been crucial to verify that (beyond the scalar case) the focusing function, as an inverse transmission response, possesses a minimum-phase property, up to back-propagation.

Furthermore, we investigated the factorization of a normal product with a minimum-phase constraint. In particular, we inspected the Wilson algorithm. We observed that, in some cases, this method perfectly reconstructs the desired minimum-phase matrix. Nevertheless, in other cases, the Wilson algorithm reconstructs a minimum-phase matrix, but not the desired one: The desired matrix was reconstructed up to an SU(2) element. It appears that the Wilson algorithm favors minimum-phase matrices that have minimum-phase diagonal elements. However, the latter statement is based on our observations but has not been proven. Moreover, we observed that the residual SU(2) elements are close to identities. Hence, the Wilson factorization may be suitable to approximate the focusing function $\mathbf{F}_1^+$.

We will continue this research project in the future. Apart from investigating fundamental properties of minimum-phase objects, we also intend to consider practical aspects such as band-limitation. Despite the remaining challenges, we believe that minimum-phase behavior has the potential to be used as a powerful tool for signal processing.

6

Impact of mode conversions on structural imaging with Marchenko multiple-elimination in geological settings akin to the Middle East

There is always a gap between theory and practice.

Claerbout, 1985.

Abstract The reflection response of elastic media with strong contrasts contains numerous events due to mode conversions and multiple scattering. Correct handling of strong elastic internal multiples is believed to be important for structural imaging. However, applications of elastic internal multiple-elimination methods, e.g. Marchenko-equation-type methods, are currently limited by unsolved theoretical challenges. In contrast, the acoustic theory is significantly easier to implement and relies on realistically-achievable preprocessing requirements. Therefore, it is desirable to identify relevant geological settings, where acoustic multiple-elimination can suffice. Here, we consider geological environments akin to the Middle East, where internal multiples remain a significant challenge, and analyze marine data because only the acoustic component is measured. Similar strategies have already been applied in existing field data examples, nevertheless, it remains unclear whether the resulting images are reliable. For this purpose, we build a synthetic model based on regional well-log data and geological understanding. The synthetic model allows us to model reflection responses with, and without, elastic scattering effects. Next, we apply the acoustic Marchenko multiple-elimination method, migrate the

---

This chapter is in preparation for publication.

results and compare the images between each other, and against a reference. This analysis demonstrates that, for the considered geology, mode conversions only have a minor effect on structural images retrieved via the acoustic Marchenko multiple-elimination method. Moreover, this synthetic study allows us to analyze the nature of internal multiples in comparable geological settings. Note that our conclusions are expected to be model-dependent.

6.1 Introduction

Internal multiples can generate undesired, highly complex, interference patterns, which become worse in the presence of strong elastic effects and can create severe imaging artifacts. Two regions where elastic multiples remain a major challenge are offshore Brazil and the Middle East [*El-Emam et al.*, 2011]. In both regions, the imaging targets are buried under complex overburdens. This is a challenge for multiple prediction methods [e.g. *Jakubowicz*, 1998], that identify individual multiple generators to predict and adaptively subtract multiples: for example, a primary could have the same kinematics as a predicted multiple, such that the primary would be erroneously subtracted. In contrast to predicting and adaptively subtracting multiples, Marchenko-equation-based multiple-elimination methods retrieve an inverse transmission through an entire overburden by solving an inverse problem [e.g. *Wapenaar et al.*, 2014a; *van der Neut and Wapenaar*, 2016; *Dukalski and de Vos*, 2017], i.e. there is no need for adaptive subtraction.

This advantage of Marchenko-type multiple-elimination methods relies on correct scaling of the reflection response. Hence, accurate data preprocessing is essential for Marchenko-type multiple-elimination methods, e.g. wavelet estimation, surface-related multiple elimination, etc. These requirements remain challenging for land seismics but can be accomplished for streamer (or other marine) data, provided the crossline spacing is sufficiently small. Note that such streamer-like acquisitions form a special case because the water layer acts as a filter that only allows for measurements associated with pressure sources and receivers. Nevertheless, the recorded data carries the imprint of elastic scattering inside the Earth.

The elastodynamic extension of Marchenko-type methods, alike other wave-equation based multiple-elimination methods [e.g. the elastic inverse scattering series, *Coates and Weglein*, 1996], relies on, (i) the availability of all components of the reflection response and, (ii) monotonicity assumptions, i.e. "correct" temporal ordering of events. Firstly, the requirement (i) is naturally violated for streamer data, which only measures one out of nine elastic components. So far, the effect of applying the Marchenko multiple-elimination method using an incomplete reflection response remains unexplored (an example can be found in Appendix A). Secondly, the monotonicity assumption (ii) often holds for acoustic waves but can be violated much easier in the elastic case due to propagation speed differences between elastic modes [*Sun and Innanen*, 2019; *Reinicke*, 2020, chapter 4 of this thesis].

In view of the theoretical challenges encountered by the elastic Marchenko method, we suggest to apply the *acoustic* Marchenko multiple-elimination method to *elastic* data. This approach can be seen as a hybrid Marchenko strategy and has already been followed in existing field data examples [e.g. *Ravasi et al.*, 2016; *Staring et al.*, 2018]. However, are the results trustworthy? The answer to this question is medium-dependent: for approximately horizontally-layered media, there are strong arguments supporting the hybrid strategy. Firstly, due to speed differences between modes, events associated with shear waves (S) tend to have lower apparent velocities than unconverted compressional waves (P). Therefore, events associated with S-waves tend to have steeper dips in the space-time domain and will be partially attenuated by wavenumber-frequency filtering, which is a necessary preprocessing step. Secondly, elastic effects only appear gradually with increasing angle of incidence, i.e. in nearly horizontally-layered media, elastic effects are minor for short-offset recordings. Further, since migration boosts the recordings that are consistent with the velocity model (in our case the P-wave velocity), events associated with conversions to S-waves are attenuated. Therefore, the aforementioned hybrid Marchenko strategy may be suitable for structural imaging but may not prove sufficiently reliable for AVO analysis.

The Middle Eastern geology, unlike the geology offshore Brazil, is characterized by dense, nearly-horizontal, layering with strong elastic contrasts, which makes it a promising candidate to inspect the hybrid Marchenko multiple-elimination strategy. For this analysis, we construct a synthetic Middle East model based on regional log data (P- and S-wave velocities as well as density) and geological understanding. The model is designed to be as close to reality as possible and contains several features that are characteristic to the region, e.g. a distinctive velocity inversion [*Christian*, 1997]. To a large extent, our observations are in agreement with those of a parallel study on field data from the same region (parallel project carried out by Staring et al.), which demonstrates the relevance of our analysis in practice. Since this field data example will be published independently, it is not discussed in this chapter . Further, using a synthetic model gives us control over the shear wave velocity, $c_s \neq 0$ or $c_s = 0$, and thus, allows us to model reflection responses with and without elastic effects, respectively. Both, i.e. acoustic and elastic, reflection responses are used as inputs for an acoustic Marchenko multiple-elimination method. The respective results are compared between each other, and against a reference.

The structure of this chapter is as follows. Firstly, we summarize the theory of the back-propagated Marchenko multiple-elimination method. Secondly, we explain how the synthetic model is built and compare the acoustic with the elastic reflection responses. Finally, the reflection responses are used to retrieve Marchenko multiple-elimination results, which are analyzed in the data domain as well as in the image domain.

6.2 Method

In this section, we outline the key steps of the elastic *back-propagated* Marchenko scheme [for details see *van der Neut and Wapenaar*, 2016; *Elison*, 2019; *Reinicke*, 2020, chapter 4 of this thesis]. This back-propagated scheme is advantageous because it does not require an estimate of waves that forward-scatter from the acquisition to the redatuming level. Hence, there is no need for prior model information. Further, we discuss the special case of an elastic reflection response recorded in an acoustic layer (water).

6.2.1 Elastic back-propagated Marchenko multiple-elimination theory

We consider 3D laterally-varying elastic media and describe wavefields as functions of time, t, and space, $\mathbf{x}_j = (x, y, z_j)$. Here, we use subscripts to refer to the z-

coordinate. We assume that the z-axis is pointing downward.

For the ease of the derivation, we assume source- and receiver-side decomposed one-way wavefields [*Frasier*, 1970; *Ursin*, 1983]. In this chapter, we consider the wavefield normalization defined by *Wapenaar and Berkhout* [1989, see chapter IV]. Nevertheless, the derived expressions also hold for flux-normalized fields (see appendix B). We organize the one-way wavefields in 3 × 3 matrices,

$$\mathbf{P}(\mathbf{x},\mathbf{x}',t) = \begin{pmatrix} P_{P,P} & P_{P,S1} & P_{P,S2} \\ P_{S1,P} & P_{S1,S1} & P_{S1,S2} \\ P_{S2,P} & P_{S2,S1} & P_{S2,S2} \end{pmatrix} (\mathbf{x},\mathbf{x}',t), \tag{6.2.1}$$

where the subscripts denote P, S1 and S2 wavefield potentials. The first and second subscripts are associated with the wavefield potentials on the source- and receiver-side, respectively. Hence, all matrix operations in this chapter are associated with matrices in P- and S-wave (P-S) space. The first and second coordinates, $\mathbf{x}$ and $\mathbf{x}'$, denote the receiver and source coordinates, respectively.

The reflection response $\mathbf{R}(\mathbf{x}_0,\mathbf{x}_0',t)$ to a downward radiating source is recorded as an upgoing field on the reflection-free surface z_0 at the top of the medium (just above the source).

Next, we define a *target reflection response* $\mathbf{R}_{tar}(\mathbf{x}_0,\mathbf{x}_0',t)$ recorded at z_0. This response propagates multiple-free through the overburden, and is corrected for overburden-related transmission losses but contains all wavefield interactions with the target. This response can be obtained from so-called back-propagated Green's functions $\mathbf{U}^{-,\pm}(\mathbf{x}_0,\mathbf{x}_0',t)$ [defined in *Reinicke*, 2020, chapter 4 of this thesis] via an *Amundsen* [2001] deconvolution,

$$\mathbf{U}^{-,+}(\mathbf{x}_0,\mathbf{x}_0',\omega) = -\int_{\partial\mathbb{D}_0} \mathbf{U}^{-,-}(\mathbf{x}_0,\mathbf{x}_0'',\omega)\mathbf{R}_{tar}(\mathbf{x}_0'',\mathbf{x}_0',\omega)\mathrm{d}^2\mathbf{x}_0''. \tag{6.2.2}$$

We formulate the above expression per angular frequency ω [*Noether*, 1918]. For an arbitrary field, $\mathbf{P}(\mathbf{x},\mathbf{x}',t)$, the mutual relation between the time and frequency domains is given by the temporal Fourier transformation,

$$\mathbf{P}(\mathbf{x},\mathbf{x}',\omega) = \int_{-\infty}^{\infty} \mathbf{P}(\mathbf{x},\mathbf{x}',t)\mathrm{e}^{\mathrm{i}\omega t}\mathrm{d}t, \tag{6.2.3}$$

with $\mathrm{i}^2 = -1$. In the special case of acoustic media, Eq. 6.2.2 is often rearranged [e.g. compare to Eq. 32 in *van der Neut and Wapenaar*, 2016; *Elison*, 2019]. The rearrangement involves source-receiver reciprocity of Green's functions (which are used to construct the $\mathbf{U}^{-,\pm}(\mathbf{x}_0,\mathbf{x}_0',\omega)$ fields) and commutation of multiplications. The latter rearrangement is not possible in the general elastic case, where each quantity is a matrix in P-S space.

The back-propagated Green's functions $\mathbf{U}^{-,\pm}(\mathbf{x}_0,\mathbf{x}_0',\omega)$ are constrained by reciprocity relations, which form an inverse problem. Together with the reflection response $\mathbf{R}(\mathbf{x}_0,\mathbf{x}_0',\omega)$ and so-called back-propagated focusing functions $\mathbf{V}^{\pm}(\mathbf{x}_0,\mathbf{x}_0',\omega)$, the fields $\mathbf{U}^{-,\pm}(\mathbf{x}_0,\mathbf{x}_0',\omega)$ satisfy the convolution- and correlation-type representation theorems [*van der Neut and Wapenaar*, 2016; *Elison*, 2019; *Reinicke*, 2020, chapter 4 of this thesis],

$$\mathbf{U}^{-,+}(\mathbf{x}_0,\mathbf{x}_0',\omega)+\mathbf{V}^{-}(\mathbf{x}_0,\mathbf{x}_0',\omega)=\int_{\partial\mathbb{D}_0}\mathbf{R}(\mathbf{x}_0,\mathbf{x}_0'',\omega)\mathbf{V}^{+}(\mathbf{x}_0'',\mathbf{x}_0',\omega)\mathrm{d}^2\mathbf{x}_0'', \quad (6.2.4)$$

and,

$$\left(\mathbf{U}^{-,-}\right)^{*}(\mathbf{x}_0,\mathbf{x}_0',\omega)+\mathbf{V}^{+}(\mathbf{x}_0,\mathbf{x}_0',\omega)=\int_{\partial\mathbb{D}_0}\mathbf{R}^{*}(\mathbf{x}_0,\mathbf{x}_0'',\omega)\mathbf{V}^{-}(\mathbf{x}_0'',\mathbf{x}_0',\omega)\mathrm{d}^2\mathbf{x}_0''. \quad (6.2.5)$$

The latter expression excludes evanescent waves on the boundaries of the overburden, $\partial\mathbb{D}_0$ and $\partial\mathbb{D}_i$ (overburden and target are separated by $\partial\mathbb{D}_i$), and the superscript "$*$" denotes complex-conjugation.

The Marchenko method retrieves the back-propagated Green's functions $\mathbf{U}^{-,\pm}(\mathbf{x}_0, \mathbf{x}_0',\omega)$ by solving the inverse problem formed by Eqs. 6.2.4 and 6.2.5. By applying temporal mutes $\mathbf{\Theta}^{\pm}(\mathbf{x}_0,\mathbf{x}_0',t)$, which act matrix element-wise, the representation theorems can be rewritten as,

$$\boldsymbol{\chi}_{-}+\mathbf{V}^{-}=\mathbf{\Theta}^{-}\left[\mathbf{R}\mathbf{V}^{+}\right], \quad (6.2.6)$$

$$\boldsymbol{\chi}_{+}+\mathbf{V}^{+}=\mathbf{\Theta}^{+}\left[\mathbf{R}^{*}\mathbf{V}^{-}\right], \quad (6.2.7)$$

where we use a detail-hiding notation that omits coordinates and integrals. Eqs. 6.2.6 and 6.2.7 together resemble a pair of coupled Marchenko equations that can be solved for $\mathbf{V}^{+}$,

$$\mathbf{V}^{+}=\sum_{k=0}^{\infty}\mathbf{\Xi}_k, \text{ with, } \mathbf{\Xi}_k=\mathbf{\Theta}^{+}\left[\mathbf{R}^{*}\mathbf{\Theta}^{-}\left[\mathbf{R}\mathbf{\Xi}_{k-1}\right]\right], \quad (6.2.8)$$

and $\mathbf{\Xi}_0=-\boldsymbol{\chi}_{+}-\mathbf{\Theta}^{+}\left[\mathbf{R}^{*}\boldsymbol{\chi}_{-}\right]$. To proceed, it is assumed that the overlap $\boldsymbol{\chi}_{-}$ vanishes, which holds conditionally [see *Reinicke*, 2020, chapter 4 of this thesis], and appears to be a sufficiently good approximation for the later presented experiment. The remaining overlap $\boldsymbol{\chi}_{+}$ can be approximated with an identity $\mathbf{\Xi}_0(\mathbf{x}_0'',\mathbf{x}_0',\omega)\approx -\mathbf{I}\delta(\mathbf{x}_0''-\mathbf{x}_0')$. In practice, the identity is spatio-temporally band-limited such that short-period multiples lead to an erroneous solution when evaluating Eq. 6.2.8. Although not implemented here, there is a strategy to correct for the short-period multiple error, by constraining the solutions $\mathbf{V}^{\pm}$ with energy conservation and the minimum-phase property of $\mathbf{V}^{+}$. So far, the short-period multiple strategy has been developed for up to 2D acoustic media with horizontally-layered overburdens [*Dukalski et al.*, 2019; *Elison*, 2019]. Finally, the remaining unknowns, $\mathbf{V}^{-}$ and $\mathbf{U}^{-,\pm}$, can be retrieved using Eqs. 6.2.4-6.2.6.

Next, we present a Marchenko double de-reverberation approach as alternative to solving Eq. 6.2.2 for the target reflection response $\mathbf{R}_{tar}$. Marchenko double de-reverberation circumvents the deconvolution of the fields, $\mathbf{U}^{-,\pm}$, which can become computationally expensive for large datasets and may not always be stable, e.g.

due to band-limitation of the fields $\mathbf{U}^{-,\pm}$. The elastodynamic extension of the Marchenko double de-reverberation method by *Staring et al.* [2018] can be written as,

$$\mathbf{R}_{tar}^{(ddr)}(\mathbf{x}_0,\mathbf{x}_0',\omega) = \int_{\partial\mathbb{D}_0} \left(\mathbf{V}^+(\mathbf{x}_0'',\mathbf{x}_0,\omega)\right)^{\mathrm{T}} \mathbf{U}^{-,+}(\mathbf{x}_0'',\mathbf{x}_0',\omega)\mathrm{d}^2\mathbf{x}_0''. \qquad (6.2.9)$$

To illustrate the term double de-reverberation, we replace the field $\mathbf{U}^{-,+}(\mathbf{x}_0'',\mathbf{x}_0',\omega)$ by Eq. 6.2.4,

$$\mathbf{R}_{tar}^{(ddr)} = \left(\mathbf{V}^+\right)^{\mathrm{T}}\mathbf{R}\mathbf{V}^+ - \left(\mathbf{V}^+\right)^{\mathrm{T}}\mathbf{V}^-. \qquad (6.2.10)$$

This expression shows that the back-propagated focusing function, $\mathbf{V}^+$, is applied on the receiver- and on the source-side of the reflection response, $\mathbf{R}$. Marchenko double de-reverberation removes multiples generated inside the overburden, but does not attenuate multiples generated between overburden and target. Hence, this approach can be seen as an approximation of the aforementioned deconvolution. In case of band-limited fields, the result $\mathbf{R}_{tar}^{(ddr)}$ has to be deconvolved with the wavelet of the initial estimate $\boldsymbol{\chi}_+$ to avoid double band-limitation.

The retrieved target reflection responses, $\mathbf{R}_{tar}$ and $\mathbf{R}_{tar}^{(ddr)}$, as well as the reflection response, $\mathbf{R}$, are scaled differently (not only a global scaling difference). Therefore, it is difficult to analyze the difference between the aforementioned responses. However, in case of Marchenko double de-reverberation, the multiple predictions can be represented explicitly. For this purpose, we expand the backprojected focusing function,

$$\mathbf{V}^+ = \boldsymbol{\chi}_+ + \mathbf{V}_{coda}^+, \qquad (6.2.11)$$

and use Eq. 6.2.4 as well as the mute $\boldsymbol{\Theta}^-$ to substitute the backprojected Green's function,

$$\mathbf{U}^{-,+} = \boldsymbol{\chi}_- + \left(1 - \boldsymbol{\Theta}^-\right)\left[\mathbf{R}\mathbf{V}^+\right]. \qquad (6.2.12)$$

We assume $\boldsymbol{\chi}_+ = \mathbf{I}\delta(\mathbf{x}_0''-\mathbf{x}_0')$ as well as $\boldsymbol{\chi}_- = \mathbf{O}$ (same assumptions as above) and use Eqs. 6.2.11-6.2.12 to rewrite Eq. 6.2.9 (omitting $\delta(\mathbf{x}_0''-\mathbf{x}_0')$ for notational convenience),

$$\begin{aligned}\mathbf{R}_{tar}^{(ddr)} = \;& \mathbf{I}\left(1-\boldsymbol{\Theta}^-\right)[\mathbf{R}\mathbf{I}] \\ & + \mathbf{I}\left(1-\boldsymbol{\Theta}^-\right)\left[\mathbf{R}\mathbf{V}_{coda}^+\right] \\ & + \left(\mathbf{V}_{coda}^+\right)^{\mathrm{T}}\left(1-\boldsymbol{\Theta}^-\right)[\mathbf{R}\mathbf{I}] \\ & + \left(\mathbf{V}_{coda}^+\right)^{\mathrm{T}}\left(1-\boldsymbol{\Theta}^-\right)\left[\mathbf{R}\mathbf{V}_{coda}^+\right]. \end{aligned} \qquad (6.2.13)$$

The first term of this expression is a muted version of the reflection response, that excludes arrivals prior to the two-way travel time through the overburden. Hence, the remaining terms describe the multiples predicted by Marchenko double de-reverberation. This representation allows for a better analysis of the predicted multiples. For a direct comparison to the reflection response, $\mathbf{R}$, i.e. not only in terms of kinematics but also in terms of amplitudes, the scaling of the spatio-temporally band-limited identity, $\mathbf{I}$, must be taken into account according to Eq. 6.2.13.

6.2.2 Special case: Elastic reflection response recorded in acoustic layer

As mentioned in the introduction, Marchenko-type multiple-elimination methods require accurate data preprocessing. Using current acquisition and processing technologies, these requirements are achievable for marine data. However, from a theoretical view point the acquisition inside a water layer is problematic, which we explain in this section.

The back-propagated focusing function $\mathbf{V}^+$ is constructed from inverse transmissions through the overburden [*van der Neut and Wapenaar*, 2016; *Dukalski and de Vos*, 2017; *Elison*, 2019; *Reinicke*, 2020, chapter 4 of this thesis]. Since water does not support shear waves, the elastic transmission response of the overburden only contains one non-zero column in P-S space (see matrix organization in Eq. 6.2.1). Consequently, the determinant of the transmission is zero such that its inverse is no longer defined. Thus, it is unclear whether the back-propagated focusing function $\mathbf{V}^+$ exists.

In the special case where not only the recording layer, but the entire medium, is acoustic, Eqs. 6.2.4-6.2.8 reduce to equations for scalar fields. Since acoustic transmissions are invertible, the back-propagated focusing function V^+ is defined. In the acoustic case, we omit the subscripts "P, P". Further, the acoustic formulation of Eqs. 6.2.4-6.2.8 only requires a single projector, $\Theta = \Theta^+_{P,P} = \Theta^-_{P,P}$, that is bounded by a spatio-temporally band-limited identity and the two-way travel time between the recording and redatuming levels [for details see *Elison*, 2019, who refers to Θ with Φ_{t_0}].

In practice, only the recording layer is acoustic and the measured reflection response, $R_{P,P}$, contains elastic effects. Evaluating the acoustic Marchenko method using the elastic reflection response, $R_{P,P}$, instead of the acoustic one, R, leads to erroneous solutions, $\tilde{V}^\pm$, $\tilde{U}^{-,\pm}$, $\tilde{R}_{tar}$ and $\tilde{R}^{(ddr)}_{tar}$. In this notation, scalars *without* a tilde on top are associated with fully acoustic media, and scalars *with* a tilde on top are associated with elastic media below the recording layer. From here onwards, we also write the elastic reflection response $R_{P,P}$ with tilde on top and omit the subscripts, i.e. $R_{P,P}$ is now written as $\tilde{R}$.

6.3 Application to marine data of synthetic Middle East model

In this section, we build a 2D synthetic Middle East model (x-z space) with a water layer on top to mimic a streamer acquisition. Further, we generate acoustic and elastic reflection responses, R and $\tilde{R}$, recorded inside the water layer and apply the back-propagated Marchenko multiple-elimination method to both of them. The resulting Marchenko solutions as well as the resulting images are compared against each other, and against a modeled reference response.

6.3.1 Acoustic and elastic reflection responses of synthetic Middle East model

We build a synthetic Middle East model with actual P- and S-wave velocities ($c_{P/S}$) as well as densities (ρ) from regional log data. Assuming that the Middle Eastern geology is nearly layered, we copy the log data to several horizontal positions, introduce small variations of layer thicknesses at each location and spline-interpolate the resulting logs along the horizontal direction. Subsequently, we account for a gentle regional dip, insert minor faults, riverbeds and small relief-structure reservoirs. The resulting model is shown in Figs. 6.1a and b where the top layer is water.

In addition, we construct a reference medium (see Fig. 6.1c) to model a reference, $R_{tar}^{(ref)}$, for the retrieved target reflection response, R_{tar}. The reference medium is identical to the true model below the redatuming level $\partial\mathbb{D}_i$, but has a smooth overburden and is acoustic ($c_s = 0\,\mathrm{m\,s}^{-1}$ in the entire reference medium). The smoothness allows us to mimic the multiple-free propagation of the target response, R_{tar}, through the overburden. However, the reference response, $R_{tar}^{(ref)}$, does not correct for overburden-related transmission-losses. Hence, the responses $R_{tar}^{(ref)}$ and R_{tar} are expected to have identical kinematic events but different amplitudes.

In this controlled experiment, we can model acoustic and elastic reflection responses[1], $R(\mathbf{x}_0, \mathbf{x}_0', t)$ and $\tilde{R}(\mathbf{x}_0, \mathbf{x}_0', t)$, respectively. Since the recording layer is water with a transparent surface (absorbing boundary conditions), there is no need for wavefield separation of the recorded elastic reflection response, which removes unnecessary inaccuracies from our analysis. Further, we use a vertical dipole source[2], convolved with a 30 Hz Ricker wavelet. In this experiment, we employ 401 collocated sources and receivers with spatial and temporal sampling rates of $\Delta x = 12.5\,\mathrm{m}$ and $\Delta t = 4\,\mathrm{ms}$, respectively.

The resulting reflection responses $R(\mathbf{x}_0, \mathbf{x}_0', t)$ and $\tilde{R}(\mathbf{x}_0, \mathbf{x}_0', t)$ as well as their difference are shown in Fig. 6.2. The strongest differences are steep events, due to the lower propagation velocity of S-waves, and amplitude deviations at far-offsets, due to stronger mode coupling at large angles of incidence. Waves that are evanescent on the boundaries $\partial\mathbb{D}_0$ and $\partial\mathbb{D}_i$ are excluded by the representation theorems, and therefore, must be removed [*Reinicke and Wapenaar*, 2019]. This suppression of evanescent waves can be achieved e.g. by the wavenumber-frequency filtering, which attenuates the elastic effects, and thereby, reduces the difference between acoustic and elastic reflection responses significantly (see second row in Fig. 6.2).

This effect becomes clearer by transforming the reflection responses to the wave-

---

[1] We used the modeling tool *fdelmodc* written by Jan Thorbecke. This software is openly available on `https://github.com/JanThorbecke/OpenSource/tree/master/fdelmodc`.

[2] This scaling can be obtained via the *fdelmodc* settings, *src_type=1, src_orient=4, src_injectionrate=0*, combined with a global scaling factor $\frac{2}{\rho(\mathbf{x}_0')}$.

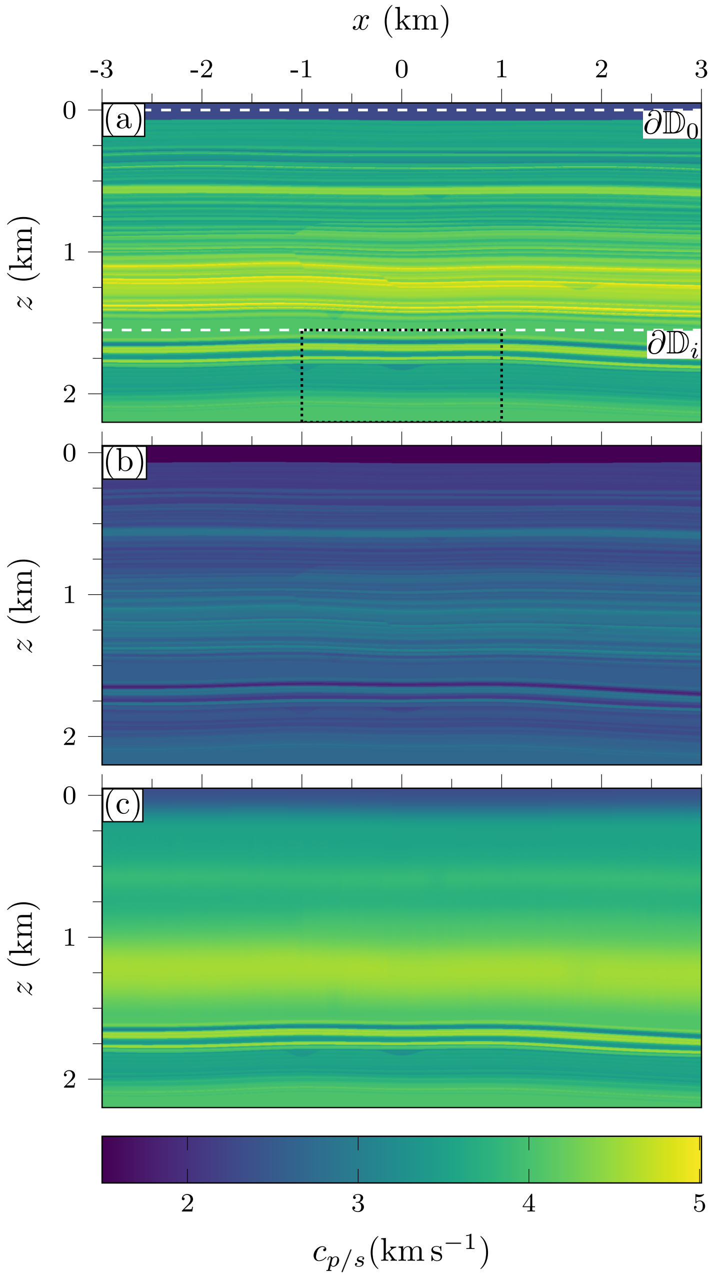

Figure 6.1: *Synthetic Middle East model: (a) P- and (b) S-wave velocity models. Dashed white lines indicate the recording and redatuming levels $\partial\mathbb{D}_0$ and $\partial\mathbb{D}_i$. The dotted black rectangle indicates the imaging area. (c) Reference P-wave velocity model with smooth overburden. The density models are not shown but have the same geometry as the respective P-wave velocity models.*

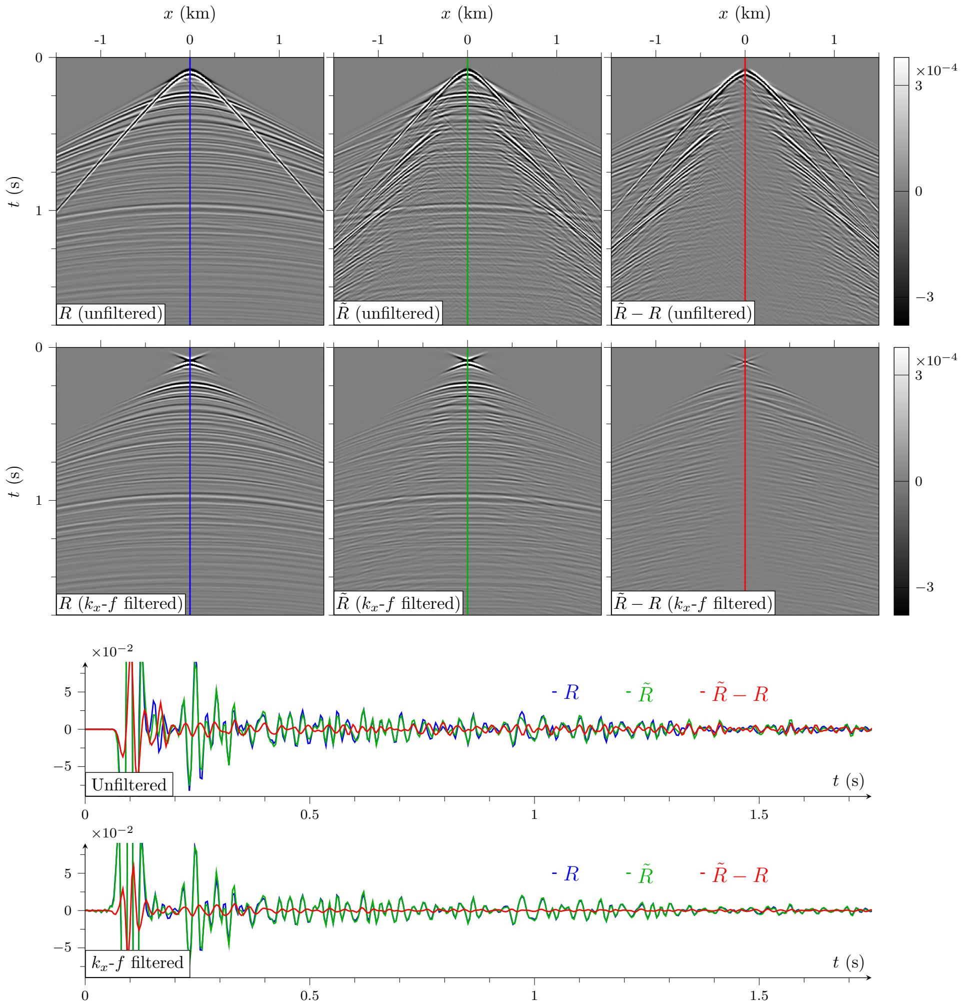

Figure 6.2: *Reflection responses of an acoustic medium (column one), an elastic medium (column two) and their difference (column three). The responses are shown before (row one) and after (row two) applying a (tapered) wavenumber-frequency (k_x-f) filter, defined by $c = 3.50\,\mathrm{km\,s^{-1}}$ and $f_{max} = 80\,\mathrm{Hz}$. The space-time panels are clipped at $5\,\%$ of the maximum value of the panel in the first column. The color-coded central traces allow for a better amplitude comparison.*

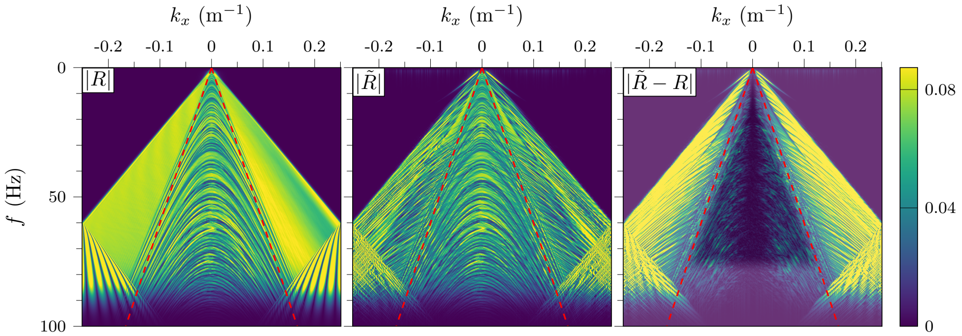

Figure 6.3: *Reflection responses after source wavelet deconvolution. The red dashed line is defined by the maximum velocity on the boundaries $\partial\mathbb{D}_0$ and $\partial\mathbb{D}_i$ ($c_p = 3.78\,\mathrm{km\,s^{-1}}$). For wavenumber-frequency components that are passed by the k_x-f filter (shown by a black shadow in the bottom panel) the difference between R and $\tilde{R}$ remains small. The panels are clipped at 50 % of the maximum value of R.*

number-frequency (k_x-f) domain,

$$R(k_x, z_0, \mathbf{x}_0', \omega) = \int_{-\infty}^{\infty}\int_{-\infty}^{\infty} R(x, z_0, \mathbf{x}_0', t) \times \mathrm{e}^{\mathrm{i}(\omega t - k_x x)} \mathrm{d}x\mathrm{d}t. \tag{6.3.1}$$

The highest velocity on the boundaries $\partial\mathbb{D}_0$ and $\partial\mathbb{D}_i$ ($c_p \approx 3.8\,\mathrm{km\,s^{-1}}$) defines the onset of evanescent waves (defined by dashed red lines in Fig. 6.3). Beyond these lines, i.e. outside of the cone defined by the dashed red lines, there are still propagating waves associated with conversions to S-waves (P-S-P events). However, these propagating waves are removed by the wavenumber-frequency filter (indicated by a black shadow in the bottom panel of Fig. 6.3), which is defined by $c_p = 3.5\,\mathrm{km\,s^{-1}}$ and $f = \frac{\omega}{2\pi} = 80\,\mathrm{Hz}$. The difference between the acoustic and elastic reflection responses in Fig. 6.3 reveals that wavenumber-frequency filtering attenuates most of the elastic effects. The high-cut frequency filter is necessary to avoid aliasing and could be increased by denser spatial sampling. In addition, source wavelet deconvolution has already been applied.

■ 6.3.2 Retrieval of back-propagated focusing and Green's functions

Now, we retrieve the back-propagated focusing and Green's functions, $\tilde{V}^{\pm}$, $U^{-,\pm}$, $\tilde{V}^{\pm}$ and $\tilde{U}^{-,\pm}$. To this end, we evaluate 20 terms of the scalar version of Eq. 6.2.8 and use Eqs. 6.2.4-6.2.6.

For recordings inside an acoustic layer, the existence of the back-propagated focusing function $\tilde{V}^{+}$ is unclear. Nevertheless, Eq. 6.2.8 converges to an elastic solution, $\tilde{V}^{+}$, and the convergence is slightly faster than in the pure acoustic case (see Fig. 6.4). We speculate that the faster convergence may occur because, due to conversions to S-waves, P-wave amplitudes tend to be lower for the reflection response $\tilde{R}$ than for R.

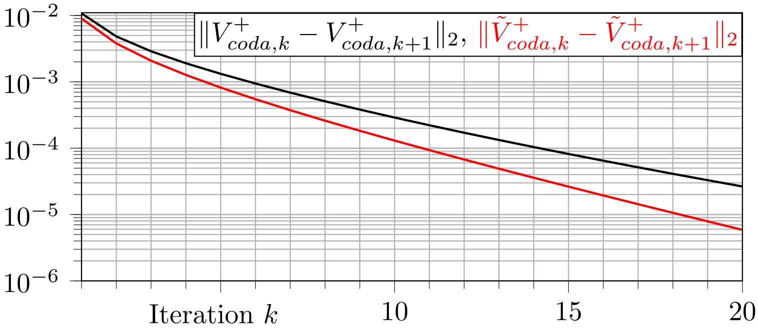

Figure 6.4: *Convergence of the back-propagated Marchenko series using the wavenumber-frequency filtered reflection data of Fig. 6.2. The Marchenko series in Eq. 6.2.8 is started with an identity as initial guess and only updates the coda of the back-propagated focusing function* V^+_{coda}*. Therefore, we measure the convergence via the* $\mathcal{L}_2$ *norm of the coda update at each iteration.*

Further, the retrieved acoustic ($\tilde{V}^{\pm}$ and $U^{-,\pm}$) and elastic ($\tilde{V}^{\pm}$ and $\tilde{U}^{-,\pm}$) solutions show a high level of agreement (see Fig. 6.5). Although the solutions $\tilde{V}^{\pm}$ and $\tilde{U}^{-,\pm}$, obtained from the elastic reflection response $\tilde{R}$, contain artifacts, which are mainly visible as steeper events, they are comparable to the solutions, $\tilde{V}^{\pm}$ and $U^{-,\pm}$, derived from the acoustic reflection response.

Fig. 6.6 shows the wavenumber-frequency spectra of the retrieved fields after source-wavelet deconvolution. The spectra of the fields derived from acoustic and elastic reflection responses are nearly identical and contain medium-characteristic amplitude distributions. The most pronounced difference between solutions derived from acoustic and elastic reflection data is formed by dot-like peaks that occur in the solutions $\tilde{V}^{\pm}$ and $\tilde{U}^{-,\pm}$. Note that, the back-propagated focusing and Green's functions, V^+, $U^{-,-}$, $\tilde{V}^+$ and $\tilde{U}^{-,-}$, contain two terms, namely a scaled identity plus a coda (see Eq. 6.2.11). Since the wavenumber-frequency spectra of the scaled identities are constant, except for spatio-temporal band-limitation, we only show the spectra of the respective codas to better visualize their amplitude fluctuations. White arrows point to coinciding peaks and troughs in the wavenumber-frequency spectra of the back-propagated focusing and Green's functions, V^+ and $U^{-,+}$, that will be relevant for the multiple-elimination step.

■ 6.3.3 Multiple-elimination results in the data domain

From the back-propagated focusing and Green's functions, $V^{\pm}$, $U^{-,\pm}$, $\tilde{V}^{\pm}$ and $\tilde{U}^{-,\pm}$, we can construct the aforementioned target responses: by Marchenko double de-reverberation, by least-square (lsqr) deconvolution of Eq. 6.2.2 and by modeling. Due to the aforementioned scaling differences, we compare the target responses in terms of events and interference patterns, but not in terms of amplitudes. In case of Marchenko double de-reverberation, we compute the predicted multiples explicitly

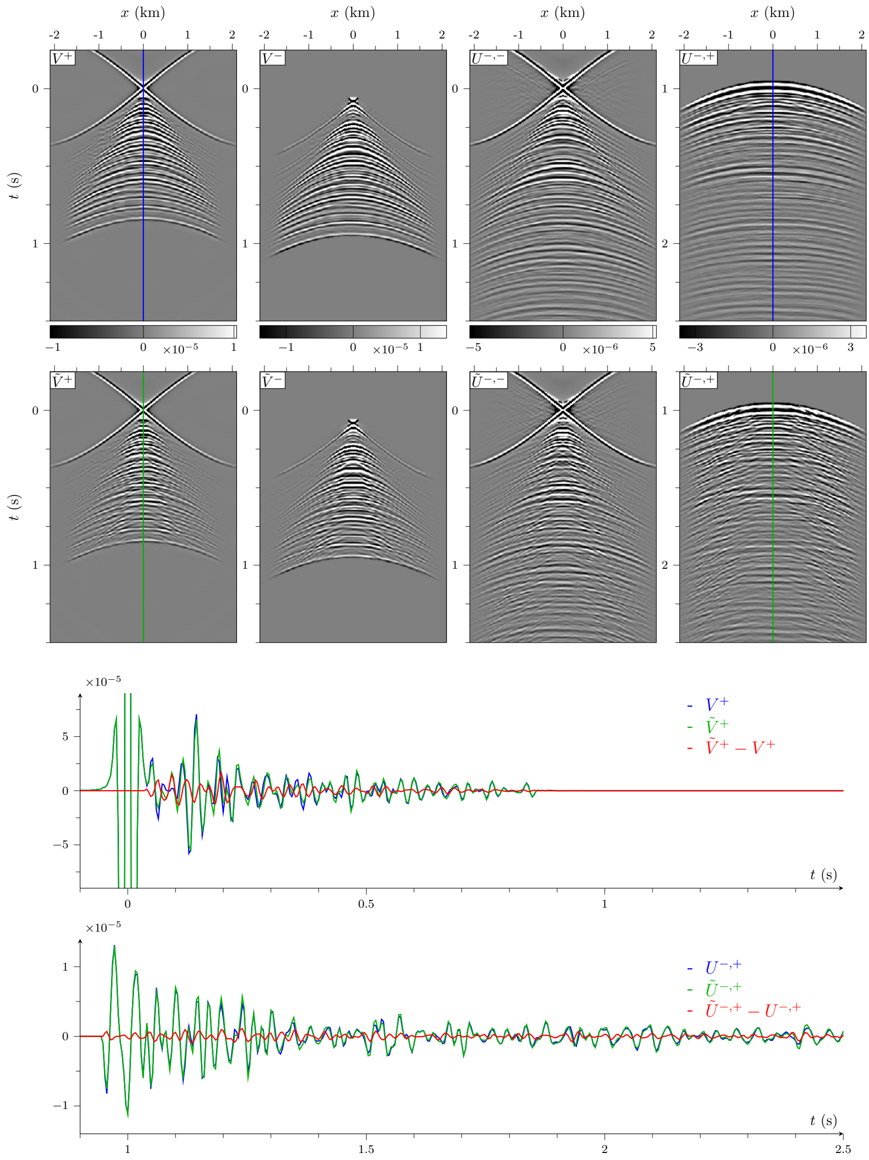

Figure 6.5: *Fields retrieved via the acoustic Marchenko method using the acoustic (first row) and elastic (second row) reflection responses R and $\tilde{R}$, respectively. The panels in the first row are clipped at their respective 99 percentile, the panels in the second row are clipped identically to those in the first row. The amplitudes can be compared easier via the color-coded central traces.*

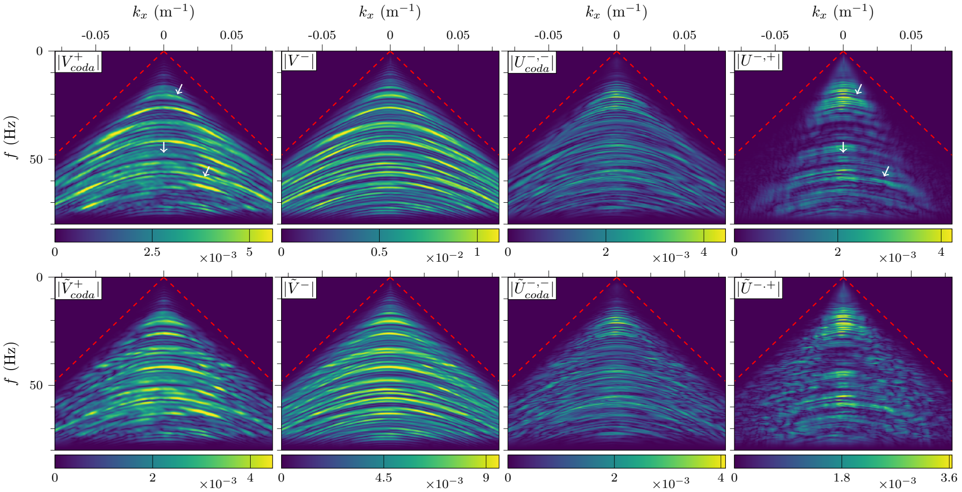

Figure 6.6: *Similar as Fig. 6.5 but after transformation to the wavenumber-frequency domain and source-wavelet deconvolution. A scaled and spatio-temporally band-limited identity was subtracted from the back-propagated focusing and Green's functions, V^+, $U^{-,-}$, $\tilde{V}^+$ and $\tilde{U}^{-,-}$, to better visualize their amplitude fluctuations. The dashed red lines are associated with the same velocity as in Fig. 6.3 ($c_p = 3.78\,\mathrm{km\,s^{-1}}$) to simplify the comparison of wavenumber-frequency spectra across figures. The white arrows point to maxima and minima of the back-propagated focusing and Green's functions that, as will be shown later, are combined by Marchenko double de-reverberation (see Eq. 6.2.9) to approximately reconstruct the wavenumber-frequency spectrum of the target reflection response $R^{(ref)}_{tar}$ (see Fig. 6.9).*

according to Eq. 6.2.13, which allows us to analyze those multiples that are only overburden-related. Further, we (de-)convolve the different target responses with the source-wavelet to ensure that the compared responses underly the same band-limitation.

Modeled target reflection response $R^{(ref)}_{tar}$

First, we compare a muted version of the reflection response, $(1 - \Theta)R$, against the reference target response, $R^{(ref)}_{tar}$. Note that, the mute, $(1 - \Theta)$, removes all arrivals prior to the two-way travel time through the overburden.

The time domain panels in Figs. 6.7 and 6.8 show that the target response, $R^{(ref)}_{tar}$, is nearly zero after about $t = 1.3\,\mathrm{s}$. Hence, after $t = 1.3\,\mathrm{s}$, almost all events of the reflection response, $(1 - \Theta)R$, are multiples. However, there are also earlier multiples, indicated by white arrows in Fig. 6.7. The observed multiples are not dominated by individual events but appear as a continuous train of events, turning them into a more complicated interference pattern. This observation is reaffirmed by the wavenumber-frequency spectra in Fig. 6.9: if the multiples were

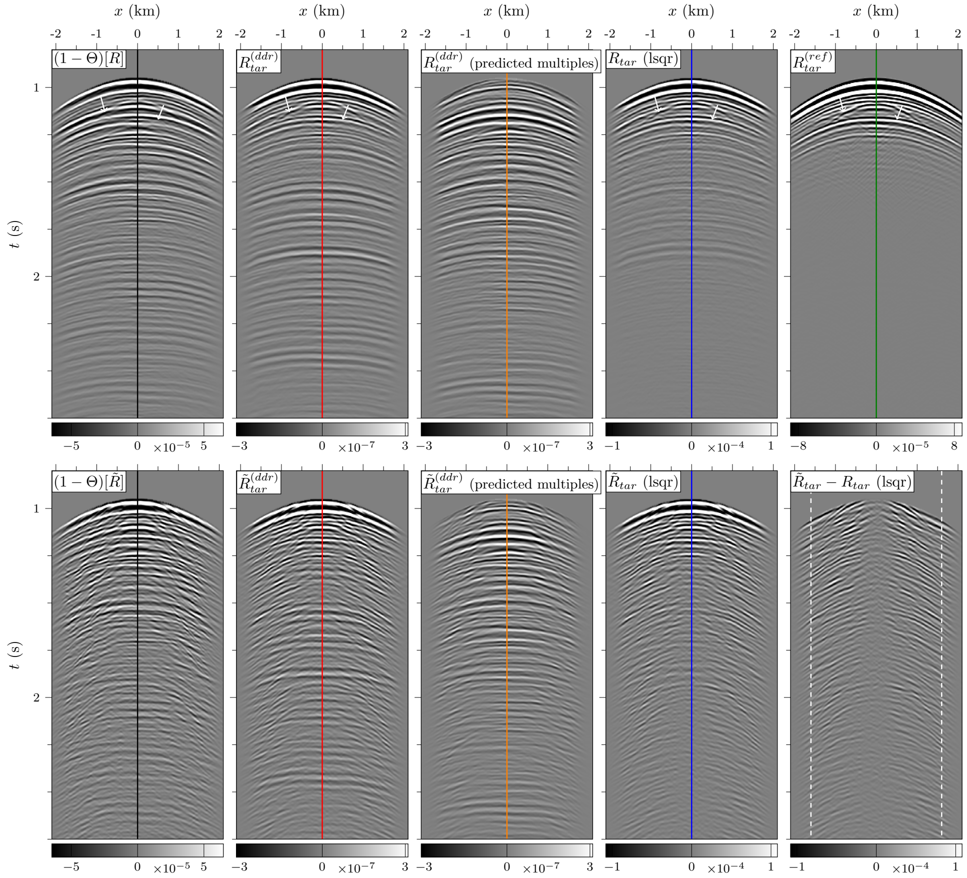

Figure 6.7: *Target reflection responses obtained by muting data, Marchenko double de-reverberation, deconvolution (via lsqr) and modeling in a reference medium. The multiples predicted by Marchenko double de-reverberation are not dominated by individual events but appear as a complicated interference pattern. The difference between the target reflection responses obtained from the acoustic and elastic reflection responses is dominated by steeper events associated with lower propagation velocities, i.e. by waves that convert to S-waves. The dashed white lines indicate the maximum offset that will be used for migration further onwards. The panels in the top row are clipped at their respective 99 percentile. The elastic responses are clipped at the same value as the respective acoustic responses. The color-coded lines label central traces that are shown in Fig. 6.8.*

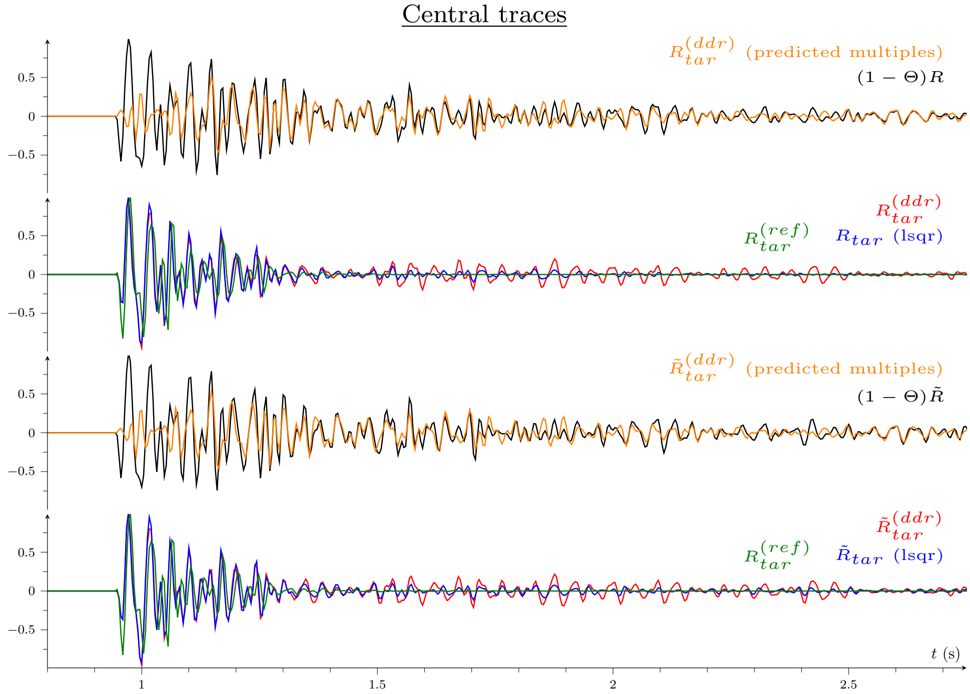

Figure 6.8: *Central traces of the target reflection responses shown in Fig. 6.7. The traces associated with the different target reflection responses are normalized to one. The traces associated with the predicted multiples are normalized by the same factor as the respective target responses obtained via Marchenko double de-reverberation, i.e. the normalization factors for orange and red traces are identical. The small phase shift between the reference responses ,* $R_{tar}^{(ref)}$*, and the retrieved target responses,* R_{tar}*,* $\tilde{R}_{tar}$*,* $R_{tar}^{(ddr)}$ *and* $\tilde{R}_{tar}^{(ddr)}$*, can be due to either the smoothening of the overburden, or short-period multiples or both.*

individual events they would generate a rather white contribution to the spectrum. Nevertheless, the multiples create sharp notches in the spectrum of the reflection response (see white arrows).

Further, the wavenumber-frequency cone of the responses in Fig. 6.9 is significantly narrower than the cone of the recorded data in Fig. 6.3 (dashed red lines serve as reference). This is expected because the target responses contain wavefield propagation through the smooth overburden but only contain reflections from the target below $\partial\mathbb{D}_i$. Therefore, the target reflection responses are associated with a smaller (effective) aperture than the recorded data.

Marchenko double de-reverberation result $R_{tar}^{(ddr)}$

Second, we analyze the effect of Marchenko double de-reverberation. Compared to the reflection response, $(1-\Theta)R$, the target response obtained by Marchenko double

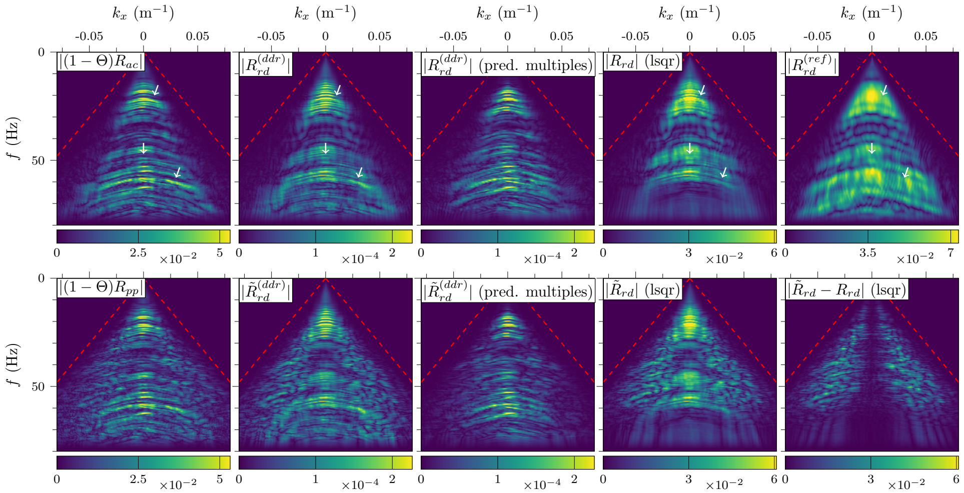

Figure 6.9: *Similar as Fig. 6.7 but after transformation to the wavenumber-frequency domain and source-wavelet deconvolution. Comparing muted reflection responses,* $(1-\Theta)R$ *and* $(1-\Theta)\tilde{R}$*, against the reference target response,* $R_{tar}^{(ref)}$*, shows that interferences with overburden-related multiples cause minima in the wavenumber-frequency spectra (see white arrows). These minima are filled by Marchenko double de-reverberation (see* $R_{tar}^{(ddr)}$ *and* $\tilde{R}_{tar}^{(ddr)}$ *as well as white arrows in Fig. 6.6) and by deconvolution of* $U^{-,\pm}$ *and* $\tilde{U}^{-,\pm}$ *(see* R_{tar} *and* $\tilde{R}_{tar}$*). The wavenumber-frequency spectra of the predicted multiples also contain characteristic peaks and troughs that suggest that, in the space-time domain, the multiples do not appear as individual events but rather as more complicated interference patterns. The dashed red lines are associated with the same velocity as in Fig. 6.3 (*$c_p = 3.78\,\mathrm{km\,s^{-1}}$*). The panels in the top row are clipped at their respective 99.9 percentile. The elastic responses are clipped at the same value as the respective acoustic responses.*

de-reverberation, $R_{tar}^{(ddr)}$, removes a significant amount of multiples: at early times (and in terms of kinematics) the Marchenko double de-reverberation result near-to-perfectly reconstructs the reference target response, $R_{tar}^{(ref)}$, revealing previously hidden primaries (see white arrows in Fig. 6.7 and see Fig. 6.8). At later times, many multiples persist because Marchenko double de-reverberation does not remove multiples that are generated between the overburden and the target. The same effect is visible in Fig. 6.8: at earlier times the multiple prediction approximately tracks parts of the reflection response, $(1-\Theta)R$, but at later times the misfit between predicted multiples and the reflection response increases.

Moreover, we observe a small phase shift between the reference response, $R_{tar}^{(ref)}$, and the Marchenko double de-reverberation response, $R_{tar}^{(ddr)}$. This phase shift could be due to the smoothening of the overburden (see Fig. 6.1c), or incorrectly handled short-period multiples, or both.

Next, we compare the wavenumber-frequency spectra of the reflection response,

$(1-\Theta)R$, the back-propagated focusing function, V^+_{coda}, and the Marchenko double de-reverberation result, $R^{(ddr)}_{tar}$. The spectra illustrate that, via the back-propagated focusing function, Marchenko double de-reverberation partially fills the notches created by multiples (see Eq. 6.2.9 and white arrows in Figs. 6.6 and 6.9). Further, frequency components above $f = 60\,\mathrm{Hz}$ are not reconstructed, which could be due to the tapered cut-off frequency at $f = 80\,\mathrm{Hz}$, the used source wavelet (30 Hz Ricker) or short-period multiples.

Target reflection response R_{tar}

Third, we inspect the target response, R_{tar}, retrieved by deconvolution of Eq. 6.2.2. This approach closely reconstructs the reference target response, $R^{(ref)}_{tar}$, at both early and late times (see Figs. 6.7 and 6.8). Compared to Marchenko double de-reverberation, this improvement in predicting multiples at later times is expected because now multiples generated between the overburden and the target are also taken into account. Remaining multiple artifacts may be due to short-period multiples, violations of the assumption, $\chi_- = 0$, as well as limited aperture and recording duration.

Moreover, we observe an enhancement in the retrieved wavenumber-frequency spectrum (see Fig. 6.9): e.g. the deconvolution result near-to-completely fills the notch generated by multiples (see white arrow at $f = 20\,\mathrm{Hz}$).

Here, we choose to evaluate the deconvolution with a least-squares (lsqr) solver. This approach only reconstructs parts of the target reflection response that can be derived from the, possibly imperfect, fields $U^{-,\pm}$. Therefore, contrary to a direct deconvolution, there is no need for stabilization, e.g. in case of band-limited fields.

The residual, i.e. the unexplained part of Eq. 6.2.2 is shown in Fig. 6.10. The coherency of the residual is rather weak and the wavenumber-frequency spectrum of the residual is dominated by frequencies above $f = 60\,\mathrm{Hz}$, which are not reconstructed in the target reflection responses, $R^{(ddr)}_{tar}$ and R_{tar}. To further analyze the performance of the least-squares deconvolution, we measure its convergence by the ratio between the $\mathcal{L}_2$-norm of the residual to the $\mathcal{L}_2$-norm of the left-hand side of Eq. 6.2.2. Fig. 6.10 shows that within ten iterations the least-squares solver converges to 2 % to 3 %.

Further, we evaluate the least-squares deconvolution in the time domain [*Paige and Saunders*, 1982a,b]. This is advantageous because, firstly, the unexplained data can be analyzed via the residual, and secondly, all frequencies are handled simultaneously.

Elastic target reflection responses $(1-\Theta)\tilde{R}$, $\tilde{R}^{(ddr)}_{tar}$ and $\tilde{R}_{tar}$

Fourth, we assess the difference of deriving the above discussed target reflection responses from the acoustic or the elastic reflection response. Although we focus on the target responses obtained via least-squares deconvolution, R_{tar} and $\tilde{R}_{tar}$, analogous observations can be made for the other target responses.

In the space-time domain (see Fig. 6.7), and for short-offsets, the target response retrieved from the elastic reflection response is nearly identical to the one retrieved

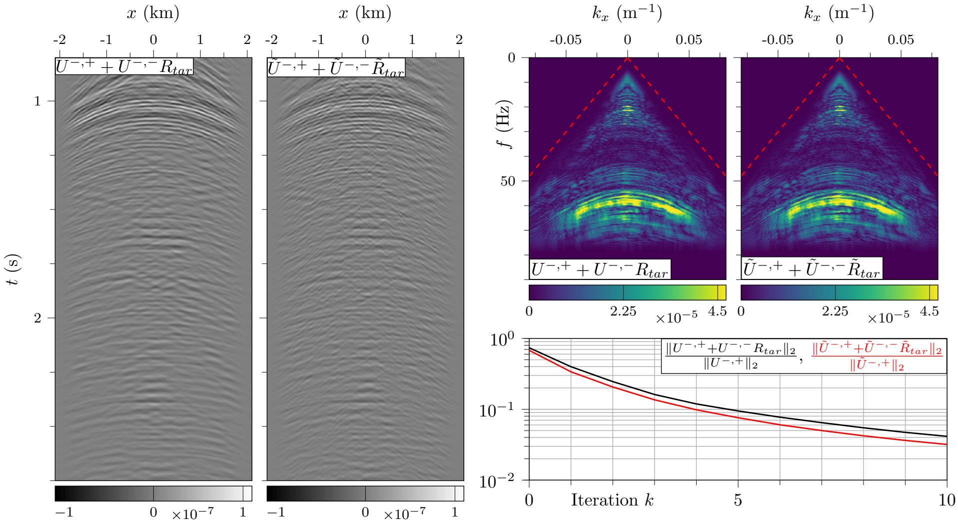

Figure 6.10: *Residuals of the least-squares deconvolution of Eq. 6.2.2 using the fields,* $U^{-,\pm}$ *and* $\tilde{U}^{-,\pm}$*, shown in Figs. 6.5 and 6.6. In the space-time domain panels, the residuals are convolved with the source wavelet and clipped at the respective 99 percentile. In the wavenumber-frequency domain panels, the residuals are not convolved with source wavelet and clipped at the respective 99.9 percentile. Again, the dashed red lines are associated with the same velocity as in Fig. 6.3 (*$c_p = 3.78\,\mathrm{km\,s^{-1}}$*). The bottom-right panel illustrates the convergence of the least-squares deconvolution as a function of number of iterations.*

from the acoustic reflection response. Their difference is dominated by steeper events that almost vanish at zero-offset. Since these events are associated with slower apparent velocities and tend to be weak for small angles of incidence, we interpret that they are associated with conversions to S-waves.

An analogous observation is made in the wavenumber-frequency domain (see Fig. 6.9), where the difference vanishes close to $k_x = 0\,\mathrm{m}^{-1}$. Moreover, the spectrum of the difference is characterized by incoherent dot-like peaks. This suggests that the difference has low coherency in the space-time domain.

We remark that, due to a practical challenge, there is no elastic version of the modeled reference, $R_{tar}^{(ref)}$. Modeling this response requires a smooth overburden, i.e. smooth P- and S-wave velocity as well as density model. However, a smooth S-wave velocity model, that features a gentle decrease to $c_s = 0\,\mathrm{km\,s^{-1}}$ inside the water layer, causes instabilities in finite difference modeling because of too small velocities. In contrast, the special case of $c_s = 0\,\mathrm{km\,s^{-1}}$ can be handled because terms containing the S-wave velocity vanish.

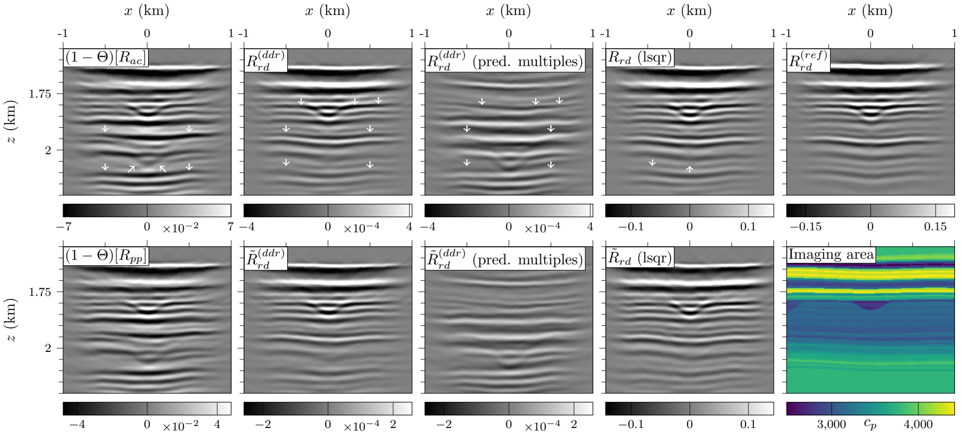

Figure 6.11: *Images obtained from the target reflection responses in Fig. 6.7. The images in the top row are clipped at their respective 99 percentile. The elastic responses are clipped at the same value as the respective acoustic responses. A close-up of c_p-model shows the imaging area. The images are computed via the PSKDM algorithm.*

■ 6.3.4 Multiple-elimination results in the image domain

Now, the target reflection responses shown in Fig. 6.7 are migrated to the image domain (see Fig. 6.11). We consider the imaging area indicated by the black rectangle in Fig. 6.1a, which is shown as a close-up in Fig. 6.11. Here, we use a pre-stack Kirchhoff depth migration (PSKDM) algorithm [e.g. *Schneider*, 1978], combined with a smooth velocity model. Further, a maximum offset of ±1.6 km is considered for the migration (see dashed white lines in Fig. 6.7).

Subsequently, we compare the resulting images. The images derived from the reference target response, $R_{tar}^{(ref)}$, and from the reflection response, $(1-\Theta)R$, clearly demonstrate that the latter one suffers from artifacts caused by overburden-related multiples (see first and last column in Fig. 6.11). Since the images are dominated by finely-layered nearly-horizontal structures, a visual analysis is challenging. White arrows highlight some of the dominant multiple-related artifacts. Marchenko double de-reverberation removes these artifacts, and thereby, reveals previously hidden structures (see second column in Fig. 6.11).

To visualize the multiple-borne artifacts, we migrate the explicitly computed multiples predicted by Marchenko double de-reverberation (see third column in Fig. 6.11). This figure shows the complexity of the multiple-borne artifacts and highlights that these multiples are not easily recognizable in the reflection response, $(1-\Theta)R$.

The images derived from the target response obtained by Marchenko double de-reverberation, $R_{tar}^{(ddr)}$, and by least-squares deconvolution, R_{tar}, are nearly identical (see second and fourth column in Fig. 6.11). Nevertheless, the latter one has a slightly higher resolution (see white arrows in fourth column in Fig. 6.11), bringing

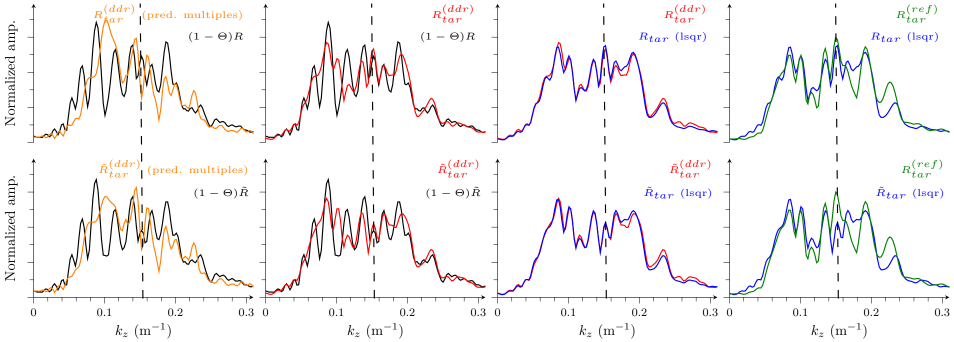

Figure 6.12: *Vertical-wavenumber spectra of the images in Fig. 6.11, computed according to Eqs. 6.3.2 and 6.3.3. The vertical dashed lines highlight the main difference between the k_z-spectra in the top and bottom row, associated with an acoustic and elastic reflection response, respectively.*

it a bit closer to the reference image (see last column in Fig. 6.11).

The final images are not very sensitive to replacing the acoustic reflection response, R, by the elastic one, $\tilde{R}$ (compare first and second row in Fig. 6.11). Using the elastic reflection response leads to a minor reduction of continuity and resolution. Due to the difficulty to point to a different feature in the images, and due to the dominantly horizontal structures, we opt for an alternative analysis: we apply a 2D spatial Fourier transformation to the images $I(x,z)$,

$$I(k_x,k_z)=\int_{-\infty}^{\infty}\int_{-\infty}^{\infty}I(x,z)\mathrm{e}^{-\mathrm{i}(k_xx+k_zz)}\mathrm{d}x\mathrm{d}z, \tag{6.3.2}$$

take the absolute value and sum the result for all horizontal wavenumbers,

$$\sum_{k_x}|I(k_x,k_z)|. \tag{6.3.3}$$

A comparison of the resulting k_z-spectra (see Fig. 6.12) shows that the images derived from acoustic and elastic reflection data mostly differ around $k_z=0.16\,\mathrm{m}^{-1}$ (indicated by vertical dashed lines). This imperfect reconstruction of the vertical-wavenumbers around $k_z=0.16\,\mathrm{m}^{-1}$ may be the reason why the images derived the elastic reflection response are not as sharp as those derived from the acoustic reflection response.

Further, the images derived from the target reflection responses, $R^{(ddr)}_{tar}$ and R_{tar}, have smoother k_z-spectra than the image derived from the reflection response, $(1-\Theta)R$. The smoothening of the k_z-spectrum is another manifestation of increased image resolution due to multiple elimination (in x-z space).

6.4 Discussion

Our analysis assessed the accuracy of applying the acoustic Marchenko multiple-elimination method to elastic data. This synthetic case study is essential to support the reliability of respective field data examples.

We built a synthetic Middle East model, which allowed us to include and exclude elastic effects. Next, we used the acoustic Marchenko method to remove multiples from the acoustic and elastic reflection responses, which were compared against each other and against a reference. For far-offsets, the retrieved target reflection responses are sensitive to the elastic effects. However, for near-offsets, which are the main contributors to migrated images, the target reflection responses retrieved from acoustic and elastic data are nearly identical. We emphasize that these results are model-dependent, and therefore, support field data examples of the acoustic Marchenko method, which are associated with comparable geologies such as offshore Middle East. Since mode conversions between P- and S-waves are weaker for smaller angles of incidence, nearly horizontally-layered media formed a very promising candidate for our case study. For significantly different, e.g. Brazil-like, geological settings the performance of the acoustic Marchenko method (or other acoustic multiple-elimination methods) may be worse but a respective case study is needed to draw any conclusions.

We defined a slightly peculiar target reflection response, which is free of overburden-generated multiples but contains direct propagations through the overburden. Further, this response is corrected for overburden-related transmission losses. We use this response because it can be easily obtained from the retrieved back-propagated Green's functions. Although the target response may appear unfamiliar, it can be migrated as any other reflection response. Moreover, since overburden-related transmission losses are absent, a reference response can be easily constructed to analyze kinematics but not amplitudes. We also inspected a Marchenko double de-reverberation strategy that can be seen as an approximation of the target reflection response. This strategy replaces a multi-dimensional deconvolution by a convolution of different fields, which can reduce computational costs and increase stability. This approach is an approximation because it ignores multiples generated between the overburden and the target, which tend to arrive at later times. Hence, if the imaging area does not expand over too large depth intervals, Marchenko double de-reverberation can be a cheaper and still very accurate alternative to the deconvolution approach.

The data requirements of the presented method are high, but feasible. As for other Marchenko applications, accurate data preprocessing was crucial, yet, realizable for marine data. To the authors, the computational costs seem relatively low: for reflection responses associated with 401 sources, 401 receiver and 1001 time samples the total computational time on our local university cluster is below half an hour, without having explored computational speed-up possibilities. During the aforementioned run time, all operations from raw data to the final images are performed for both, the acoustic and elastic reflection responses.

6.5 Conclusions

We conclude that the acoustic Marchenko method can suffice to handle multiples in marine data recorded in the Middle East. This insight is important for applications because, despite recording data in an acoustic medium, there are imprints of elastic scattering effects. Our conclusion extends to comparable, i.e. nearly horizontally-layered, media. The data requirements can be fulfilled by current acquisition and processing technologies. In addition, the presented results are in agreement with field data examples from a parallel project by Staring et al. Note that, the field data was recorded close to the location of the well-logs used for our synthetic model. Thus, the similarities between independently obtained results emphasize the relevance and reliability of the presented work.

Acknowledgements

We are grateful to Roald van Borselen, Rob Hegge and Rolf Baardman for their advice on analyzing our results. Moreover, we thank Patrick Elison for support with PSKDM software and advice. This work is partly funded by the European Union's Horizon 2020 research and innovation program: European Research Council (grant agreement 742703).

6A 1.5D Elastic multiple-elimination with an incomplete reflection response

We provide a brief example of elastic Marchenko multiple-elimination without all components of the reflection response. Only a minimum of the underlying theory is shown in this chapter but details can be found in *Wapenaar* [2014] and in chapter 4 of this thesis [*Reinicke*, 2020].

A simple, yet non-trivial, example is formed by horizontally-layered elastic media in x-z space. Here, elastodynamic wavefields, $\mathbf{P}(\mathbf{x}, \mathbf{x}', t)$, reduce to 2×2 matrices (see Eq. 6.2.1) and can be described independently per horizontal-slowness s_x. To this end, we transform wavefields, $\mathbf{P}(\mathbf{x}, \mathbf{x}', t)$ to the horizontal-slowness intercept-time domain,

$$\mathbf{P}(s_x, z, \mathbf{x}', \tau) = \int_{-\infty}^{\infty} \mathbf{P}(x, z, \mathbf{x}', \tau + s_x x)\mathrm{d}x. \tag{6A.1}$$

Similar Eq. 6.2.8 the focusing function $\mathbf{F}_1^+$ is retrieved via the Marchenko method,

$$\bar{\mathbf{F}}_1^+ = \sum_{k=0}^{\infty} \boldsymbol{\Xi}_k, \text{ with, } \boldsymbol{\Xi}_k = \boldsymbol{\Theta}^+ \left[\mathbf{R}^\dagger \boldsymbol{\Theta}^- \left[\mathbf{R}\boldsymbol{\Xi}_{k-1}\right]\right], \tag{6A.2}$$

using $\boldsymbol{\Xi}_0 = -\boldsymbol{\chi}^+$. In contrast to $\mathbf{V}^+$ in Eq. 6.2.8, the focusing function $\mathbf{F}_1^+$ is not back-propagated from the redatuming level to the acquisition surface. For this reason the initial estimate $\boldsymbol{\chi}^+$ is no longer an identity but (in simple cases) consists of all forward-scattered waves propagating from the redatuming level $\partial\mathbb{D}_i$ to the acquisition surface $\partial\mathbb{D}_0$. Further, the functions $\mathbf{\Theta}^{\pm}$ are temporal mutes, the superscript "$\dagger$" denotes a transpose combined with a time-reversal and the bar distinguishes the retrieved from the true focusing functions $\mathbf{F}_1^{+}$.

Now we model the reflection response $\mathbf{R}$ of the layered model described by Tab. 4C.1 for a range of horizontal-slownesses and the recording depth $z_0 = 0\,\mathrm{km}$. Note that, we parameterize the medium by P- and S-wave velocities, c_p and c_s respectively, as well as density ρ. We choose the redatuming level at $z_i = 1.9\,\mathrm{km}$ and retrieve the focusing function according to Eq. 6A.2 (see first column in Fig. 6.13). The result is correct except for horizontal-slownesses, $|s_x| \geq 2.54 \times 10^{-4}\,\mathrm{s\,m^{-1}}$, which violate the monotonicity, i.e. separability, condition of the Marchenko method.

In practice, components of the reflection response associated with S-wave sources, R_{ps} and R_{ss}, are often absent. The R_{ps} component may be reconstructed via source-receiver reciprocity. However, the R_{ss} component will remain missing, which leads to an erroneous focusing function (see second column in Fig. 6.13), and therefore, to artifacts in the multiple-elimination result. Similar errors are observed when further components of the reflection response are ignored, i.e. when only the R_{pp} component is used (see third column in Fig. 6.13).

Finally, we evaluate an acoustic, i.e. scalar, version of Eq. 6A.2 using the R_{pp} component of the elastic reflection response. In contrast to the previous experiment, the initial estimate $\boldsymbol{\chi}^{+}$ and the projectors $\mathbf{\Theta}^{\pm}$ are now defined according to the acoustic Marchenko method. Thus, the initial estimate $\boldsymbol{\chi}^{+}$ only contains a time-reversed direct P-wave propagating from the redatuming to the acquisition surface, rather than all forward-scattered waves. Moreover, the definition of the projectors $\mathbf{\Theta}^{\pm}$ is slightly different [defined as in *Reinicke*, 2020, chapter 4 of this thesis, but ignoring the shear-wave velocity]. The retrieved focusing function (see fourth column in Fig. 6.13) still has incorrect amplitudes, except for $s_x = 0\,\mathrm{s\,m^{-1}}$ where elastic modes are decoupled. Nevertheless, the retrieved focusing function contains less events because of the simplified initial estimate $\boldsymbol{\chi}^{+}$. In this case, the retrieved focusing function only contains the events associated with an acoustic medium. Further, the violation of the (elastic) monotonicity condition for $s_x \geq 2.54 \times 10^{-4}\,\mathrm{s\,m^{-1}}$ does not cause additional artifacts.

In all of these experiments, the artifacts gradually disappear with decreasing angles of incidence, $s_x \to 0\,\mathrm{s\,m^{-1}}$, which is expected because of the nature of elastic scattering. The last experiment suggests that the acoustic Marchenko method, using the R_{pp} component of an elastic reflection response, approximately retrieves the acoustic focusing function. Due to the amplitude errors, the solution will be unreliable for AVO analysis but may be sufficiently accurate for structural imaging. These observations do not generalize to all elastic media but are expected to hold for nearly horizontally-layered media, alike the above-presented synthetic example.

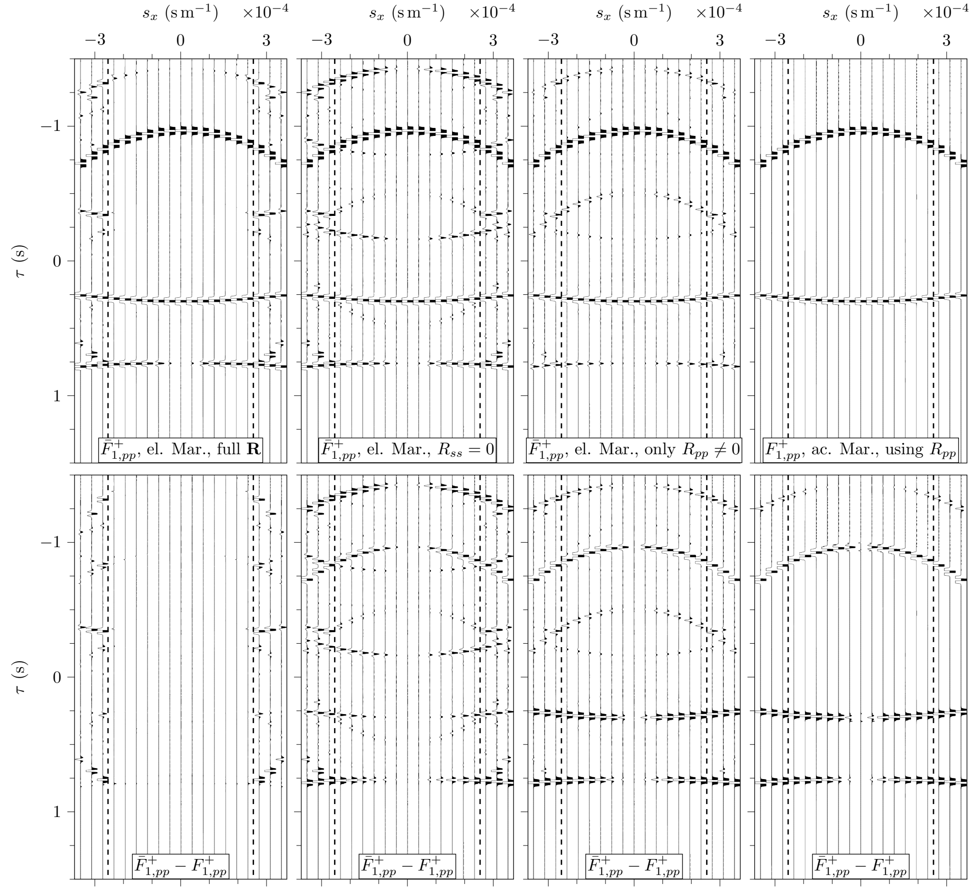

Figure 6.13: *Focusing function* $\bar{\mathbf{F}}_1^+$ *(pp component) retrieved via Eq. 6A.2 (or via its acoustic version in case of column four) using different components of the reflection response. The bottom row shows the difference with respect to a modeled (elastic) focusing function* $\mathbf{F}_1^+$ *. The vertical dashed lines confine the regime of horizontal-slownesses, which satisfy the monotonicity condition of the elastic Marchenko method* ($s_x < 2.54 \times 10^{-4}\,\mathrm{s\,m^{-1}}$)*. All panels are clipped at* $2\,\%$ *of the maximum amplitude of the top-left panel.*

z (km)	c_p (m s^{-1})	c_s (m s^{-1})	ρ (kg m^{-3})
$-\infty$ - 0.5	1994	898	4200
0.5 - 1.7	1898	1099	1100
1.7 - 2.5	2500	1387	6000
2.5 - ∞	2695	1611	3500

Table 4C.1: *Model of layered medium [identical to the model in Reinicke, 2020, chapter 4 of this thesis, Fig. 2a].*

6B Wavefield normalization

In this appendix, we discuss the effect of the wavefield normalization on the back-propagated Marchenko method. In the main part of the paper, we use a normalization defined by *Wapenaar and Berkhout* [1989], which is often referred to as pressure-normalization. We demonstrate that equations associated with the back-propagated Marchenko method equally hold for flux-normalized fields, i.e. without any modification.

The full one-way Green's matrix contains all combinations of up- $(-)$ and down-going $(+)$ source- and receiver components,

$$\mathbf{G}_{fl,p}(\mathbf{x},\mathbf{x}',\omega) = \begin{pmatrix} \mathbf{G}^{+,+}_{fl,p} & \mathbf{G}^{+,-}_{fl,p} \\ \mathbf{G}^{-,+}_{fl,p} & \mathbf{G}^{-,-}_{fl,p} \end{pmatrix}(\mathbf{x},\mathbf{x}',\omega). \tag{6B.1}$$

We use subscripts p and fl to distinguish between pressure and flux-normalized fields, respectively. The normalization is defined by the (de-)composition operators $\mathbf{L}^{\pm 1}_{fl,p}(\mathbf{x},\omega)$, that decompose the two-way Green's matrix, $\boldsymbol{\mathcal{G}}(\mathbf{x},\mathbf{x}',\omega)$ [*Ursin*, 1983; *De Hoop*, 1992; *Wapenaar and Berkhout*, 1989],

$$\mathbf{G}_{fl,p}(\mathbf{x},\mathbf{x}',\omega) = \mathbf{L}^{-1}_{fl,p}(\mathbf{x},\omega)\boldsymbol{\mathcal{G}}(\mathbf{x},\mathbf{x}',\omega)\mathbf{L}_{fl,p}(\mathbf{x}',\omega). \tag{6B.2}$$

Hence, the one-way Green's matrices associated with pressure- and flux-normalization are mutually related via successive wavefield composition and decomposition,

$$\mathbf{G}_{p}(\mathbf{x},\mathbf{x}',\omega) = \mathbf{L}^{-1}_{p}(\mathbf{x},\omega)\mathbf{L}_{fl}(\mathbf{x},\omega)\mathbf{G}_{fl}(\mathbf{x},\mathbf{x}',\omega) \times \mathbf{L}^{-1}_{fl}(\mathbf{x}',\omega)\mathbf{L}_{p}(\mathbf{x}',\omega). \tag{6B.3}$$

It can be shown that the successive composition and decomposition operators, $\mathbf{L}^{-1}_{p}(\mathbf{x},\omega)\mathbf{L}_{fl}(\mathbf{x},\omega)$, reduce to a diagonal operator,

$$\mathbf{L}^{-1}_{p}(\mathbf{x},\omega)\mathbf{L}_{fl}(\mathbf{x},\omega) = \begin{pmatrix} \mathbf{D}_3 & \mathbf{O} \\ \mathbf{O} & \mathbf{D}_3 \end{pmatrix}(\mathbf{x},\omega) \tag{6B.4}$$

where $\mathbf{D}_3$ is a 3×3 diagonal operator matrix [*Ursin*, 1983; *Wapenaar and Berkhout*, 1989]. The structure of the diagonal operator allows us to scale the submatrices of the one-way Green's matrix, $\mathbf{G}_{fl,p}(\mathbf{x},\mathbf{x}',\omega)$, independently,

$$\mathbf{G}_{p}^{\pm,\pm}(\mathbf{x},\mathbf{x}',\omega)=\mathbf{D}_3(\mathbf{x},\omega)\mathbf{G}_{fl}^{\pm,\pm}(\mathbf{x},\mathbf{x}',\omega)\mathbf{D}_3^{-1}(\mathbf{x}',\omega). \tag{6B.5}$$

The diagonal operator $\mathbf{D}_3$ scales, but does not couple, the components of the Green's matrix. Further onwards, we will demonstrate that this insight justifies that the back-propagated Marchenko method can be evaluated with flux- and pressure-normalized reflection data without any modification.

Firstly, we consider the flux-normalized representation theorems [see Eqs. 32 and 33 in *Wapenaar*, 2014],

$$\mathbf{G}_{fl}^{-,+}(\mathbf{x}_0,\mathbf{x}_i,\omega)+\mathbf{F}_{1,fl}^{-}(\mathbf{x}_0,\mathbf{x}_i,\omega)=\int_{\partial\mathbb{D}_0}\mathbf{R}_{fl}(\mathbf{x}_0,\mathbf{x}_0'',\omega)\mathbf{F}_{1,fl}^{+}(\mathbf{x}_0'',\mathbf{x}_i,\omega)\mathrm{d}^2\mathbf{x}_0'', \tag{6B.6}$$

and,

$$\left(\mathbf{G}_{fl}^{-,-}\right)^*(\mathbf{x}_0,\mathbf{x}_i,\omega)+\mathbf{F}_{1,fl}^{+}(\mathbf{x}_0,\mathbf{x}_i,\omega)=\int_{\partial\mathbb{D}_0}\mathbf{R}_{fl}^{*}(\mathbf{x}_0,\mathbf{x}_0'',\omega)\mathbf{F}_{1,fl}^{-}(\mathbf{x}_0'',\mathbf{x}_i,\omega)\mathrm{d}^2\mathbf{x}_0'', \tag{6B.7}$$

where $\mathbf{F}_{1,fl}^{\pm}$ and $\mathbf{G}_{fl}^{-,\pm}$ are the focusing and Green's functions, respectively. Upon multiplying Eqs. 6B.6 and 6B.7 by an unknown operator $\mathbf{B}_{fl}(\mathbf{x}_i,\mathbf{x}_0',\omega)$ from the right, and integrating the result over the redatuming surface $\partial\mathbb{D}_i$,

$$\int_{\partial\mathbb{D}_i}\{\cdot\}\,\mathbf{B}_{fl}(\mathbf{x}_i,\mathbf{x}_0',\omega)\,\mathrm{d}^2\mathbf{x}_i, \tag{6B.8}$$

we obtain the back-propagated representation theorems (in detail-hiding notation),

$$\mathbf{G}_{fl}^{-,+}\mathbf{B}_{fl}+\mathbf{F}_{1,fl}^{-}\mathbf{B}_{fl}=\mathbf{R}_{fl}\mathbf{F}_{1,fl}^{+}\mathbf{B}_{fl}, \tag{6B.9}$$

and,

$$\left(\mathbf{G}_{fl}^{-,-}\right)^*\mathbf{B}_{fl}+\mathbf{F}_{1,fl}^{+}\mathbf{B}_{fl}=\mathbf{R}_{fl}^{*}\mathbf{F}_{1,fl}^{-}\mathbf{B}_{fl}. \tag{6B.10}$$

Note that, the operator $\mathbf{B}_{fl}$ back-propagates the focusing and Green's functions, $\mathbf{V}_{fl}^{\pm}=\mathbf{F}_{1,fl}^{\pm}\mathbf{B}_{fl}$, $\mathbf{U}_{fl}^{-,+}=\mathbf{G}_{fl}^{-,+}\mathbf{B}_{fl}$ and $\mathbf{U}_{fl}^{-,-}=\mathbf{G}_{fl}^{-,-}\mathbf{B}_{fl}^{*}$.

Secondly, we exploit the aforementioned insight (see Eq. 6B.5). Upon multiplying Eqs. 6B.9 and 6B.10 by $\mathbf{D}_3$ from the right and by $\mathbf{D}_3^{-1}$ from the left, and by inserting the identity $\mathbf{D}_3\mathbf{D}_3^{-1}$ between matrix products, we obtain pressure-normalized fields,

$$\mathbf{G}_{p}^{-,+}\mathbf{B}_{p}+\mathbf{F}_{1,p}^{-}\mathbf{B}_{p}=\mathbf{R}_{p}\mathbf{F}_{1,p}^{+}\mathbf{B}_{p}, \tag{6B.11}$$

and,

$$\left(\mathbf{G}_{p}^{-,-}\right)^*\mathbf{B}_{p}+\mathbf{F}_{1,p}^{+}\mathbf{B}_{p}=\mathbf{R}_{p}^{*}\mathbf{F}_{1,p}^{-}\mathbf{B}_{p}. \tag{6B.12}$$

Since the matrix $\mathbf{D}_3$ only scales, but does not couple, the components of the one-way fields, the temporal separations applied by the Marchenko method do not need to be modified. Hence, using pressure- or flux-normalized reflection data merely affects the normalization of the retrieved fields.

7

Conclusions and recommendations

This chapter highlights the main conclusions of this thesis. Furthermore, recommendations and an outlook on future research are presented.

7.1 Conclusions

Marchenko-type methods pave the way for a change away from event-based and towards wavefield-based multiple-elimination strategies. Instead of combining triplets of primaries, i.e. individual events, the Marchenko method solves an inverse problem for an inverse transmission response. This strategy is advantageous because it preserves the correct amplitudes such that there is no need to adaptively subtract the predicted multiples. Amplitude fidelity is particularly important in practice when internal multiples cannot be identified as individual events but generate complicated interference patterns (chapter 6). In the following, we summarize the three main conclusions of this thesis.

Firstly, the formal generalization of the Marchenko method to the elastodynamic case is rather simple, but solving the generalized inverse problem is difficult. For example, we could formulate the single-sided homogeneous Green's function representation for elastodynamic waves (chapter 2). Another example is the freedom to modify the aforementioned inverse problem, which also generalizes beyond the acoustic case. The latter freedom was exploited by the elastodynamic extension of the plane-wave Marchenko method (chapter 3) and the backpropagation scheme (chapter 4).

In all of the aforementioned examples, solving the respective inverse problem relies on separability conditions and the availability of an initial estimate. The separability conditions are a weaker form of the monotonicity assumptions required by event-based multiple elimination methods. The advantage over event-based strategies is due to treating the overburden as one complex multiple generator rather than a stack of layers. Moreover, the original elastodynamic formulation of the Marchenko method requires an estimate of a forward-scattered transmission response as initial estimate. The backpropagated scheme (derived in chapter 4) replaces this, usually unknown, initial estimate by a trivial one.

Secondly, complete overburden-removal requires additional constraints. We demonstrated that the backpropagated scheme partially removes overburden-related internal multiples (chapter 4). However, forward-scattered waves through the overburden as well as fast multiples persist. Hence, the backpropagated Marchenko scheme postpones the problem of estimating forward-scattered waves and fast multiples. To overcome this challenge, further constraints are needed.

We showed that the desired focusing function as a matrix possesses, a so-far unexploited, minimum-phase property (up to a compensating temporal shift). This mathematical attribute is generated by the backpropagated focusing function, which is in agreement with (acoustic) observations by *Elison* [2019] and suggests that the backpropagated focusing function plays a fundamental role for Marchenko multiple-elimination methods. In chapter 5, we presented initial attempts of exploiting this property to remove the overburden-related wavefield interactions that are not addressed by the Marchenko method. In particular, we investigated how to retrieve the desired focusing function from its normal product using a minimum-phase constraint. Note that a better understanding of minimum-phase properties would be beneficial for a wide range of signal processing techniques.

Thirdly, we proposed to apply the acoustic Marchenko method to elastodynamic reflection data. Even if the aforementioned minimum-phase constraint can be used, the monotonicity condition remains (see chapter 4). In the presence of finely laminated layers with high velocity contrasts, which are characteristic for the Middle Eastern geology (e.g. see synthetic model in chapter 6), the (elastodynamic) monotonicity requirements are easily violated. Nevertheless, by applying the acoustic Marchenko method, we could remove a significant amount of multiple-related artifacts from the imaging result. In this controlled experiment, we could confirm that the retrieved structural image is nearly insensitive to unexplained elastic effects. Since the synthetic model is representative for geological settings in the Middle East, this example underlines the economic relevance of the Marchenko multiple-elimination strategy.

7.2 Recommendations and outlook

In this section, we summarize recommendations and ideas for future research. Firstly, we discuss theoretical aspects, which are mainly associated with normal product factorization. Secondly, we outline research questions that are relevant for Marchenko multiple-elimination in practice.

■ 7.2.1 Considerations for fundamental research

Geophysicists are familiar with reflection and transmission responses. The Marchenko method can be used to retrieve the usually unknown transmissions from reflections. However, this strategy solves an underdetermined inverse problem, such that the retrieved solutions are often not the desired ones. To further constrain this problem, one should consider the minimum-phase property of the desired solution, i.e. the focusing function which is an inverse transmission. For this purpose, we started to analyze the factorization of normal products with a minimum-phase constraint. The latter investigation leads to a wide range of relevant research questions.

Firstly, in chapter 5, we presented an example of approximately retrieving the focusing function (including forward-scattering) from its normal product. It should be investigated whether this approximation is sufficiently accurate to proceed with the redatuming strategy proposed in chapter 4. If this approximation is indeed sufficiently accurate, the elastodynamic Marchenko method could be brought a step closer towards applications. Note that the presented examples of normal product factorization are based on experimental observations. Therefore, further theoretical research, or at least further numerical experiments, are needed to evaluate whether this approach generalizes to other media (different medium parameters).

Secondly, chapter 5 revealed that the Wilson factorization method for minimum-phase matrices (associated with the backpropagated focusing function) utilizes the same mute as the backpropagated Marchenko method in chapter 4. This parallel combined with the fact that the backpropagated focusing function is a minimum-phase object suggest that the Marchenko method can be seen as a minimum-phase reconstruction method. Hence, further insights may be gained from the field of control-theory, which has been discussing minimum-phase matrix reconstruction for several decades.

Thirdly, our investigation of normal product factorization is limited to full-bandwidth wavefields. For applications, this analysis must be generalized to account for band-limitation. Note that band-limited normal product factorization is crucial to exploit minimum-phase properties in practice, not only in the elastodynamic case, but also in the 2D acoustic case. Besides, initial numerical experiments (not presented here) indicate that further generalizations, e.g. to dissipative media, may be possible. The latter approach has been tested for scalars. In these experiments, we factorized the crosscorrelation, as opposed to the autocorrelation, of two distinct minimum-phase functions.

■ 7.2.2 Practical considerations

In this thesis, we presented several numerical examples. When conducting these experiments, we made several observations that are beyond the scope of this thesis but should be investigated further in the future.

Firstly, correct scaling of the reflection operator is essential for the Marchenko method [also see *Brackenhoff*, 2016]. During the case study in chapter 6, we performed a series of quality checks of the amplitude scaling. We found an analysis of the water-bottom reflection particularly useful to easily recognize incorrectly scaled reflection data. For this purpose, a zero-incidence component of the reflection data is determined by stacking common-shot gathers along the receiver direction (positive and negative offsets are needed). The resulting water-bottom reflection should approximately agree with the reflection coefficient derived from impedances.

Moreover, we recommend to investigate whether accurate, automated and frequency-dependent scaling algorithms can be designed. In the presence of multicomponent data such as ocean-bottom systems, automated scaling methods would be extremely valuable and bring the Marchenko method closer to the end-users.

Secondly, the synthetic model in chapter 6 offers the opportunity to investigate how well short-period multiples can be handled. *Elison* [2019] presents a Marchenko strategy that accounts for short-period multiples under the assumption of a horizontally-layered acoustic overburden. Using the nearly horizontally-layered Middle East model, the robustness of the scheme by *Elison* [2019] can be analyzed. It can be evaluated how well the short-period multiple scheme performs in the presence of small lateral medium variations, and how well the scheme handles elastic effects.

Finally, synthetic experiments with the Middle East model could be made even more realistic. For example, one could account for noise, imperfect sampling etc. Such experiments help to evaluate the benefit that can be expected from applications to field data from the Middle East, a region where the handling of internal multiples can be a game changer.

A

An acoustic imaging method for layered non-reciprocal media

Abstract Given the increasing interest for non-reciprocal materials, we propose a novel acoustic imaging method for layered non-reciprocal media. The method we propose is a modification of the Marchenko imaging method, which handles multiple scattering between the layer interfaces in a data-driven way. We start by reviewing the basic equations for wave propagation in a non-reciprocal medium. Next, we discuss Green's functions, focusing functions, and their mutual relations, for a non-reciprocal horizontally layered medium. These relations form the basis for deriving the modified Marchenko method, which retrieves the wave field inside the non-reciprocal medium from reflection measurements at the boundary of the medium. With a numerical example we show that the proposed method is capable of imaging the layer interfaces at their correct positions, without artifacts caused by multiple scattering.

Published as: Wapenaar, K., and Reinicke, C. (2019), An acoustic imaging method for layered non-reciprocal media, *EPL (Europhysics Letters)*, **125** (3), 34003, https://doi.org/10.1209/0295-5075/125/34003.
Note that minor changes have been introduced to make the text consistent with the other chapters.

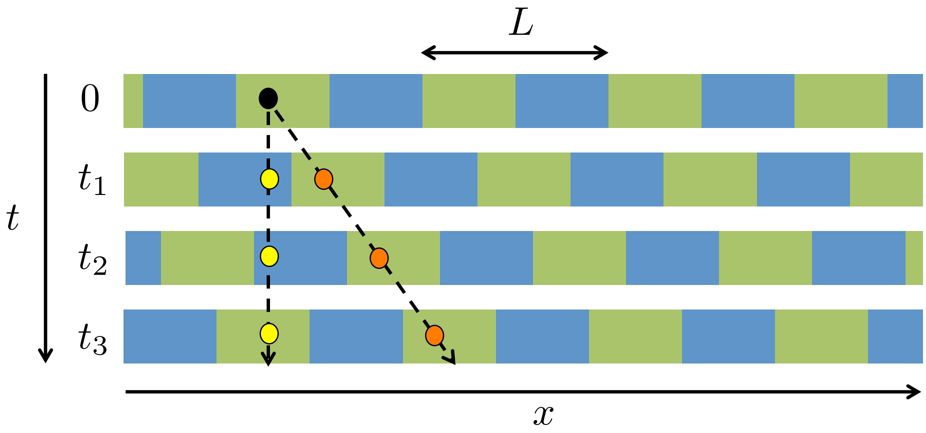

Figure A.1: *A modulated 1D phononic crystal [after Nassar et al., 2017a]. An observer at a fixed spatial position, indicated by the yellow dots, experiences a time-dependent medium, whereas an observer moving along with the modulating wave, indicated by the red dots, experiences a time-independent medium.*

1.1 Introduction

Currently there is an increasing interest for elastic wave propagation in non-reciprocal materials [*Willis*, 2012; *Norris et al.*, 2012; *Trainiti and Ruzzene*, 2016; *Nassar et al.*, 2017a; *Attarzadeh and Nouh*, 2018]. We propose a novel method that uses the single-sided reflection response of a layered non-reciprocal medium to form an image of its interior. Imaging of layered media is impeded by multiple scattering between the layer interfaces. Recent work, building on the Marchenko equation [*Marchenko*, 1955], has led to imaging methods that account for multiple scattering in 2D and 3D inhomogeneous media [*Broggini and Snieder*, 2012; *Wapenaar et al.*, 2013; *van der Neut and Wapenaar*, 2016; *Ravasi et al.*, 2016]. Here we modify Marchenko imaging for non-reciprocal media. We restrict ourselves to horizontally layered media, but the proposed method can be generalized to 2D and 3D inhomogeneous media in a similar way as has been done for reciprocal media in the aforementioned references.

1.2 Wave equation for a non-reciprocal medium

For simplicity, in this paper we approximate elastic wave propagation by an acoustic wave equation. Hence, we only consider compressional waves and ignore the conversion from compressional waves to shear waves and vice versa. This approximation is often used in reflection imaging methods and is acceptable as long as the propagation angles are moderate.

We review the basics of non-reciprocal acoustic wave propagation. For a more thorough discussion we refer to the citations given in the introduction. An example of a non-reciprocal material is a phononic crystal of which the parameters are modulated in a wave-like fashion [*Nassar et al.*, 2017a]. Figure A.1 shows a modulated 1D phononic crystal at a number of time instances. The different colors represent different values of a particular medium parameter, for example the compressibility κ. This parameter varies as a function of space and time, according to $\kappa(x,t) = \kappa(x - c_m t)$, where c_m is the modulation speed. The modulation wavelength is L. We define a moving coordinate $x' = x - c_m t$. The parameter κ in the moving coordinate system, $\kappa(x')$, is a function of space only. The same holds for the mass density $\rho(x')$. Acoustic wave propagation in a modulated material is analyzed in a moving coordinate system, hence, in a time-independent medium. In this paper we assume the modulation speed is smaller than the lowest acoustic wave propagation velocity. Moreover, for the acoustic field we consider low frequencies, so that the wavelength of the acoustic wave is much larger than the modulation wavelength L. Using homogenization theory, the small-scale parameters of the modulated material can be replaced by effective medium parameters. The theory for 3D elastic wave propagation in modulated materials, including the homogenization procedure, is extensively discussed by *Nassar et al.* [2017a]. Here we present the main equations (some details are given in the supplementary material of the published paper). We consider a coordinate system $\mathbf{x} = (x_1, x_2, x_3)$ that moves along with the modulating wave (for notational convenience we dropped the primes). The x_3-axis is pointing downward. In this moving coordinate system the macroscopic acoustic deformation equation and equation of motion for a lossless non-reciprocal material read (leading order terms only)

$$\begin{aligned} \kappa\partial_t p + (\partial_i + \xi_i\partial_t)v_i &= 0, & (1.2.1)\\ (\partial_j + \xi_j\partial_t)p + \rho^o_{jk}\partial_t v_k &= 0. & (1.2.2) \end{aligned}$$

Operator ∂_t stands for temporal differentiation and ∂_i for differentiation in the x_i-direction. Latin subscripts (except t) take on the values 1 to 3. Einstein's summation convention applies to repeated Latin subscripts, except for subscript t. Field quantities $p = p(\mathbf{x},t)$ and $v_i = v_i(\mathbf{x},t)$ are the macroscopic acoustic pressure and particle velocity, respectively. Medium parameters $\kappa = \kappa(\mathbf{x})$ and $\rho^o_{jk} = \rho^o_{jk}(\mathbf{x})$ are the effective compressibility and mass density, respectively. Note that the effective mass density may be anisotropic, even when it is isotropic at the micro scale. It obeys the symmetry relation $\rho^o_{jk} = \rho^o_{kj}$. Parameter $\xi_i = \xi_i(\mathbf{x})$ is an effective coupling parameter.

We obtain the wave equation for the acoustic pressure p by eliminating the particle velocity v_i from equations (1.2.1) and (1.2.2). To this end, define ϑ_{ij} as the inverse of ρ^o_{jk}, hence, $\vartheta_{ij}\rho^o_{jk} = \delta_{ik}$, where δ_{ik} is the Kronecker delta function. Note that $\vartheta_{ij} = \vartheta_{ji}$. Apply ∂_t to equation (1.2.1) and $(\partial_i + \xi_i\partial_t)\vartheta_{ij}$ to equation (1.2.2) and subtract the results. This gives

$$(\partial_i + \xi_i\partial_t)\vartheta_{ij}(\partial_j + \xi_j\partial_t)p - \kappa\partial_t^2 p = 0. \qquad (1.2.3)$$

As an illustration, we consider a homogeneous isotropic effective medium, with

$\vartheta_{ij} = \delta_{ij}\rho^{-1}$. For this situation the wave equation simplifies to

$$(\partial_i + \xi_i\partial_t)(\partial_i + \xi_i\partial_t)p - \frac{1}{c^2}\partial_t^2 p = 0, \tag{1.2.4}$$

with $c = 1/\sqrt{\rho\kappa}$. Consider a plane wave $p(\mathbf{x}, t) = p(t - s_i x_i)$, with s_i being the slowness in the x_i-direction. Substituting this into equation (1.2.4) we find the following relation for the slowness surface

$$(s_1 - \xi_1)^2 + (s_2 - \xi_2)^2 + (s_3 - \xi_3)^2 = \frac{1}{c^2}, \tag{1.2.5}$$

which describes a sphere with radius $1/c$ and its centre at (ξ_1, ξ_2, ξ_3). The asymmetry of this sphere with respect to the origin $(0, 0, 0)$ is a manifestation of the non-reciprocal properties of the medium.

1.3 Green's functions and focusing functions

The Marchenko method, which we discuss in the next section, makes use of specific relations between Green's functions and focusing functions. Here we introduce these functions for a lossless non-reciprocal horizontally layered acoustic medium at the hand of a numerical example. Figure A.2 shows the parameters of the layered medium as a function of the depth coordinate x_3. The half-space above the upper boundary $x_{3,0} = 0$ is homogeneous. For convenience we consider wave propagation in the (x_1, x_3)-plane (where x_1 and x_3 are moving coordinates, as discussed in the previous section). Hence, from here onward subscripts i, j and k in equations (1.2.1) and (1.2.2) take on the values 1 and 3 only.

For horizontally layered media it is convenient to decompose wave fields into plane waves and analyze wave propagation per plane-wave component. We define the plane-wave decomposition of a wave field quantity $u(x_1, x_3, t)$ as

$$u(s_1, x_3, \tau) = \int_{-\infty}^{\infty} u(x_1, x_3, \tau + s_1 x_1)\mathrm{d}x_1. \tag{1.3.1}$$

Here s_1 is the horizontal slowness and τ is a new time coordinate, usually called intercept time [*Stoffa*, 2012]. The relation with the more common plane-wave decomposition by Fourier transform becomes clear if we apply the temporal Fourier transform, $u(\omega) = \int_{-\infty}^{\infty} u(\tau)\exp(i\omega\tau)\mathrm{d}\tau$ to both sides of equation (1.3.1), which gives

$$\tilde{u}(s_1, x_3, \omega) = \int_{-\infty}^{\infty} u(x_1, x_3, \omega)\exp(-i\omega s_1 x_1)\mathrm{d}x_1. \tag{1.3.2}$$

The tilde denotes the (s_1, x_3, ω)-domain The right-hand side of equation (1.3.2) represents a spatial Fourier transform, with wavenumber $k_1 = \omega s_1$, where each wavenumber k_1 corresponds to a specific plane-wave component. Similarly, each horizontal slowness s_1 in equation (1.3.1) refers to a plane-wave component.

Consider an impulsive downgoing plane wave, with horizontal slowness $s_1 = 0.22$ ms/m, which is incident to the layered medium at $x_{3,0} = 0$. We model its response,

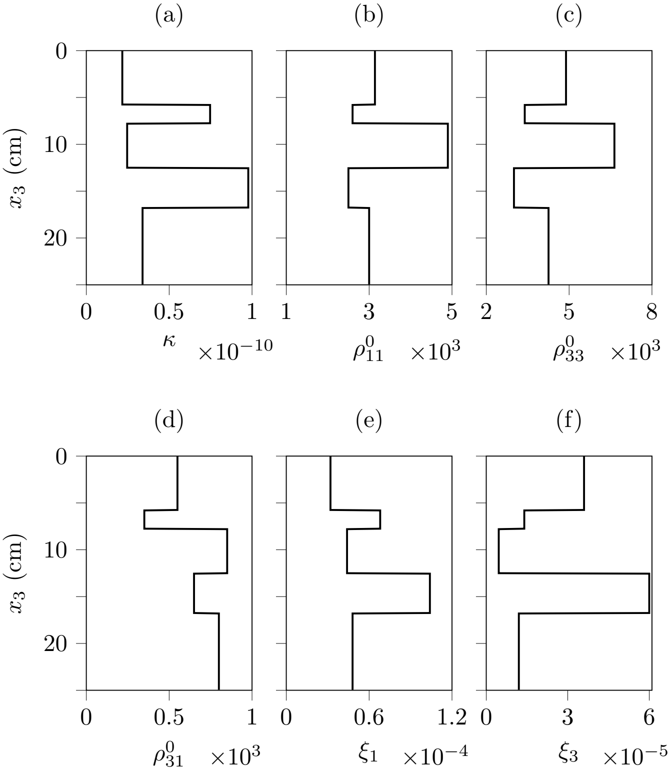

Figure A.2: *Parameters of the non-reciprocal layered medium.*

employing a (s_1, x_3, ω)-domain modeling method [*Kennett and Kerry*, 1979], adjusted for non-reciprocal media (based on equations (1.2.1) and (1.2.2), transformed to the (s_1, x_3, ω)-domain). The result, transformed back to the (s_1, x_3, τ)-domain, is shown in Figure A.3(a) (for fixed s_1). Since it is the response to an impulsive source, we denote this field as a Green's function $G(s_1, x_3, x_{3,0}, \tau)$ (actually Figure A.3(a) shows a band-limited version of the Green's function, in accordance with physical measurements, which are always band-limited). Note the different angles of the downgoing and upgoing waves directly left and right of the dotted vertical line in the first layer. This is a manifestation of the non-reciprocity of the medium. Figure A.3(b) shows the decomposed fields at $x_{3,0} = 0$ and $x_{3,A}$, where $x_{3,A}$ denotes an arbitrary depth level inside the medium (taken in this example as $x_{3,A} = 13.5$ cm). The superscripts + and − stand for downgoing and upgoing, respectively. For the downgoing field at the upper boundary we have $G^+(s_1, x_{3,0}, x_{3,0}, \tau) = \delta(\tau)$, where $\delta(\tau)$ is the Dirac delta function. For the upgoing response at the upper boundary we write $G^-(s_1, x_{3,0}, x_{3,0}, \tau) = R(s_1, x_{3,0}, \tau)$, where $R(s_1, x_{3,0}, \tau)$ is the reflection response. This is the response one would obtain from a physical reflection experiment carried

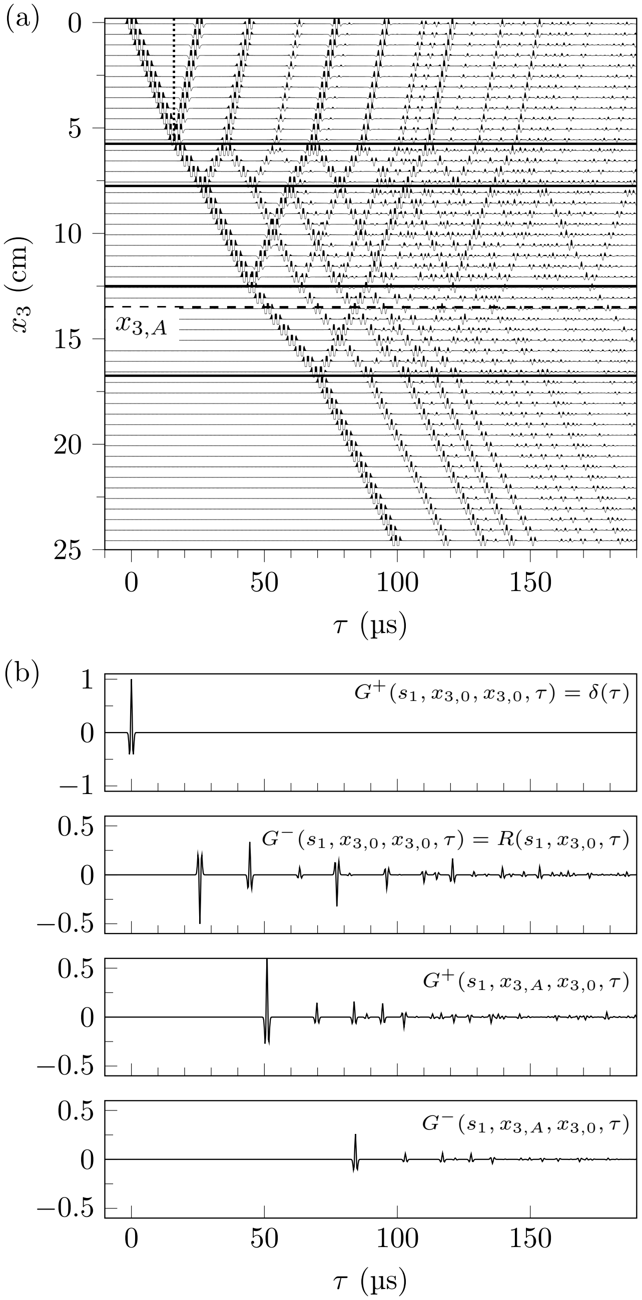

Figure A.3: *(a) Green's function $G(s_1, x_3, x_{3,0}, \tau)$, for $s_1 = 0.22$ ms/m. (b) Decomposed Green's functions at $x_{3,0} = 0$ and $x_{3,A}$.*

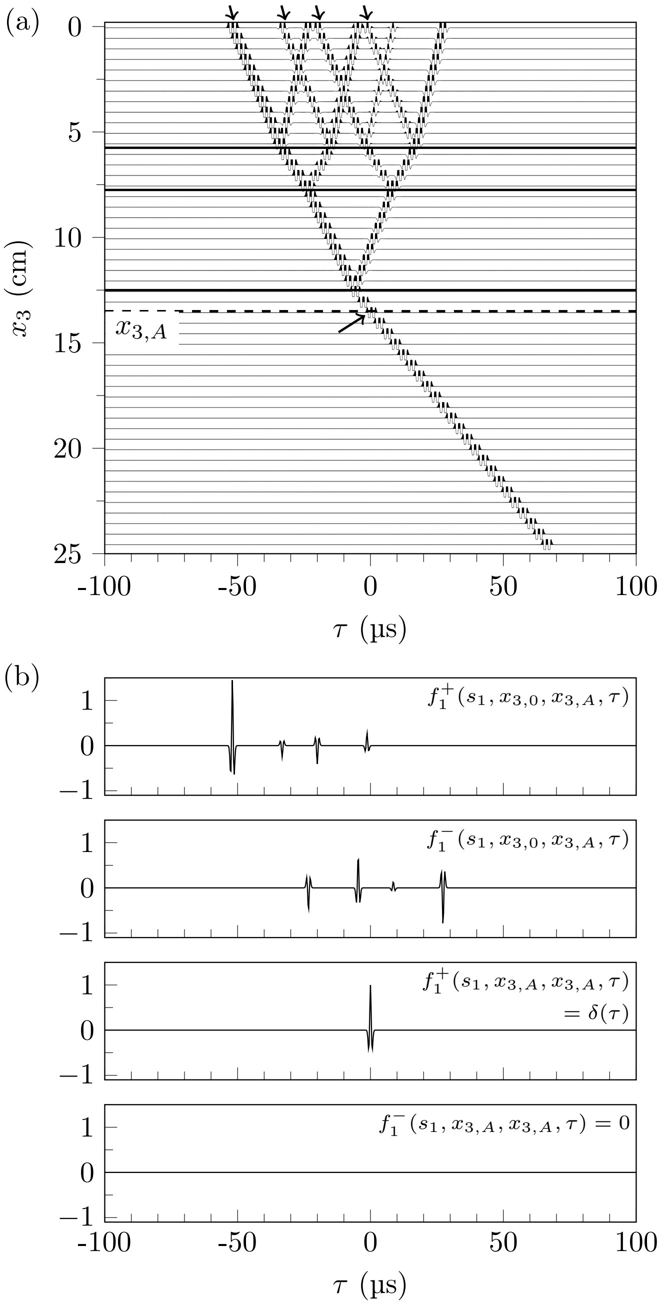

Figure A.4: *(a) Focusing function $f_1(s_1, x_3, x_{3,A}, \tau)$, for $s_1 = 0.22$ ms/m. (b) Decomposed focusing functions at $x_{3,0} = 0$ and $x_{3,A}$.*

out at the upper boundary of the layered medium, translating it to the moving coordinate system and transforming it to the plane-wave domain, using equation (1.3.1). The decomposed responses inside the medium, $G^{\pm}(s_1, x_{3,A}, x_{3,0}, \tau)$, which were obtained here by numerical modeling, are not available in a physical experiment. In the next section we discuss how these responses can be obtained from $R(s_1, x_{3,0}, \tau)$ using the Marchenko method. For this purpose, we introduce an auxiliary wave field, the so-called focusing function $f_1(s_1, x_3, x_{3,A}, \tau)$, which is illustrated in Figure A.4(a). Here $x_{3,A}$ denotes the focal depth. The focusing function is defined in a truncated version of the medium, which is identical to the actual medium above $x_{3,A}$ and homogeneous below $x_{3,A}$. The four arrows at the top of Figure A.4(a) indicate the four events of the focusing function leaving the surface $x_{3,0} = 0$ as downgoing waves; the arrow just below the dashed line indicates the focus. Figure A.4(b) shows the decomposed focusing functions at $x_{3,0} = 0$ and $x_{3,A}$. The downgoing focusing function $f_1^+(s_1, x_{3,0}, x_{3,A}, \tau)$ at the upper boundary is designed such that, after propagation through the truncated medium, it focuses at $x_{3,A}$. The focusing condition at $x_{3,A}$ is $f_1^+(s_1, x_{3,A}, x_{3,A}, \tau) = \delta(\tau)$. The upgoing response at the upper boundary is $f_1^-(s_1, x_{3,0}, x_{3,A}, \tau)$. Because the half-space below the truncated medium is by definition homogeneous, there is no upgoing response at $x_{3,A}$, hence $f_1^-(s_1, x_{3,A}, x_{3,A}, \tau) = 0$. Note that the downgoing and upgoing parts of the focusing function at $x_{3,0}$ each contain 2^{n-1} pulses, where n is the number of interfaces in the truncated medium.

In a similar way as for reciprocal media [*Wapenaar et al.*, 2013; *Slob et al.*, 2014], we derive relations between the decomposed Green's functions and focusing functions. For this we use general reciprocity theorems for decomposed wave fields $\tilde{u}^{\pm}(s_1, x_3, \omega)$ in two independent states A and B. These theorems read

$$\big(\tilde{u}_A^{+(\mathrm{c})}\tilde{u}_B^{-} - \tilde{u}_A^{-(\mathrm{c})}\tilde{u}_B^{+}\big)_{x_{3,0}} = \big(\tilde{u}_A^{+(\mathrm{c})}\tilde{u}_B^{-} - \tilde{u}_A^{-(\mathrm{c})}\tilde{u}_B^{+}\big)_{x_{3,A}} \tag{1.3.3}$$

and

$$\big(\tilde{u}_A^{+*}\tilde{u}_B^{+} - \tilde{u}_A^{-*}\tilde{u}_B^{-}\big)_{x_{3,0}} = \big(\tilde{u}_A^{+*}\tilde{u}_B^{+} - \tilde{u}_A^{-*}\tilde{u}_B^{-}\big)_{x_{3,A}}, \tag{1.3.4}$$

respectively, where superscript $*$ denotes complex conjugation. These theorems, but without the superscripts (c) in equation (1.3.3), were previously derived for reciprocal media [*Wapenaar*, 1996a]. Whereas equation (1.3.3) holds for propagating and evanescent waves, equation (1.3.4) only holds for propagating waves. The extension to non-reciprocal media is derived in the published supplementary material. For non-reciprocal media, the superscript (c) at a wave field indicates that this field is defined in the complementary medium, in which the coupling parameter ξ_i, appearing in equations (1.2.1) and (1.2.2), is replaced by $-\xi_i$. The terminology "complementary medium" is adopted from the literature on non-reciprocal electromagnetic wave theory [*Kong*, 1972; *Lindell et al.*, 1995]. Note that, when wave fields with a tilde are written without their arguments (as in equations 1.3.3 and 1.3.4), it is tacitly assumed that fields indicated by the superscript (c) are evaluated at $(-s_1, x_3, \omega)$.

To obtain relations between the decomposed Green's functions and focusing functions, we now take $\tilde{u}_A^{\pm} = \tilde{f}_1^{\pm}$ and $\tilde{u}_B^{\pm} = \tilde{G}^{\pm}$. The conditions at $x_{3,0}$ and $x_{3,A}$ discussed above are, in the (s_1, x_3, ω)-domain, $\tilde{G}^+(s_1, x_{3,0}, x_{3,0}, \omega) = 1$, $\tilde{G}^-(s_1, x_{3,0}, x_{3,0}, \omega) = \tilde{R}(s_1, x_{3,0}, \omega)$, $\tilde{f}_1^+(s_1, x_{3,A}, x_{3,A}, \omega) = 1$ and $\tilde{f}_1^-(s_1, x_{3,A}, x_{3,A}, \omega) = 0$. Making the appropriate substitutions in equations (1.3.3) and (1.3.4) we thus obtain

$$\begin{aligned}&\tilde{G}^-(s_1, x_{3,A}, x_{3,0}, \omega) + \tilde{f}_1^{-(\mathrm{c})}(-s_1, x_{3,0}, x_{3,A}, \omega)\\&\quad = \tilde{R}(s_1, x_{3,0}, \omega)\tilde{f}_1^{+(\mathrm{c})}(-s_1, x_{3,0}, x_{3,A}, \omega)\end{aligned} \tag{1.3.5}$$

and

$$\begin{aligned}&\tilde{G}^+(s_1, x_{3,A}, x_{3,0}, \omega) - \{\tilde{f}_1^+(s_1, x_{3,0}, x_{3,A}, \omega)\}^*\\&\quad = -\tilde{R}(s_1, x_{3,0}, \omega)\{\tilde{f}_1^-(s_1, x_{3,0}, x_{3,A}, \omega)\}^*,\end{aligned} \tag{1.3.6}$$

respectively. These representations express the wave field at $x_{3,A}$ inside the non-reciprocal medium in terms of reflection measurements at the surface $x_{3,0}$ of the medium. These expressions are similar to those in reference [*Slob et al.*, 2014], except that the focusing functions in equation (1.3.5) are defined in the complementary medium. Therefore we cannot follow the same procedure as in *Slob et al.* [2014] to retrieve the focusing functions from equations (1.3.5) and (1.3.6). To resolve this issue, we derive a symmetry property of the reflection response $\tilde{R}(s_1, x_{3,0}, \omega)$ and use this to obtain a second set of representations. For the fields at $x_{3,0}$ in states A and B we choose $\tilde{u}_A^+ = \tilde{u}_B^+ = 1$ and $\tilde{u}_A^- = \tilde{u}_B^- = \tilde{R}$. Substituting this into the left-hand side of equation (1.3.3) yields $\tilde{R}(s_1, x_{3,0}, \omega) - \tilde{R}^{(\mathrm{c})}(-s_1, x_{3,0}, \omega)$. We replace $x_{3,A}$ at the right-hand side of equation (1.3.3) by $x_{3,M}$, which is chosen below all inhomogeneities of the medium, so that there are no upgoing waves at $x_{3,M}$. Hence, the right-hand side of equation (1.3.3) is equal to 0. We thus find

$$\tilde{R}^{(\mathrm{c})}(-s_1, x_{3,0}, \omega) = \tilde{R}(s_1, x_{3,0}, \omega). \tag{1.3.7}$$

We obtain a second set of representations by replacing all quantities in equations (1.3.5) and (1.3.6) by the corresponding quantities in the complementary medium. Using equation (1.3.7), this yields

$$\begin{aligned}&\tilde{G}^{-(\mathrm{c})}(-s_1, x_{3,A}, x_{3,0}, \omega) + \tilde{f}_1^-(s_1, x_{3,0}, x_{3,A}, \omega)\\&\quad = \tilde{R}(s_1, x_{3,0}, \omega)\tilde{f}_1^+(s_1, x_{3,0}, x_{3,A}, \omega)\end{aligned} \tag{1.3.8}$$

and

$$\begin{aligned}&\tilde{G}^{+(\mathrm{c})}(-s_1, x_{3,A}, x_{3,0}, \omega) - \{\tilde{f}_1^{+(\mathrm{c})}(-s_1, x_{3,0}, x_{3,A}, \omega)\}^*\\&\quad = -\tilde{R}(s_1, x_{3,0}, \omega)\{\tilde{f}_1^{-(\mathrm{c})}(-s_1, x_{3,0}, x_{3,A}, \omega)\}^*,\end{aligned} \tag{1.3.9}$$

respectively.

1.4 Marchenko method for non-reciprocal media

In the previous section we obtained four representations, which we regroup into two sets. Equations (1.3.6) and (1.3.8) form the first set, containing only focusing functions in the truncated version of the actual medium. The second set is formed by equations (1.3.5) and (1.3.9), which contain only focusing functions in the truncated version of the complementary medium. All equations contain the reflection response $\tilde{R}(s_1, x_{3,0}, \omega)$ of the actual medium (i.e., the measured data, transformed to the $(s_1, x_{3,0}, \omega)$-domain).

We now outline the procedure to retrieve the focusing functions and Green's functions from the reflection response, using the Marchenko method. The procedure is similar to that described in reference *Slob et al.* [2014]. For details we refer to this reference; here we emphasize the differences. The first set of equations, (1.3.6) and (1.3.8), is transformed from the (s_1, x_3, ω)-domain to the (s_1, x_3, τ)-domain. Using time windows, the Green's functions are suppressed from these equations. Because one of the Green's functions is defined in the actual medium and the other in the complementary medium, two different time windows are needed, unlike in the Marchenko method for reciprocal media, which requires only one time window. Having suppressed the Green's functions, we are left with two equations for the two unknown focusing functions $f_1^+(s_1, x_{3,0}, x_{3,A}, \tau)$ and $f_1^-(s_1, x_{3,0}, x_{3,A}, \tau)$. These can be resolved from the reflection response $R(s_1, x_{3,0}, \tau)$ using the Marchenko method. This requires an initial estimate of the focusing function $f_1^+(s_1, x_{3,0}, x_{3,A}, \tau)$, which is defined as the inverse of the direct arrival of the transmission response of the truncated medium. In practice we define the initial estimate simply as $\delta(\tau + \tau_{\rm d})$, where $\tau_{\rm d} = \tau_{\rm d}(s_1, x_{3,0}, x_{3,A}, \tau)$ is the travel time of the direct arrival, which can be derived from a background model of the medium. Since we only need a travel time, a smooth background model suffices; no information about the position and strength of the interfaces is needed. Once the focusing functions have been found, they can be substituted in the time domain versions of equations (1.3.6) and (1.3.8), which yields the Green's functions $G^+(s_1, x_{3,A}, x_{3,0}, \tau)$ and $G^{-({\rm c})}(-s_1, x_{3,A}, x_{3,0}, \tau)$. Note that only the retrieved downgoing part of the Green's function, G^+, is defined in the actual medium. Therefore the procedure continues by applying the Marchenko method to the time domain versions of equations (1.3.5) and (1.3.9). This yields the focusing functions $f_1^{+({\rm c})}(-s_1, x_{3,0}, x_{3,A}, \tau)$ and $f_1^{-({\rm c})}(-s_1, x_{3,0}, x_{3,A}, \tau)$ and, subsequently, the Green's functions $G^{+({\rm c})}(-s_1, x_{3,A}, x_{3,0}, \tau)$ and $G^-(s_1, x_{3,A}, x_{3,0}, \tau)$. Here the retrieved upgoing part of the Green's function, G^-, is defined in the actual medium. This completes the procedure for the retrieval of the downgoing and upgoing parts of the Green's functions in the actual medium at depth level $x_{3,A}$ for horizontal slowness s_1. This procedure can be repeated for any slowness corresponding to propagating waves and for any focal depth $x_{3,A}$.

Finally, we discuss how the retrieved Green's functions can be used for imaging. Similar as in a reciprocal medium, the relation between these Green's functions in the (s_1, x_3, ω)-domain is

$$\tilde{G}^-(s_1, x_{3,A}, x_{3,0}, \omega) = \tilde{R}(s_1, x_{3,A}, \omega)\tilde{G}^+(s_1, x_{3,A}, x_{3,0}, \omega), \tag{1.4.1}$$

where $\tilde{R}(s_1, x_{3,A}, \omega)$ is the plane-wave reflection response at depth level $x_{3,A}$ of the medium below $x_{3,A}$. Inverting this equation yields an estimate of the reflection response, according to

$$\langle \tilde{R}(s_1, x_{3,A}, \omega)\rangle = \frac{\tilde{G}^-(s_1, x_{3,A}, x_{3,0}, \omega)}{\tilde{G}^+(s_1, x_{3,A}, x_{3,0}, \omega)}. \tag{1.4.2}$$

Imaging the reflectivity at $x_{3,A}$ involves selecting the $\tau = 0$ component of the inverse Fourier transform of $\langle \tilde{R}(s_1, x_{3,A}, \omega)\rangle$, hence

$$\langle R(s_1, x_{3,A}, \tau = 0)\rangle = \frac{1}{2\pi}\int_{-\infty}^{\infty} \langle \tilde{R}(s_1, x_{3,A}, \omega)\rangle \mathrm{d}\omega. \tag{1.4.3}$$

Substituting equation (1.4.2), stabilizing the division (and suppressing the arguments of the Green's functions), we obtain

$$\langle R(s_1, x_{3,A}, 0)\rangle = \frac{1}{2\pi}\int_{-\infty}^{\infty} \frac{\tilde{G}^-\{\tilde{G}^+\}^*}{\tilde{G}^+\{\tilde{G}^+\}^* + \epsilon}\mathrm{d}\omega. \tag{1.4.4}$$

1.5 Numerical example

We consider again the layered medium of Figure A.2. Using the same modeling approach as before, we model the reflection responses to tilted downgoing plane waves at $x_{3,0} = 0$, this time for a range of horizontal slownesses s_1. The result, transformed to the $(s_1, x_{3,0}, \tau)$-domain and convolved with a wavelet with a central frequency of 600 kHz, is shown in Figure A.5(a). To emphasize the multiples (only for the display), a time-dependent amplitude gain, using the function $\exp\{3\tau/375\mu s\}$, has been applied. Note the asymmetry with respect to $s_1 = 0$ as a result of the non-reciprocity of the medium. The last trace (for $s_1 = 0.22$ ms/m) corresponds with the second trace in Figure A.3(b).

We define the focal depth in the fourth layer, at $x_{3,A} = 13.5$ cm. Using the Marchenko method, we retrieve the focusing functions $f_1^{\pm}(s_1, x_{3,0}, x_{3,A}, \tau)$ and $f_1^{\pm(\mathrm{c})}(-s_1, x_{3,0}, x_{3,A}, \tau)$ from the reflection response $R(s_1, x_{3,0}, \tau)$ and the travel times τ_{d} between $x_{3,0}$ and $x_{3,A}$. One of these focusing functions, $f_1^+(s_1, x_{3,0}, x_{3,A}, \tau)$, is shown in Figure A.5(b). The last trace (for $s_1 = 0.22$ ms/m) corresponds with the first trace in Figure A.4(b).

Using the reflection response and the retrieved focusing functions, we obtain the Green's functions $G^+(s_1, x_{3,A}, x_{3,0}, \tau)$ and $G^-(s_1, x_{3,A}, x_{3,0}, \tau)$ from the time domain versions of equations (1.3.6) and (1.3.5), see Figure A.6 (same amplitude gain as in Figure A.5(a)). From the Fourier transform of these Green's functions, an image is obtained at $x_{3,A}$ as a function of s_1, using equation (1.4.4). Repeating this for all $x_{3,A}$ we obtain what we call the Marchenko image, shown in Figure A.7(c). For comparison, Figure A.7(a) shows an image obtained by a primary imaging method, ignoring the non-reciprocal aspects of the medium, and Figure A.7(b) shows the improvement when non-reciprocity is taken into account (but multiples are still ignored). For comparison, Figure A.7(d) shows the true reflectivity with the same filters applied as for the imaging results. Note that the match of the Marchenko imaging result with the true reflectivity is very accurate. The relative errors, except for the leftmost traces, are less than 2%.

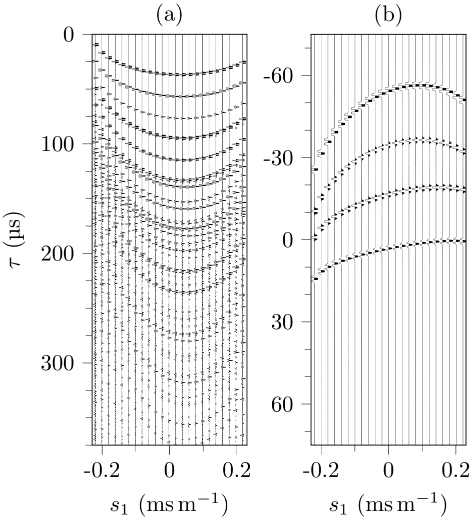

Figure A.5: *(a) Modeled reflection response* $R(s_1, x_{3,0}, \tau)$*. (b) Retrieved focusing function* $f_1^+(s_1, x_{3,0}, x_{3,A}, \tau)$*.*

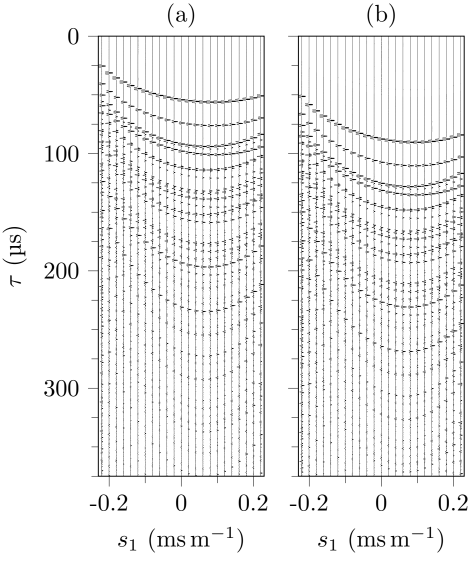

Figure A.6: *(a) Retrieved Green's function* $G^+(s_1, x_{3,A}, x_{3,0}, \tau)$*. (b) Idem,* $G^-(s_1, x_{3,A}, x_{3,0}, \tau)$*.*

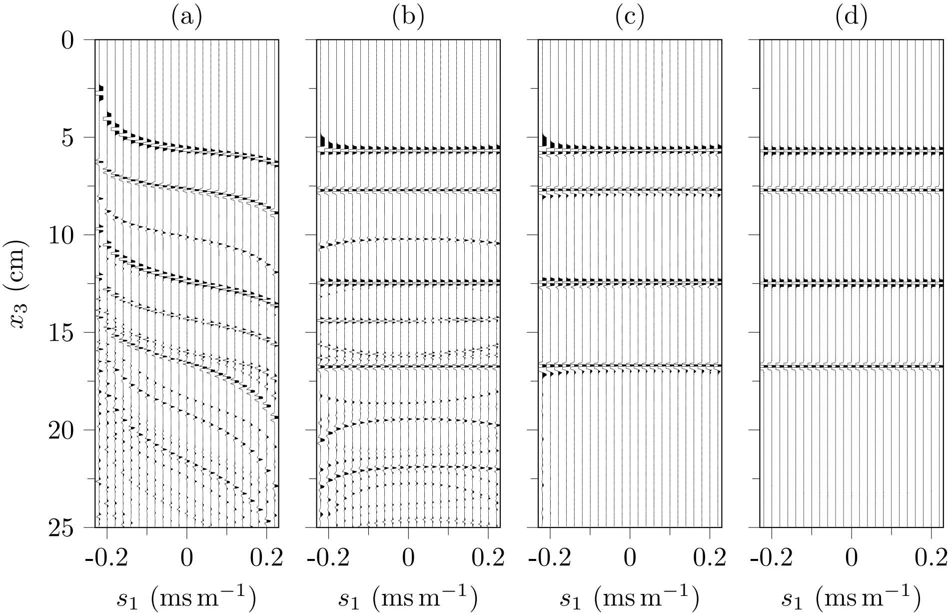

Figure A.7: *Images of the layered non-reciprocal medium. (a) Primary image, accounting for anisotropy but ignoring non-reciprocity. (b) Idem, but accounting for non-reciprocity. (c) Marchenko image. (d) True reflectivity.*

Note that we assumed that the medium is lossless. In case of a medium with losses, modifications are required. For moderate losses that are approximately constant throughout the medium, one can apply a time-dependent loss compensation factor to the reflection response $R(s_1, x_{3,0}, \tau)$ before applying the Marchenko method (assuming an estimate of the loss parameter is available). Alternatively, when the medium is accessible from two sides, the Marchenko imaging method of *Slob* [2016], modified for non-reciprocal media, can be applied directly to the data. This removes the need to apply a loss compensation factor.

1.6 Conclusions

We have introduced a new imaging method for layered non-reciprocal materials. The proposed method is a modification of the Marchenko imaging method, which is capable of handling multiple scattering in a data-driven way (i.e., no information is required about the layer interfaces that cause the multiple scattering). To account for the non-reciprocal properties of the medium, we derived two sets of representations for the Marchenko method, one set for the actual medium and one set for the complementary medium. Using a symmetry relation between the reflection responses of both media, we arrived at a method which retrieves all quantities needed for imaging (focusing functions and Green's functions in the actual and the complementary medium) from the reflection response of the actual medium. We illustrated the method with a numerical example, demonstrating the improvement over standard primary imaging methods. The proposed method can be extended for 2D and 3D inhomogeneous media, in a similar way as has been done for the Marchenko method in reciprocal media.

Acknowledgments

We thank an anonymous reviewer for a constructive review, which helped us to improve the readability of the paper. This work has received funding from the European Union's Horizon 2020 research and innovation program: European Research Council (grant agreement 742703) and Marie Skłodowska-Curie (grant agreement 641943).

B

Unified wave field retrieval and imaging method for inhomogeneous non-reciprocal media

Abstract Acoustic imaging methods often ignore multiple scattering. This leads to false images in cases where multiple scattering is strong. Marchenko imaging has recently been introduced as a data-driven way to deal with internal multiple scattering. Given the increasing interest in non-reciprocal materials, both for acoustic and electromagnetic applications, we propose to modify the Marchenko method for imaging such materials. We formulate a unified wave equation for non-reciprocal materials, exploiting the similarity between acoustic and electromagnetic wave phenomena. This unified wave equation forms the basis for deriving reciprocity theorems that interrelate wave fields in a non-reciprocal medium and its complementary version. Next, we reformulate these theorems for downgoing and upgoing wave fields. From these decomposed reciprocity theorems we derive representations of the Green's function inside the non-reciprocal medium, in terms of the reflection response at the surface and focusing functions inside the medium and its complementary version. These representations form the basis for deriving a modified version of the Marchenko method to retrieve the wave field inside a non-reciprocal medium and to form an image, free from artefacts related to multiple scattering. We illustrate the proposed method at the hand of the numerically modeled reflection response of a horizontally layered medium.

Published as: Wapenaar, K., and Reinicke, C. (2019), Unified wave field retrieval and imaging method for inhomogeneous non-reciprocal media, *The Journal of the Acoustical Society of America*, **146** (1), 810–825, https://doi.org/10.1121/1.5114912.
Note that minor changes have been introduced to make the text consistent with the other chapters.

2.1 Introduction

Acoustic imaging methods are traditionally based on the single-scattering assumption [*Claerbout*, 1971; *Stolt*, 1978; *Berkhout and Palthe*, 1979; *Williams and Maynard*, 1980; *Devaney*, 1982; *Bleistein and Cohen*, 1982; *Maynard et al.*, 1985; *Langenberg et al.*, 1986; *McMechan*, 1983; *Esmersoy and Oristaglio*, 1988; *Oristaglio*, 1989; *Norton*, 1992; *Wu*, 2004; *Lindsey and Braun*, 2004; *Etgen et al.*, 2009]. Multiply scattered waves are not properly handled by these methods and may lead to false images overlaying the desired primary image. Several approaches have been developed that account for multiple scattering. For the sake of the discussion it is important to distinguish between different classes of multiply scattered waves. Waves that have scattered at least once at the surface of the medium are called surface-related multiples. This type of multiple scattering is particularly severe in exploration geophysics. However, because the scattering boundary is known, this class of multiples is relatively easily dealt with. Successful methods have been developed to suppress surface-related multiples prior to imaging [*Verschuur et al.*, 1992; *Carvalho et al.*, 1992; *Van Borselen et al.*, 1996; *Biersteker*, 2001; *Pica et al.*, 2005; *Dragoset et al.*, 2010]. Waves that scatter several times inside the medium before being recorded at the surface are called internal multiples. Internal multiple scattering may occur at heterogeneities at many scales. We may distinguish between deterministic scattering at well-separated scatterers, giving rise to long period multiples, and diffuse scattering in stochastic media. Of course this distinction is not always sharp. In this paper we only consider the first type of internal multiple scattering, which typically occurs in layered media (which, in general, may have curved interfaces and varying parameters in the layers). Several imaging approaches that account for deterministic internal multiples are currently under development, such as the inverse scattering series approach [*Weglein et al.*, 1997; *ten Kroode*, 2002; *Weglein et al.*, 2003], full wave field migration [*Berkhout*, 2014; *Davydenko and Verschuur*, 2017], and Marchenko imaging. The latter approach builds on a 1D autofocusing procedure [*Rose*, 2002a,b; *Broggini and Snieder*, 2012], which has been generalised for 2D and 3D inhomogeneous media [*Wapenaar et al.*, 2012, 2014b; *Broggini et al.*, 2014; *Behura et al.*, 2014; *Meles et al.*, 2014; *van der Neut et al.*, 2015; *van der Neut and Wapenaar*, 2016; *Thorbecke et al.*, 2017; *van der Neut et al.*, 2017; *Singh et al.*, 2017; *Mildner et al.*, 2017; ?]. This methodology retrieves the wave fields inside a medium, including all internal multiples, in a data-driven way. Such wave fields could be used, for example, to monitor changes of the material over time. Moreover, in a next step these wave fields can be used to form an image of the material, in which artefacts due to the internal multiples are suppressed. Promising results have been obtained with geophysical [*Ravasi et al.*, 2016; *Ravasi*, 2017; *Staring et al.*, 2018; *Brackenhoff et al.*, 2019; *Wapenaar et al.*, 2018] and ultrasonic data [*Wapenaar et al.*, 2018; *Cui et al.*, 2018].

To date, the application of the Marchenko method has been restricted to reciprocal media. With the increasing interest in non-reciprocal materials, both in electromagnetics [*Willis*, 2011; *He et al.*, 2011; *Ardakani*, 2014] and in acoustics and elastodynamics [*Willis*, 2012; *Norris et al.*, 2012; *Gu et al.*, 2016; *Trainiti and*

Ruzzene, 2016; *Nassar et al.*, 2017b,a; *Attarzadeh and Nouh*, 2018], it is opportune to modify the Marchenko method for non-reciprocal media. We start with a brief review of the wave equation for non-reciprocal media. By restricting this to scalar waves in a 2D plane, it is possible to capture different wave phenomena by a unified wave equation. Next, we formulate reciprocity theorems for waves in a non-reciprocal medium and its complementary version (the complementary medium will be defined later). From these reciprocity theorems we derive Green's function representations, which form the basis for the Marchenko method in non-reciprocal media. We illustrate the new method with a numerical example, showing that it has the potential to accurately retrieve the wave fields inside a non-reciprocal medium and to image this medium, without false images related to multiply scattered waves.

2.2 Unified wave equation for non-reciprocal media

Consider the following unified equations in the low-frequency limit for 2D wave propagation in the (x_1, x_3)-plane in inhomogeneous, lossless, anisotropic, non-reciprocal media

$$\alpha\partial_t P + (\partial_r + \gamma_r\partial_t)Q_r = B, \tag{2.2.1}$$

$$(\partial_r + \gamma_r\partial_t)P + \beta_{rs}\partial_t Q_s = C_r. \tag{2.2.2}$$

These equations hold for transverse-electric (TE), transverse-magnetic (TM), horizontally-polarised shear (SH) and acoustic (AC) waves. They are formulated in the space-time $(\mathbf{x}, t)$ domain, with $\mathbf{x} = (x_1, x_3)$. Operator ∂_r stands for differentiation in the x_r direction. Lower-case subscripts r and s take the values 1 and 3 only; Einstein's summation convention applies for repeated subscripts. Operator ∂_t stands for temporal differentiation. The wave field quantities ($P = P(\mathbf{x}, t)$ and $Q_r = Q_r(\mathbf{x}, t)$) and source quantities ($B = B(\mathbf{x}, t)$ and $C_r = C_r(\mathbf{x}, t)$) are macroscopic quantities. These are often denoted as $\langle P\rangle$ etc. [*Willis*, 2011], but for notational convenience we will not use the brackets. The medium parameters ($\alpha = \alpha(\mathbf{x})$, $\beta_{rs} = \beta_{rs}(\mathbf{x})$ and $\gamma_r = \gamma_r(\mathbf{x})$) are effective parameters. In general they are anisotropic at macro scale (with $\beta_{rs} = \beta_{sr}$), even when they are isotropic at micro scale. Wave field quantities, source quantities and medium parameters are specified for the different wave phenomena in Table 1. For TE and TM waves, the macroscopic wave field quantities are E (electric field strength) and H (magnetic field strength), the macroscopic source functions are J^{e} (external electric current density) and J^{m} (external magnetic current density), and the effective medium parameters are ε^o (permittivity), μ (permeability) and ξ (coupling parameter). For SH and AC waves, the macroscopic wave field quantities are v (particle velocity), τ (stress) and p (acoustic pressure), the macroscopic source functions are F (external force density), h (external deformation-rate density) and q (volume injection-rate density), and the effective medium parameters are ρ^o(mass density), s (compliance), κ (compressibility) and ξ (coupling parameter). For further details we refer Appendix A of the published paper.

By eliminating Q_r from equations (2.2.1) and (2.2.2) we obtain a scalar wave equation for field quantity P, according to

$$(\partial_r + \gamma_r\partial_t)\vartheta_{rs}(\partial_s + \gamma_s\partial_t)P - \alpha\partial_t^2 P = (\partial_r + \gamma_r\partial_t)\vartheta_{rs}C_s - \partial_t B, \quad (2.2.3)$$

see Appendix A of the published paper for the derivation. Here ϑ_{rs} is the inverse of β_{rs}. Compare equation (2.2.3) with the common scalar wave equation for waves in isotropic reciprocal media

$$\partial_r \frac{1}{\beta}\partial_r P - \alpha\partial_t^2 P = \partial_r \frac{1}{\beta}C_r - \partial_t B. \quad (2.2.4)$$

In equation (2.2.3), $\partial_r + \gamma_r\partial_t$ replaces ∂_r, with γ_r being responsible for the non-reciprocal behaviour. Moreover, ϑ_{rs} replaces $1/\beta$, thus accounting for anisotropy of the effective non-reciprocal medium.

To illustrate the physical meaning of the parameter γ_r, we consider the 1D version of equation (2.2.3) for a homogeneous, isotropic, source-free medium, i.e.

$$(\partial_1 + \gamma\partial_t)(\partial_1 + \gamma\partial_t)P - \alpha\beta\partial_t^2 P = 0. \quad (2.2.5)$$

Its solution reads

$$P^{\pm}(x_1, t) = S\Big(t \mp \frac{x_1}{c}(1 \pm \gamma c)\Big), \quad (2.2.6)$$

with $S(t)$ being an arbitrary time-dependent function and $c = (\alpha\beta)^{-1/2}$ the propagation velocity of the corresponding reciprocal medium. Note that $P^+(x_1, t)$ propagates in the positive x_1-direction with slowness $(1 + \gamma c)/c$, whereas $P^-(x_1, t)$ propagates in the negative x_1-direction with slowness $(1 - \gamma c)/c$. Hence, γ determines the asymmetry of the slownesses in opposite directions. Throughout this paper we assume that $|\gamma_r|$ is smaller than the lowest inverse propagation velocity of the corresponding reciprocal anisotropic medium.

2.3 Reciprocity theorems for a non-reciprocal medium and its complementary version

We derive reciprocity theorems in the space-frequency $(\mathbf{x}, \omega)$-domain for wave fields in a non-reciprocal medium and its complementary version. To this end, we define the temporal Fourier transform of a space- and time-dependent function $P(\mathbf{x}, t)$ as

$$P(\mathbf{x}, \omega) = \int_{-\infty}^{\infty} P(\mathbf{x}, t)\exp(i\omega t)\mathrm{d}t, \quad (2.3.1)$$

where ω is the angular frequency and i the imaginary unit. For notational convenience we use the same symbol for quantities in the time domain and in the frequency domain. We use equation (2.3.1) to transform equations (2.2.1) and (2.2.2) to the space-frequency domain. The temporal differential operators ∂_t are thus replaced by $-i\omega$, hence

$$-i\omega\alpha P + (\partial_r - i\omega\gamma_r)Q_r = B, \quad (2.3.2)$$

$$(\partial_r - i\omega\gamma_r)P - i\omega\beta_{rs}Q_s = C_r, \quad (2.3.3)$$

with $P = P(\mathbf{x},\omega)$, $Q_r = Q_r(\mathbf{x},\omega)$, $B = B(\mathbf{x},\omega)$ and $C_r = C_r(\mathbf{x},\omega)$. A reciprocity theorem formulates a mathematical relation between two independent states [*Fokkema and van den Berg*, 2013; *de Hoop*, 1995; *Achenbach and Achenbach*, 2003]. We indicate the wave fields, sources and medium parameters in the two states by subscripts A and B. Consider the quantity

$$\partial_r(P_A Q_{r,B} - Q_{r,A} P_B). \tag{2.3.4}$$

Applying the product rule for differentiation, using equations (2.3.2) and (2.3.3) for states A and B, using $\beta_{sr} = \beta_{rs}$ [*Nassar et al.*, 2017a; *Kong*, 1972; *Birss and Shrubsall*, 1967], integrating the result over domain $\mathbb{D}$ enclosed by boundary $\partial\mathbb{D}$ with outward pointing normal vector $\mathbf{n} = (n_1, n_3)$ and applying the theorem of Gauss, we obtain

$$\begin{aligned}
&\oint_{\partial\mathbb{D}} (P_A Q_{r,B} - Q_{r,A} P_B) n_r \mathrm{d}\mathbf{x} = \qquad (2.3.5)\\
&i\omega \int_{\mathbb{D}} \Big((\alpha_B - \alpha_A) P_A P_B - (\beta_{rs,B} - \beta_{rs,A}) Q_{r,A} Q_{s,B}\Big) \mathrm{d}\mathbf{x}\\
&+ i\omega \int_{\mathbb{D}} (\gamma_{r,B} + \gamma_{r,A})(P_A Q_{r,B} - Q_{r,A} P_B) \mathrm{d}\mathbf{x}\\
&+ \int_{\mathbb{D}} (C_{r,A} Q_{r,B} - Q_{r,A} C_{r,B} + P_A B_B - B_A P_B) \mathrm{d}\mathbf{x}.
\end{aligned}$$

This is the general reciprocity theorem of the convolution type. When the medium parameters α, β_{rs} and γ_r are identical in both states, then the first integral on the right-hand side vanishes, but the second integral, containing γ_r, does not vanish. When we choose $\gamma_{r,A} = -\gamma_{r,B} = -\gamma_r$, then the second integral also vanishes. For this situation we call state B, with parameters α, β_{rs} and γ_r, the actual state, and state A, with parameters α, β_{rs} and $-\gamma_r$, the complementary state [*Kong*, 1972; *Lindell et al.*, 1995] (also known as the Lorentz-adjoint state [*Altman and Suchy*, 2011]). We indicate the complementary state by a superscript (c). Hence

$$\begin{aligned}
&\oint_{\partial\mathbb{D}} (P_A^{(\mathrm{c})} Q_{r,B} - Q_{r,A}^{(\mathrm{c})} P_B) n_r \mathrm{d}\mathbf{x} = \qquad (2.3.6)\\
&\int_{\mathbb{D}} (C_{r,A}^{(\mathrm{c})} Q_{r,B} - Q_{r,A}^{(\mathrm{c})} C_{r,B} + P_A^{(\mathrm{c})} B_B - B_A^{(\mathrm{c})} P_B) \mathrm{d}\mathbf{x}.
\end{aligned}$$

This reciprocity theorem will play a role in the derivation of Green's function representations for the Marchenko method for non-reciprocal media (section 2.4). Here we use it to derive a relation between Green's functions in states A and B. For the complementary state A we choose a unit monopole point source at $\mathbf{x}_S$ in $\mathbb{D}$, hence $B_A^{(\mathrm{c})}(\mathbf{x},\omega) = \delta(\mathbf{x} - \mathbf{x}_S)$, where $\delta(\mathbf{x})$ is the Dirac delta function. The response to this point source is the Green's function in state A, hence $P_A^{(\mathrm{c})}(\mathbf{x},\omega) = G^{(\mathrm{c})}(\mathbf{x},\mathbf{x}_S,\omega)$. Similarly, for state B we choose a unit monopole point source at $\mathbf{x}_R$ in $\mathbb{D}$, hence $B_B(\mathbf{x},\omega) = \delta(\mathbf{x} - \mathbf{x}_R)$ and $P_B(\mathbf{x},\omega) = G(\mathbf{x},\mathbf{x}_R,\omega)$. We substitute these expressions into equation (2.3.6) and set the other source quantities, $C_{r,A}^{(\mathrm{c})}$ and $C_{r,B}$, to zero.

Further, we assume that Neumann or Dirichlet boundary conditions apply at $\partial\mathbb{D}$, or that the medium at and outside $\partial\mathbb{D}$ is homogeneous and reciprocal. In each of these cases the boundary integral vanishes. We thus obtain [*Slob and Wapenaar*, 2009; *Willis*, 2012]

$$G^{(\mathrm{c})}(\mathbf{x}_R,\mathbf{x}_S,\omega) = G(\mathbf{x}_S,\mathbf{x}_R,\omega). \tag{2.3.7}$$

The left-hand side is the response to a source at $\mathbf{x}_S$ in the complementary medium (with parameter $-\gamma_r$), observed by a receiver at $\mathbf{x}_R$. The right-hand side is the response to a source at $\mathbf{x}_R$ in the actual medium (with parameter γ_r), observed by a receiver at $\mathbf{x}_S$. Note the analogy with the flow-reversal theorem for waves in flowing media [*Lyamshev*, 1961; *Godin*, 1997; *Wapenaar and Fokkema*, 2004].
Next, we consider the quantity

$$\partial_r(P_A^*Q_{r,B} + Q_{r,A}^*P_B). \tag{2.3.8}$$

Superscript $*$ denotes complex conjugation. Following the same steps as before, we obtain

$$\begin{aligned}
&\oint_{\partial\mathbb{D}}(P_A^*Q_{r,B} + Q_{r,A}^*P_B)n_r\mathrm{d}\mathbf{x} = \qquad\qquad (2.3.9)\\
&i\omega\int_{\mathbb{D}}\Big((\alpha_B-\alpha_A)P_A^*P_B + (\beta_{rs,B}-\beta_{rs,A})Q_{r,A}^*Q_{s,B}\Big)\mathrm{d}\mathbf{x}\\
&+i\omega\int_{\mathbb{D}}(\gamma_{r,B}-\gamma_{r,A})(P_A^*Q_{r,B} + Q_{r,A}^*P_B)\mathrm{d}\mathbf{x}\\
&+\int_{\mathbb{D}}(C_{r,A}^*Q_{r,B} + Q_{r,A}^*C_{r,B} + P_A^*B_B + B_A^*P_B)\mathrm{d}\mathbf{x}.
\end{aligned}$$

This is the general reciprocity theorem of the correlation type. When the medium parameters α, β_{rs} and γ_r are identical in both states, then the first and second integral on the right-hand side vanish. Hence

$$\begin{aligned}
&\oint_{\partial\mathbb{D}}(P_A^*Q_{r,B} + Q_{r,A}^*P_B)n_r\mathrm{d}\mathbf{x} = \qquad\qquad (2.3.10)\\
&\int_{\mathbb{D}}(C_{r,A}^*Q_{r,B} + Q_{r,A}^*C_{r,B} + P_A^*B_B + B_A^*P_B)\mathrm{d}\mathbf{x}.
\end{aligned}$$

Also this reciprocity theorem will play a role in the derivation of Green's function representations for the Marchenko method for non-reciprocal media.

2.4 Green's function representations for the Marchenko method

We use the reciprocity theorems of the convolution and correlation type (equations (2.3.6) and (2.3.10)) to derive Green's function representations for the Marchenko method for non-reciprocal media. The derivation is similar to that for reciprocal media [*Wapenaar et al.*, 2014b]; here we emphasise the differences. We consider a spatial domain $\mathbb{D}$, enclosed by two infinite horizontal boundaries $\partial\mathbb{D}_0$ and $\partial\mathbb{D}_A$ (with $\partial\mathbb{D}_A$ below $\partial\mathbb{D}_0$), and two finite vertical side boundaries (at $x_1 \to \pm\infty$), see Figure

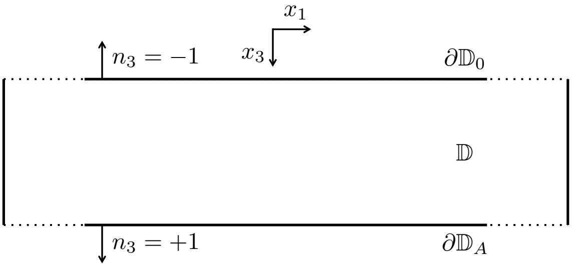

Figure B.1: *Modified configuration for the reciprocity theorems.*

B.1. The positive x_3-axis points downward. The normal vectors at $\partial\mathbb{D}_0$ and $\partial\mathbb{D}_A$ are $\mathbf{n}=(0,-1)$ and $\mathbf{n}=(0,1)$, respectively. The boundary integrals in equations (2.3.6) and (2.3.10) along the vertical side boundaries vanish [*Wapenaar and Berkhout*, 1989]. Assuming there are no sources in $\mathbb{D}$ in both states, the reciprocity theorems thus simplify to

$$\int_{\partial\mathbb{D}_0}(P_A^{(\mathrm{c})}Q_{3,B}-Q_{3,A}^{(\mathrm{c})}P_B)\mathrm{d}\mathbf{x}=\int_{\partial\mathbb{D}_A}(P_A^{(\mathrm{c})}Q_{3,B}-Q_{3,A}^{(\mathrm{c})}P_B)\mathrm{d}\mathbf{x} \quad (2.4.1)$$

and

$$\int_{\partial\mathbb{D}_0}(P_A^{*}Q_{3,B}+Q_{3,A}^{*}P_B)\mathrm{d}\mathbf{x}=\int_{\partial\mathbb{D}_A}(P_A^{*}Q_{3,B}+Q_{3,A}^{*}P_B)\mathrm{d}\mathbf{x}. \quad (2.4.2)$$

For the derivation of the representations for the Marchenko method it is convenient to decompose the wave field quantities in these theorems into downgoing and upgoing fields in both states. Consider the following relations

$$\mathbf{q}=\boldsymbol{\mathcal{L}}\mathbf{p},\quad \mathbf{p}=\boldsymbol{\mathcal{L}}^{-1}\mathbf{q}, \quad (2.4.3)$$

with wave vectors $\mathbf{q}=\mathbf{q}(\mathbf{x},\omega)$ and $\mathbf{p}=\mathbf{p}(\mathbf{x},\omega)$ defined as

$$\mathbf{q}=\begin{pmatrix}P\\Q_3\end{pmatrix},\quad \mathbf{p}=\begin{pmatrix}U^+\\U^-\end{pmatrix}. \quad (2.4.4)$$

Here $U^+=U^+(\mathbf{x},\omega)$ and $U^-=U^-(\mathbf{x},\omega)$ are downgoing and upgoing flux-normalized wave fields, respectively. Operator $\boldsymbol{\mathcal{L}}=\boldsymbol{\mathcal{L}}(\mathbf{x},\omega)$ in equation (2.4.3) is a pseudo-differential operator that composes the total wave field from its downgoing and upgoing constituents [*Corones et al.*, 1983; *Fishman et al.*, 1987; *Wapenaar and Berkhout*, 1989; *Fishman*, 1993; *De Hoop*, 1992; *de Hoop*, 1996; *Wapenaar*, 1996c; *Haines and de Hoop*, 1996; *Fishman et al.*, 2000]. Its inverse decomposes the total wave field into downgoing and upgoing fields. For inhomogeneous isotropic reciprocal media, the theory for this operator is well developed. For anisotropic non-reciprocal media, we restrict the application of this operator to the laterally invariant situation. In

Appendix B (see publication) we use equations (2.4.3) and (2.4.4) at boundaries $\partial\mathbb{D}_0$ and $\partial\mathbb{D}_A$ to recast reciprocity theorems (2.4.1) and (2.4.2) as follows

$$\int_{\partial\mathbb{D}_0}\big(U_A^{+(\mathrm{c})}U_B^- - U_A^{-(\mathrm{c})}U_B^+\big)\mathrm{d}\mathbf{x} = \int_{\partial\mathbb{D}_A}\big(U_A^{+(\mathrm{c})}U_B^- - U_A^{-(\mathrm{c})}U_B^+\big)\mathrm{d}\mathbf{x} \quad (2.4.5)$$

and

$$\int_{\partial\mathbb{D}_0}\big(U_A^{+*}U_B^+ - U_A^{-*}U_B^-\big)\mathrm{d}\mathbf{x} = \int_{\partial\mathbb{D}_A}\big(U_A^{+*}U_B^+ - U_A^{-*}U_B^-\big)\mathrm{d}\mathbf{x}. \quad (2.4.6)$$

Equation (2.4.5) is exact, whereas in equation (2.4.6) evanescent waves are neglected at boundaries $\partial\mathbb{D}_0$ and $\partial\mathbb{D}_A$. Note that the assumption of lateral invariance only applies to boundaries $\partial\mathbb{D}_0$ and $\partial\mathbb{D}_A$; the remainder of the medium (in- and outside $\mathbb{D}$) may be arbitrary inhomogeneous.

In the following we define $\partial\mathbb{D}_0$ (at $x_3 = x_{3,0}$) as the upper boundary of an inhomogeneous, anisotropic, non-reciprocal, lossless medium. Furthermore, we define $\partial\mathbb{D}_A$ (at $x_3 = x_{3,A}$, with $x_{3,A} > x_{3,0}$) as an arbitrary boundary inside the medium. We assume that the medium above $\partial\mathbb{D}_0$ is homogeneous. For state B we consider a unit source for downgoing waves at $\mathbf{x}_S = (x_{1,S}, x_{3,S})$, just above $\partial\mathbb{D}_0$ (hence, $x_{3,S} = x_{3,0} - \epsilon$, with $\epsilon \to 0$). The response to this unit source at any observation point $\mathbf{x}$ is given by $U_B^\pm(\mathbf{x},\omega) = G^\pm(\mathbf{x},\mathbf{x}_S,\omega)$, where G^+ and G^- denote the downgoing and upgoing components of the Green's function. For $\mathbf{x}$ at $\partial\mathbb{D}_0$, i.e., just below the source, we have $U_B^+(\mathbf{x},\omega) = G^+(\mathbf{x},\mathbf{x}_S,\omega) = \delta(x_1 - x_{1,S})$ and $U_B^-(\mathbf{x},\omega) = G^-(\mathbf{x},\mathbf{x}_S,\omega) = R(\mathbf{x},\mathbf{x}_S,\omega)$, with $R(\mathbf{x},\mathbf{x}_S,\omega)$ denoting the reflection response at $\partial\mathbb{D}_0$ of the medium below $\partial\mathbb{D}_0$. At $\partial\mathbb{D}_A$, we have $U_B^\pm(\mathbf{x},\omega) = G^\pm(\mathbf{x},\mathbf{x}_S,\omega)$. For state A we consider a focal point at $\mathbf{x}_A = (x_{1,A}, x_{3,A})$ at $\partial\mathbb{D}_A$. The medium in state A is a truncated medium, which is identical to the actual medium between $\partial\mathbb{D}_0$ and $\partial\mathbb{D}_A$, and homogeneous below $\partial\mathbb{D}_A$. At $\partial\mathbb{D}_0$ a downgoing focusing function $U_A^+(\mathbf{x},\omega) = f_1^+(\mathbf{x},\mathbf{x}_A,\omega)$, with $\mathbf{x} = (x_1, x_{3,0})$, is incident to the truncated medium. This function focuses at $\mathbf{x}_A$, hence, at $\partial\mathbb{D}_A$ we have $U_A^+(\mathbf{x},\omega) = f_1^+(\mathbf{x},\mathbf{x}_A,\omega) = \delta(x_1 - x_{1,A})$. The response to this focusing function at $\partial\mathbb{D}_0$ is $U_A^-(\mathbf{x},\omega) = f_1^-(\mathbf{x},\mathbf{x}_A,\omega)$. Because the truncated medium is homogeneous below $\partial\mathbb{D}_A$, we have $U_A^-(\mathbf{x},\omega) = 0$ at $\partial\mathbb{D}_A$. The quantities for both states are summarised in Table 2.

Note that the downgoing focusing function $f_1^+(\mathbf{x},\mathbf{x}_A,\omega)$, for $\mathbf{x}$ at $\partial\mathbb{D}_0$, is the inverse of the transmission response $T(\mathbf{x}_A,\mathbf{x},\omega)$ of the truncated medium [*Wapenaar et al.*, 2014b], hence

$$f_1^+(\mathbf{x},\mathbf{x}_A,\omega) = T^{\mathrm{inv}}(\mathbf{x}_A,\mathbf{x},\omega), \quad (2.4.7)$$

for $\mathbf{x}$ at $\partial\mathbb{D}_0$. To avoid instabilities in the evanescent field, the focusing function is in practice spatially band-limited.

Substituting the quantities of Table 2 into equations (2.4.5) and (2.4.6) gives

$$G^-(\mathbf{x}_A,\mathbf{x}_S,\omega) + f_1^{-(\mathrm{c})}(\mathbf{x}_S,\mathbf{x}_A,\omega) = \int_{\partial\mathbb{D}_0} R(\mathbf{x},\mathbf{x}_S,\omega) f_1^{+(\mathrm{c})}(\mathbf{x},\mathbf{x}_A,\omega)\mathrm{d}\mathbf{x} \quad (2.4.8)$$

and

$$G^{+}(\mathbf{x}_A,\mathbf{x}_S,\omega)-\{f_1^{+}(\mathbf{x}_S,\mathbf{x}_A,\omega)\}^{*}=\\ -\int_{\partial\mathbb{D}_0}R(\mathbf{x},\mathbf{x}_S,\omega)\{f_1^{-}(\mathbf{x},\mathbf{x}_A,\omega)\}^{*}\mathrm{d}\mathbf{x}, \tag{2.4.9}$$

respectively. These are two representations for the upgoing and downgoing parts of the Green's function between $\mathbf{x}_S$ at the acquisition surface and $\mathbf{x}_A$ inside the non-reciprocal medium. They are expressed in terms of the reflection response $R(\mathbf{x},\mathbf{x}_S,\omega)$ and a number of focusing functions. Unlike similar representations for reciprocal media [*Slob et al.*, 2014; *Wapenaar et al.*, 2014b], the focusing functions in equation (2.4.8) are defined in the complementary version of the truncated medium. Therefore we cannot use the standard approach to retrieve the focusing functions and Green's functions from the reflection response $R(\mathbf{x},\mathbf{x}_S,\omega)$. We obtain a second set of representations by replacing all quantities in equations (2.4.8) and (2.4.9) by the corresponding quantities in the complementary medium. For the focusing functions in equation (2.4.8) this implies they are replaced by their counterparts in the truncated actual medium. We thus obtain

$$G^{-(\mathrm{c})}(\mathbf{x}_A,\mathbf{x}_S,\omega)+f_1^{-}(\mathbf{x}_S,\mathbf{x}_A,\omega)=\\ \int_{\partial\mathbb{D}_0}R^{(\mathrm{c})}(\mathbf{x},\mathbf{x}_S,\omega)f_1^{+}(\mathbf{x},\mathbf{x}_A,\omega)\mathrm{d}\mathbf{x} \tag{2.4.10}$$

and

$$G^{+(\mathrm{c})}(\mathbf{x}_A,\mathbf{x}_S,\omega)-\{f_1^{+(\mathrm{c})}(\mathbf{x}_S,\mathbf{x}_A,\omega)\}^{*}=\\ -\int_{\partial\mathbb{D}_0}R^{(\mathrm{c})}(\mathbf{x},\mathbf{x}_S,\omega)\{f_1^{-(\mathrm{c})}(\mathbf{x},\mathbf{x}_A,\omega)\}^{*}\mathrm{d}\mathbf{x}, \tag{2.4.11}$$

respectively. Because in practical situations we do not have access to the reflection response $R^{(\mathrm{c})}(\mathbf{x},\mathbf{x}_S,\omega)$ in the complementary medium, we derive a relation analogous to equation (2.3.7) for this reflection response. To this end, consider the quantities in Table 3, with $\mathbf{x}_S$ and $\mathbf{x}_R$ just above $\partial\mathbb{D}_0$, and with $\partial\mathbb{D}_M$ denoting a boundary below all inhomogeneities, so that there are no upgoing waves at $\partial\mathbb{D}_M$. Substituting the quantities of Table 3 into equation (2.4.5) (with $\partial\mathbb{D}_A$ replaced by $\partial\mathbb{D}_M$) gives

$$R^{(\mathrm{c})}(\mathbf{x}_R,\mathbf{x}_S,\omega)=R(\mathbf{x}_S,\mathbf{x}_R,\omega). \tag{2.4.12}$$

Equations (2.4.8) – (2.4.11), with $R^{(\mathrm{c})}(\mathbf{x},\mathbf{x}_S,\omega)$ replaced by $R(\mathbf{x}_S,\mathbf{x},\omega)$, form the basis for the Marchenko method, discussed in the next section.

2.5 The Marchenko method for non-reciprocal media

The standard multidimensional Marchenko method for reciprocal media [*Slob et al.*, 2014; *Wapenaar et al.*, 2014b] uses the representations of equations (2.4.8) and (2.4.9), but without the superscript (c), to retrieve the focusing functions from the reflection response. Here we discuss how to modify this method for non-reciprocal media. We separate the representations of equations (2.4.8) − (2.4.11) into two sets, each set containing focusing functions in one and the same truncated medium. These sets are equations (2.4.9) and (2.4.10), with the focusing functions in the truncated actual medium, and equations (2.4.8) and (2.4.11), with the focusing functions in the truncated complementary medium. We start with the set of equations (2.4.9) and (2.4.10), which read in the time domain (using equation (2.4.12))

$$\begin{aligned} &G^{+}(\mathbf{x}_A,\mathbf{x}_S,t) - f_1^{+}(\mathbf{x}_S,\mathbf{x}_A,-t) = \\ &-\int_{\partial\mathbb{D}_0} \mathrm{d}\mathbf{x} \int_{-\infty}^{t} R(\mathbf{x},\mathbf{x}_S,t-t') f_1^{-}(\mathbf{x},\mathbf{x}_A,-t')\mathrm{d}t' \end{aligned} \tag{2.5.1}$$

and

$$\begin{aligned} &G^{-(\mathrm{c})}(\mathbf{x}_A,\mathbf{x}_S,t) + f_1^{-}(\mathbf{x}_S,\mathbf{x}_A,t) = \\ &\int_{\partial\mathbb{D}_0} \mathrm{d}\mathbf{x} \int_{-\infty}^{t} R(\mathbf{x}_S,\mathbf{x},t-t') f_1^{+}(\mathbf{x},\mathbf{x}_A,t')\mathrm{d}t', \end{aligned} \tag{2.5.2}$$

respectively. We introduce time windows to remove the Green's functions from these representations. Similar as in the reciprocal situation, we assume that the Green's function and the time-reversed focusing function on the left-hand side of equation (2.5.1) are separated in time, except for the direct arrivals [*Wapenaar et al.*, 2014b]. This is a reasonable assumption for media with smooth lateral variations, and for limited horizontal source-receiver distances. Let $t_\mathrm{d}(\mathbf{x}_A,\mathbf{x}_S)$ denote the travel time of the direct arrival of $G^{+}(\mathbf{x}_A,\mathbf{x}_S,t)$. We define a time window $w(\mathbf{x}_A,\mathbf{x}_S,t) = u(t_\mathrm{d}(\mathbf{x}_A,\mathbf{x}_S) - t_\epsilon - t)$, where $u(t)$ is the Heaviside function and t_ϵ a small positive time constant. Under the above-mentioned assumption, we have $w(\mathbf{x}_A,\mathbf{x}_S,t)G^{+}(\mathbf{x}_A,\mathbf{x}_S,t) = 0$. For the focusing function on the left-hand side of equation (2.5.1) we write [*Wapenaar et al.*, 2014b]

$$\begin{aligned} f_1^{+}(\mathbf{x}_S,\mathbf{x}_A,t) &= T^{\mathrm{inv}}(\mathbf{x}_A,\mathbf{x}_S,t) \\ &= T_\mathrm{d}^{\mathrm{inv}}(\mathbf{x}_A,\mathbf{x}_S,t) + M^{+}(\mathbf{x}_S,\mathbf{x}_A,t), \end{aligned} \tag{2.5.3}$$

where $T_\mathrm{d}^{\mathrm{inv}}(\mathbf{x}_A,\mathbf{x}_S,t)$ is the inverse of the direct arrival of the transmission response of the truncated medium and $M^{+}(\mathbf{x}_S,\mathbf{x}_A,t)$ the scattering coda. The travel time of $T_\mathrm{d}^{\mathrm{inv}}(\mathbf{x}_A,\mathbf{x}_S,t)$ is $-t_\mathrm{d}(\mathbf{x}_A,\mathbf{x}_S)$ and the scattering coda obeys $M^{+}(\mathbf{x}_S,\mathbf{x}_A,t) = 0$ for $t \leq -t_\mathrm{d}(\mathbf{x}_A,\mathbf{x}_S)$. Hence, $w(\mathbf{x}_A,\mathbf{x}_S,t)f_1^{+}(\mathbf{x}_S,\mathbf{x}_A,-t) = M^{+}(\mathbf{x}_S,\mathbf{x}_A,-t)$. Applying the time window $w(\mathbf{x}_A,\mathbf{x}_S,t)$ to both sides of equation (2.5.1) thus yields

$$\begin{aligned} &M^{+}(\mathbf{x}_S,\mathbf{x}_A,-t) = \\ &w(\mathbf{x}_A,\mathbf{x}_S,t)\int_{\partial\mathbb{D}_0} \mathrm{d}\mathbf{x} \int_{-\infty}^{t} R(\mathbf{x},\mathbf{x}_S,t-t') f_1^{-}(\mathbf{x},\mathbf{x}_A,-t')\mathrm{d}t'. \end{aligned} \tag{2.5.4}$$

Under the same conditions as those mentioned for equation (2.5.1), we assume that the Green's function and the focusing function in the left-hand side of equation (2.5.2) are separated in time (without overlap). Unlike for reciprocal media, we need a different time window to suppress the Green's function, because the latter is defined in the complementary medium. To this end we define a time window $w^{(\mathrm{c})}(\mathbf{x}_A,\mathbf{x}_S,t)=u(t_{\mathrm{d}}^{(\mathrm{c})}(\mathbf{x}_A,\mathbf{x}_S)-t_\epsilon-t)$, where $t_{\mathrm{d}}^{(\mathrm{c})}(\mathbf{x}_A,\mathbf{x}_S)$ denotes the travel time of the direct arrival in the complementary medium. Applying this window to both sides of equation (2.5.2) yields

$$\begin{aligned}&f_1^-(\mathbf{x}_S,\mathbf{x}_A,t)=\\&w^{(\mathrm{c})}(\mathbf{x}_A,\mathbf{x}_S,t)\int_{\partial\mathbb{D}_0}\mathrm{d}\mathbf{x}\int_{-\infty}^{t}R(\mathbf{x}_S,\mathbf{x},t-t')f_1^+(\mathbf{x},\mathbf{x}_A,t')\mathrm{d}t'.\end{aligned}\tag{2.5.5}$$

Equations (2.5.4) and (2.5.5), with f_1^+ given by equation (2.5.3), form a set of two equations for the two unknown functions $M^+(\mathbf{x},\mathbf{x}_A,t)$ and $f_1^-(\mathbf{x},\mathbf{x}_A,t)$ (with $\mathbf{x}$ at $\partial\mathbb{D}_0$). These functions can be resolved from equations (2.5.4) and (2.5.5), assuming $R(\mathbf{x},\mathbf{x}_S,t)$, $R(\mathbf{x}_S,\mathbf{x},t)$, $t_{\mathrm{d}}(\mathbf{x}_A,\mathbf{x}_S)$, $t_{\mathrm{d}}^{(\mathrm{c})}(\mathbf{x}_A,\mathbf{x}_S)$ and $T_{\mathrm{d}}^{\mathrm{inv}}(\mathbf{x}_A,\mathbf{x}_S,t)$ are known for all $\mathbf{x}$ and $\mathbf{x}_S$ at $\partial\mathbb{D}_0$. The reflection responses $R(\mathbf{x},\mathbf{x}_S,t)$ and $R(\mathbf{x}_S,\mathbf{x},t)$ are obtained from measurements at the upper boundary $\partial\mathbb{D}_0$ of the medium. This involves deconvolution for the source function, decomposition and, when the upper boundary is a reflecting boundary, elimination of the surface-related multiple reflections [*Verschuur et al.*, 1992]. Because the deconvolution is limited by the bandwidth of the source function, the time constant t_ϵ in the window function is taken equal to half the duration of the source function. This implies that the method will not account for short period multiples in layers with a thickness smaller than the wavelength [*Slob et al.*, 2014]. The travel times $t_{\mathrm{d}}(\mathbf{x}_A,\mathbf{x}_S)$ and $t_{\mathrm{d}}^{(\mathrm{c})}(\mathbf{x}_A,\mathbf{x}_S)$, and the inverse of the direct arrival of the transmission response, $T_{\mathrm{d}}^{\mathrm{inv}}(\mathbf{x}_A,\mathbf{x}_S,t)$, can be derived from a background model of the medium and its complementary version (once the background model is known, its complementary version follows immediately). A smooth background model is sufficient to derive these quantities, hence, no information about the scattering interfaces inside the medium is required. The iterative Marchenko scheme to solve for $M^+(\mathbf{x},\mathbf{x}_A,t)$ and $f_1^-(\mathbf{x},\mathbf{x}_A,t)$ reads

$$\begin{aligned}&f_{1,k}^-(\mathbf{x}_S,\mathbf{x}_A,t)=\\&w^{(\mathrm{c})}(\mathbf{x}_A,\mathbf{x}_S,t)\int_{\partial\mathbb{D}_0}\mathrm{d}\mathbf{x}\int_{-\infty}^{t}R(\mathbf{x}_S,\mathbf{x},t-t')f_{1,k}^+(\mathbf{x},\mathbf{x}_A,t')\mathrm{d}t',\end{aligned}\tag{2.5.6}$$

$$\begin{aligned}&M_{k+1}^+(\mathbf{x}_S,\mathbf{x}_A,-t)=\\&w(\mathbf{x}_A,\mathbf{x}_S,t)\int_{\partial\mathbb{D}_0}\mathrm{d}\mathbf{x}\int_{-\infty}^{t}R(\mathbf{x},\mathbf{x}_S,t-t')f_{1,k}^-(\mathbf{x},\mathbf{x}_A,-t')\mathrm{d}t',\end{aligned}\tag{2.5.7}$$

with

$$f_{1,k}^+(\mathbf{x},\mathbf{x}_A,t)=T_{\mathrm{d}}^{\mathrm{inv}}(\mathbf{x}_A,\mathbf{x},t)+M_k^+(\mathbf{x},\mathbf{x}_A,t),\tag{2.5.8}$$

starting with $M_0^+(\mathbf{x},\mathbf{x}_A,t)=0$. Once $M^+(\mathbf{x},\mathbf{x}_A,t)$ and $f_1^-(\mathbf{x},\mathbf{x}_A,t)$ are found, $f_1^+(\mathbf{x},\mathbf{x}_A,t)$ is obtained from equation (2.5.3) and, subsequently, the Green's functions $G^+(\mathbf{x}_A,\mathbf{x}_S,t)$ and $G^{-(\mathrm{c})}(\mathbf{x}_A,\mathbf{x}_S,t)$ are obtained from equations (2.5.1) and

(2.5.2). Note that only $G^+(\mathbf{x}_A,\mathbf{x}_S,t)$ is defined in the actual medium. To obtain $G^-(\mathbf{x}_A,\mathbf{x}_S,t)$ in the actual medium we consider the set of equations (2.4.8) and (2.4.11), which read in the time domain (using equation (2.4.12))

$$\begin{aligned}&G^-(\mathbf{x}_A,\mathbf{x}_S,t)+f_1^{-(\mathrm{c})}(\mathbf{x}_S,\mathbf{x}_A,t)=\\&\int_{\partial\mathbb{D}_0}\mathrm{d}\mathbf{x}\int_{-\infty}^{t}R(\mathbf{x},\mathbf{x}_S,t-t')f_1^{+(\mathrm{c})}(\mathbf{x},\mathbf{x}_A,t')\mathrm{d}t'\end{aligned}\tag{2.5.9}$$

and

$$\begin{aligned}&G^{+(\mathrm{c})}(\mathbf{x}_A,\mathbf{x}_S,t)-f_1^{+(\mathrm{c})}(\mathbf{x}_S,\mathbf{x}_A,-t)=\\&-\int_{\partial\mathbb{D}_0}\mathrm{d}\mathbf{x}\int_{-\infty}^{t}R(\mathbf{x}_S,\mathbf{x},t-t')f_1^{-(\mathrm{c})}(\mathbf{x},\mathbf{x}_A,-t')\mathrm{d}t',\end{aligned}\tag{2.5.10}$$

respectively. The same reasoning as above leads to the following iterative Marchenko scheme for the focusing functions in the truncated complementary medium

$$\begin{aligned}&f_{1,k}^{-(\mathrm{c})}(\mathbf{x}_S,\mathbf{x}_A,t)=\\&w(\mathbf{x}_A,\mathbf{x}_S,t)\times\int_{\partial\mathbb{D}_0}\mathrm{d}\mathbf{x}\int_{-\infty}^{t}R(\mathbf{x},\mathbf{x}_S,t-t')f_{1,k}^{+(\mathrm{c})}(\mathbf{x},\mathbf{x}_A,t')\mathrm{d}t'\end{aligned}\tag{2.5.11}$$

$$\begin{aligned}&M_{k+1}^{+(\mathrm{c})}(\mathbf{x}_S,\mathbf{x}_A,-t)=\\&w^{(\mathrm{c})}(\mathbf{x}_A,\mathbf{x}_S,t)\int_{\partial\mathbb{D}_0}\mathrm{d}\mathbf{x}\int_{-\infty}^{t}R(\mathbf{x}_S,\mathbf{x},t-t')f_{1,k}^{-(\mathrm{c})}(\mathbf{x},\mathbf{x}_A,-t')\mathrm{d}t',\end{aligned}\tag{2.5.12}$$

with

$$f_{1,k}^{+(\mathrm{c})}(\mathbf{x},\mathbf{x}_A,t)=T_{\mathrm{d}}^{\mathrm{inv(c)}}(\mathbf{x}_A,\mathbf{x},t)+M_k^{+(\mathrm{c})}(\mathbf{x},\mathbf{x}_A,t),\tag{2.5.13}$$

starting with $M_0^{+(\mathrm{c})}(\mathbf{x},\mathbf{x}_A,t)=0$. Here $T_{\mathrm{d}}^{\mathrm{inv(c)}}(\mathbf{x}_A,\mathbf{x},t)$ can be derived from the complementary background model. Once the focusing functions $f_1^{+(\mathrm{c})}(\mathbf{x},\mathbf{x}_A,t)$ and $f_1^{-(\mathrm{c})}(\mathbf{x},\mathbf{x}_A,t)$ are found, the Green's functions $G^-(\mathbf{x}_A,\mathbf{x}_S,t)$ and $G^{+(\mathrm{c})}(\mathbf{x}_A,\mathbf{x}_S,t)$ are obtained from equations (2.5.9) and (2.5.10).

We conclude this section by showing how $G^+(\mathbf{x}_A,\mathbf{x}_S,t)$ and $G^-(\mathbf{x}_A,\mathbf{x}_S,t)$ can be used to image the interior of the non-reciprocal medium. First we derive a mutual relation between these Green's functions. To this end, consider the quantities in Table 4. Here $R^{(\mathrm{c})}(\mathbf{x},\mathbf{x}_A,\omega)$ in state A is the reflection response at $\partial\mathbb{D}_A$ of the complementary medium below $\partial\mathbb{D}_A$, with $\mathbf{x}_A$ defined just above $\partial\mathbb{D}_A$ and the medium in state A being homogeneous above $\partial\mathbb{D}_A$. Substituting the quantities of Table 4 into equation (2.4.5) (with $\partial\mathbb{D}_0$ and $\partial\mathbb{D}_A$ replaced by $\partial\mathbb{D}_A$ and $\partial\mathbb{D}_M$, respectively) and using equation (2.4.12), gives

$$G^-(\mathbf{x}_A,\mathbf{x}_S,\omega)=\int_{\partial\mathbb{D}_A}R(\mathbf{x}_A,\mathbf{x},\omega)G^+(\mathbf{x},\mathbf{x}_S,\omega)\mathrm{d}\mathbf{x},\tag{2.5.14}$$

or, applying an inverse Fourier transformation to the time domain,

$$G^-(\mathbf{x}_A, \mathbf{x}_S, t) = \int_{\partial\mathbb{D}_A} \mathrm{d}\mathbf{x} \int_{-\infty}^{t} R(\mathbf{x}_A, \mathbf{x}, t - t')G^+(\mathbf{x}, \mathbf{x}_S, t')\mathrm{d}t'. \quad (2.5.15)$$

Given the Green's functions $G^+(\mathbf{x}, \mathbf{x}_S, t)$ and $G^-(\mathbf{x}_A, \mathbf{x}_S, t)$ for all $\mathbf{x}_A$ and $\mathbf{x}$ at $\partial\mathbb{D}_A$ for a range of source positions $\mathbf{x}_S$ at $\partial\mathbb{D}_0$, the reflection response $R(\mathbf{x}_A, \mathbf{x}, t)$ for all $\mathbf{x}_A$ and $\mathbf{x}$ at $\partial\mathbb{D}_A$ can be resolved by multidimensional deconvolution [*Wapenaar et al.*, 2000; *Amundsen*, 2001; *Holvik and Amundsen*, 2005; *Wapenaar and van der Neut*, 2010; *van der Neut et al.*, 2011; *Ravasi et al.*, 2015]. An image can be obtained by selecting $R(\mathbf{x}_A, \mathbf{x}_A, t = 0)$ and repeating the process for any $\mathbf{x}_A$ in the region of interest.

We discuss an alternative imaging approach for the special case of a laterally invariant medium. To this end we first rewrite equation (2.5.14) as a spatial convolution, taking $x_{1,S} = 0$, hence

$$G^-(x_{1,A}, x_{3,A}, x_{3,S}, \omega) = \int_{-\infty}^{\infty} R(x_{1,A} - x_1, x_{3,A}, \omega)G^+(x_1, x_{3,A}, x_{3,S}, \omega)\mathrm{d}x_1. \quad (2.5.16)$$

We define the spatial Fourier transform of a function $P(x_1, x_3, \omega)$ as

$$\tilde{P}(s_1, x_3, \omega) = \int_{-\infty}^{\infty} P(x_1, x_3, \omega) \exp(-i\omega s_1 x_1)\mathrm{d}x_1, \quad (2.5.17)$$

with s_1 being the horizontal slowness. In the (s_1, x_3, ω)-domain, equation (2.5.16) becomes

$$\tilde{G}^-(s_1, x_{3,A}, x_{3,S}, \omega) = \tilde{R}(s_1, x_{3,A}, \omega)\tilde{G}^+(s_1, x_{3,A}, x_{3,S}, \omega), \quad (2.5.18)$$

or, applying an inverse Fourier transformation to the time domain,

$$G^-(s_1, x_{3,A}, x_{3,S}, \tau) = \int_{-\infty}^{\tau} R(s_1, x_{3,A}, \tau - \tau')G^+(s_1, x_{3,A}, x_{3,S}, \tau')\mathrm{d}\tau'. \quad (2.5.19)$$

Given the Green's functions $G^+(s_1, x_{3,A}, x_{3,S}, \tau)$ and $G^-(s_1, x_{3,A}, x_{3,S}, \tau)$, the reflection response $R(s_1, x_{3,A}, \tau)$ for each horizontal slowness s_1 can be resolved by 1D deconvolution. An image can be obtained by selecting $R(s_1, x_{3,A}, \tau = 0)$ and repeating the process for all s_1 and for any $x_{3,A}$ in the region of interest.

2.6 Numerical example

We illustrate the proposed methodology with a numerical example, mimicking an ultrasound experiment. For simplicity we consider a horizontally layered medium, consisting of three homogeneous layers and a homogeneous half-space below the deepest layer. The medium parameters of the layered medium, $\alpha(x_3)$, $\beta_{rs}(x_3)$ and $\gamma_r(x_3)$ are shown in Figure B.2. In many practical situations the parameters $\beta_{31}(x_3)$

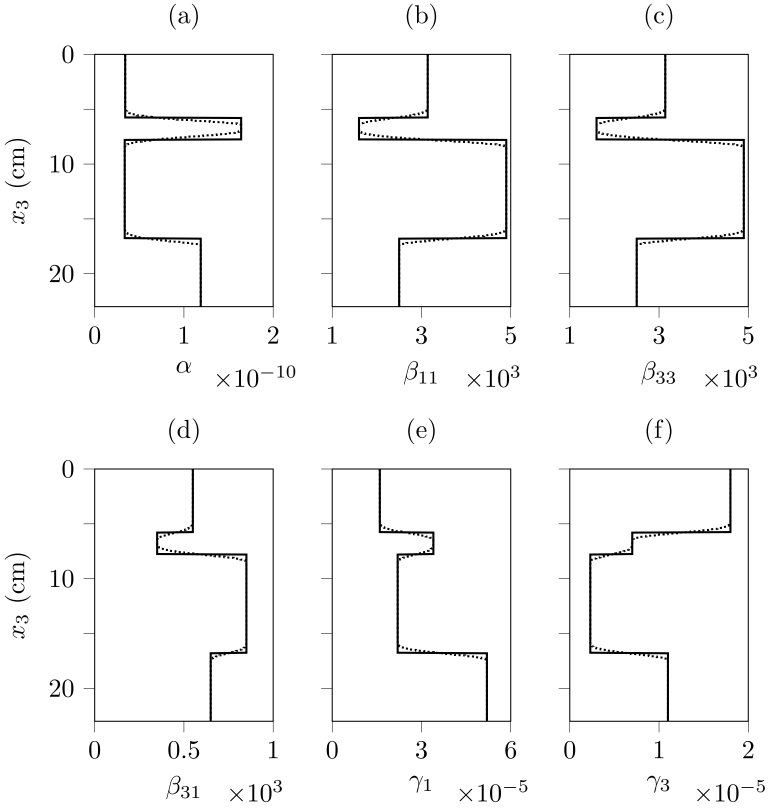

Figure B.2: *Solid lines: parameters $\alpha(x_3)$, $\beta_{11}(x_3)$, $\beta_{33}(x_3)$, $\beta_{31}(x_3)$, $\gamma_1(x_3)$ and $\gamma_3(x_3)$ of the layered medium. Dotted lines: smoothed medium parameters, used to model the initial estimate of the focusing functions.*

and $\gamma_3(x_3)$ will be zero, but we choose them to be non-zero to demonstrate the generality of the method. We define a source at $\mathbf{x}_S = (0, 0)$ at the top of the first layer, which emits a time-symmetric wavelet $S(t)$ with a central frequency of 600 kHz into the layered medium. We use a wavenumber-frequency domain modelling method [*Kennett and Kerry*, 1979], adjusted for non-reciprocal media, to model the response to this source. The modelled reflection response, $R(\mathbf{x}, \mathbf{x}_S, t) * S(t)$ at $\partial\mathbb{D}_0$ (the asterisk denoting convolution), is shown in Figure B.3. To emphasise the multiple scattering, a time-dependent amplitude gain has been applied, using the function $\exp\{3t/375\mu s\}$. Note that the apices of the reflection hyperbolae drift to the left with increasing time, which is a manifestation of the non-reciprocal medium parameters. Because the medium is laterally invariant, the response to any other source at the surface is just a laterally shifted version of the response in Figure B.3. We apply the Marchenko method, discussed in detail in the previous section, to

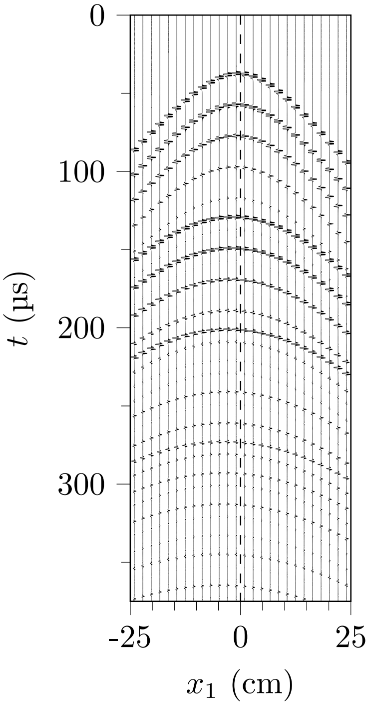

Figure B.3: *The modeled reflection response $R(\mathbf{x}, \mathbf{x}_S, t) * S(t)$ at $\partial\mathbb{D}_0$. Note the asymmetry with respect to the dashed line due to the non-reciprocal medium parameters.*

derive the focusing functions $f_1^{\pm}(\mathbf{x}_S, \mathbf{x}_A, t)$ and $f_1^{\pm(\mathrm{c})}(\mathbf{x}_S, \mathbf{x}_A, t)$ for fixed $\mathbf{x}_S = (0, 0)$ and variable $\mathbf{x}_A$. As input we use the reflection response $R(\mathbf{x}, \mathbf{x}_S, t) * S(t)$ of the actual medium and the direct arrivals $T_\mathrm{d}(\mathbf{x}_A, \mathbf{x}, t)$ and $T_\mathrm{d}^{(\mathrm{c})}(\mathbf{x}_A, \mathbf{x}, t)$, modelled in a smoothed version of the truncated medium and its complementary version (the smoothed medium is indicated by the dotted lines in Figure B.2). For simplicity we approximate the inverse direct arrivals $T_\mathrm{d}^{\mathrm{inv}}(\mathbf{x}_A, \mathbf{x}, t)$ and $T_\mathrm{d}^{\mathrm{inv(c)}}(\mathbf{x}_A, \mathbf{x}, t)$ in equations (2.5.8) and (2.5.13) by the time-reversals $T_\mathrm{d}(\mathbf{x}_A, \mathbf{x}, -t)$ and $T_\mathrm{d}^{(\mathrm{c})}(\mathbf{x}_A, \mathbf{x}, -t)$. For t_ϵ in the time windows $w(\mathbf{x}_A, \mathbf{x}_S, t)$ and $w^{(\mathrm{c})}(\mathbf{x}_A, \mathbf{x}_S, t)$ we choose half the duration of the symmetric wavelet $S(t)$, i.e., $t_\epsilon = 0.65\mu$s, and the Heaviside functions are tapered. Because we consider a laterally invariant medium, the integrals in the right-hand sides of equations (2.5.6), (2.5.7), (2.5.11) and (2.5.12) are efficiently replaced by multiplications in the wavenumber-frequency domain. In total we apply 20 iterations of the Marchenko scheme to derive the focusing functions $f_1^{\pm}(\mathbf{x}_S, \mathbf{x}_A, t) * S(t)$ and the same number of iterations to derive $f_1^{\pm(\mathrm{c})}(\mathbf{x}_S, \mathbf{x}_A, t) * S(t)$. These focusing functions are substituted into equations (2.5.1) and (2.5.9) (of which the integrals are also evaluated via the wavenumber-frequency domain) to obtain the wave fields $G^+(\mathbf{x}_A, \mathbf{x}_S, t) * S(t)$ and $G^-(\mathbf{x}_A, \mathbf{x}_S, t) * S(t)$. The superposition of these wave fields

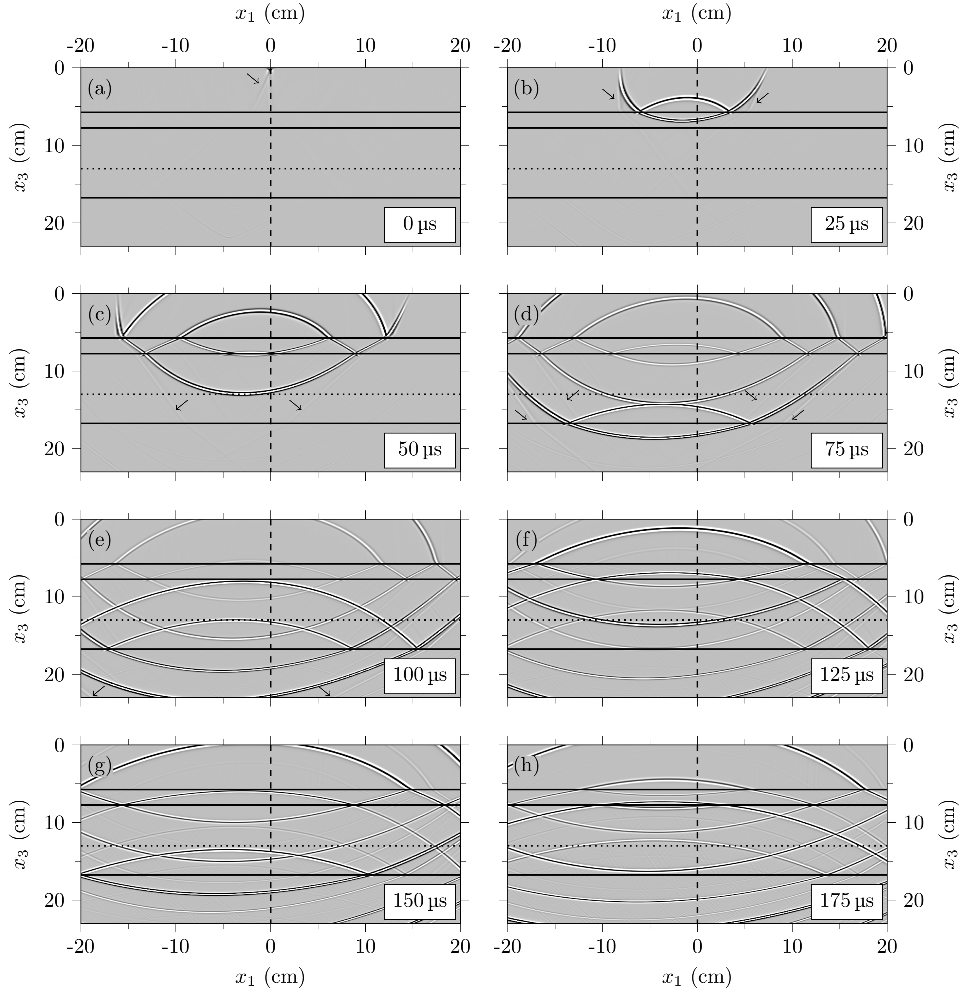

Figure B.4: *Snapshots of* $\{G^{+}(\mathbf{x}_A,\mathbf{x}_S,t) + G^{-}(\mathbf{x}_A,\mathbf{x}_S,t)\} * S(t)$*, retrieved via equations (2.5.1) and (2.5.9), for* $\mathbf{x}_S = (0,0)$ *and variable* $\mathbf{x}_A$*.*

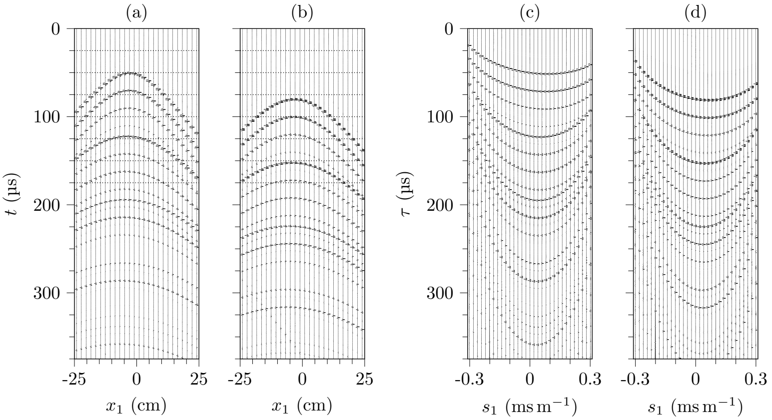

Figure B.5: *Downgoing and upgoing wave fields at* $x_{3,A} = 13$ *cm. (a)* $G^+(x_1, x_{3,A}, x_{3,S}, t) * S(t)$*, (b)* $G^-(x_1, x_{3,A}, x_{3,S}, t) * S(t)$*, (c)* $G^+(s_1, x_{3,A}, x_{3,S}, \tau) * S(\tau)$*, (d)* $G^-(s_1, x_{3,A}, x_{3,S}, \tau) * S(\tau)$*.*

is shown in grey-level display in Figure B.4 in the form of snapshots (i.e., wave fields at frozen time), for fixed $\mathbf{x}_S = (0, 0)$ and variable $\mathbf{x}_A$. The amplitudes are clipped at 8% of the maximum amplitude. This figure clearly shows the propagation of the wave field from the source through the layered non-reciprocal medium. The wavefronts are asymmetric as a result of the non-reciprocal medium parameters (for a reciprocal medium these snapshots would be symmetric with respect to the vertical dashed lines). Multiple scattering between the layer interfaces is also clearly visible. The interfaces, indicated by the solid horizontal lines in each of the panels in Figure B.4, are only shown here to aid the interpretation of the retrieved Green's functions. However, no explicit information of these interfaces has been used to retrieve these Green's functions; all information about the scattering at the layer interfaces comes directly from the reflection response $R(\mathbf{x}, \mathbf{x}_S, t) * S(t)$. The snapshots also exhibit some weak spurious linear events (indicated by the arrows in Figure B.4), which are mainly caused by the negligence of evanescent waves and the absence of very large propagation angles in the reflection response.

Next, we image the interfaces of the layered medium, following the approach for a laterally invariant medium described at the end of the previous section. Figures B.5a,b show the downgoing and upgoing wave fields $G^+(x_1, x_{3,A}, x_{3,S}, t) * S(t)$ and $G^-(x_1, x_{3,A}, x_{3,S}, t) * S(t)$, respectively, for $x_{3,A} = 13$ cm (the depth of the horizontal dotted lines in Figure B.4). The horizontal dotted lines in Figures B.5a,b indicate the times of the snapshots in Figure B.4. Figures B.5c,d show the downgoing and upgoing wave fields $G^+(s_1, x_{3,A}, x_{3,S}, \tau) * S(\tau)$ and $G^-(s_1, x_{3,A}, x_{3,S}, \tau) * S(\tau)$, respectively, for a range of horizontal slownesses s_1. From these wave fields we derive the reflection response $R(s_1, x_{3,A}, \tau)$ by inverting equation (2.5.19) for each horizontal slowness s_1. The image at $x_{3,A}$ is obtained as $R(s_1, x_{3,A}, \tau = 0)$. We repeat this for all $x_{3,A}$ between 0 and 25 cm, in steps of 0.25 mm. The result is shown

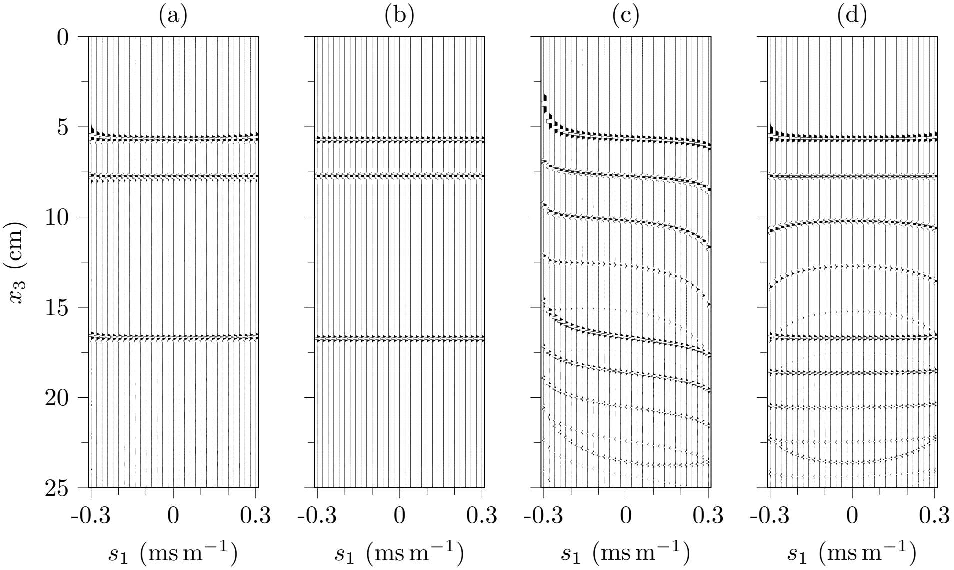

Figure B.6: *Images in the* (s_1, x_3)*-domain of the layered medium of Figure B.2. (a) Marchenko imaging, accounting for non-reciprocity. (b) Reference reflectivity. (c) Primary imaging, ignoring non-reciprocity. (d) Primary imaging, accounting for non-reciprocity.*

in Figure B.6a. This figure clearly shows images of the three interfaces in Figure B.2. For comparison, Figure B.6b shows, as a reference, the true reflectivity. The relative amplitude errors of the imaged interfaces are between 0.5% and 2%, except for slownesses $|s_1| > 0.2$ ms/m, close to the evanescent field. Figure B.6c shows the result of standard primary imaging, ignoring non-reciprocity. The trace at $s_1 = 0$ contains images of the three interfaces at the correct depths, but it also contains false images caused by the internal multiples. Moreover, the traces for $s_1 \neq 0$ contain images at wrong depths only. Finally, Figure B.6d is the result of primary imaging, taking non-reciprocity into account (by applying one iteration with our method). The three interfaces are imaged at the correct depths for all horizontal slownesses, but the false images are not suppressed.

2.7 Conclusions

Marchenko imaging has recently been introduced as a novel approach to account for multiple scattering in multidimensional acoustic and electromagnetic imaging. Given the recent interest in non-reciprocal materials, here we have extended the Marchenko approach for non-reciprocal media. We have derived two iterative Marchenko schemes, one to retrieve focusing functions in a truncated version of the actual medium and one to retrieve these functions in a truncated version of the complementary medium. Both schemes use the reflection response of the actual medium as input, plus estimates of the direct arrivals of the transmission response of the truncated actual medium (for the first scheme) and of the truncated complementary medium (for the second scheme). We have derived Green's function representations, which express the downgoing and upgoing part of the Green's function inside the non-reciprocal medium, in terms of the reflection response at the surface of the actual medium and the focusing functions in the truncated actual and complementary medium. From these downgoing and upgoing Green's functions, a reflectivity image of the medium can be obtained. We have illustrated the proposed approach at the hand of a numerical example for a horizontally layered non-reciprocal medium. This example shows an accurate wave field, propagating through the medium and scattering at its interfaces, retrieved from the reflection response at the surface. Moreover, it shows an accurately obtained artefact-free reflectivity image of the non-reciprocal medium, which confirms that the proposed method properly handles internal multiple scattering in a non-reciprocal medium.

Acknowledgements

We thank our colleague Evert Slob for his advise about electromagnetic waves in non-reciprocal media and reviewers Patrick Elison and Ivan Vasconcelos for their constructive comments, which helped to improve the paper. This work has received funding from the European Union's Horizon 2020 research and innovation programme: European Research Council (grant agreement 742703) and Marie Skłodowska-Curie (grant agreement 641943).

Bibliography

Achenbach, J. A., and J. D. Achenbach (2003), *Reciprocity in elastodynamics*, Cambridge University Press.

Altman, C., and K. Suchy (2011), *Reciprocity, spatial mapping and time reversal in electromagnetics*, Springer Science & Business Media.

Amundsen, L. (2001), Elimination of free-surface related multiples without need of the source wavelet, *Geophysics*, *66*(1), 327–341, doi:https://doi.org/10.1190/1.1444912.

Ardakani, A. G. (2014), Nonreciprocal electromagnetic wave propagation in one-dimensional ternary magnetized plasma photonic crystals, *JOSA B*, *31*(2), 332–339.

Arfken, G. (1985), *Mathematical Methods for Physicists*, p.p. 810-814, 3rd ed., Academic Press.

Attarzadeh, M. A., and M. Nouh (2018), Non-reciprocal elastic wave propagation in 2D phononic membranes with spatiotemporally varying material properties, *Journal of Sound and Vibration*, *422*, 264–277.

Bava, G. P., and G. Ghione (1984), Inverse scattering for optical couplers. Exact solution of Marchenko equations, *Journal of Mathematical Physics*, *25*(6), 1900–1904, doi:10.1063/1.526379.

Behura, J., K. Wapenaar, and R. Snieder (2014), Autofocus imaging: Image reconstruction based on inverse scattering theory, *Geophysics*, *79*(3), A19—-A26, doi:10.1190/geo2013-0398.1.

Berkhout, A., and M. de Graaff (1982), The inverse scattering problem in terms of multiple elimination and seismic migration, in *SEG Technical Program Expanded Abstracts 1982*, pp. 113—-114, Society of Exploration Geophysicists, doi:10.1190/1.1826839.

Berkhout, A. J. (1982), *Seismic Migration: Imaging of Acoustic Energy by Wave Field Extrapolation, Part A: Theoretical Aspects*, Elsevier.

Berkhout, A. J. (2014), Review paper: An outlook on the future of seismic imaging, *Part II: Full-wavefield migration: Geophysical Prospecting*, *62*, 931–949.

Berkhout, A. J., and D. W. V. W. Palthe (1979), Migration in terms of spatial deconvolution, *Geophysical Prospecting*, *27*(1), 261–291.

Bernstein, D. S. (2005), *Matrix Mathematics: Theory, Facts, and Formulas.*

Biersteker, J. (2001), MAGIC: Shell's surface multiple attenuation technique, in *SEG Technical Program Expanded Abstracts 2001*, pp. 1301–1304, Society of Exploration Geophysicists.

Billette, F., and G. Lambaré (1998), Velocity macro-model estimation from seismic reflection data by stereotomography, *Geophysical Journal International*, *135*(2), 671–690.

Birss, R. R., and R. G. Shrubsall (1967), The propagation of electromagnetic waves in magnetoelectric crystals, *Philosophical Magazine*, *15*(136), 687–700.

Bleistein, N., and J. K. Cohen (1982), The velocity inversion problem-Present status, new directions, *Geophysics*, *47*(11), 1497–1511.

Bode, H. W. (1940), Relations between attenuation and phase in feedback amplifier design, *The Bell System Technical Journal*, *19*(3), 421—-454.

Bode, H. W. (1945), Network analysis and feedback amplifier design, *D. van Nostrand Company, INC.*

Brackenhoff, J. (2016), Rescaling of incorrect source strength using Marchenko Redatuming, master thesis, Delft University of Technology.

Brackenhoff, J., J. Thorbecke, and K. Wapenaar (2019), Monitoring induced distributed double-couple sources using Marchenko-based virtual receivers, *Solid Earth*, *10*, 1301–1319.

Broggini, F., and R. Snieder (2012), Connection of scattering principles: a visual and mathematical tour, *European Journal of Physics*, *33*, 593–613.

Broggini, F., R. Snieder, and K. Wapenaar (2012a), Focusing the wavefield inside an unknown 1D medium: Beyond seismic interferometry, *Geophysics*, *77*(5), A25—-A28.

Broggini, F., R. Snieder, and K. Wapenaar (2012b), Focusing inside an unknown medium using reflection data with internal multiples: numerical examples for a laterally-varying velocity model, spatially-extended virtual source, and inaccurate direct arrivals, in *SEG Technical Program Expanded Abstracts 2012*, pp. 1–5, Society of Exploration Geophysicists.

Broggini, F., R. Snieder, and K. Wapenaar (2014), Data-driven wavefield focusing and imaging with multidimensional deconvolution: Numerical examples for reflection data with internal multiples, *Geophysics*, *79*(3), WA107—-WA115.

Carvalho, P. M., A. B. Weglein, and R. H. Stolt (1992), Nonlinear inverse scattering for multiple suppression: Application to real data. Part I, in *SEG Technical Program Expanded Abstracts 1992*, pp. 1093–1095, Society of Exploration Geophysicists.

Christian, L. (1997), Cretaceous subsurface geology of the Middle East region, *GeoArabia*, *2*(3), 239–256.

Claerbout, J. F. (1968), Synthesis of a layered medium from its acoustic transmission response, *Geophysics*, *33*(2), 264—-269, doi:https://doi.org/10.1190/1.1439927.

Claerbout, J. F. (1971), Toward a unified theory of reflector mapping, *Geophysics*, *36*, 467–481.

Claerbout, J. F. (1985), *Fundamentals of Geophysical Data Processing: With Applications to Petroleum Prospecting*, Blackwell Scientific Publications.

Coates, R. T., and A. B. Weglein (1996), Internal multiple attenuation using inverse scattering: Results from prestack 1 & 2D acoustic and elastic synthetics, in *SEG Technical Program Expanded Abstracts 1996*, pp. 1522—-1525, Society of Exploration Geophysicists.

Cornwell, J. F. (1997), *Group theory in physics: an introduction*, Academic Press.

Corones, J. P., M. E. Davison, and R. J. Krueger (1983), Direct and inverse scattering in the time domain via invariant imbedding equations, *The Journal of the Acoustical Society of America*, *74*(5), 1535–1541, doi:10.1121/1.390166.

Cui, T., T. S. Becker, D.-j. V. Manen, J. E. Rickett, and I. Vasconcelos (2018), Marchenko Redatuming in a Dissipative Medium : Numerical and Experimental Implementation, *Physical Review Applied*, *10*(1), 1, doi:10.1103/PhysRevApplied.10.044022.

Da Costa Filho, C. A., M. Ravasi, A. Curtis, and G. A. Meles (2014), Elastodynamic Green's function retrieval through single-sided Marchenko inverse scattering, *Physical Review E - Statistical, Nonlinear, and Soft Matter Physics*, *90*(6), doi:10.1103/PhysRevE.90.063201.

Davydenko, M., and D. J. Verschuur (2017), Full-wavefield migration: Using surface and internal multiples in imaging, *Geophysical Prospecting*, *65*(1), 7—-21, doi:10.1111/1365-2478.12360.

de Hoop, A. T. (1995), *Handbook of radiation and scattering of waves: Acoustic waves in fluids, elastic waves in solids, electromagnetic waves*, Academic Press, London.

De Hoop, M. (1992), Directional decomposition of transient acoustic wave fields, Ph.D. thesis, Delft University of Technology.

de Hoop, M. V. (1996), Generalization of the Bremmer coupling series, *Journal of Mathematical Physics*, *37*(7), 3246–3282.

de Hoop, M. V., and A. T. de Hoop (1994), Elastic wave up/down decomposition in inhomogeneous and anisotropic media: an operator approach and its approximations, *Wave Motion*, *20*(1), 57–82.

Devaney, A. J. (1982), A filtered backpropagation algorithm for diffraction tomography, *Ultrasonic imaging*, *4*(4), 336–350.

Dix, C. H. (1955), Seismic velocities from surface measurements, *Geophysics*, *20*(1), 68—-86.

Doherty, S. M., and J. F. Claerbout (1976), Structure independent velocity estimation, *Geophysics*, *41*(5), 850—-881.

Dragoset, B., E. Verschuur, I. Moore, and R. Bisley (2010), A perspective on 3D surface-related multiple elimination, *Geophysics*, *75*(5), 75A245—-75A261.

Dukalski, M., and K. de Vos (2017), Marchenko inversion in a strong scattering regime including surface-related multiples, *Geophysical Journal International*, *212*(2), 760–776, doi:10.1093/gji/ggx434.

Dukalski, M., E. Mariani, and K. de Vos (2018), Short Period Internal De-multiple Using Energy and Causality Constrained Bandlimited Marchenko Redatuming, *EAGE Technical Program Extended Abstracts 2018*, (June 2018).

Dukalski, M., E. Mariani, and K. de Vos (2019), Handling short period scattering using augmented Marchenko autofocusing, *Geophysical Journal International*, *216*(3), 2129—-2133, doi:10.1093/gji/ggy544.

El-Emam, A., A. Mohamed, and H. Al-Qallaf (2001), Multiple attenuation techniques, case studies from Kuwait, in *SEG Technical Program Expanded Abstracts 2001*, pp. 1317—-1320, Society of Exploration Geophysicists, doi:https://doi.org/10.1190/1.1816339.

El-Emam, A., K. S. Al-Deen, A. Zarkhidze, and A. Walz (2011), Advances in interbed multiples prediction and attenuation: Case study from onshore Kuwait, in *SEG Technical Program Expanded Abstracts*, pp. 3546–3550, doi:https://doi.org/10.1190/1.3627936.

Elison, P. (2019), Data-driven focusing and two-way wave modeling with applications to seismic processing and imaging, Ph.D. thesis, Eidgenössische Technische Universität Zürich.

Elison, P., M. Dukalski, C. Mildner, K. De Vos, C. Reinicke, D.-J. Van Manen, and J. O. Robertsson (2019), Short-period internal multiple removal for a horizontally layered overburden using augmented Marchenko focusing, in *81st EAGE Conference and Exhibition 2019*.

Elison, P., M. Dukalski, K. de Vos, D. van Manen, and J. Robertsson (2020), Data-driven control over short-period internal multiples in media with a horizontally layered overburden, *Geophysical Journal International*, doi:10.1093/gji/ggaa020.

Esmersoy, C., and M. Oristaglio (1988), Reverse-time wave-field extrapolation, imaging, and inversion, *Geophysics*, *53*(7), 920–931.

Etgen, J., S. H. Gray, and Y. Zhang (2009), An overview of depth imaging in exploration geophysics, *Geophysics*, *74*(6), WCA5—-WCA17.

Fishman, L. (1993), One-way wave propagation methods in direct and inverse scalar wave propagation modeling, *Radio Science*, *28*(5), 865–876.

Fishman, L., J. J. McCoy, and S. C. Wales (1987), Factorization and path integration of the Helmholtz equation: Numerical algorithms, *The Journal of the Acoustical Society of America*, *81*(5), 1355–1376.

Fishman, L., M. V. de Hoop, and M. J. N. Van Stralen (2000), Exact constructions of square-root {H}elmholtz operator symbols: The focusing quadratic profile, *Journal of Mathematical Physics*, *41*(7), 4881–4938.

Fokkema, J. T., and P. M. van den Berg (2013), *Seismic applications of acoustic reciprocity*, Elsevier.

Frasier, C. W. (1970), Discrete time solution of plane P-SV waves in a plane layered medium, *Geophysics*, *35*, 197–219.

Godin, O. A. (1997), Reciprocity and energy theorems for waves in a compressible inhomogeneous moving fluid, *Wave motion*, *25*(2), 143–167.

Gu, Z.-m., J. Hu, B. Liang, X.-y. Zou, and J.-c. Cheng (2016), Broadband non-reciprocal transmission of sound with invariant frequency, *Scientific reports*, *6*, 19,824.

Haines, A. J., and M. V. de Hoop (1996), An invariant imbedding analysis of general wave scattering problems, *Journal of Mathematical Physics*, *37*, 3854–3881.

Hamada, M. (2015), On Parameterizations of Rotations, *Tamagawa University Quantum ICT Research Institute bulletin*, *5*(1), 25–28.

He, C., M.-H. Lu, X. Heng, L. Feng, and Y.-F. Chen (2011), Parity-time electromagnetic diodes in a two-dimensional nonreciprocal photonic crystal, *Physical Review B*, *83*(7), 75,117.

Holvik, E., and L. Amundsen (2005), Elimination of the overburden response from multicomponent source and receiver seismic data, with source designature and decomposition into PP-, PS-, SP-, and SS-wave responses, *Geophysics*, *70*(2), S43—-S59.

Horowitz, I. M., S. Oldak, and O. Yaniv (1986), An important property of non-minimum-phase multiple-input-multiple-output feedback systems, *International Journal of Control*, *44*(3), 677–688, doi:10.1080/00207178608933626.

Hubral, P., S. Treitel, and P. R. Gutowski (1980), A sum autoregressive formula for the reflection response, *Geophysics*, *45*(11), 1697–1705.

Jakubowicz, H. (1998), Wave equation prediction and removal of interbed multiples, in *SEG technical program expanded abstracts 1998*, pp. 1527–1530, doi:10.1190/1.1820204.

Janashia, G., E. Lagvilava, and L. Ephremidze (2013), Matrix spectral factorization and wavelets, *Journal of Mathematical Sciences*, *195*(4), 445–454.

Johansson, K. H. (1997), Relay feedback and multivariable control, Ph.D. thesis, Lund University.

Kennett, B. L. N., and N. J. Kerry (1979), Seismic waves in a stratified half-space, *Geophysical Journal International*, *57*(3), 557–583.

Kennett, B. L. N., K. Koketsu, and A. J. Haines (1990), Propagation invariants, reflection and transmission in anisotropic, laterally heterogeneous media, *Geophysical Journal International*, *103*, 95–101.

Kong, J. A. (1972), Theorems of bianisotropic media, *Proceedings of the IEEE*, *60*(9), 1036–1046.

Langenberg, K. J., M. Berger, T. Kreutter, K. Mayer, and V. Schmitz (1986), Synthetic aperture focusing technique signal processing, *NDT international*, *19*(3), 177–189.

Levin, F. K. (1971), Apparent velocity from dipping interface reflections, *Geophysics*, *36*(3), 510—-516.

Lin, T. T. Y., and F. J. Herrmann (2013), Robust estimation of primaries by sparse inversion via one-norm minimization, *Geophysics*, *78*(3), 1MJ—-Z75, doi:10.1190/geo2012-0097.1.

Lindell, I. V., A. H. Sihvola, and K. Suchy (1995), Six-vector formalism in electromagnetics of bi-anisotropic media, *Journal of electromagnetic Waves and Applications*, *9*(7-8), 887–903.

Lindsey, C., and D. C. Braun (2004), Principles of seismic holography for diagnostics of the shallow subphotosphere, *The Astrophysical Journal Supplement Series*, *155*(1), 209.

Lyamshev, L. M. (1961), On certain integral relations in the acoustics of a moving medium, in *Soviet Physics Doklady*, vol. 6, p. 410.

Marchenko, V. A. (1955), On reconstruction of the potential energy from phases of the scattered waves, *Dokl. Akad. Nauk SSSR*, *104*(5), 695—-698.

Maynard, J. D., E. G. Williams, and Y. Lee (1985), Nearfield acoustic holography: I. Theory of generalized holography and the development of NAH, *The Journal of the Acoustical Society of America*, *78*(4), 1395–1413.

McMechan, G. A. (1983), Migration by extrapolation of time-dependent boundary values, *Geophysical Prospecting*, *31*(3), 413–420.

Meles, G. A., K. Löer, M. Ravasi, A. Curtis, and C. A. da Costa Filho (2014), Internal multiple prediction and removal using Marchenko autofocusing and seismic interferometry, *Geophysics*, *80*(1), A7—-A11.

Meles, G. A., K. Wapenaar, and J. Thorbecke (2018), Virtual plane-wave imaging via Marchenko redatuming, *Geophysical Journal International*, *214*(1), 508–519, doi:10.1093/gji/ggy143.

Mildner, C., F. Broggini, J. O. A. Robertsson, D. J. van Manen, and S. Greenhalgh (2017), Target-oriented velocity analysis using Marchenko-redatumed data, *Geophysics*, *82*(2), R75—-R86.

Mildner, C., F. Broggini, K. de Vos, and J. O. Robertsson (2019a), Accurate source wavelet estimation using Marchenko focusing functions, *Geophysics*, *84*(6), 1—-68, doi:10.1190/geo2018-0726.1.

Mildner, C., M. Dukalski, P. Elison, K. D. Vos, F. Broggini, and J. O. A. Robertsson (2019b), True amplitude-versus-offset Green's function retrieval using augmented Marchenko focusing, in *81st EAGE Conference and Exhibition 2019*.

Nassar, H., X. C. Xu, A. N. Norris, and G. L. Huang (2017a), Modulated phononic crystals: Non-reciprocal wave propagation and Willis materials, *Journal of the Mechanics and Physics of Solids*, *101*, 10–29.

Nassar, H., H. Chen, A. N. Norris, M. R. Haberman, and G. L. Huang (2017b), Non-reciprocal wave propagation in modulated elastic metamaterials, *Proceedings of the Royal Society A: Mathematical, Physical and Engineering Science*, *473*(2202), 20170,188, doi:10.1098/rspa.2017.0188.

Nita, B. G., and A. B. Weglein (2009), Pseudo-depth/intercept-time monotonicity requirements in the inverse scattering algorithm for predicting internal multiple reflections, *Communications in Computational Physics*, *5*(1), 163.

Noether, E. (1918), Invariante Variationsprobleme. Nachrichten von der Königlichen Gesellschaft der Wissenschaften zu Göttingen. Mathematisch-physikalische Klasse.

Norris, A. N., A. Shuvalov, and A. Kutsenko (2012), Analytical formulation of three-dimensional dynamic homogenization for periodic elastic systems, *Proceedings of the Royal Society A: Mathematical, Physical and Engineering Sciences*, *468*(2142), 1629—-1651.

Norton, S. J. (1992), Annular array imaging with full-aperture resolution, *The Journal of the Acoustical Society of America*, *92*(6), 3202–3206.

Oristaglio, M. L. (1989), An inverse scattering formula that uses all the data, *Inverse Problems*, *5*(6), 1097.

Paige, C. C., and M. A. Saunders (1982a), Algorithm 583: LSQR: Sparse linear equations and least squares problems, *ACM Transactions on Mathematical Software (TOMS)*, *8*(2), 195–209.

Paige, C. C., and M. A. Saunders (1982b), LSQR: An algorithm for sparse linear equations and sparse least squares, *ACM Transactions on Mathematical Software (TOMS)*, *8*(1), 43—-71, doi:10.1145/355984.355989.

Pica, A., G. Poulain, B. David, M. Magesan, S. Baldock, T. Weisser, P. Hugonnet, and P. Herrmann (2005), 3D surface-related multiple modeling, *The Leading Edge*, *24*(3), 292–296.

Porter, R. P. (1970), Diffraction-limited, scalar image formation with holograms of arbitrary shape, *JOSA*, *60*(8), 1051–1059.

Porter, R. P., and A. J. Devaney (1982), Holography and the inverse source problem, *JOSA*, *72*(3), 327–330.

Ravasi, M. (2017), Rayleigh-Marchenko redatuming for target-oriented, true-amplitude imaging, *Geophysics*, *82*(6), S439—-S452, doi:10.1190/geo2017-0262.1.

Ravasi, M., G. Meles, A. Curtis, Z. Rawlinson, and L. Yikuo (2015), Seismic interferometry by multidimensional deconvolution without wavefield separation, *Geophysical Journal International*, *202*(1), 1–16.

Ravasi, M., I. Vasconcelos, A. Kritski, A. Curtis, C. A. da Costa Filho, and G. A. Meles (2016), Target-oriented Marchenko imaging of a North Sea field, *Geophysical Journal International*, *205*(1), 99–104, doi:10.1093/gji/ggv528.

Reinicke, C. (2020), Elastodynamic Marchenko inverse scattering, Ph.D. thesis, Delft University of Technology.

Reinicke, C., and K. Wapenaar (2019), Elastodynamic single-sided homogeneous Green's function representation: Theory and numerical examples, *Wave Motion*, *89*, 245–264, doi:10.1016/j.wavemoti.2019.04.001.

Reinicke, C., G. A. Meles, and K. Wapenaar (2018), Elastodynamic plane wave Marchenko redatuming: theory and examples, in *80th EAGE Conference and Exhibition 2018*.

Rietveld, W. E. A., A. J. Berkhout, and C. P. A. Wapenaar (1992), Optimum seismic illumination of hydrocarbon reservoirs, *Geophysics*, *57*(10), 1334–1345.

Rose, J. H. (2002a), Single-sided focusing of the time-dependent Schrödinger equation, *Physical Review A - Atomic, Molecular, and Optical Physics*, *65*(1), 6, doi:10.1103/PhysRevA.65.012707.

Rose, J. H. (2002b), 'Single-sided' autofocusing of sound in layered materials, *Inverse problems*, *18*(6), 1923.

Rosenbrock, H. (1969), Design of sampled-data multivariable control systems using the inverse nyquist array, *IEEE*, *116*(11), 1929 – 1936, doi:10.1049/piee.1969.0354.

Sattlegger, J. W. (1978), Migration velocity determination: Part I. philosophy, *Geophysics*, *40*(1), 1—-5.

Schneider, W. A. (1978), Integral formulation for migration in two and three dimensions, *Geophysics*, *43*(1), 49—-76, doi:https://doi.org/10.1190/1.1440828.

Shaked, U., and E. Soroka (1986), Explicit Solution to the Unstable Stationary Filtering Problem, *IEEE Transactions on Automatic Control*, *31*(2), 185–189, doi:10.1109/TAC.1986.1104216.

Sherwood, J., and A. Trorey (1965), Minimum-phase and related properties of the response of a horizontally stratified absorptive earth to plane acoustic waves, *Geophysics*, *30*(2), 191—-197, doi:https://doi.org/10.1190/1.1439552.

Singh, S., R. Snieder, J. van der Neut, J. Thorbecke, E. Slob, and K. Wapenaar (2017), Accounting for free-surface multiples in Marchenko imaging, *Geophysics*, *82*(1), R19–R30, doi:10.1190/geo2015-0646.1.

Skingle, C. W., K. H. Heron, and D. R. Gaukroger (1977), *The application of the Hilbert transform to system response analysis*, HM Stationery Office.

Slob, E. (2016), Green's function retrieval and Marchenko imaging in a dissipative acoustic medium, *Physical Review Letters*, *116*(16), 164,301, doi:10.1103/PhysRevLett.116.164301.

Slob, E., K. Wapenaar, F. Broggini, and R. Snieder (2014), Seismic reflector imaging using internal multiples with Marchenko-type equations, *Geophysics*, *79*(2), S63–S76, doi:10.1190/geo2013-0095.1.

Slob, E. C., and K. Wapenaar (2009), Retrieving the Green's function from cross correlation in a bianisotropic medium, *Progress In Electromagnetics Research*, *93*, 255–274.

Smith, J. O. (2007), *Introduction to digital filters: with audio applications*, Julius Smith.

Staring, M., R. Pereira, H. Douma, J. van der Neut, and K. Wapenaar (2018), Source-receiver Marchenko redatuming on field data using an adaptive double-focusing method, *Geophysics*, *83*(6), S579—-S590, doi:10.1190/segam2017-17641718.1.

Stewart, G. W. (1993), On the early history of the singular value decomposition, *SIAM review*, *35*(4), 551–566.

Stoffa, P. L. (2012), *Tau-p: A plane wave approach to the analysis of seismic data*, vol. 8, Springer Science & Business Media.

Stolt, R. H. (1978), Migration by Fourier transform, *Geophysics*, *43*(1), 23–48.

Sun, J., and K. A. Innanen (2019), A plane-wave formulation and numerical analysis of elastic multicomponent inverse scattering series internal multiple prediction, *Geophysics*, *84*(5), 1–62, doi:10.1190/geo2018-0259.1.

Sword, C. (1944), Tomographic determination of interval velocities from CDR data - preliminary results, *SEP*, *44*(4).

ten Kroode, F. (2002), Prediction of internal multiples, *Wave Motion*, *35*(4), 315—-338.

Thomson, C. J. (2015), Seismic transmission operator reciprocity - II: impedance-operator symmetry via elastic lateral modes, *Geophysical Journal International*, *202*, 1071–1087.

Thorbecke, J., E. Slob, J. Brackenhoff, J. van der Neut, and K. Wapenaar (2017), Implementation of the Marchenko method, *Geophysics*, *82*(6), WB29—-WB45.

Trainiti, G., and M. Ruzzene (2016), Non-reciprocal elastic wave propagation in spatiotemporal periodic structures, *New Journal of Physics*, *18*(8), 83,047.

Tunnicliffe-Wilson, G. (1972), The factorization of matricial spectral densities, *Siam J. Appl. Math*, *23*(4), 420–426.

Ursin, B. (1983), Review of elastic and electromagnetic wave propagation in horizontally layered media, *Geophysics*, *48*(8), 1063–1081, doi:10.1190/1.1441529.

Van Borselen, R. G., J. T. Fokkema, and P. M. den Berg (1996), Removal of surface-related wave phenomena-The marine case, *Geophysics*, *61*(1), 202–210.

van der Neut, J., and K. Wapenaar (2016), Adaptive overburden elimination with the multidimensional Marchenko equation, *Geophysics*, *81*(5), T265–T284, doi:10.1190/geo2016-0024.1.

van der Neut, J., J. Thorbecke, K. Mehta, E. Slob, and K. Wapenaar (2011), Controlled-source interferometric redatuming by crosscorrelation and multidimensional deconvolution in elastic media, *Geophysics*, *76*(4), SA63—-SA76.

van der Neut, J., I. Vasconcelos, and K. Wapenaar (2015), On Green's function retrieval by iterative substitution of the coupled Marchenko equations, *Geophysical Journal International*, *203*(2), 792–813, doi:10.1093/gji/ggv330.

van der Neut, J., M. Ravasi, Y. Liu, and I. Vasconcelos (2017), Target-enclosed seismic imaging, *Geophysics*, *82*(6), Q53—-Q66.

Vasconcelos, I., K. Wapenaar, J. van der Neut, C. Thomson, and M. Ravasi (2015), Using inverse transmission matrices for Marchenko redatuming in highly complex media, in *SEG, Expanded Abstracts*, pp. 5081–5086.

Verschuur, D. J. (2013), *Seismic multiple removal techniques: past, present and future*, revised ed ed., EAGE publications.

Verschuur, D. J., A. J. Berkhout, and C. P. A. Wapenaar (1992), Adaptive surfacerelated multiple elimination, *Geophysics*, *57*(9), 1166—-1233, doi:10.1190/1.1443330.

Virieux, J., and S. Operto (2009), An overview of full-waveform inversion in exploration geophysics, *Geo*, *74*(6), WCC1—-WCC26.

Wang, Y. (2015), Frequencies of the Ricker wavelet, *Geophysics*, *80*(2), A31—-A37, doi:10.1190/geo2014-0441.1.

Wapenaar, C. (1996a), Reciprocity theorems for two-way and one-way wave vectors: A comparison, *The Journal of the Acoustical Society of America*, *100*(6), 3508–3518.

Wapenaar, C. P., D. Draganov, J. Thorbecke, and T. Uchida (2003), Relations between codas in reflection and transmission data and their applications in seismic imaging, in *6th SEGJ International Symposium, Tokyo*, pp. 152–159.

Wapenaar, C. P. A. (1996b), One-way representations of seismic data, *Geophysical Journal International*, *127*(1), 178–188.

Wapenaar, C. P. A. (1996c), Reciprocity theorems for two-way and one-way wave vectors: A comparison, *The Journal of the Acoustical Society of America*, *100*(6), 3508–3518.

Wapenaar, C. P. A., and A. J. Berkhout (1989), *Elastic wave field extrapolation: Redatuming of single-and multi-component seismic data*, Elsevier.

Wapenaar, K. (1998), Reciprocity properties of one-way propagators, *Geophysics*, *63*, 1795—-1798.

Wapenaar, K. (2014), Single-sided Marchenko focusing of compressional and shear waves, *Physical Review E*, *90*(6), 63,202.

Wapenaar, K., and J. Fokkema (2004), Reciprocity theorems for diffusion, flow, and waves, *A.S.M.E. J. Appl. Mech.*, *71*(1), 145–150.

Wapenaar, K., and E. Slob (2015), Initial conditions for elastodynamic Green's function retrieval by the Marchenko method, *SEG Technical Program Expanded Abstracts 2015*, pp. 5074–5080, doi:10.1190/segam2015-5916768.1.

Wapenaar, K., and J. van der Neut (2010), A representation for Green's function retrieval by multidimensional deconvolution, *The Journal of the Acoustical Society of America*, *128*(6), EL366—-EL371.

Wapenaar, K., and J. van IJsseldijk (2019), Representations for the Marchenko method for imperfectly sampled data, in *SEG Technical Program Expanded Abstracts 2019*.

Wapenaar, K., J. Fokkema, M. Dillen, and P. Scherpenhuijsen (2000), One-way acoustic reciprocity and its applications in multiple elimination and time-lapse seismics, in *SEG Technical Program Expanded Abstracts 2000*, pp. 2377–2380, Society of Exploration Geophysicists.

Wapenaar, K., F. Broggini, and R. Snieder (2012), Creating a virtual source inside a medium from reflection data: Heuristic derivation and stationary-phase analysis, *Geophysical Journal International*, *190*(2), 1020–1024, doi:10.1111/j.1365-246X.2012.05551.x.

Wapenaar, K., F. Broggini, E. Slob, and R. Snieder (2013), Three-dimensional single-sided Marchenko inverse scattering, data-driven focusing, Green's function retrieval, and their mutual relations, *Physical Review Letters*, *110*(8), 084,301, doi:https://doi.org/10.1103/PhysRevLett.110.084301.

Wapenaar, K., J. Thorbecke, J. van der Neut, F. Broggini, E. Slob, and R. Snieder (2014a), Marchenko imaging, *Geophysics*, *79*(3), WA39–WA57, doi:10.1190/geo2013-0302.1.

Wapenaar, K., J. Thorbecke, J. van der Neut, F. Broggini, E. Slob, and R. Snieder (2014b), Green's function retrieval from reflection data, in absence of a receiver at the virtual source position, *The Journal of the Acoustical Society of America*, *135*(5), 2847–2861.

Wapenaar, K., J. van der Neut, and E. Slob (2016a), Unified double- and single-sided homogeneous Green's function representations, in *Proc. R. Soc. A*, vol. 472, p. 20160162, The Royal Society.

Wapenaar, K., J. Thorbecke, and J. van der Neut (2016b), A single-sided homogeneous Green's function representation for holographic imaging, inverse scattering, time-reversal acoustics and interferometric Green's function retrieval, *Geophysical Journal International*, *205*(1), 531–535.

Wapenaar, K., J. Brackenhoff, J. Thorbecke, J. van der Neut, E. Slob, and E. Verschuur (2018), Virtual acoustics in inhomogeneous media with single-sided access, *Scientific reports*, *8*(1), 2497, doi:10.1038/s41598-018-20924-x.

Ware, J. A., and K. Aki (1969), Continuous and Discrete Inverse-Scattering Problems in a Stratified Elastic Medium . I . Plane Waves at Normal Incidence, *The journal of the Acoustical Society of America*, *45*(4), 911—-921, doi:10.1121/1.1911568.

Weglein, A. B., F. A. Gasparotto, P. M. Carvalho, and R. H. Stott (1997), An inverse-scattering series method for attenuating multiples in seismic reflection data, *Geophysics*, *62*(6), 1975–1989.

Weglein, A. B., F. V. Araújo, P. M. Carvalho, R. H. Stolt, K. H. Matson, R. T. Coates, D. Corrigan, D. J. Foster, S. A. Shaw, and H. Zhang (2003), Inverse scattering series and seismic exploration, *Inverse problems*, *19*(6), R27.

Wiener, N. (1955), On the factorization of matrices, *Commentarii Mathematici Helvetici*, *29*(1), 97–111.

Wiggins, J. W. (1988), Attenuation of complex water-bottom multiples by wave-equation-based prediction and subtraction, *Geophysics*, *53*(12), 1503–1637, doi:https://doi.org/10.1190/1.1442434.

Williams, E. G., and J. D. Maynard (1980), Holographic imaging without the wavelength resolution limit, *Physical review letters*, *45*(7), 554.

Willis, J. R. (2011), Effective constitutive relations for waves in composites and metamaterials, *Proceedings of the Royal Society A: Mathematical, Physical and Engineering Sciences*, *467*(2131), 1865–1879.

Willis, J. R. (2012), The construction of effective relations for waves in a composite, *Comptes Rendus Mécanique*, *340*(4-5), 181—-192.

Wilson, G. (1969), Factorization of the covariance generating function of a pure moving average process, *SIAM Journal on Numerical Analysis*, *6*(1), 1—-7.

Wu, S. F. (2004), Hybrid near-field acoustic holography, *The Journal of the Acoustical Society of America*, *115*(1), 207–217.

Yilmaz, Ö. (2001), *Seismic data analysis: Processing, inversion, and interpretation of seismic data*, Society of exploration geophysicists.

Zakharov, V. E., and A. B. Shabat (1973), Interaction between solitons in a stable medium, *Sov. Phys. JETP*, *37*(5), 823–828.

Zhang, L., and E. Slob (2018), Free-surface and internal multiple elimination in one step without adaptive subtraction, *Geophysics*, *84*(1), A7—-A11, doi:10.1190/geo2018-0548.1.

Curriculum Vitæ

Christian Reinicke Urruticoechea

17-08-1992	Born in Munich, Germany.

Education

2002–2011	Secondary school Werner Heisenberg Gymnasium, Garching (Germany).
2011–2013	B.Sc. in physics Technical University of Munich, Garching (Germany).
2013–2015	M.Sc. in applied geophysics Delft University of Technology, Delft (Netherlands). Distinction: *cum laude*
2015–2019	Ph.D. research Delft University of Technology, Delft (Netherlands). Promotor: Prof. dr. ir. C. P. A. Wapenaar
Since 2020	Research geophysicist Aramco Overseas Company B.V., Delft (Netherlands).

List of publications

List of journal publications

[1] C. Reinicke, and K. Wapenaar (2019), Elastodynamic single-sided homogeneous Green's function representation: Theory and numerical examples, *Wave Motion*, 89, 245–264.

[2] K. Wapenaar, and C. Reinicke (2019), An acoustic imaging method for layered non-reciprocal media, *EPL (Europhysics Letters)*, 125(3), 34003.

[3] K. Wapenaar, and C. Reinicke (2019), Unified wave field retrieval and imaging method for inhomogeneous non-reciprocal media, *The Journal of the Acoustical Society of America*, 146(1), 810–825.

[4] C. Reinicke, M. Dukalski, and K. Wapenaar, Comparison of monotonicity challenges encountered by the inverse scattering series and the Marchenko de-multiple method for elastic waves, currently under review by *Geophysics.*

List of conference abstracts

[1] C. Reinicke, G. J. A. Groenestijn, and G. Blacquière (2016), Seismic blending and deblending in 3D, *78th EAGE Conference and Exhibition 2016.*

[2] C. Reinicke, and K. Wapenaar (2017), Elastodynamic single-sided homogeneous Green's function representation - theory and examples, *79th EAGE Conference and Exhibition 2017.*

[3] C. Reinicke, G. A. Meles, and K. Wapenaar (2018), Elastodynamic plane wave Marchenko redatuming: theory and examples, *80th EAGE Conference and Exhibition 2018.*

[4] G. A. Meles, C. Reinicke, K. Wapenaar, J. Brackenhoff, and J. W. Thorbecke (2018), Focusing conditions: a comparison between different Marchenko imaging strategies, *80th EAGE Conference and Exhibition 2018 Workshop Programme.*

[5] I. Vasconcelos, C. Reinicke, and J. Brackenhoff (2019), Estimating overburden-only transmission waveforms from surface reflection data, *80th EAGE Conference and Exhibition 2018.*

[6] P. Elison, M. Dukalski, C. Mildner, K. de Vos, C. Reinicke, D. J. van Manen, and J. O. A. Robertsson (2019), Short-period internal multiple removal for a horizontally layered overburden using augmented Marchenko focusing, *81st EAGE Conference and Exhibition 2019.*

[7] C. Reinicke, M. Dukalski, and K. Wapenaar (2019), Tackling different velocity borne challenges of the elastodynamic Marchenko method, *81st EAGE Conference and Exhibition 2019.*

[8] C. Reinicke, M. Dukalski, and K. Wapenaar (2019), Do we need elastic internal de-multiple offshore Middle East, or will acoustic Marchenko suffice?, *KOC Workshop: Seismic Multiples - The Challenges and the Way Forward.*

[9] C. Reinicke, M. Dukalski, and K. Wapenaar (2020), Effective media theory consistent multiple-elimination with Marchenko-equation-based methods, submitted to *82nd EAGE Conference and Exhibition 2020.*

[10] C. Reinicke, M. Dukalski, and K. Wapenaar (2020), Elastodynamic Marchenko method: advances and remaining challenges, submitted to *82nd EAGE Conference and Exhibition 2020.*

Acknowledgements

Writing this thesis would not have been possible
without the unconditional support of coffee.

Me, 2020.

At this final point, I would like to thank the many people who have contributed to my thesis, and who have supported me during this period of my life. Since there have been so many of you, I hope to remember everyone and apologize if anyone is missing.

Foremost, I would like to express my deep gratitude to my promotor **Prof. Kees Wapenaar** and my industry supervisor **Dr. Marcin Dukalski**. Throughout my PhD, and beyond, I have perceived you as scientific role models who honor the title 'Doktorvater' as we say in German.

Kees, I remember very well when you called me to ask whether I was interested in doing a PhD at TU Delft. Initially, my excitement about this opportunity was still overshadowed with a worry whether this was the right path. Today, I know that this worry was a waste of time, and I happily look back at four wonderful years! Throughout the entire project, you always granted me a lot of freedom, which was challenging in the beginning, but helped me to become an independent researcher and allowed me to find my own research interests. By critically questioning my work, you often assisted me to find remaining flaws in my reasoning and taught me how to argue with equations. However, you still have to teach me how you manage to review papers and abstracts with such a high speed and with such a high attention to detail.

Marcin, it feels like yesterday when you visited us to share some thoughts about the Marchenko method, in particular, a conceptual strategy to tackle the elastic case. Since I had a similar idea, it was natural to team-up (although I was much less aware of all the theoretical challenges ahead). Very soon we developed a cyclic routine of discussing an idea, me trying to work it out and you critically questioning the result. This process lead us to several side tracks, required a lot of endurance and filled up my mailbox to the extent where its maximum storage capacity was reached, more than once. However, eventually, we identified fundamental challenges of the elastic Marchenko method and explored different solution strategies. Apart from your contributions to the actual research, I am very grateful for your efforts to help me improve my scientific writing and presentation skills.

Sometimes PhDs are pictured as individuals working in nearly complete isolation. However, these days, working on Marchenko at TU Delft makes you part of an entire team. In the beginning, there were so many black-box equations and algorithms, which slowly demystified, thanks to the support and patience of **Jan**, **Evert**, **Kees** and particularly **Joost**. Moreover, it was a great pleasure to be surrounded by a group of knowledgeable and helpful PhD-buddies with a closely-related research focus: **Lele**, **Myrna**, **Joeri**, **Binkun**, **Aydin** and **Johno**, thanks for your collaboration, countless discussions and mental support. Last but not least, I would like to thank my dear friend **Giovanni** for teaching me about reciprocity theorems (although you always insist on plane waves) as well as his life wisdoms.

Initially, the gap between myself and experienced researchers appeared to be tremendous. However, thanks to the networking opportunities within the Waves project, I quickly felt like an integrate part of the research community and could build valuable connections with researchers from academia and industry. The Waves meetings paved the way for fruitful collaborations, particularly with **Ivan Vasconcelos** from Utrecht university, **Patrick Elison** from ETH Zürich and **Marcin Dukalski**. The latter collaboration has culminated in an internship at Aramco Overseas Company B.V., where I had the privilege to regularly receive advice, not only by Marin, but also by the other team members, particularly **Roald van Borselen**, **Rob Hegge**, **Rolf Baardman** and **Mikhail Belonosov**. This project helped me to make my initially rather theoretical PhD research more industry-relevant. Moreover, the expertise of the Aramco office facilitated my work significantly, e.g. support by **Jewoo Yoo** to reverse-time migrate my data, or by **Rob** to translate the summary of my thesis to Dutch, which requires quite some creativity when it comes to geophysics jargon. Apart from research support, I also enjoyed daily lunch discussion with **Diego**, **Apostolos**, **Yimin**, **Paul**, **Hannes**, **Janny**, **Myrna** and **Chiel**.

While focused on our research, it can be easy to forget about the world around us. Luckily, we have had a very supportive group of **secretaries** who were always available and could take care of nearly everything. Thank you!

During my time at TU Delft, there were three major waves of PhDs and Postdocs, who, to me, are the old guys, my generation and the new guys. When I started, the old guys gave me a very warm welcome and quickly introduced me to all the unwritten need-to-knows such a as the desktop computer that actually was the secret good-coffee machine. Daily breaks with **Koen**, **Kevin**, **Helena**, **Navid**, **Iris** and many other guys soon turned this office into my second home. Moreover, the old guys were very patient with passing on crucial software and geophysics knowledge:

Boris frequently saved me when it came to handling seismic unix, **Carlos** always had valuable advice on modeling issues, **Niels** refreshed my knowledge on wavefield decomposition, **Pieter** facilitated my life by sharing great latex templates including the one for this thesis, and of course **Max** had a lot to teach. When you try to think of a correlation between Fourier transforms and pregnant cows, and how this correlation can help you to generate a tikz figure, then **Max** is your guy! I am not sure whether I would like to thank, or blame, you for the Max-lunch-conversations, but they were definitely very entertaining.

Being surrounded by several guys, who started their projects approximately at the same time, turned the PhD journey into a group experience and enriched my life with many new friends. One of them is **Gil** who was also part of the Waves project. You have taught me a lot during our discussions about modeling elastic waves, but most importantly you have been a great buddy to go for beers and chat about life outside the walls of TU Delft. With **Reuben** joining the office shortly after me, I had the good fortune to share everyday life with a close friend. Spending time with you, **Katja** and your wonderful kids, **Anfim** and **Miron**, has always been a great treatment for my mind! Another memorable office buddy is **Lisanne** who did not only start, but also finish, her PhD on exactly the same days as myself. You have been an always cheerful office mate, which made it easy to forget about the occasional writing-related frustrations.

After about one and a half years of research, I started to understand how challenging my research questions actually were. This realization had the potential to turn excitement into frustration. Nevertheless, during this period, the first new guys started joining and did a great job in keeping my mood up: **Diego** distracted me with pub evenings, **Martha** took care of my fitness by signing me up for a half marathon and hiking up the Kilimanjaro with me (you made it, I tried hard...), **Musab** kept me entertained with his great sense of humor, **Billy** invited me to the always entertaining Colombian nights, **Florencia** made sure I survived the writing period ("in order to complete your PhD, you have to stay alive!"), and many others. Guys, I am really glad to have met you and hope as many of you as possible will stay close-by!

Last but not least, dear **friends from outside of the university**, **parents**, **siblings** and **extended family**, all this work would not have been worth it without having you in my life. Thanks for your love and support.

Chris